Characterization of lamellar or nanostrutured materials based on transition metal oxides for liquid phase catalysis

Ghinwa Fayad

Normandie Université

THÈSE

Pour obtenir le diplôme de doctorat

Spécialité CHIMIE

Préparée au sein de l'Université de Caen Normandie

Characterization of lamellar or nanostrutured materials based on transition metal oxides for liquid phase catalysis

Présentée et soutenue par
Ghinwa FAYAD

Thèse soutenue publiquement le 05/12/2018 devant le jury composé de		
Mme GUYLÈNE COSTENTIN	Directeur de recherche, UNIVERSITE PARIS 6 PIERRE ET MARIE CURIE	Rapporteur du jury
M. STEPHANE LORIDANT	Chargé de recherche HDR, UNIVERSITE LYON 1 CLAUDE BERNARD	Rapporteur du jury
M. PHILIPPE BOULAY	Directeur de recherche, 14 ENSI de Caen	Membre du jury
M. MARCO DATURI	Professeur des universités, UNIVERSITE CAEN NORMANDIE	Président du jury
Mme NATHALIE TANCHOUX	Chargé de recherche HDR, ENSCM MONTPELLIER	Membre du jury
M. GUILLAUME CLET	Maître de conférences HDR, UNIVERSITE CAEN NORMANDIE	Directeur de thèse

Thèse dirigée par GUILLAUME CLET, Laboratoire catalyse et spectrochimie (Caen)

UNIVERSITÉ CAEN NORMANDIE

ED 508 NC Normande de Chimie

LCS Laboratoire Catalyse & Spectrochimie

To my parents - - -

To my sisters - - -

To the soul of grandfather Najib - - -

“ Nothing is impossible,

the word itself says “I’m possible”! ”

Audrey Hepburn

ACKNOWLEDGEMENTS

This section is dedicated to all people who in one way or another have been a part of this long journey.

This work has been accomplished at Laboratoire Catalyse et Spectrochimie (LCS) - Caen, from October 2015 to December 2018 under the supervision of Dr. Guillaume Clet.

I am very honored that Dr. Stéphane Loridant, Chargé de Recherches at Loboratoire Catalyse et l'Environnement de Lyon and Dr. Guylène Costentin, Directeur de Recherche at Laboratoire Réactivité de Surface at Sorbonne Université - Paris, kindly accepted to be the referees of this work.

My sincere thanks to the other jury members, Dr. Nathalie Tanchoux, Chargé de Recherches at Ecole National Superieur de chimie de Montpellier, Dr. Philippe Boullay, Directeur de Recherches at Laboratoire de Cristallographie et Science de Matériaux (CRISMAT) and to Dr. Marco Daturi, Professor at Université Caen Normandie, for accepting to examine this research work.

I would like to express my deepest gratitude to my supervisor, Dr. Guillaume Clet, for his guidance, valuable and constructive suggestions during the planning and development of this research. His patience, tranquility and willingness to generously give his time have been very much appreciated. Without his help this work could not be accomplished.

I gratefully thank Dr. Philippe Boullay who shared his precious time, valuable knowledge, ideas and special expertise especially in the refinement of the PXRD patterns.

Many thanks to Sylvie Collin, a technical assistant at Laboratoire de Cristallographie et Science de Matériaux (CRISMAT), who taught and helped me, at the beginning of this work, to synthesize the starting precursors of the layered solids.

I would like to express my gratitude to Dr. Moussa Zaarour, a researcher at Laboratoire Catalyse et Spectrochimie (LCS), for his sincere and hard work on the catalytic activity of the layered solids, without him this part would not be fulfilled.

Special thanks are addressed to all LCS staff (technicians, engineers, …) for all their helpful services and to all my colleagues who have been like my family during these three years.

French Ministry of Education and Research and the Labex EMC3 (project EMC3 - 2016 - PC - OXYLAC) are greatly acknowledged for the financial supports.

Finally, to all my family there are no words that can adequately express my gratitude, happiness and appreciation to have you in my life. Thank you so much from the bottom of my heart for your love, support, help and understanding. As Desmond Tutu said "*You don't choose your family. They are God's gift to you, as you are to them*".

TABLE OF CONTENTS

GENERAL INTRODUCTION

The discovery of crude oil in the 19th century, created an inexpensive liquid fuel source that helped industrialize the world and improved standards of living [1]. Up to now, these non- renewable feedstocks are used to provide liquid hydrocarbons mainly used in the transportation sector and to supply unsaturated hydrocarbons that serve as a feedstock for the manufacturing of valuable chemicals and products [2, 3].

However, the diminishing of the non-renewable fossil fuels resources and eventually increasing in oil prices, increasing demand for energy in the future [4] and realizing the drawbacks associated with the use of these sources such as global warming issues [5], the combustion of fossil fuels has been considered as the largest human sources of green house gas emissions, particularly CO_2 [5], stimulate researchers around the world to find alternative sources of energy and organic carbon.

Biomass, a non-fossil feedstock, is comprised mainly of plant and plant derived materials in addition to forest residues, manure, waste oil and fats [4, 6]. It represents a potential alternative source of liquid fuels and valuable chemicals since it is a widely available carbon-neutral renewable energy source and has low impact on the environment due to its lower or neutral green house gas emissions if efficient production methods were developed [7, 8].

Despite all of that, biomass conversion into the desired products is not an easy task due to its diversity, complexity and high oxygen content; it often requires multi-step reactions that are not successfully achieved without the use of an efficient catalyst [9].

Homogeneous acid catalysts such as hydrochloric and hydrosulfuric acids were widely used for petroleum refining due to their high activity and selectivity since they are totally soluble in the reaction media thus making all their acidic sites accessible to the substrates [10]. However, due to their toxicity and corrosiveness [11] and in order to reduce capital and operating costs associated with separation and purification steps the use of heterogeneous catalysts was promoted [12].

Therefore, from 1940s onward, the homogeneous catalysts were replaced with solid acid catalysts in the petroleum refining [13]. This logic also applies for biomass conversions. Recently, several solid acid catalysts have been used for the biomass conversion processes such as zeolites [11], supported solid acid catalysts [10], heteropoly compounds [14], metal oxides [14] such as niobic acid, tungsten trioxides and titanium oxides, and acidic and ion-exchange resins [14]. All these catalysts can show noticeable catalytic activity, but they may also exhibit some drawbacks that limit their applicability in such conversions. Coke and tar formation can

be a problem but it should be also noted that biomass products are generally associated with water. Besides because of the polymeric nature of many biomass molecules, catalysts employed should be stable in aqueous or highly polar media.

Consequently, the development of a new type of solid acid catalysts exhibiting high catalytic activity and stability in aqueous media is crucial. Lamellar or Layered materials could be of a particular interest as they are stable, combine acidity inherent to conventional oxides (Nb_2O_5,...), possess layered structures and can accommodate transition metal oxides affecting both acid amount and acid strength [15]. Moreover, they exhibit an important feature that does not exist in any other solid acid catalyst. They are characterized by a two dimensional expandable interlayer space, a free space localized between the layers of the host solid, dominated by the presence of the active sites [16]. This space can accommodate several guest species such as anions, complexes and organic chemicals, a process known as intercalation [16], therefore, the resultant intercalated compounds are interesting as they combine the advantages of both the host and the intercalated guest species.

These catalysts had been used since the beginning of the petrochemical industry. In 1936, the hydrocracking process was based on acid-treated clays (a group of cationic layered solids) [17, 18]. Some reactions such as methylation, esterification and dehydration [19] are catalyzed by these acid catalysts.

The possible use of layered materials in biomass conversions deserves specific studies which concern their activation, the characterization of their structure, their acidity and their ability for intercalation and also their evaluation as catalyst. Noteworthy, many previous characterizations of these materials were conducted in the gas phase while little was addressed in the liquid phase. This is all the more important as many reactions involving biomass are carried out in the liquid phase or in presence of various quantities of water.

Accordingly, our work is devoted to the characterization of layered materials based on transition metal oxides such as $HNbMoO_6$, $HNbWO_6$, H_2WO_4 and $H_2W_2O_7$. In the frame of a collaboration project within the LABEX EMC3 (project Oxylac) with the laboratory CRISMAT, new types of layered catalysts based on Nb and W transition metal oxides and characterized by an Aurivillius phases and a stair-like structure were also used. Several of these different materials were characterized directly in the liquid phase, hence closer to the actual reaction media, in order to understand the influence of the intercalant functions such as pyridine, n-alkylamines, n-alcohols and 2,5-hexanediol on the structural modifications and to

characterize the acidity and the catalytic active sites. The catalytic activity of the layered oxides have also been examined through a newly developed catalytic test (cyclization of 2,5-hexanediol) under various reaction conditions.

References

1 G. W. Huber, S. Iborra and A. Corma, *Chem. Rev.*, 2006, **106**, 4044–4098.

2 J. C. Serrano-Ruiz and J. A. Dumesic, *Energy Environ. Sci.*, 2011, **4**, 83–99.

3 K. R. Vuyyuru and P. Strasser, *Catal. Today*, 2012, **195**, 144–154.

4 J. C. Serrano-Ruiz, R. Luque and A. Sepúlveda-Escribano, *Chem. Soc. Rev.*, 2011, **40**, 5266–5281.

5 C. Day and G. Day, *Econ. Model.*, 2017, **63**, 153–160.

6 P. Bhaumik and P. L. Dhepe, *Catal. Rev.*, 2016, **58**, 36–112.

7 G. Chen, J. Andries and H. Spliethoff, *Renew. Energy*, 2003, **28**, 985–994.

8 J. N. Chheda, G. W. Huber and J. A. Dumesic, *Angew. Chem. Int. Ed.*, 2007, **46**, 7164–7183.

9 R. Rinaldi and F. Schüth, *Energy Environ. Sci.*, 2009, **2**, 610–626.

10 M. Hara, K. Nakajima and K. Kamata, *Sci. Technol. Adv. Mater.*, 2015, **16**, 034903.

11 P. Gupta and S. Paul, *Catal. Today*, 2014, **236**, 153–170.

12 A. J. Ragauskas, C. K. Williams, B. H. Davison, G. Britovsek, J. Cairney, C. A. Eckert, W. J. Frederick Jr., J. P. Hallett, D. J. Leak, C. L. Liotta, J. R. Mielenz, R. Murphy, R. Templer and T. Tschaplinski, *Science*, 2006, **311**, 484–489.

13 A. Takagaki, C. Tagusagawa, S. Hayashi, M. Hara and K. Domen, *Energy Environ. Sci.*, 2010, **3**, 82–93.

14 F. Guo, Z. Fang, C. C. Xu and R. L. Smith Jr., *Prog. Energy Combust. Sci.*, 2012, **38**, 672–690.

15 C. Tagusagawa, A. Takagaki, K. Takanabe, K. Ebitani, S. Hayashi and K. Domen, *J. Phys. Chem. C*, 2009, **113**, 17421–17427.

16 M. Ogawa and K. Kuroda, *Chem. Rev.*, 1995, **95**, 399–438.

17 M. L. Occelli, S. D. Landau and T. J. Pinnavaia, *J. Catal.*, 1984, **90**, 256–260.

18 M. L. Occelli and R. J. Rennard, *Catal. Today*, 1988, **2**, 309–319.

19 S. Cheng, *Catal. Today*, 1999, **49**, 303–312.

CHAPTER ONE

BIBLIOGRAPHIC PART

Over the past centuries, the developed world has enjoyed cheap and abundant energy supplies from non-renewable sources such as oil, coal and natural gas [1]. However, large scale utilization of fossil fuels is associated with several important issues such as availability, global warming and unequal geographic distribution of reserves worldwide [2]. Fossil fuel resources are finite and their current consumption rate is higher than their natural regeneration cycle leading progressively to depletion thus becoming more and more expensive and less attractive as a carbon source [1, 2]. In addition to that, the combustion of fossil fuels or their derivatives for the production of heat and power is associated with a net increase of greenhouse gas levels worldwide such as CH_4 and N_2O and in particular CO_2 therefore boosting global warming [3]. Besides, fossil fuel reserves are not equally distributed worldwide, i.e. 60% of the oil reserves and 41% of natural gas supplies are situated in the middle-east countries and only three countries (China, USA and Russia) account for 60% of the world coal reserves [2]. This situation can create political and security problems worldwide, can lead to economic instabilities and requires long distance transportation of fossil fuel resources [2]. These drawbacks have propelled researchers toward discovering and investigating alternative means of energy production using environmentally friendly renewable sources. Similar questions arise for the production of the chemicals currently based on petroleum derivatives. Therefore, one solution to this problem might be found in the use of biomass as a possible feedstock [4, 5, 6].

Biomass is a non-fossil feedstock and may be comprised of complex industrial wastes such as saw dust or pulp process wastes and of all plant and plant derived materials including animal manure, clean wood waste from landfills, forest and plant residues such as lignocellulosic materials and agricultural pumping [7, 8]. It is considered as one of the promising choices as an alternative resource to fossil fuels due to several reasons. Firstly, biomass is a very valuable feed stock, it is the only sustainable renewable source of energy and organic carbon currently available on Earth, which in the future could replace crude oil and gas as the current major raw materials and eventually decreases our reliance on non-renewable fossil fuel resources [1, 9]. Secondly, it is abundant and locally accessible in most countries that necessitates no liquid fuel transportation from one place to another [2]. Thirdly, it has a low impact on the environment as it generates lower greenhouse gas emissions in comparison to fossil fuel combustion, statistics showed that ethanol produced from sugar cane emits 91% less CO_2 than gasoline, on the contrary only 18% CO_2 was emitted upon producing ethanol from maize [10, 11]. As a consequence, biomass and biomass-derived chemicals have received

considerable attention as a sustainable feedstock that can replace diminishing fossil fuel resources for the production of energy or chemicals [12].

1.1. Catalytic properties for biomass conversion

Many different routes of biomass transformation are considered but these conversion processes often necessitates the use of catalysts [10]. These transformation processes have to take into account the wide variety of biomass types such as wood and agricultural products, solid waste, wet and dry manures, landfill gas and saw dust [7]. This complexity implies series of different reactions such as hydrolysis, dehydration, hydrogenation, hydrogenolysis, C-C cracking, isomerisation and selective oxidation [1, 13]. In this first section, the main properties of catalysts able to convert biomass efficiently will be highlighted.

1.1.1. Active sites

Among the biomass conversion reactions, it is noteworthy that several reactions such as hydrolysis, dehydration, cracking, isomerization and hydrogenolysis often require acid catalysts [10]. For instance, acid catalysis plays a significant role in the saccharification of cellulosic biomass (cellulose hydrolysis) [10]. The obtained sugars can subsequently be converted into a range of industrially important chemicals including ethanol, hydrocarbons and starting materials for polymers. We will focus on acidic properties. Nevertheless, acid catalysis plays an important role for many bio-based processes, and for this reason will be the focus of this work, metal or basic catalysts have also a role in bio-refinery processes. There are several important transformations of oxygenated molecules that take place more efficiently with base catalysts such as aldol-condensation, which is a key intermediate reaction to produce large organic molecules using carbohydrate-derived carbonyl compounds [1, 14] as well as depolymerization of lignin that is usually more efficient with base catalyzed reactions than with acid-catalyzed ones as it lessens the undesirable formation of coke and tar [10].

The type of acid catalysts (Brønsted or Lewis acidity) can have a great influence on the activity and selectivity of several biomass conversion processes. For example, the effect of Lewis acidity on the catalytic activity of cellulose hydrolysis was examined using the salts of $PW_{12}O_{40}^{3-}$ ($M_{3/n}PW_{12}O_{40}$) with different kinds of metal ions such as Ag^{2+}, Ca^{2+}, Co^{2+}, Y^{3+}, etc…. Results revealed that the rate of the reaction increases with Lewis acidity of the cation

[15]. Additionally, Shimizu et al. [16] reported the importance of solid Lewis acids in the Friedel-Crafts alkylation and acylation of aromatic compounds with metal salts of heteropolyacids and hydrolysis of cellulose into saccharides.

Similar test reaction (hydrolysis of cellobiose) was investigated to understand the effect of Brønsted acidity on the conversion yield. To achieve the goal, Schimizu et al. [15] used several catalysts with different Brønsted acidity such as $H_3PW_{12}O_{40}$, $H_4SiW_{12}O_{40}$, $HClO_4$, H_2SO_4 and H_3PO_4, respectively. Results showed that higher conversion yields were obtained with stronger Brønsted acidity. Therefore, not only the strength of the catalyst should be taken into consideration in the design of an active catalyst for green chemical and biomass conversion processes but also the type of the active sites.

1.1.2. Porosity and selectivity of the catalyst

Porosity is one of the most important properties of solid materials, it is crucial for many applications such as catalysis, necessary to create sufficiently high surface areas to achieve high activity [10] and important in tuning reaction selectivity by controlling reagent, product and transition-state selectivity [17]. Reagent selectivity occurs when only one type of reactant molecule with similar dimension to the pore size can be transported and further processed into the desired products. If several products are formed, product selectivity allows only those with dimensions close or similar to the pore size to diffuse out as the observed products. Finally, transition-state selectivity occurs when reactions for which certain transition-states have a geometry compatible with the space available in the cavities, thus preventing formation of several products [10, 17].

Macroporous and mesoporous solid materials are the first choice in biomass conversion processes since most of biomass components have high molecular weight (10^3 to 10^7 g/mol^{-1}) [9, 10]. Macroporous materials can be highly active due to the high exposure of their active sites to very bulky substrates; however, there are no restrictions that would direct the reaction pathway to selective transformations. Therefore, mesoporous materials are more suitable as they have well defined pore architecture, narrow pore size distribution and pore size from 2 to 30 nm allowing the processing of large organic molecules present in wood-based biomass feedstock such as lignocelluloses [18, 19]. For instance, Stöcker et al. [8] and Antonakou and co-workers [20] had shown that mesoporous MCM-41 was the most favourable regarding the formation of phenols and hydrocarbons from lignocellulose (originated from beech wood) and miscantus (energy crop).

1.1.3. Thermal and Hydrothermal stability

Obviously, catalysts should be able to operate under the conditions usually found in biomass processing. Regarding temperature, except for pyrolysis where a thermal decomposition process usually takes place at high temperatures with a controlled amount of oxygen and steam [21], most other biomass procedures are carried out at moderate temperatures, therefore, the need of a catalyst able to work within low to medium range temperature is required [10].

Another important aspect is related to the medium involved. Considering that the nature of biomass components is essentially polymeric, then polar solvents or dispersants should be implemented for their chemical processing, consequently, catalysts used should be stable in aqueous or highly polar media to prevent poisoning of their active sites and therefore their deactivation or leaching [10, 21].

1.1.4. Multi-step reactions and bifunctionality of the catalysts

Biomass conversion processes are complex; they require several successive multistep syntheses to produce a target product. For example, aldol condensation results from consecutive reactions of aldol addition and dehydration. Therefore, the development of cascade reactions (combined catalytic reactions) is important as it reduces operating time and costs as well as consumption of auxiliary chemicals and use of energy [22]. This can be achieved by the utilization of multifunctional catalysts such as solid catalysts which provide the ability to combine several types of active sites in a unique catalyst. Xia et al. [23] examined the direct production of liquid alkanes from aldol adducts of furfural and/or 5-hydroxymethyltetrahydrofuran (HMF) by utilizing bifunctional metal/solid acid catalyst ($Pd/NbOPO_4$). High conversion yield was encountered and this is due to the multifunctional important roles that this catalyst can play. First: noble metal (Pd) acts as the active center for hydrogenation. Second: NbO_x species helps to cleave C-O bond and Third: a niobium-based solid catalyst can catalyze the dehydration step thus enabling the furan-derived adducts into liquid alkanes.

Therefore, the potential multi-functionality of solid catalysts opens the possibility to carry out complex biomass transformations possibly in a one-pot process.

1.1.5. Surface hydrophilicity/hydrophobicity of the catalyst

Biomass transformations involve hydrophilic and hydrophobic molecules or even both properties in different parts of the same compound. For example, lignocelluloses, the largest feedstock for ethanol, are composed of cellulose and hemicelluloses that are very hydrophilic in nature and lignin which exhibit both hydrophilic and hydrophobic functions [10]. Consequently, the surface hydrophobicity and hydrophilicity of the catalysts involved in biomass transformations should be studied extensively as these surface properties not only have a great influence on the key catalytic steps of adsorption and desorption processes and therefore on the overall potential catalytic activity but also on their catalytic selectivity [10, 24]. Karimi et al. [25] investigated the influence of hydrophilic/hydrophobic properties of several ordered mesoporous sulfonic solid acid catalysts on the catalytic selectivity of fructose dehydration into 5-hydroxymethylfurfural (HMF). Results revealed that catalysts with lower surface hydrophobicity provided faster departure of HMF from the system thus retarding the rehydration of HMF into undesired by-products and therefore enhancing selectivity. Additionally, Liu et al. [26] emphasized the development of solid acids with suitable hydrophobicity since it is a fundamental factor influencing their catalytic applications especially in acid catalyzed liquid reactions such as biomass transformation processes. For instance, Liu et al. [26, 27] revealed that the superhydrophobic property of mesoporous polydivinylbenzene-based solid acids enhances the anti-deactivation of catalytic sites or hydrolysis of framework and significantly increases exposure of acidic sites on the solid acids contributing to their good activity and stability in the water contained reactions.

Taking these requirements into consideration, several catalysts can be envisioned for biomass conversion processes. The next section will shed light on some of the catalysts (especially solid acid catalysts) that were either successfully used in the literature for converting biomass or that proved their efficiency for other related conversions.

1.2. Possible catalysts

1.2.1. Homogeneous catalysts

1.2.1.1. Hydrochloric and Hydrosulfuric acid utilization

Until the first half of the 20th century, mineral acids such as hydrochloric acid (HCl) and hydrosulfuric acid (H_2SO_4) were the most commonly used catalysts in the fields of oil refining and petrochemicals for the production of a variety of fuels and bulk chemicals [28, 29].

Faith [30] described in the early 1900s cellulose hydrolysis into sugars, known as Scholler process, in the presence of mineral acids (0.5 wt% H_2SO_4). This process was carried out by firstly hydrolyzing wood wastes at 170 °C yielding sugars and oligomers and secondly fermenting the obtained products to achieve 50% yield of sugars. Additionally, around the same time in Russia, many industrial processes for the hydrolysis of softwood (corn, grain, molasses) and hardwood into sugars, ethanol and furfural were employed using dilute mineral acids and fermentation methods [31]. Moreover, levulinic acid, one of the most important compounds of platform molecules derived from biomass, can be produced by acid treatment of lignocelluloses using strong homogeneous acids such as hydrosulfuric acid and hydrochloric acid [13].

1.2.1.2. Advantages and drawbacks of homogeneous acid utilization

Several researches have shown that many chemical transformations into fuels and chemicals are attractive using homogeneous acids as they generally offer relatively high activity and selectivity due to their total solubility in the reaction media making all acidic sites accessible to substrates [32]. However, several serious drawbacks can be encountered using these catalysts which make them unsuitable for biomass conversion processes. Such drawbacks can be illustrated as follows: acid corrosion of reactors and equipments, difficulty in catalyst separation and product recovery, poor catalyst recyclability, formation of degradation products (at high temperatures and using concentrated acids), generation of neutralization wastes, utilization of large amounts of catalysts and energy, toxicity, etc.....[33, 34, 35].

Consequently, from the 1940s onward, homogeneous acids have often been replaced by solid acid catalysts as they possess many unique advantages and properties required for oil or biomass conversion processes as well as the ability to overcome many of the homogeneous catalysts restrictions [28].

1.2.2. Heterogeneous catalysts: Solid acid catalysts

1.2.2.1. Replacement of liquid acids with solid acids

Solid-acid catalysts have received particular interest for environmentally-friendly synthesis of fuel and energy from bio-based products, statistics revealed that more than 80% of petrochemical processes are currently catalyzed by heterogeneous catalysts, as they exhibit

interesting and important properties. These catalysts can be re-used several times without loss of activity, play a critical role in the economic biomass conversion processes as they save energy and reduce waste, eliminate bio-fuel washing step as a result of easy separation from the reaction media [36, 37]. Moreover, reactions catalyzed by these catalysts are generally selective, clean and products are obtained in high purity [35, 36].

Several types of heterogeneous catalysts such as zeolites, mesoporous materials, supported metal catalysts, acidic and ion-exchange resins, mixed metal oxides, heteropoly compounds, etc…. for biomass conversion processes are investigated and discussed in details in the following sections:

1.2.2.2. Zeolites

Zeolites having a general formula $(M^{n+})_{x/n}[(AlO_2)_x(SiO_2)_y]^{x-}.mH_2O$, where M is the cation, m is the number of moles of water of crystallization, x and y are number of $[AlO_4]^{5-}$ and $[SiO_4]^{4-}$ tetrahedron, are defined as tri-dimensional microporous crystalline inorganic polymer material of aluminium and silicon oxide tetrahedra linked with each other via oxygen atom [38]. Zeolites have been utilized as heterogeneous catalysts for more than four decades for a wide number of applications such as cracking, isomerization and fuel synthesis [35, 39] but also for adsorption and separation [37]. They may contain both Brønsted and Lewis acid sites [39, 40]. Protons compensating the excess charge on the bridging oxygen of a Si-O-Al bond form hydroxyl groups which act as Brønsted acid sites, while other cationic or extra framework species can act as Lewis acid sites due to their electron acceptor properties [41]. Moreover, zeolites are interesting due to their channel structure, their porosity which can be tuned to accommodate a dual micro/mesoporosity favouring excellent mass transfer limitation, tunable hydrophilicity and high thermal stability [37, 42].

Danuthai et al. [43] reported a very high conversion yield of methyl esters (methyl octanoate) to hydrocarbons via two-stepped process, deoxygenating of methyl octanoate forming higher molecular weight ketone and octanoic acid and cracking of the obtained products to produce hydrocarbons (C_1-C_7) and aromatic compounds, using H-ZSM-5 zeolite. This high catalytic activity can be attributed to the presence of a large number of Brønsted and Lewis acid sites in the H-ZSM-5 framework which is attributed to high Si/Al ratio. It also showed high selectivity due to a network of internal canals and well-defined diameters [43]. Aghaziarati and co-worker [44] revealed the high catalytic activity of H-ZSM-5 in the production of tetrahydrofuran by dehydration of 1,4-butanediol.

Si/Al ratio of zeolites is crucial as it has a large impact not only on the number of active sites of a certain zeolite as indicated in the first example, but also on the zeolite hydrophobicity which in turn influences catalytic activity. Onda et al. [45] showed that among H-form zeolite catalysts, those with higher Si/Al ratio encountered higher catalytic activity for cellulose hydrolysis into glucose. This can be due to both the presence of stronger acid sites and a higher hydrophobic character of zeolites with high Si/Al ratios which promotes an easy adsorption on the catalyst surface and therefore improves catalytic activity [45]. Despite all of that, the recovery and reusability of these catalysts is a critical issue since tar and coke usually form during most of the pyrolysis reactions resulting in catalyst deactivation [46]. Moreover and most importantly to utilize zeolites in biomass conversion processes, its water resistance is desirable as most of these transformations occur in the presence of water or in aqueous media.

Zeolite-supported metals [46], have also been investigated. For example, Moliner et al. [47] had shown that metal-supported zeolite (Sn-Beta zeolite) is able to isomerize glucose to fructose in aqueous media with high activity and selectivity. This can be attributed to its high stability in acidic medium (pH < 2) and over a wide temperature range (343-413K) where similar activities with almost unchanged selectivity were encountered even after several calcinations at high temperatures indicating the regenerability of these catalysts and also due to the presence of silanol groups adjacent to the active sites Sn metal center that can simultaneously perform isomerization and epimerization of glucose.

To sum up, the hydrothermal stability, regenerability with conserving activity, hydrophilicity and textural properties of zeolites must be carefully considered as the composition and the structure of biomass raw materials are totally different from petroleum. In particular, the difficult balance between hydrophobicity and acidity will be of paramount importance for processes in presence of water.

1.2.2.3. Acidic and ion-exchange resins

Ion (cation) exchanged resins are co-polymers of divinylbenzene (DVB), styrene and sulfonic acid groups (-SO_3H) grafted on benzene, the later acts as the active sites-Brønsted acidity which is a key factor for catalytic activity in addition to their cross-linking component [35, 37]. Lower cross linking causes higher swelling of ion-exchange resins. In turn this swelling capacity can control the reactants accessibility to acid sites and hence affects their overall reactivity [35]. Therefore, due to their interesting properties, ion-exchange resins have been used in various acid catalyzed reactions such as esterification, alkylation, hydration/dehydration,

condensation reactions, etc…. [48]. They also have the potential to hydrolyze many kinds of biomass compounds such as sucrose, maltose and aliphatic esters [48].

Takagaki et al. [33] confirmed that Amberlyst 15, Nafion NR-50 and Nafion SAC-13 can catalyze hydrolysis of disaccharides, such as maltose, sucrose and cellubiose, and starch at 80 °C. Plazl et al. [49] have also shown that the cationic-exchange resins (Amberlite A120) is an efficient catalyst for sucrose hydrolysis to glucose and fructose under thermal and microwave heating. Ohara and co-workers [50] reported the efficient catalytic activity of Amberlyst 15 in the dehydration of fructose to produce 5-Hydroxymethylfurfural (HMF). Shinde et al. [51] also investigated the applicability of the latter catalyst for tetrahydrofuran production through cyclization of 1,4-butanediol. Despite all of that, ion-exchange resins lack stability in hydrothermal reaction conditions, the presence of water diminishes accessibility of reactants to the acid sites resulting in the deterioration of catalytic activity [45, 48]. To overcome this problem, Abreu et al. [52] had demonstrated a way to improve catalytic activity of ion-exchange resins by loading active sites such as tin oxide onto the resin materials. Results showed that tin-oxide modified ion-exchange resins were highly active for the transesterification reaction of soybean oil and methanol; however, since tin oxide can be easily leached from the modified ion-exchange resins, these catalysts have a limited use.

As a consequence, these drawbacks in addition to their poor resistance to bases is likely to limit their utilization as heterogeneous catalysts for biomass conversion processes [46].

1.2.2.4. Heteropoly compounds

Heteroployacids (HPAs) are complex proton acids that incorporate polyoxometalate anions (heteropolyanions) having metal-oxygen octahedral as the basic structural units [53]. These catalysts can be divided into four types including Anderson, Preyssler, Well Dawson and Keggin [54]. The latter is the first characterized and the best known subclass of heteropolyacid that is typically represented by the general formula $XM_{12}O_{40}^{x-8}$. As indicated in its formula, Keggin heteropolyacid consists of 12 coordinated ions (M) (tungsten (W^{6+}) or molybdenum (Mo^{6+})) and oxygen ions arranged symmetrically around a central atom (X) which is normally phosphorous (P^{5+}) or silicon (Si^{4+}) [36].

The catalytic applications of heteropolyacids, polyoxometalates (POM) as efficient homogeneous or heterogeneous solid acid catalysts have received greater attention during the last few decades as promising solid acids to supplant environmentally unsafe and hazardous

liquid acids as they possess inherent characteristics such as strong Brønsted acidity, high proton mobility, low volatility, low corrosivity and high catalytic activity and selectivity for several reactions when compared to conventional mineral acids [48, 55]. For instance, Misono et al. [56] studied the hydration of isobutylene using heteropolyacids and conventional mineral acids such as H_2SO_4. Results indicated excellent selectivity and activity with HPA catalysts (10 fold higher than with mineral acids). The high catalytic activity was attributed to the strong Brønsted acidity, high solubility of benzenes and the formation of a complex with a carbenium intermediate and the high selectivity was achieved due to the preferential coordination of heteropolyanion with isobutylene. Moreover, Misono et al. [56] showed that HPA catalysts exhibited a very high catalytic activity in the polymerization process for the conversion of tetrahydrofuran (THF) to polyoxytetramethyleneglycol (PTMG). Chidambaram and co-workers [57] reported the high catalytic activity and selectivity for the dehydration of glucose into 5-HMF using 12-molybdophosphoric acid (12-MPA) in a solution of 1-ethyl-3-methylimidazolium chloride (EMIMCI) and acetonitrile. Although heteropolyacids can act as efficient homogeneous catalysts, their recovery is a problematic issue and this might limit their reusability [48]. Also, they are not appropriate for the biodiesel production due to their high solubility in polar medium, low number of accessible surface acidic sites and low surface area (< 5 m^2/g) [36]. To overcome this problem, these catalysts can be transformed to solid acid catalysts by combining them with monovalent cations such as NH_4^+, K^+, Ag^+ and Cs^+. The latter are being used as green catalysts for several applications [55].

For example, Zhao et al. [58] developed a facile and environmentally friendly method for the production of 5-HMF from fructose using the solid heteropolyacid $Cs_{2.5}H_{0.5}PW_{12}O_{40}$. Okuhara et al. [59] proved that $Cs_{2.5}H_{0.5}PW_{12}O_{40}$ was remarkably active for the hydrolysis for 2-methylphenylacetate in excess water in comparison with other inorganic solid acids such as HZSM-5 or Nb_2O_5. This high catalytic activity can be attributed to the strong acidity, reduction of the poisoning effect of water by the hydrophobic nature of the surface and to the mesoporous structure that allows easier diffusion of the bulky reactants into the pores. However, when $Cs_{2.5}H_{0.5}PW_{12}O_{40}$ is thermally treated with hot water, its surface structure and acidity change and this was confirmed by the decrease in the acid amount. Moreover, this catalyst has good affinity toward glycerine which causes the deactivation of catalyst during the recycling process [59].

Consequently, the drawbacks encountered for both heterogeneous and homogeneous heteropolyacids show they may not be the most suitable solid acid catalysts for biomass conversion processes.

1.2.2.5. Metal oxides

Metal oxides catalysts have been successfully utilized in various transformations for example in isomerization, dehydration [46] and hydrolysis reactions as they possess many favourable properties such as enhanced thermal stability and high catalytic efficiency notably due to the presence of both Lewis and/or Brønsted acid sites on the surface [32, 48, 60]. Notably, transition metal oxides such as TiO_2, Nb_2O_5 and WO_3 have been studied as heterogeneous acid catalysts [48].

TiO_2 has been largely studied due to its electrochemical properties, high chemical stability, high refractive index (higher than any conventional colorless substance), good heat resistance, low cost, non-toxicity and availability [61, 62, 63] which made it useful for many different applications such as photocatalytic applications, catalytic supports, biocompatible implants and solar cells for hydrogen production and electric energy [61, 62, 63]. It has also been proposed as heterogeneous solid acid catalysts for biomass conversions. For example, Lanziano and co-workers [64] investigated the catalytic activity of TiO_2 catalyst in the reaction of isomerization of glucose and simultaneously in the dehydration of fructose into HMF. To overcome the possible crystallization of pure TiO_2 when calcined at high temperatures, thus resulting in the destruction of the original mesoporous structure and the development of larger pores, thermally stable mesoporous TiO_2 could also be prepared by mixing pure mesoporous TiO_2 with other transition metals such as Al, Zr or Nb as reported by Kondo and co-workers [65].

Tungsten trioxide (WO_3) has also been widely studied in the last few decades and is reported to exhibit several interesting properties suitable for many applications. WO_3 is a non-toxic and photostable n-semiconductor with a band gap of 2.6 eV, resulting in visible light absorption and therefore allowing it to be widely utilized as a visible light responsive photocatalyst and as an anode material of photovoltaic devices [66, 67, 68]. It also exhibits electrochromic properties which makes it suitable to be used in sunglasses, automotive rear-view mirrors, sun roofs, variable sun protection systems and building windows [69, 70]. Additionally, it is characterized by a good chemical stability in aqueous solutions. For instance, Darwent and co-workers [71] indicated its high catalytic activity for water oxidation to

oxygen. Besides, WO_3 is well known to be efficient as a solid catalyst for several acid catalyzed reactions such as hydrocracking, dehydrogenation, isomerization and alcohol dehydration. For instance, WO_3 is active for the dehydration of isopropanol [72].

However, high reaction temperatures are often required since WO_3 is characterized by low surface area and a low number of acid sites thus limiting their catalytic applications [73]. For this reason it may be necessary to use it as a supported phase on other metal oxides such as Nb_2O_5 as this can modify significantly its catalytic performance [74].

Niobium oxide (Nb_2O_5) is another promising metal oxide that should be also taken into consideration. Hydrated niobium pentoxide ($Nb_2O_5.nH_2O$) usually called niobic acid has attracted researchers attention owing to its versatile properties that are suitable for a wide range of industrial processes such as esterification, oxidation, dehydration and hydration [75, 76]. This metal oxide catalyst is an air stable solid, characterized by its relatively strong acidity equivalent to the acid strength of about 70% sulfuric acid, the presence of both Lewis and Brønsted acidic sites and its stability even in the presence of components of a reducing capacity. Most importantly it was shown to retain high catalytic activity, selectivity and stability even in the presence of water vapour which is the case for many other metal oxides due to the deactivation of their acidic sites as a result of water adsorption [75, 77]. Therefore, the utilization of niobic acid as a water-tolerant solid acid catalyst can be an efficient option.

For example, Okazaki et al. [78] investigated the hydration of dicyclopentadiene over various solid catalysts: at 170 °C and atmospheric pressure, higher yields were achieved using niobic acid (3-10 times higher) than with any other solid acid catalyst such as ion-exchange resins, other metal oxides such as TiO_2 or SiO_2 and mixed metal oxides such as TiO_2-SiO_2 or SiO_2-Al_2O_3. Nakajima and co-workers [79] observed that $Nb_2O_5.nH_2O$ can function as an efficient acid catalyst for conversion of glucose into 5-HMF. Yamaguchi and co-workers [80] examined the reaction of isobutyraldehyde with isobutene for octadiene synthesis over several solid acid catalysts. Results revealed that niobic acid has a superior catalytic activity than the other tested catalysts as it exhibited the highest conversion yield and this was due to its highest acidic strength. Interestingly it could also convert 2,2,5,5-tetramethyltetrahydrofuran or 2,5-Dimethyl-2,5-hexanediol to octadiene, like tungstated titania. With another polyol, Chai and co-workers [76] demonstrated that Nb_2O_5 catalysts were efficient for the gas phase dehydration of aqueous glycerol. The optimum number of the strongest acid sites was obtained after calcination at 400 °C, before crystallization really occurred. Zirconium and niobium mixed oxides were also reported for the same reaction. In this case, the suppression

of unselective Lewis acid sites (mostly related to zirconia) induced a consequent change in acrolein selectivity and stability [81], [82].

For Nb_2O_5, the calcination temperature is the key factor that affects both acidic and catalytic behaviour. To illustrate this, Okazaki et al. [78] showed that the catalytic activity of niobic acid fell sharply upon heating at temperatures higher than 400 °C due to the simultaneous decrease in the acidity of its surface. Tanabe [83] investigated similar behaviour where the catalytic activity of niobic acid in olefin isomerization, polymerization processes and dehydration reaction declined with increase in the evacuation temperature due to the decrease in the number of Brønsted acid sites catalyzing the reactions. Therefore, to exhibit the highest catalytic activity with this metal oxide, it is important to optimize the calcination temperature.

Molybdenum oxide (MoO_3) exhibits structural, chemical, electrical and optical interesting properties such as mechanical hardness. In addition to that, orthorhombic MoO_3 (α-MoO_3) exhibits a unique layered structure allowing intercalation processes [84, 85] to take place which is a useful feature as described in the next section. The latter feature also permits its applicability in various types of applications such as catalysts, gas sensors, self-developing photography and electrochromic devices [85]. Also, it is widely used in bulk-heterojunction solar cells, as gas sensors in some applications [86]. Like WO_3, it shows some acidity. For example, Haber et al. [87] revealed its efficient catalytic activity for isomerization of 3,3-dimethylbutene-1 into 2,3-dimethylbutene-2. It has also been used for a variety of selective oxidation of organic compounds such as for oxidation of methanol to formaldehyde as investigated by Pernicone and co-workers [88]. Prasmorsi and co-workers [89] showed an efficient catalytic activity of MoO_3 for the hydrodeoxygenation (HDO) of lignin-derived oxygenates such as phenol, anisole and diphenyl ether into high yields aromatic hydrocarbons.

1.2.2.6. Supported solid acid catalysts

Supported metal solid acid catalysts can combine the advantages of two bulk oxides while maintaining sufficient surface area. Several interesting properties such as substantial surface acidic species compared to zeolites and transition metal oxides, thermal and mechanical stability, large pore size and pore volume [48] also permits their wide applicability in large scale industrial processes such as in oil refinery, petrochemistry, exhaust gas scrubbing, energy production [32] and chemical synthesis such as hydrogenation and oxidation [90].

For instance, zirconia supported tungsten oxide is known to catalyze butane and pentane isomerization [91]. Raveendra et al. [92] revealed the good catalytic performance of WO_3/SnO_2 catalyst in the dehydration of fructose to 5-HMF. Similarly, Du et al. [93] examined the efficient catalytic performance of WO_3/MoO_3 in glucose dehydration into 5-HMF. Li and co-workers [94] investigated the catalytic activity of MoO_3/ZrO_2 prepared by impregnation and precipitation for two different reactions: the esterification of acetic acid with ethanol and hydrolysis of ethyl acetate in excess water. Results revealed the high catalytic efficiency of this catalyst for both reactions. This was attributed to the enhanced hydrophobic character of the surface upon thermal treatment. Chary et al. [95] also examined the high catalytic activity of this catalyst (higher than that of MoO_3/TiO_2 and MoO_3/Nb_2O_5) for the ammoxidation of toluene into benzonitrile due to the stronger interaction between the surface of zirconium oxyhydroxide precursors and dispersed metal oxides.

WO_x/ZrO_2 and NbO_x/ZrO_2 were both shown to catalyze the gas phase dehydration of glycerol with good yields. This was also the case when both W and Nb oxides were supported on zirconia [96]. Several other catalytic systems based on supported oxides also gave good results [97]. Supported tungsten oxides also catalyze efficiently the conversion of sorbitol to biofuels, especially when supported on titania [98]. In view of all their characteristics, oxides are clearly potential candidates as catalysts for many acidic processes. Nevertheless, the often low surface area for the main candidates (WO_3, Nb_2O_5 or TiO_2) and the limited possibilities to modulate their properties is a drawback. Supported oxides are more flexible but depending on the support they may not always withstand the contacts with water. However, it is noteworthy that some of the advantages of acidic oxides can also be found in another class of materials, the layered materials.

1.2.3. Specificity of Layered materials

1.2.3.1. Definition of layered solids

A layered compound can be defined as a crystalline material consisting of stacked array of two dimensional sheets or platelets having high aspect ratio one above the other to form a three dimensional macromolecular structure [99, 100]. Generally, a solid can be described or tolerated as layered, only when the atoms of the same plane are cross-linked by strong chemical bonds, while, atoms of the adjacent layers interact with weaker physical forces [100]. The majorities of layered solids, such as anionic and cationic clays, are connected by covalent

bonds between the atoms in the same layers and are linked together by van der Waals forces between atoms in the adjacent sheets, taking into consideration that covalent bonds are much stronger than van der Waals forces [101]. The various terms used to describe layered solids are highlighted in the schematic drawing in Figure **1.1**:

- **Interlayer spacing:** is the distance between the barycenters of the two adjacent layers of a layered solid. It is synonymous to basal spacing, d-spacing or interlayer (interlamellar) distance.
- **Gallery height:** it is the free distance between the adjacent layers. It can be obtained by subtracting the thickness of the layer from the interlayer region.
- **Interlayer region:** it is the free space between two adjacent layers.
- **Laminate (or layer) thickness:** it is the thickness of lamellae. It can also be donated as layer thickness.

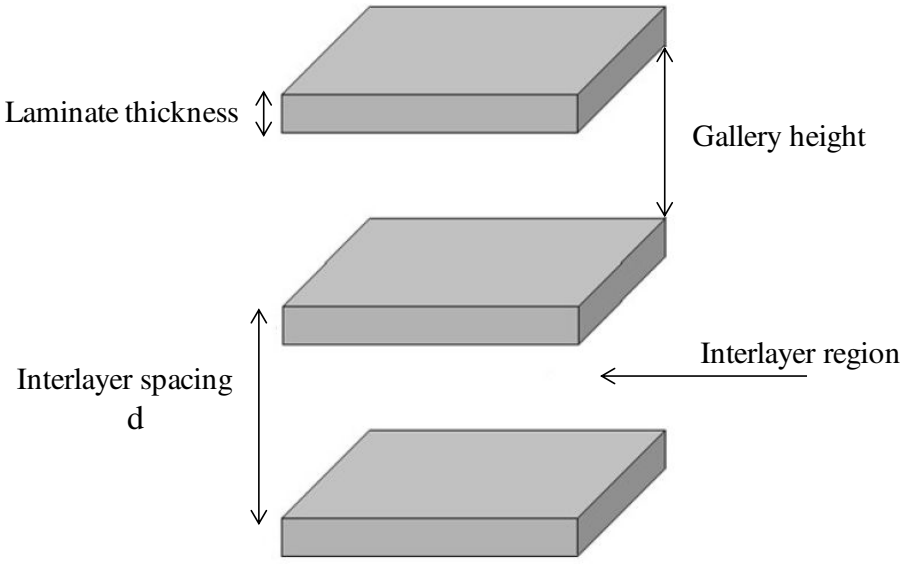

Figure 1.1: Schematic representation of a typical layered solid [101].

1.2.3.2. Classification of Layered solids

Layered materials can be classified or divided into different groups according to the: inorganic or organic nature of the constituent layers [101], the thickness of the constituent layers of the layered solids as demonstrated by Solin [102] or the presence/absence of fixed charges on the layers of the planar macromolecules.

Taking into consideration the third criterion, layered materials can be divided into two large groups: uncharged (neutral) or charged ones [103]. Neutral layered solids in turn can be subdivided into electrically conducting layers such as graphite, metal phosphonates chalcogenides and non-conducting ones such as clays, α-metal (IV) phosphonates and α-metal (IV) phosphites [103]. Concerning the charged layered compounds, they are also separated into cationic and anionic solids. Cationic layered solids are those constituted of negatively charged layers with cations in the interlayer region like cationic or smectite clays, alkali transition metal oxides and layered titanates [103]. On the contrary, anionic layered solids are the inverse of cationic ones: they are made of positively charged layers with anions in the interlayer regions such as α-zirconium aminophosphonates, hydrotalcite and hydrotalcite-like compounds (also referred to as anionic clays) [103]. The most widely studied cationic and anionic layered solids in each group are illustrated in the next paragraphs.

1.2.3.2.1. Anionic layered solids: Layered metal hydroxides

Layered double hydroxides and hydroxy double salts are the two most occurring and studied types of layered metal hydroxides.

a. Layered double hydroxides

Layered double hydroxides (LDHs) are also known as hydrotalcites-like compounds since most of LDHs minerals found in nature are similar in structure to the hydrotalcite minerals or its hexagonal analogous, manasseite. The former is the most common mineral found in nature having the composition: $Mg_6Al_2(OH)_{16}CO_3.4H_2O$ [104]. Additionally, LDHs can be readily synthesized in the laboratory with wide ranging compositions.

Layered double hydroxides can be derived from the mineral brucite structure $Mg(OH)_2$, where Mg^{2+} can be substituted by trivalent cations of ionic radius very close to that of Mg^{2+} such as Al^{3+}, resulting in a positively charged layered solid [104, 105]. The latter will restore charge neutrality by intercalating anions such as carbonate anions between two brucite-like layers along with water molecules [105, 106]. LDHs are represented by the general formula: $M^{II}_{1-x}M^{III}_x(OH)_2(A^{n-})_{x/n}\cdot mH_2O$ [107], where M^{2+} and M^{3+} are divalent and trivalent cations, whose ionic radius is very close to that of Mg^{2+}, located in the octahedral positions within the hydroxide layers with x normally between 0.17 and 0.33 [106]. These octahedral, form two-dimensional sheets via edge sharing and may stack together by hydrogen bonding between the hydroxyl groups of adjacent atoms. A^{n-} can be any charge compensating anion

(organic or inorganic) such as CO_3^{2-}, NO_3^- or SO_4^{2-} located in the lamellar region and y is the amount of water present in the same region [106, 108].

LDHs are used in many different applications such as flame retardants [109, 110], molecular sieves [111], ion exchangers [108], adsorbents [108] and recently they have been used in the medicine field [112] and corrosion protection [113]. Additionally, they are widely used as catalysts and catalysts supports, [108] for instance, Das et al. [114] had demonstrated the possibility of using palladium supported on calcined MgAl-LDH to synthesize 4-methyl-2-pentanone (methyl isobutyl ketone, MIBK), a product of high industrial interest, from acetone. Dinka et al. [115] reported that vanadium oxide catalysts supported on calcined MgAl-LDHs are effective for the vapour phase synthesis of isobutyraldehyde from methanol and n-propanol. Moreover, catalysts derived from LDHs have fundamental catalytic activity, for example, Manikandan et al. [116] reported that Ni-based mixed oxide catalysts derived from NiMgAl-LDH can be used for the selective hydrogenation of furfural, one of the most promising chemicals in addition to 5-HMF in the production of fuels and value-added chemicals from renewable biomass, into furfural alcohols. Similarly, Yan and co-workers [117] reported that the noble-metal free Cu catalysts (Cu-Al, Cu-Cr, Cu-Fe) derived from hydrotalcite were highly efficient for the hydrogenation of biomass-derived furfural and levulinic acid.

b. Hydroxy double salts

Structurally, hydroxy double salts (HDSs) are similar to LDHs as they both consist of positively charged layered solids with anions in their interlayer regions [118]. Nevertheless, while LDHs contain a mixture of trivalent, divalent and monovalent cations, HDSs contain only divalent metal cations.

The typical chemical composition of HDSs can be expressed as follows: $[M^{2+}N^{2+}(OH)_x\ (A^{m-})_{2/m}].nH_2O$ [119, 120] , where M^{2+} can be a single divalent metal cation such as Zn, Cu, Ni or Co located in the octahedral sites and N^{2+} can be Zn or Cu localized in the tetrahedral sites. A mixture of cations can also be observed. A^{m-} can be a single or mixture of exchangeable anions such as CH_3COO^-, NO_3^- or Cl^-. The latter can be readily replaced through an ion exchange route, therefore, a wide range of anions could be intercalated such as ClO_4^-, MnO_4^-, SO_4^{2-}, metal complexes, alkylsulfates, carboxylic acids and thiophenes. n is the amount of water molecule residing in the interlayer region.

HDSs exhibit a wide range of applications such as adsorbents, catalysts, separators, optical memory and electrodes. Moreover, Kaassis et al. [118] had demonstrated the use of

HDSs for drug delivery. Additionally, Hara et al. [121] had reported that Pd supported on Ni-Zn mixed basic salt, can be used as an efficient heterogeneous catalyst for the oxidation of alcohols under air atmosphere. NiZn classified as a type of HDS were chosen as a catalyst support due to its high crystallinity, facile preparation and strongly isolated anion-exchangeable sites.

1.2.3.2.2. Cationic layered solids: Layered metal oxides

a. Layered titanates

Layered titanates can exist in several forms; such as lepidocrocite (γ-FeOOH)-type layered structure [122, 123]. Their chemical composition can be expressed as follows: $A_xTi_{2-y}M_yO_4$, [123, 124] where A is the interlayer cation and can be K, Rb or Cs and M represents a vacancy or metal ion such as Li, Co, Mg, Ni, Cu, Zn or Mn. These layered materials usually exhibit an orthorhombic structure consisting of two-dimensional layer of edge and corner sharing TiO_6 octahedra with interlayer alkali metal ions compensating for the negative charge of the titanate sheets. The latter is highly exchangeable with a variety of inorganic and organic cations [123].

Layered titanates are widely used in many different applications due to their interesting physical ion-exchange [123], photocatalytic activity [122, 125] and electrochemical intercalation property [123]. These layered materials have found use as filters [126], nuclear waste cleanup [123, 127], adsorbents for water treatment [127, 128] functional nanosheets [129] and photocatalysts [125].

Despite of these properties, layered titanates, have little or rarely been addressed as solid acid catalysts. Nakano et al. [130] and Sasaki et al. [131] have reported the intercalation of alcohol molecules and pyridine into a layered titanate, thus favouring their accessibility into the interlayer region, the location of the acidic sites, but this could not be achieved for other titanates like $H_2Ti_3O_7$, $H_2Ti_4O_9.1.2H_2O$, and $H_2Ti_5O_{11}.3H_2O$. This impossible intercalation was attributed to the large negative charge density of the layers [131].

By contrast, titanates in the form of nanosheets were used as solid acid catalysts for several catalytic reactions. Kitano et al. [34] showed the high catalytic activity of protonated titanate nanotubes (HTiNTs) in the Friedel-Crafts alkylation of toluene with benzyl-chloride. Li and co-workers [132] reported the high catalytic activity and efficiency of protonated titanate nanotube for the hydroxyalkylation/alkylation of 2-methylfuran and n-butanal from

lignocellulose. However, one of the drawbacks is that the acidity of exfoliated nanosheets has been reported weaker than that of the original layered metal oxide [133].

However, it is expected that layered titanates are less acidic than niobates and tantalates. Due to the periodic electronegativity trends [134], layered materials possessing metals of groups V and VI exhibit higher acidity than those exhibiting metals of Group IV. Therefore, the use of protonated layered transition metal oxides, preferentially of groups V and VI, without any modification/exfoliation would be more beneficial.

b. Layered $HNbMoO_6$ and $HNbWO_6$

$HNbMoO_6$ and $HNbWO_6$ layered oxides, the scope of our work, are interesting as they exhibit several important properties. These oxides are prepared by treating their Li-precursors by nitric acid (HNO_3).

Both $HNbMoO_6$ and $HNbWO_6$ layered oxides as all other layered oxides can be exfoliated to form nanosheets. The latter was utilized as efficient solid acid catalysts in several acid catalyzed reactions. For instance, $HNbWO_6$ nanosheets exhibited a higher catalytic activity for Friedel-Crafts alkylation of anisole with benzyl alcohol than HNb_3O_8 and $HTiNbO_5$ nanosheets due to its higher acid strength as demonstrated by Takagaki et al. [28]. Moreover, Zhong et al. [135] reported the use of $HNbMoO_6$ nanosheets in the dehydration of fructose to 5-HMF (5-hydroxymethylfurfural).

It is also noteworthy that layered $HNbMoO_6$ and $HNbWO_6$ were discovered to function as efficient solid acid catalysts without any modification/exfoliation. For instance, the catalytic activity of layered oxides is higher than that of nanosheets. Tagusagawa et al. [133] showed that layered $HNbMoO_6$ have higher catalytic activity for the alkylation of toluene than any other tested catalysts such as $HNbMoO_6$ nanosheets. This interesting property raised some interest as these layered oxides can be directly utilized as solid acid catalysts for several acid catalyzed reactions. Layered $HNbMoO_6$ have been widely explored and results revealed its very high catalytic activity for several catalyzed reactions such as hydrolysis of saccharides like sucrose, cellobiose and starch [33], esterification of hydrocarboxylic acid [136], acetalization [137], hydration [137] and dehydration reactions [138]. $HNbWO_6$ was also examined and revealed its efficiency to be utilized for acetic acid esterification [139] and dehydration of biomass based fructose into 5-HMF [135]. This high catalytic activity is due to the capability of these layered oxides to intercalate organic bases [33, 133, 136, 140] within their strongly acidic interlayer region, therefore accessing acidic sites, the key factor for any catalytic reaction.

Interestingly $HNMbO_6$ possess both Nb, which can enhance the stability of the catalyst in the aqueous medium or in presence of water as well as increase the acid amount, and M (Mo, W) which can increase acid strength. Tagusagawa et al. [141] had previously demonstrated the effect of varying amount of Nb and Mo transition metals in the Friedel-Crafts alkylation of toluene with benzyl alcohol and for the hydrolysis of cellobiose and esterification of acetic acid.

c. Layered $H_2W_2O_7$ and H_2WO_4

$H_2W_2O_7$ is related to the Aurivillius family of the layered perovskites synthesized from the $Bi_2W_2O_9$ precursors through selective leaching of $Bi_2O_2^{2+}$ sheets by hydrochloric acid treatment [134, 142].

WO_3 monohydrate or H_2WO_4 is characterized by a two dimensional crystalline corner shared WO_6 octahedra. The latter are formed with a water molecule substituted for one apical oxygen of the tungsten oxygen atom and terminal oxygen completing the structure [143].

These layered tungsten based oxides have been the subject of many researches since they exhibit several interesting physical and electronic properties [144] and due to their wide applicability in electronics, optics and catalysis [142]. Tai and co-workers [145] revealed that the binary catalyst of Raney Ni and H_2WO_4 exhibited the highest catalytic activity among other binary catalysts (Raney Ni/$H_4SiW_{12}O_4$ and Raney Ni/$H_3PW_{12}O_{40}$) in the conversion of cellulose into ethylene glycol. Also, Yue et al. [146] reported the efficient catalytic activity of $WO_3.H_2O$ for the dehydration of glucose into 5-HMF. Additionally, these layered oxides has shown its capability to be readily exfoliated to form WO_3 nanosheets as demonstrated by Waller et al.[147], Schaak et al.[134] and Ban et al. [148]. Its ability to intercalate organic ions and molecules such as n-alkylamines in the interlayer spacing can also ease this exfoliation as demonstrated by Chen et al. [149] and Wang et al. [150].

These layered oxides possessing only W in their structure will be used in this work for comparison with the $HNbMO_6$ mixed oxides possessing both Nb and W or Mo in their structure.

1.2.3.3. Properties and characteristics of layered solid acids

Layered solids had been the field of enquiry in many historical and current interests [102]. They had been used since the beginning of the petrochemical industry, i.e. 80 years ago, in

1936, hydrocracking process was based on acid-treated clays (a group of cationic layered solids) [103, 151, 152]. Until recently, these layered solids are still found to be efficient in the field of catalysis; they are mainly used in many acid catalyzed reactions such as ethylation, alkylation, isomerisation, hydrodealkylation, ring-opening, hydrodehydrogenation [103] and as an additive in fluid catalytic cracking (FCC) catalysts [151]. Moreover, they have been utilized in the area of polymerization as a polymer additive [103]. In addition to clays, several layered solids such as layered perovskites, layered double hydroxides and layered transition metal oxides have been widely used in many different applications especially as photocatalysts and as efficient catalysts in several acid catalyzed reactions as discussed before.

Layered materials are interesting as they exhibit important features which do not exist in any other compound. These layered materials have the capability of structural expandability, ion-exchange properties and some flexibility in the layer composition [153]. The latter features can be achieved by intercalating guest species such as anions, complexes and organic chemicals between the sheets (within the interlayer region) of the host layered solids [154]. Consequently, the resultant intercalated layered compounds are interesting as they integrate both the advantages of the intercalant and the layered host. This important characteristic open new opportunities to produce novel solids like hybrid materials, nanocomposites, and multi-functional materials [154], with desirable physical and chemical properties that can be widely utilized in many different applications such as, catalysis or supports for the catalytic reactions, conductors, photoactive materials, magnets, polymer additives, ion-exchangers and electrodes [155].

Furthermore, because of these interesting properties, layered materials have proven to be not only of technological interest in a variety of industrial and medical applications including catalysis, molecular separations, drug delivery but also in a number of environmental issues involving the fate of contaminants and ground water quality [104].

1.2.3.4. Intercalation in layered materials

Layered compounds are characterized by a two-dimensional expandable interlayer space [155], a free space localized between the layers of the host solid and dominated by the presence of the active sites. Eventually, this space can serve as an important place to accommodate several ions/molecules, a process known as intercalation [155].

Intercalation, schematically represented in Figure **1.2**, [155] implies the insertion of guest species into the host layered solids; therefore, the layers that are held together by van der Waals forces will be separated depending on the size of the ions or molecules being inserted. This process is known to be topotactic and reversible meaning that the structural features of the hosts during insertion or de-insertion of the guest species remains intact [155].

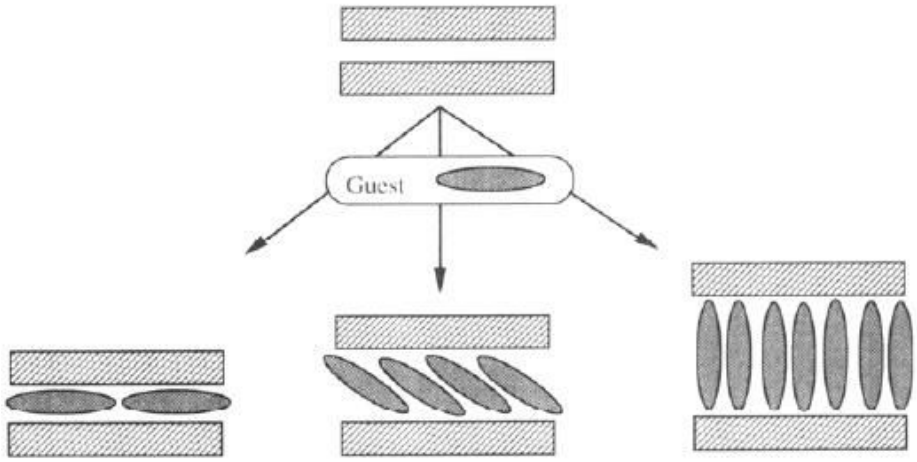

Figure 1.2: Schematic illustration of layered solids [155].

The motivation to study the intercalation process, is that it can alter the optical, electronic and physical properties of both the host solids and the intercalated guest species. Therefore, the newly developed intercalated material can be utilized as catalysts and catalyst supports, shape-selective adsorbents, ion-exchangers, ionic conductors, electrodes and as photo-functional materials [156, 157, 158].

Intercalation processes are unselective ones and they are usually driven by several reaction mechanisms including ion-exchange method, ion-dipole interactions, hydrogen bonding, redox and acid-base reactions [150, 159]. The intercalation chemistry into layered solids began from more than a century, when Schauffault in 1841, first reported the intercalation of sulphuric acid into graphite. Until recently, the intercalation process had been the subject of considerable interest and it is widely examined by several researchers on various layered solids.

For instance, Alberti and co-workers [160] reported the insertion of primary n-alkylamines and Casciola et al. [161] investigated the intercalation of heterocyclic bases such as diazoles and diazines into α- and γ-type layered zirconium phosphates (ZrP) within their interlayer region. Consequently, the latter was found to be a suitable place to perform several

important reactions such as polymerization of aniline [162] and for isopropyl alcohol decomposition [163].

Rives et al. [164] had demonstrated the intercalation of halocomplexes into the interlayer regions of layered double hydroxides (LDHs) and investigated the use of the newly formed LDH-halocomplexes intercalated compounds as catalysts for chloride-exchange reactions and also as modified electrodes. Moreover, they reported the use of intercalated LDHs with cyano complexes of iron, cobalt, molybdenum and some other metals for the hydrocarbon adsorption and electrochemical behaviour [164].

The intercalation behaviour into layered transition metal oxides has been investigated and reported in several articles. Concerning, layered titanates, Rodriguez et al. [165] had reported the intercalation of different primary n-alkylamines and investigated its applications for high temperature solid lubrication. Nakano et al. [130] had examined extensively the intercalation of alcohol molecules at ambient pressure into the layered titanates having the lepidocrocite (γ-FeOOH) type structure. Sasaki et al. [131] also examined the intercalation ability of layered titanates and showed the facile intercalation of pyridine molecules into the interlayer gallery.

Regarding layered oxides with transition metals of groups V and VI, their intercalation property has also been extensively studied and revealed its importance in several acid catalyzed reactions [133, 137, 166, 167]. For example, the intercalation behaviour of a variety of organic bases such as n-alkylamines, pyridine and n-alcohols into $HNbWO_6$ and $HNbMoO_6$ layered oxides has been the scope of interest in several articles [137, 140, 168]. Some of these will be reported in the next paragraph.

Bhat et al.[140] and Bhuvanesh et al.[168] have investigated the intercalation of n-alkylamines and pyridine into $HNbWO_6$ and $HNbMoO_6$ layered oxides, through an acid-base interaction. Takagaki et al. [33] demonstrated that $HNbMoO_6$ layered oxides can be utilized as efficient catalysts for hydrolysis of saccharides due to its ability to intercalate sucrose, cellobiose and starch into its interlayer gallery thus accessing the acidic sites within. Similarly, He et al. [139] reported that due to the facile intercalation of acetic acid into the interlayer gallery of $HNbMoO_6$ layered oxide, it can serve as an efficient catalyst for acetic acid esterification. Furthermore, Tagusagawa et al. [133] showed the high catalytic activity of $HNbMoO_6$ layered oxide for Friedel-Crafts alkylation due to the facility of benzyl alcohol intercalation.

The intercalation property of the tungsten layered solids was also monitored. Chen at al.[142, 149] and Wang et al. [150] have investigated the successful intercalation of n-alkylamines into $H_2W_2O_7$ layered perovskite.

To monitor whether intercalation is successfully achieved or not, several techniques were used in the literature such as powder X-ray diffraction (PXRD) or infrared spectroscopy. (PXRD) can provide lots of information upon reacting the protonated layered oxides with the guest species. First, the shift of the (001) diffraction peak, distance between two consecutive layers, to lower angles corresponding to an increase in the basal spacing and c-parameter, can confirm the process of intercalation of the guest species into the interlayers of the host oxides. Second, the similarity of a and b lattice parameter values or the presence of (110) diffraction peak at the same identical position before and after intercalation is an indication of the structural preservation of the layered oxides.

In addition to PXRD, Fourier-transform Infrared spectroscopy can monitor the interaction between the layered oxides and the guest species. It can also provide structural orientation of the latter, whether they are located in a cis- or trans-conformation depending on the position of the newly appeared peaks after intercalation into the host layered oxides. For instance, Wang and co-workers [150] deduced from the observed IR CH_2 band positions, situated at 2918 and 2849 cm^{-1}, upon n-alkylamines (n = 7, 12 and 16) intercalation into $H_2W_2O_7$ layered oxide that the guest species possess an all trans conformation. Similar conclusion was withdrawn by Tsunoda et al. [169] after intercalating n-alkylamines (n = 12 and 18) into $H_{1.8}(Sr_{0.8}Bi_{0.2}Ta_2O_7)$ (HST) layered oxide. Moreover, the IR characterization spectra of $H_2W_2O_7$ layered oxide intercalated with n-alkylamines as investigated by Chen el al. [142] confirmed their interaction due to the appearance of a broad band situated at 2110 cm^{-1} which is attributed to the combination of the asymmetrical bending vibrations and torsional oscillation of the $-NH_3^+$ groups interacting with the apical oxygen of the W-O framework. Additionally, IR characterization was also used to reveal information regarding the acidic sites type after intercalating for example pyridine or aniline. This was observed by Bhuvanesh et al. [168] who showed the appearance of a strong absorption band at 1490 cm^{-1} in the IR spectra of $HNbMoO_6$ layered oxide interacted with aniline, revealing the formation of anilinium ions.

After confirming the process of intercalation, thermogravimetric or elemental analysis can be used to estimate the amount of intercalated guest species.

1.3. Acidity characterization for liquid phase applications

To evaluate the catalytic activity of a solid for any acid-catalyzed reaction, its acidic property should be examined. Until recently, the acidity of the layered oxides was mostly evaluated using several techniques in the gaseous phase. For example, He et al. [139] have used NH_3-temperature programmed desorption (NH_3-TPD) technique, one of the basic methods to measure acid strength and acid amount from the desorbed NH_3 quantity and desorbed temperature, to evaluate the acidic properties of several layered solid acids such as $HNbMoO_6.H_2O$, $HNbWO_6.1.5H_2O$ and $HTiNbO_5$ respectively. Results indicated the presence of two peaks in the NH_3-TPD profile for each of the layered solids, demonstrating the existence of two types of acid sites. For $HTiNbO_5$, two sharp peaks were situated at 481 and 591 K, whereas, for $HNbMoO_6.H_2O$, $HNbWO_6.1.5H_2O$, two broad peaks were situated at 598, 700-755 K and 535-583, 690-740 K respectively. Therefore, $HNbMoO_6.H_2O$ and $HNbWO_6.1.5H_2O$ show a higher acid strength than that of $HTiNbO_5$.

Zhong et al. [135] examined the catalytic activity of several layered transition metal oxides ($HTaWO_6$, $HNbWO_6$ and $HNbMoO_6$) using NH_3-TPD analysis. Results revealed the presence of two distinct peaks situated at 578 and 808 K and at 510 and 859 K for $HNbWO_6$ and $HNbMoO_6$ respectively. Those situated at low temperature are attributable to weak acid sites, while peaks found at higher temperatures are due to strong acid sites. For $HTaWO_6$, broad peaks at high temperature (at 709, 782 and 849 K) were encountered. In addition to the acid strength analysis, the total acid amount for all layered oxides was calculated from the peak area and results revealed 0.466, 0.312 and 0.278 mmol/g for $HTaWO_6$, $HNbMoO_6$ and $HNbWO_6$ respectively. Consequently, results indicated that $HTaWO_6$ possessed stronger acidic sites and higher acid amounts than the other tested oxides. Tagusagawa et al. [141] have used the same method to evaluate the difference in the acidic strength of $H_{1-x}Nb_{1-x}Mo_{1+x}O_6$ with different Nb and Mo ratios. Results indicated the presence of a large peak situated at high temperature between 663 and 700 K for layered protonated $H_{1-x}Nb_{1-x}Mo_{1+x}O_6$ with x ranging between -0.15 and 0.15, however, for bulk Nb-Mo oxides, x = -0.5 or 0.5, only a small peak was encountered in a low temperature range (between 512 and 485 K). Therefore, this can confirm that the layered protonated Nb-Mo oxides possess strong accessible acidity whereas Nb-Mo bulk oxides do not. This can be attributed to the preservation of the layered structure with x ranging between -0.15 and 0.15. On the contrary, if x values are equal to -0.5 or 0.5, the layered structure was lost, PXRD patterns revealed the disappearance of (001) and

(110) diffraction peaks and the appearance of new peaks attributed to the presence of several other oxides such as Nb_2O_5 or MoO_3 or mixed ones as $LiNb_3O_8$ and/or $Mo_3Nb_2O_{14}$, therefore decreasing the number of acidic sites.

The acidity of the layered oxides can thus be examined in the gaseous phase. Nevertheless, the accessibility to molecules like NH_3 does not imply that the acidic sites measured in this manner will interact on bulkier reagent molecules. By contrast, little was addressed for acid characterization in the liquid phase. This is a general problem encountered for any catalyst in the determination of the acidity accessible in the liquid phase. One approach was demonstrated by Tagusagawa et al. [133] who monitored the catalytic activity of several solid acid catalysts such as layered $HNbMoO_6$, Niobic-acid, Nb_2O_5-MoO_3, ion-exchange resins and H-type zeolites for liquid phase Friedel-Crafts alkylation with benzyl alcohol by ^{31}P magic angle spinning (MAS) nuclear magnetic resonance (NMR) using trimethylphosphine oxide (TMPO) as a probe molecule. The strength of the acid is usually determined from the ^{31}P chemical shift of the protonated TMPO ($TMPOH^+$), in other words the higher downfield chemical shift of $TMPOH^+$, the higher is the protonic acid strength. Results revealed that among all tested solids, layered $HNbMoO_6$ exhibited the highest ^{31}P chemical shift; two distinct peaks were situated at 80 and 86 ppm, attributable to strong acid sites.

Another one was investigated by Glazneva et al. [170] and recently by Weingarten and co-workers [171] who evaluated the concentration of acid sites using aqueous-phase titration method. This can be achieved by poisoning the active sites with a base and then measuring the catalytic activity versus poisoning concentration. In the work of Weingarten and co-workers [171], the catalysts studied, ZrP, SiO_2-Al_2O_3, γ-Al_2O_3, HY and WO_x/ZrO_2, were mixed with sodium hydroxide aqueous solution, filtered then titrated with hydrochloric acid. The acid amounts estimated by this method were compared with those obtained using the temperature-programmed desorption in the gas phase. Results indicated the inconsistency of the values between the methods. Additionally, Glazneva et al.[170] had shown the weakness of this method in which the poisons are adsorbed not only on the active sites but also on inactive ones. Therefore, this raises a question whether the method of aqueous titration for acidity quantification is reliable or not. Similar inconsistencies were obtained by Vilcoq et al. [98] when comparing the acidity of supported tungsten oxides measured by NH_3-TPD or in the liquid phase through a catalytic test: cyclohexanol dehydration.

Because of that, new techniques could advantageously be developed for the characterization of the solid acid catalysts in the liquid phase. In our work, we are going to focus on these possible characterization methods for the protonated layered transition metal oxides directly in the liquid phase.

1.4. Biomass - representative catalytic testing

1.4.1. Catalytic conversion of biomass:

Biomass is essential since it is the only renewable carbon source and widely available sustainable raw material for the production of fuels, chemicals and carbon-based materials that could replace in the future fossil fuel resources [32]. The general classes of feedstocks derived from biomass can be divided into edible (triglycerides and starch) and non-edible (lignocelluloses) [32]. The latter is essential since it can not only be considered as an important low cost feedstock for the production of liquid hydrocarbons chemically similar to those currently used in the transportation sector, chemicals and new bio-based materials such as bio-plastics [4] but also it can be widely utilized without affecting food supplies [13].

The carbohydrate content of lignocelluloses is typically 75%, which can be converted into soluble sugars directly through an acid hydrolysis process. The obtained sugars can then be converted into ethanol (the main biomass-derived fuel used nowadays), other bio-fuels, various chemicals, food and medicines via chemical and/or biological routes [37].

In order to efficiently convert cellulose into valuable products, much effort has been devoted to develop the catalytic processes over the past two decades, notably using solid acid catalysts.

Fukuoka and co-workers [172] examined the catalytic degradation of cellulose into sugar alcohols (sorbitol and mannitol) at 463 K. Results revealed the highest conversion using Pt or Ru catalysts supported on γ-Al_2O_3, HUSY (40), SiO_2-Al_2O_3 and HUSY (20).

Layered double hydroxides also known as hydrotalcites were also utilized for the biomass conversion processes. Moreau et al. [173] had firstly reported the utilization of hydrotalcites for the isomerization of glucose into fructose and compared its catalytic efficiency to that of alkaline-exchanged zeolites. Results indicated that the two tested layered double hydroxides (Mg/Al = 2.5 and 3.0) exhibited the highest catalytic yield (up to 42% for Mg/Al = 3).

Moreover, several biomass conversion processes were efficiently catalyzed by protonated $HNbMoO_6$ layered oxide. This was reported by Takagaki et al. [33, 174] who examined its efficient catalytic activity for the epimerization of sugars including glucose, mannose, xylose and arabinose in water and for the hydrolysis of saccharides such as sucrose, cellobiose, starch and cellulose. Tagusagawa et al. [141] also studied the hydrolysis of cellobiose at 368 K over $H_{1-x}Nb_{1-x}Mo_{1+x}O_6$ with various Nb and Mo ratios. Results revealed that the rate of reaction increased in the following order: $H_{1.1}Nb_{1.1}Mo_{0.9}O_6$ < $HNbMoO_6$ < $H_{0.9}Nb_{0.9}Mo_{1.1}O_6$ with the increase in Mo content due to the increase in the acidic strength. Therefore, one can deduce that the rate of this reaction is directly correlated to the acidic strength.

In addition to that, tungsten based species can also be employed as an efficient catalyst for converting sugars into valuable chemicals as investigated by Yong Liu et al. [175] and Yue Liu et al. [176] who examined the effective catalytic conversion of cellulose into hexanes or ethylene glycol, propylene glycol and sorbitol on layered $HNbWO_6$ or Ru/C catalyst in the presence of WO_3 respectively.

All these acid-catalyzed reactions had provided a subsequent transformation processes to convert some of biomass derivative molecules into the so-called platform molecules: polyols and sugars with shorter chains such as fructose and sucrose. These two platform molecules are crucial for the production of furans, a chemical platform molecule that serve for the production of liquid fuels and valuable fine chemicals.

1.4.2. Furan derivatives:

HMFs are considered as a versatile platform chemical that can be produced by the dehydration of sugars such as glucose, fructose, cellulose and lignocellulosic biomass [177]. HMFs in themselves have little use due to their high reactivity, high solubility in water, high boiling point, low energy density and excess oxygen content [13]. On the contrary, HMFs can serve as an important intermediate for the synthesis of linear alkanes for diesel or jet fuels, green solvents and bio-chemicals, for the production of polymer monomers such as 2,5-furandicarboxylic acid, para-xylene and 1,6-hexanediol and they are considered as key platform molecules for a variety of value-added chemicals such as 2,5-dimethylfuran, 2,5-diformylfuran, 2,5-furandicarboxylic acid and γ-valerolactone [178, 179].

The conversion of HMF into the crucial liquid bio-fuels can be achieved through a series of cascade reactions such as hydrogenation, deoxygenation, etherification, different C-C formation reactions such as aldol condensation, alkylation and hydroxyalkylation. Among the most attractive furan derivatives are Dimethylfuran (DMF) and 2,5-dimethyltetrahydrofuran (DMTHF) [13, 180].

DMF is not soluble in water, its high energy density and volatility are similar to that of gasoline and 40% higher than ethanol and it is considered as one of the most crucial substituent for gasoline blending used in the transportation sector [181, 182]. DMF can be formed through several reactions for example; Román-Leshkov et al. [181] had reported the production of DMF in good yields (76-79%) by a two-step process: first, production of HMF starting from fructose, second, hydrogenation over carbon supported copper/ruthenium catalyst using butanol as a solvent. Moreover, Thananatthanachon et al.[183] had demonstrated the transformation of DMF through fructose dehydration in a one-step process using formic acid, a by-product coming from biomass degradation, as a homogeneous acid catalyst.

In addition to DMF, 2,5-dimethyltetrahydrofuran (DMTHF) is another attractive furan derivative. This molecule has similar solubility, volatility and energy density to that of DMF. However, as a saturated molecule, it is more stable and is thus a better candidate than DMF for liquid fuel [182]. Depending on the initial feedstock, DMTHF was obtained using either Rh or Ir catalysts or under harsh conditions (high temperature, high pressure, multi-phase step processes, several catalysts). For instance, Yang and co-workers [182] had reported the synthesis of DMTHF from fructose with high yields (81%) at 140 °C under hydrogen atmosphere (H_2) using HI and $RhCl_3.xH_2O$ as catalysts and C_6H_5Cl as organic solvent to extract insoluble carbonaceous materials (unstable reaction intermediates formed upon heating fructose at 80 °C) from the aqueous layer. Additionally, Zhou et al.[184] had reported the high conversion of 2,5-hexanedione into DMTHF (yield = 99%) under hydrogen atmosphere through consecutive processes (Hydrogenation and dehydration) using Pt/C as the supported solid acid catalyst and Amberlite IR-120H as solid acid catalyst.

Alternatively, polyalcohols can act as reagents for furan production. Yamaguchi and co-workers [185] had represented another way for synthesizing DMTHF. In this process, the intermolecular dehydration of chiral 2,5-hexanediol (2R,5R) or (2S, 5S) to cis-2,5-dimethyltetrahydrofuran was achieved using high temperature liquid water (523 K) and high pressure carbon-dioxide. The latter was used to enhance the rate of dehydration step. Other works relate the cyclodehydration of 2,5-hexanediol using an enzyme and an intermediate

transesterification step [186]. 2,5-hexanediol could also be directly converted to DMTHF using homogeneous acid catalysts like sulfuric or phosphoric acids [187], or metal chlorides like $PdCl_2$ or $AlCl_3$ [188]. The production of DMTHF through the cyclodehydration of a polyalcohol could thus act as a simplified reaction in the liquid phase to evaluate the activity of a catalyst in presence of carbohydrates. This will be used in our work, as a catalytic test for the evaluation of layered materials.

1.5. Objectives of our work

This chapter has illustrated various aspects associated with the biomass valorization. These opportunities and constraints indicate the need of adapted catalysts. Obviously, several of the existing catalysts like zeolites or oxides retain great potential for one or the other transformation. Nevertheless, the parallel search for alternative materials able to withstand the specific reaction conditions required is an important challenge. Layered materials have been shown to present several features that could interestingly be applied to these biomass conversions. Existing solids, but also new materials should be more extensively studied in this context. The above data show that for these materials the understanding of the intercalation process is an important aspect of their activity.

Another aspect related to the development of such new catalysts is the characterization of these (layered) materials, in particular directly in the liquid phase where intercalation and reaction will proceed. Currently, the acid sites characterization carried out by gas phase adsorption shows its limitations and in the case of layered materials, the direct monitoring of the acidity in the liquid phase would be beneficial. Similarly the interaction of the intercalating molecule or the reagents with layered solids requires specific studies that could be provided by vibrational spectroscopies, and Raman in particular.

Finally, it is noteworthy that simplified test reactions are not readily available in the literature while many standard tests have been developed over the years to mimic various processes related to the petroleum-based conversions. This could be of interest, notably for the evaluation of layered materials.

Therefore, these 3 aspects related to the development and understanding of layered materials will be the focus of this PhD work.

While the **second chapter** will quickly present the methods used here, the **third chapter** is devoted to the structural characterization using Raman spectroscopy (solid phase) and XRD analysis of lamellar materials based on transition metal oxides such as $LiNbMoO_6$, $LiNbWO_6$, Bi_2WO_6 and $Bi_2W_2O_9$ before protonation and their modification upon acid treatments. Moreover, these known layered oxides are compared to newly synthesized layered solids that are based on Nb and W transition metal oxides and characterized by an Aurivillius phase and a stair-like structure. The protonation of the latter oxides will also be studied.

In the **fourth chapter**, the extensive investigation of the intercalation process of the successfully protonated lamellar oxides ($HNbMoO_6$, $HNbWO_6$, H_2WO_4, $H_2W_2O_7$ and H-

$Bi_{17}Nb_3W_6O_{51}$) using several organic bases such as pyridine, n-alkylamines (butylamine and octylamine), n-alcohols and 2,5-hexanediol is carried out. Pyridine and n-alkylamines are used for the acidity identification of all layered oxides whereas n-alcohols and diol intercalation provides crucial information to understand more the catalytic activity of the layered oxides that is carried out in the next chapter. To monitor the intercalation process, we used several techniques: Raman spectroscopy in the liquid phase, XRD and Thermogravimetric analysis. These allow examining the interaction between the probes and layered oxides, estimating quantitatively the amount of guest species or probe molecules intercalated and comparing the acidic strength of all tested layered oxides.

In the **fifth chapter**, a novel test reaction (cyclization of 2,5-hexanediol into 2,5-dimethyltetrahydrofuran) is developed to examine the catalytic activity of the following layered oxides: $HNbMoO_6$, $HNbWO_6$ and $H_2W_2O_7$ in comparison to other conventional solid acid catalysts such as Nb_2O_5 and several zeolites. This test is investigated under different reaction conditions and with different diol/H_2O ratios to examine the catalyst stability. Additionally, the catalysts were structurally characterized using Raman spectroscopy and XRD to correlate the intercalation process with that of the catalytic activity.

1.6. References

1 J. N. Chheda, G. W. Huber and J. A. Dumesic, *Angew. Chem. Int. Ed.*, 2007, **46**, 7164–7183.

2 J. C. Serrano-Ruiz and J. A. Dumesic, *Energy Environ. Sci.*, 2011, **4**, 83–99.

3 M. Höök and X. Tang, *Energy Policy*, 2013, **52**, 797–809.

4 D. M. Alonso, J. Q. Bond and J. A. Dumesic, *Green Chem.*, 2010, **12**, 1493–1513.

5 G. Chen, J. Andries and H. Spliethoff, *Renew. Energy*, 2003, **28**, 985–994.

6 J. A. Geboers, S. Van de Vyver, R. Ooms, B. Op de Beeck, P. A. Jacobs and B. F.Sels, *Catal. Sci. Technol.*, 2011, **1**, 714–726.

7 K. Parmar, *Int. J. Appl. Sci.*, 2017, **7**, 42–51.

8 M. Stöcker, *Angew. Chem. Int. Ed.*, 2008, **47**, 9200–9211.

9 A. J. Ragauskas, C. K. Williams, B. H. Davison, G. Britovsek, J. Cairney, C. A. Eckert, W. J. Frederick Jr., J. P. Hallett, D. J. Leak, C. L. Liotta, J. R. Mielenz, R. Murphy, R. Templer and T. Tschaplinski, *Science*, 2006, **311**, 484–489.

10 R. Rinaldi and F. Schüth, *Energy Environ. Sci.*, 2009, **2**, 610–626.

11 J. Goldemberg, *Energy Environ. Sci.*, 2008, **1**, 523–525.

12 G. W. Huber, S. Iborra and A. Corma, *Chem. Rev.*, 2006, **106**, 4044–4098.

13 M. J. Climent, A. Corma and S. Iborra, *Green Chem.*, 2014, **16**, 516.

14 R. M. West, Z. Y. Liu, M. Peter and J. A. Dumesic, *ChemSusChem*, 2008, **1**, 417–424.

15 K. -i. Shimizu, H. Furukawa, N. Kobayashi, Y. Itaya and A. Satsuma, *Green Chem.*, 2009, **11**, 1627–1632.

16 K. -i. Shimizu and A. Satsuma, *Energy Environ. Sci.*, 2011, **4**, 3140.

17 S. M. Csicsery, *Zeolites*, 1984, **4**, 116–126.

18 A. Taguchi and F. Schüth, *Microporous Mesoporous Mater.*, 2005, **77**, 1–45.

19 Y. Wan, H. Yang and D. Zhao, *Acc. Chem. Res.*, 2006, **39**, 423–432.

20 E. Antonakou, A. Lappas, M. H. Nilsen, A. Bouzga and M. Stöcker, *Fuel*, 2006, **85**, 2202–2212.

21 J.-P. Lange, *Biofuels, Bioprod. Biorefining*, 2007, **1**, 39–48.

22 A. Bruggink, R. Schoevaart and T. Kieboom, *Org. Process Res. Dev.*, 2003, **7**, 622–640.

23 Q.-N. Xia, Q. Cuan, X.-H. Liu, X.-Q. Gong, G.-Z. Lu and Y.-Q. Wang, *Angew. Chem. Int. Ed.*, 2014, **53**, 9755–9760.

24 X. Chen, P. Qian, T. Zhang, Z. Xu, C. Fang, X. Xu, W. Chen, P. Wu, Y. Shen, S. Li, J. Wu, B. Zheng, W. Zhang and F. Huo, *Chem. Commun.*, 2018, **54**, 3936–3939.

25 B. Karimi and H. M. Mirzaei, *RSC Adv.*, 2013, **3**, 20655–20661.

26 F. Liu, K. Huang, A. Zheng, F.-S. Xiao and S. Dai, *ACS Catal.*, 2018, **8**, 372−391.

27 F. Liu, W. Kong, C. Qi, L. Zhu and F. S. Xiao, *ACS Catal.*, 2012, **2**, 565–572.

28 A. Takagaki, C. Tagusagawa, S. Hayashi, M. Hara and K. Domen, *Energy Environ. Sci.*, 2010, **3**, 82–93.

29 P. Shen, H. T. Zhang, H. Liu, J. Y. Xin, L. F. Fei, X. G. Luo, R. Z. Ma and S. J. Zhang, *J. Mater. Chem. A*, 2015, **3**, 3456–3464.

30 W. L. Faith, *Ind. Eng. Chem.*, 1949, **37**, 9–11.

31 M. L. Rabinovich, *Cellul. Chem. Technol.*, 2010, **44**, 173–186.

32 M. Hara, K. Nakajima and K. Kamata, *Sci. Technol. Adv. Mater.*, 2015, **16**, 034903.

33 A. Takagaki, C. Tagusagawa and K. Domen, *Chem. Commun.*, 2008, **0**, 5363–5365.

34 M. Kitano, K. Nakajima, J. N. Kondo, S. Hayashi and M. Hara, *J. Am. Chem. Soc.*, 2010, **132**, 6622–6623.

35 P. Gupta and S. Paul, *Catal. Today*, 2014, **236**, 153–170.

36 N. Mansir, Y. H. Taufiq-Yap, U. Rashid and I. M. Lokman, *Energy Convers. Manag.*, 2017, **141**, 171–182.

37 S. De, S. Dutta and B. Saha, *Catal. Sci. Technol.*, 2016, **6**, 7364–7385.

38 A. Corma, *Chem. Rev.*, 1995, **95**, 559–614.

39 J. A. Lercher, A. Jentys and A. Brait, *Mol Sieves*, 2008, **6**, 153–212.

40 P. Bhanja and A. Bhaumik, *Fuel*, 2016, **185**, 432–441.

41 R. C. Deka, *Indian J. Chem. Technol.*, 1998, **5**, 109–123.

42 C. S. Cundy and P. A. Cox, *Chem. Rev.*, 2003, **103**, 663–701.

43 T. Danuthai, S. Jongpatiwut, T. Rirksomboon, S. Osuwan and D. E. Resasco, *Appl. Catal. A Gen.*, 2009, **361**, 99–105.

44 M. Aghaziarati, M. Kazemeini, M. Soltanieh and S. Sahebdelfar, *Ind. Eng. Chem. Res.*, 2007, **46**, 726–733.

45 A. Onda, T. Ochi and K. Yanagisawa, *Green Chem.*, 2008, **10**, 1033.

46 L. Jin, C.-h. Kuo and S. L. Suib, in the New and Future Developments in Catalysis: Catalytic Biomass conversion, S. L. Suib, *Elsevier*, 2013, Chapter 11.

47 M. Moliner, Y. Roman-Leshkov and M. E. Davis, *Proc. Natl. Acad. Sci.*, 2010, **107**, 6164–6168.

48 F. Guo, Z. Fang, C. C. Xu and R. L. Smith Jr., *Prog. Energy Combust. Sci.*, 2012, **38**, 672–690.

49 I. Plazl, S. Leskovšek and T. Koloini, *Chem. Eng. J.*, 1995, **59**, 253–257.

50 M. Ohara, A. Takagaki, S. Nishimura and K. Ebitani, *Appl. Catal. A Gen.*, 2010, **383**, 149–155.

51 V. M. Shinde, G. N. Patil, A. Katariya and Y. S. Mahajan, *Chem. Eng. Process.*, 2015, **95**, 241–248.

52 F. R. Abreu, M. B. Alves, C. C. S. Macêdo, L. F. Zara and P. A. Z. Suarez, *J. Mol. Catal. A Chem.*, 2005, **227**, 263–267.

53 I. V. Kozhevnikov, *Chem. Rev.*, 1998, **98**, 171−198.

54 M. M. Heravi, M. Vazin Fard and Z. Faghihi, *Green Chem. Lett. Rev.*, 2013, **6**, 282–300.

55 Y. C. Sharma and B. Singh., *Biofuels, Bioprod. Biorefining*, 2011, **5**, 69–92.

56 M. Misono, I. Ono, G. Koyano and A. Aoshima, *Pure Appl. Chem.*, 2000, **72**, 1305–1311.

57 M. Chidambaram and A. T. Bell, *Green Chem.*, 2010, **12**, 1253–1262.

58 Q. Zhao, L. Wang, S. Zhao, X. Wang and S. Wang, *Fuel*, 2011, **90**, 2289–2293.

59 T. Okuhara, M. Kimura and T. Nakato, *Appl. Catal. A Gen.*, 1997, **155**, L9–L13.

60 T. Okuhara, *Chem. Rev.*, 2002, **102**, 3641–3666.

61 A. Di Paola, M. Bellardita and L. Palmisano, *Catalysts*, 2013, **3**, 36–73.

62 K.-S. Lin, H.-W. Cheng, W.-R. Chen and J.-F. Wu, *J. Environ. Eng. Manag.*, 2010, **20**, 69–76.

63 T. Fröschl, U. Hörmann, P. Kubiak, G. Kučerová, M. Pfanzelt, C. K. Weiss, R. J. Behm, N. Hüsing, U. Kaiser, K. Landfester and M. Wohlfahrt-Mehrens, *Chem. Soc. Rev.*, 2012, **41**, 5313–5360.

64 C. S. Lanziano, F. Rodriguez, S. C. Rabelo, R. Guirardello, V. T. da silva and C. B. Rodella, *Chem. Eng. Trans.*, 2014, **37**, 589–594.

65 J. N. Kondo, T. Yamashita, K. Nakajima, D. Lu, M. Hara and K. Domen, *J. Mater. Chem.*, 2005, **15**, 2035–2040.

66 F. Kishimoto, D. Mochizuki, M. M. Maitani, E. Suzuki and Y. Wada, *RSC Adv.*, 2015, **5**, 77839–77846.

67 J. Yan, T. Wang, G. Wu, W. Dai, N. Guan, L. Li and J. Gong, *Adv. Mater.*, 2015, **27**, 1580–1586.

68 J. Cao, B. Luo, H. Lin, B. Xu and S. Chen, *Appl. Catal. B Environ.*, 2012, **111**–**112**, 288–296.

69 J. Díaz-Reyes, V. Dorantes-García, A. Pérez-Benítez and J. A. Balderas-López, *Superf. y Vacio*, 2008, **21**, 12–17.

70 N. Prabhu, S. Agilan, N. Muthukumarasamy and C. K. Senthilkumaran, *Dig. J. Nanomater. Biostructures*, 2013, **8**, 1483–1490.

71 J. R. Darwent and A. Mills, *J. Chem. Soc. Faraday Trans*, 1982, **78**, 359–367.

72 A. E. A. Said, M. M M. Abd El-Wahab and M. Abd El-Aal, *Chem. Mater. Eng.*, 2016, **4**, 17–25.

73 D. G. Barton, S. L. Soled and E. Iglesia, *Top. Catal.*, 1998, **6**, 87–99.

74 C. Martín, G. Solana, P. Malet and V. Rives, *Catal. Today*, 2003, **78**, 365–376.

75 F. A. Chernyshkova, *Russ. Chem. Rev.*, 2007, **62**, 743–749.

76 S.-H. Chai, H.-P. Wang, Y. Liang and B.-Q. Xu, *J. Catal.*, 2007, **250**, 342–349.

77 Q. Sun, Y. Fu, H. Yang, A. Auroux and J. Shen, *J. Mol. Catal. A Chem.*, 2007, **275**,

183–193.

78 S. Okazaki and H. Harada, *Chem. Lett.*, 1988, **17**, 1313–1316.

79 K. Nakajima, Y. Baba, R. Noma, M. Kitano, N. J. Kondo, S. Hayashi and M. Hara, *J. Am. Chem. Soc*, 2011, **133**, 4224–4227.

80 T. Yamaguchi and C. Nishimichi, *Catal. Today*, 1993, **16**, 555–562.

81 P. Lauriol-Garbey, J. M.M. Millet, S. Loridant, V. Belliere-Baca and P. Rey, *J. Catal.*, 2011, **281**, 362–370.

82 P. Lauriol-Garbey, G. Postole, S. Loridant, A. Auroux, V. Belliere-Baca, P. Rey and J. M. M. Millet, *Appl. Catal. B Environ.*, 2011, **106**, 94–102.

83 K. Tanabe, *Mater. Chem. Phys.*, 1987, **17**, 217–225.

84 J. Song, X. Wang, X. Ni, H. Zheng, Z. Zhang, M. Ji, T. Shen and X. Wang, *Mater. Res. Bull.*, 2005, **40**, 1751–1756.

85 J. Z. Ou, J. L Campbell, D. Yao, W. Wlodarski and K. Kalantar-zadeh, *J. Phys. Chem. C*, 2011, **115**, 1757–1763.

86 X. Fan, G. Fang, P. Qin, N. Sun, N. Liu, Q. Zheng, F. Cheng, L. Yuan and X. Zhao, *J. Phys. D. Appl. Phys.*, 2011, **44**, 045101–045107.

87 J. Haber and E. Lalik, *Catal. Today*, 1997, **33**, 119–137.

88 N. Pernicone, F. Lazzerin, G. Liberti, G. Lanzavecchia, *J. Catal.*, 1969, **14**, 391–393.

89 T. Prasomsri, M. Shetty, K. Murugappan and Y. Román-Leshkov, *Energy Environ. Sci.*, 2014, **7**, 2660–2669.

90 S.-C. Qi, X.-Y. Wei, Z.-M. Zong and Y.-K. Wang, *RSC Adv.*, 2013, **3**, 14219.

91 L. M.Petkovic, J. R. Bielenberg and G. Larsen, *J. Catal.*, 1998, **178**, 533–539.

92 G. Raveendra, M. Surendar and P. S. Sai Prasad, *New J. Chem.*, 2017, **41**, 8520–8529.

93 C. H. Du and Z. W. Zhang, *Adv. Mater. Res.*, 2013, **724–725**, 365–368.

94 L. Li, Y. Yoshinaga and T. Okuhara, *Phys. Chem. Chem. Phys.*, 1999, **1**, 4913–4918.

95 K. V. R. Chary, K. R. Reddy, G. Kishan, J. W. Niemantsverdriet and G. Mestl, *J. Catal.*, 2004, **226**, 283–291.

96 M. Massa, A. Andersson, E. Finocchio, G. Busca, F. Lenrick and L. R. Wallenberg, *J.*

Catal., 2013, **297**, 93–109.

97 B. Katryniok, S. Paul and F. Dumeignil, *ACS Catal.*, 2013, **3**, 1819–1834.

98 L. Vilcocq, R. Koerin, A. Cabiac, C. Especel, S. Lacombe and D. Duprez, *Appl. Catal. B, Environ.*, 2014, **148**–**149**, 499–508.

99 R. A. Schoonheydt, T. Pinnavaia, G. Lagaly and N. Gangas, *Pure Appl. Chem.*, 1999, **71**, 2367–2371.

100 V. Nicolosi, M. Chhowalla, M. G. Kanatzidis, M. S. Strano and J. N. Coleman, *Science*, 2013, 340, 1226419.

101 G. Alberti and T. Bien, in the Comprehensive supramolecular chemistry, J-M. Lehn G. Alberti and T. Bein, *Pergamon press, Oxford*, 1996, Chapter 1.

102 S. A. Solin, *J. Mol. Catal.*, 1984, **27**, 293–303.

103 G. Centi and S. Perathoner, *Microporous Mesoporous Mater.*, 2008, **107**, 3–15.

104 R. T. Cygan, J. A. Greathouse, H. Heinz and A. G. Kalinichev, *J. Mater. Chem.*, 2009, **19**, 2470–2481.

105 V. Rives and S. Kannan, *J. Mater. Chem.*, 2000, **10**, 489–495.

106 Q. Tao, B. J. Reddy, H. He, R. L. Frost, P. Yuan and J. Zhu, *Mater. Chem. Phys.*, 2008, **112**, 869–875.

107 A. I. Khan and D. O'Hare, *J. Mater. Chem.*, 2002, **12**, 3191–3198.

108 J. J. Bravo-Suárez, E. A. Páez-Mozo and S. T. Oyama, *Quim. Nov.*, 2004, **27**, 601–614.

109 F. Cavani, F. Trifirò and A. Vaccari, *Catal. Today*, 1991, **11**, 173–301.

110 G. Camino, A. Maffezzoli, M. Braglia, M. De Lazzaro and M. Zammarano, *Polym. Degrad. Stab.*, 2001, **74**, 457–464.

111 S. Miyata and T. Kumura, *Chem. Lett.*, 1973, **2**, 843–848.

112 V. Ambrogi, G. Fardella, G. Grandolini and L. Perioli, *Int. J. Pharm.*, 2001, **220**, 23–32.

113 R. G. Buchheit, *J. Appl. Electrochem.*, 1998, **28**, 503–510.

114 N. Das, D. Tichit, R. Durand, P. Graffin and B. Coq, *Catal. Letters*, 2001, **71**, 181–185.

115 P. Dinka, K. Prandová and M. Hronec, *Appl. Clay Sci.*, 1998, **13**, 467–477.

116 M. Manikandan, A. K. Venugopal, K. Prabu, R. K. Jha and T. Raja, J. *Mol. Catal. A: Chem.* 2016, **417**, 153-162.

117 K. Yan, Y. Liu, Y. Lu, J. Chai, L. Sun, *Catal. Sci. Technol.*, 2017, **7**, 1622-1645.

118 A. Y. A. Kaassis, S.-M. Xu, S. Guan, D. G. Evans, M. Wei and G. R. Williams, *J. Solid State Chem.*, 2016, **238**, 129–138.

119 G. R. Williams, J. Crowder, J. C. Burley and A. M. Fogg, *J. Mater. Chem.*, 2012, **22**, 13600–13611.

120 J.-H. Choy, Y.-M. Kwon, S.-W. Song and S. H. Chang, *Bull. Korean Chem. Soc.*, 1997, **18**, 450–453.

121 T. Hara, M. Ishikawa, J. Sawada, N. Ichikuni and S. Shimazu, *Green Chem.*, 2009, **11**, 2034–2040.

122 H. Song, A. O. Sjåstad, H. Fjellvåg, H. Okamoto, Ø. B. Vistad, B. Arstad and P. Norby, *J. Solid State Chem.*, 2011, **184**, 3135–3143.

123 M. Shirpour, J. Cabana and M. Doeff, *Chem. Mater.*, 2014, **26**, 2502–2512.

124 Y. Ide, M. Sadakane, T. Sano and M. Ogawa, *J. Nanosci. Nanotechnol.*, 2014, **14**, 2135–2147.

125 M. Milanović, I. Stijepović and L. M. Nikolić, *Process. Appl. Ceram. Ceram.*, 2010, **4**, 69–73.

126 Y. Fuse, Y. Ide and M. Ogawa, *Polym. Chem.*, 2010, **1**, 849–853.

127 D. Yang, Z. Zheng, H. Liu, H. Zhu, X. Ke, Y. Xu, D. Wu and Y. Sun, *J. Phys. Chem. C*, 2008, **112**, 16275–16280.

128 Y. Ide and M. Ogawa, *Angew. Chem. Int. Ed.*, 2007, **46**, 8449–8451.

129 M. Osada, Y. Ebina, H. Funakubo, S. Yokoyama, T. Kiguchi, K. Takada and T. Sasaki, *Adv. Mater.*, 2006, **18**, 1023–1027.

130 S. Nakano, T. Sasaki, K. Takemura and M. Watanabe, *Chem. Mater.*, 1998, **10**, 2044–2046.

131 T. Sasaki, F. Izumi and M. Watanabe, *Chem. Mater.*, 1996, **8**, 777–782.

132 S. Li, N. Li, G. Li, L. Li, A. Wang, Y. Cong, X. Wang, G. Xu and T. Zhang, *Appl. Catal. B Environ.*, 2015, **170–171**, 124–134.

133 C. Tagusagawa, A. Takagaki, S. Hayashi and K. Domen, *Catal. Today*, 2009, **142**, 267–271.

134 R. E. Schaak and T. E. Mallouk, *Chem. Commun.*, 2002, **0**, 706–707.

135 J. Zhong, Y. Guo and J. Chen, *J. Energy Chem.*, 2017, **26**, 147–154.

136 A. Takagaki, R. Sasaki, C. Tagusagawa and K. Domen, *Top. Catal.*, 2009, **52**, 592–596.

137 C. Tagusagawa, A. Takagaki, S. Hayashi and K. Domen, *J. Am. Chem. Soc.*, 2008, **130**, 7230–7231.

138 Y. Morita, S. Furusato, A. Takagaki, S. Hayashi, R. Kikuchi and S. T. Oyama, *ChemSusChem*, 2014, **7**, 748–752.

139 J. He, Q. J. Li, Y. Tang, P. Yang, A. Li, R. Li and H. Z. Li, *Appl. Catal. A Gen.*, 2012, **443**–**444**, 145–152.

140 V. Bhat and J. Gopalakrishnan, *Solid State Ionics*, 1988, **26**, 25–32.

141 C. Tagusagawa, A. Takagaki, K. Takanabe, K. Ebitani, S. Hayashi and K. Domen, *J. Phys. Chem. C*, 2009, **113**, 17421–17427.

142 D. Chen and Y. Sugahara, *Chem. Mater.*, 2007, **19**, 1808–1815.

143 B. Ingham, S. V. Chong and J. L. Tallon, *J. Phys. Chem. B*, 2004, **109**, 4936–4940.

144 S. V. Chong, B. Ingham and J. L. Tallon, *Curr. Appl. Phys.*, 2004, **4**, 197–201.

145 Z. Tai, J. Zhang, A. Wang, J. Pang, M. Zheng and T. Zhang, *ChemSusChem*, 2013, **6**, 652–658.

146 C. Yue, G. Li, E. A. Pidko, J. J. Wiesfeld, M. Rigutto and E. J. M. Hensen, *ChemSusChem*, 2016, **9**, 2421–2429.

147 M. R. Waller, T. K. Townsend, J. Zhao, E. M. Sabio, R. L. Chamousis, N. D. Browning and F. E. Osterloh, *Chem. Mater.*, 2012, **24**, 698–704.

148 T. Ban, T. Ito and Y. Ohya, *Inorg. Chem.*, 2013, **52**, 10520–10524.

149 D. Chen, T. Li, L. Yin, X. Hou, X. Yu, Y. Zhang, B. Fan, H. Wang, X. Li, R. Zhang, T. Hou, H. Lu, H. Xu, J. Sun and L. Gao, *Mater. Chem. Phys.*, 2011, **125**, 838–845.

150 B. Wang, X. Dong, Q. Pan, Z. Cheng and Y. Yang, *J. Solid State Chem.*, 2007, **180**, 1125–1129.

151 M. L. Occelli, S. D. Landau and T. J. Pinnavaia, *J. Catal.*, 1984, **90**, 256–260.

152 S. Cheng, *Catal. Today*, 1999, **49**, 303–312.

153 E. M. Serwicka and K. Bahranowski, *Catal. Today*, 2004, **90**, 85–92.

154 S. P. Newman and W. Jones, *New J. Chem.*, 1998, **22**, 105–115.

155 M. Ogawa and K. Kuroda, *Chem. Rev.*, 1995, **95**, 399–438.

156 K. Imaeda, F. Tian, H. Inokuchi and K. Ichimura, *J. Solid State Chem.*, 1999, **145**, 421–426.

157 W. Sugimoto, M. Omoto, K. Yokoshima, Y. Murakami and Y. Takasu, *J. Solid State Chem.*, 2004, **177**, 4542–4545.

158 S. Dasgupta, M. Agarwal and A. Datta, *J. Mol. Catal. A Chem.*, 2004, **223**, 167–176.

159 A. M. Fogg, V. M. Green, H. G. Harvey and D. O'Hare, *Adv. Mater.*, 1999, **11**, 1466–1469.

160 G. Alberti, S. Cavalaglio, C. Dionigi and F. Marmottini, *Langmuir*, 2000, **16**, 7663–7668.

161 M. Casciola, S. Chieli, U. Costantino and A. Peraio, *Solid State Ionics*, 1991, **46**, 53–59.

162 G. L. Rosenthal, J. Caruso and S. G. Stone, *Polyhedron*, 1994, **13**, 1311–1314.

163 A. Guerrero-Ruiz, I. Rodriguez-Ramos, J. L. G. Fierro, A. Jimenez Lopez, P. Olivera Pastor and P. Maireles Torres, *Appl. Catal. A Gen.*, 1992, **92**, 81–92.

164 V. Rives and M. A. Ulibarri, *Coord. Chem. Rev.*, 1999, **181**, 61–120.

165 P. G. Rodriguez, H. Yuan, K. J. H. Van Den Nieuwenhuizen, W. Lette, D. J. Schipper and J. E. Ten Elshof, *ACS Appl. Mater. Interfaces*, 2016, **8**, 28926–28934.

166 C. Tagusagawa, A. Takagaki, K. Takanabe, K. Ebitani, S. Hayashi and K. Domen, *J. Catal.*, 2010, **270**, 206–212.

167 Li-F. Hu, Y. Tang, J. He, K. Chen and W. Lv, *Russ. J. Phys. Chem. A.*, 2017, **91**, 511–516.

168 N. S. P. Bhuvanesh and J. Gopalakrishnan, *Inorg. Chem.*, 1995, **34**, 3760–3764.

169 Y. Tsunoda, W. Sugimoto and Y. Sugahara, *Chem. Mater.*, 2003, **15**, 632–635.

170 T. S. Glazneva, N. S. Kotsarenko and E. A. Paukshtis, *Kinet. Catal.*, 2008, **49**, 859–867.

171 R. Weingarten, G. A. Tompsett, W m. C. Conner Jr. and G. W. Huber, *J. Catal.*, 2011, **279**, 174–182.

172 A. Fukuoka and P. L. Dhepe, *Angew. Chem. Int. Ed.*, 2006, **45**, 5161–5163.

173 C. Moreau, R. Durand, A. Roux and D. Tichit, *Appl. Catal. A Gen.*, 2000, **193**, 257–264.

174 A. Takagaki, S. Furusato, R. Kikuchi and S. T. Oyama, *ChemSusChem*, 2015, **8**, 3769–3772.

175 Y. Liu, L. Chen, T. Wang, X. Zhang, J. Long, Q. Zhang and L. Ma, *RSC Adv.*, 2015, **5**, 11649–11657.

176 Y. Liu, C. Luo and H. Liu, *Angew. Chem. Int. Ed.*, 2012, **51**, 3249–3253.

177 R.-J. Van Putten, J. C. Van Der Waal, E. de Jong, C. B. Rasrendra, H. J. Heeres and J. G. de Vries, *Chem. Rev.*, 2013, **113**, 1499–1597.

178 L. Hu, X. Tang, J. Xu, Z. Wu, L. Lin and S. Liu, *Ind. Eng. Chem. Res.*, 2014, **53**, 3056–3064.

179 X. Tang, J. Wei, N. Ding, Y. Sun, X. Zeng, L. Hu, S. Liu, T. Lei and L. Lin, *Renew. Sustain. Energy Rev.*, 2017, **77**, 287–296.

180 K. R. Vuyyuru and P. Strasser, *Catal. Today*, 2012, **195**, 144–154.

181 Y. Román-Leshkov, C. J. Barrett, Z. Y. Liu and J. A. Dumesic, *Nature*, 2007, **447**, 982–985.

182 W. Yang and A. Sen, *ChemSusChem*, 2010, **3**, 597–603.

183 T. Thananatthanachon and T. B. Rauchfuss, *ChemSusChem*, 2010, **3**, 1139–1141.

184 H. Zhou, J. Song, Q. Meng, Z. He, Z. Jiang, B. Zhou, H. Liu and B. Han, *Green Chem.*, 2015, **18**, 220–225.

185 A. Yamaguchi, N. Hiyoshi, O. Sato and M. Shirai, *ACS Catal.*, 2011, **1**, 67–69.

186 M. -J. Kim and I. -S. Lee, *J. Org. Chem.*, 1993, **58**, 6483–6485.

187 M. Lj. Mihailovic, S. Gojkovic and Z. Cekovic, *J. Chem. Soc., Perkin Trans. 1,* 1972, **0**, 1–5.

188 A. Molnar, K. Felfoldi and M. Bartok, *Tetrahedron*, 1981, **37**, 2149–2151.

CHAPTER TWO

EXPERIMENTAL PART

2.1. Synthesis and Protonation of the catalysts

The various catalysts in this study required a preliminary synthesis of Li- or Bi-precursors. These solids were then subsequently protonated to make the solids acidic.

2.1.1. Synthesis of metal oxides precursors

For all synthesis, Li_2CO_3 (99%), Nb_2O_5 (99.5%), MoO_3 (99.5%) and WO_3 (99.8%) precursors were purchased from Alfa Aesar company and used without any further purification.

a. $LiNbMoO_6$ and $LiNbWO_6$: Layered $LiNbMoO_6$ and $LiNbWO_6$ were synthesized as reported by He and co-workers [1], via a solid-state reaction mechanism. For $LiNbMoO_6$, a stoichiometric amount of 0.5 mole Li_2CO_3, 0.5 mol Nb_2O_5 and 1 mole MoO_3, i.e. 0.117, 0.423 and 0.458 grams, respectively, were mixed together then calcined under air at 853 K for 24 hours in a programmable furnace with a heating rate of 3 ºC/min and with one intermediate grinding during the heating treatment to obtain 1 g of $LiNbMoO_6$ layered oxide.

Regarding $LiNbWO_6$, to obtain 1 gram of the layered oxide, a stoichiometric amount of 0.5 mole Li_2CO_3, 0.5 mol Nb_2O_5 and 1 mole WO_3, i.e. 0.092, 0.331 and 0.577 grams, respectively, were mixed then calcined under air at 1023 K for 72 hours in the furnace with one intermediate grinding during the heating treatment.

b. $Bi_2W_2O_9$ and Bi_2WO_6: Different modes of preparation were employed to synthesize the two layered bismuth oxides. Regarding the synthesis of $Bi_2W_2O_9$, it was based on a method described by Waller and co-workers [2] and Schaak et al. [3]. Using the traditional solid state reaction method, a stoichiometric amount of bismuth trioxide (Bi_2O_3, 99.975%) and tungsten trioxide (WO_3, 99.8%), purchased from Alfa Aesar and corresponding to 2.50 and 2.49 grams, respectively, were mixed together, ground to a fine powder with a mortar and pestle, pressed into pellets, placed in a porcelain crucible and finally heated at 1023K for 20 hours under air with a heating rate of 3 ºC/min to obtain 5 grams of yellowish bismuth tungstate powder.

For Bi_2WO_6, as depicted by Nithya et al. [4] and Saison et al. [5] the stoichiometric amounts of bismuth and sodium tungstate solutions were obtained by dissolving 0.472 grams of $Bi(NO_3)_3.5H_2O$ (Alfa Aesar, 99.5%) in 50 ml nitric acid and 1.39 grams of $Na_2WO_4.2H_2O$ (Alfa Aesar, 99.5%) in 50 ml distilled water, respectively. Then 15 ml of each solution were

mixed together in a Teflon reactor and heated in a microwave oven at 473K for 4 hours. Finally, the solid was centrifuged, washed for three times in distilled water and dried under air to obtain 1 gram of pale yellow powder.

c. New mixed oxides ($Bi_xNb_yW_zO_n$): Bismuth layered oxides with general formula $Bi_{2p}A_{n-p}B_nO_{3(n+p)}$ such as $Bi_7Nb_3WO_{21}$, $Bi_9Nb_3W_2O_{27}$, $Bi_{11}Nb_3W_3O_{33}$ and $Bi_{17}Nb_3W_6O_{51}$ were synthesized using solid state reaction mechanism similarly to the other layered metal oxides. As described by Steciuk et al. [6], stoichiometric amounts of the starting Bi_2O_3, WO_3 and Nb_2O_5 precursors with cationic ratios Bi:W:Nb of 7:3:1, 9:3:2, 11:3:3 and 17:3:6 were mixed together, pressed into self-supported disks or pellets (3 tons.cm^{-2}), placed on a platinum plate in an alumina tray and then calcined in a tubular oven under air at 1073K for 24 hours. After an intermediate regrinding and pelletizing step, a second calcination cycle at 1273K for 24 hours was required to obtain the crystallized phases.

2.1.2. Protonation of all layered samples

a. $LiNbMoO_6$ and $LiNbWO_6$: The proton-exchange process to produce $HNbMoO_6$ and $HNbWO_6$ was performed similarly as reported by Hu et al. [7, 8] by stirring 1g of the lithium precursors in 100 ml of 2 M acid solution (HNO_3) at room temperature for three days with one replacement of the acid with a fresh one in between. After three days of stirring, the products were washed several times with distilled water then dried in air at 423K.

b. $Bi_2W_2O_9$ and Bi_2WO_6: The protonation of $Bi_2W_2O_9$ and Bi_2WO_6 was carried out as demonstrated by Waller et al. [2] and Kudo et al. [9], where samples were suspended in HCl solution of 6 M concentration and stirred at ambient temperature for 72 hours. After three days of stirring, the mixture was centrifuged once and the acidic supernatant was discarded. The resultant solids were resuspended in fresh acid, stirred for another 72 hours, then centrifuged off and washed several times with distilled water before drying in air at 423K.

c. New mixed oxides ($Bi_xNb_yW_zO_n$): The protonation of the new layered oxides was performed for the first time. Therefore, to achieve successful protonation, several reaction conditions were employed. The experimental details of the synthesis procedures carried out are summarized in the table below.

Table 2.1: Detailed experimental conditions for the protonation trials of the new layered oxides.

Acid used	Concentration (M)	Salt added	Stirring time	Temperature
HCl	6	-	1 week	RT
HNO_3	2	-	1 week	RT
HCl	12	-	2 days	RT
H_3PO_4	3	-	1 week	RT
H_3PO_4	3	LiCl	1 week	RT
HCl	6	LiCl	3 days	RT
H_3PO_4	3	KCl	1 week	RT
H_2SO_4	0.5	-	1 week	RT
HNO_3	5	-	4 days	Oil bath, 70 °C
HCl	3	-	3 hours	Microwave heating

RT = Room Temperature.

2.2. Characterization techniques

2.2.1. Powder X-ray diffraction (PXRD)

All layered oxides were qualitatively analyzed by Powder X-ray diffraction (PXRD) at room temperature on a PANalytical X'Pert Pro diffractometer operated at 45 KV and 20 mA with a CuKα irradiation, λ=1.54060, as the X-ray source. All patterns were recorded in an angular range between 3 and 75° (2θ) with a step scan of 0.017°.

The recorded patterns were analyzed using the crystallographic program Jana 2006 [10]. For the layered metal oxides precursors, whose structures are known and documented in the literature, the PXRD patterns were analyzed using the Rietveld method [11]. This method allows a structure refinement based on the exploitation of the overall profile of the powder X-ray or neutron diffraction patterns. It consists of comparing the experimental patterns with simulated ones that take into account both the structure (atomic positions, occupancies …) and parameters such as unit cell, zero shift or profile functions in order to optimize (refine) the structural model. To achieve this, several steps should be followed during the refinement

procedure: first, registration of the expected cell parameters (a, b, c) and lattice angles (α, β, γ) (if available, these parameters may be taken from the crystallographic information files (CIF) found in the literature). Second: background fitting. Third: refinement of the powder profile (peak shape (Gaussian or Lorentzian) and zero shift. Fourth: cell parameters refinement and finally the structural model itself. The refined diffraction patterns should match with the experimental ones (peak shape, position and intensity) to ascertain that the refined structural model is the correct one.

For the protonated and intercalated compounds whose structures were not known, PXRD patterns were still used to obtain cell parameters using whole powder pattern decomposition methods (also referred as Pawley [12]) or Le Bail methods [13]. In these methods the intensities of the peaks are not calculated based on a structural model but estimated from the experimental data. Only the peak shape and position are refined against experimental data. This does not allow refining the structural model but it is suitable for cell parameters identification. Even though, hypothesis about the space group of the unknown compound should be made.

2.2.2. Thermogravimetry-Infrared analysis (TG-IR)

Thermogravimetry consists in following the mass variations of a sample during the rise in temperature. This technique was used here to monitor the amounts of moisture and organics intercalated in the layered oxides. Moreover, it is possible to determine whether the physical transformations or chemical reactions, likely to occur during the rise in temperature, are endo- or exothermic ones by recording the heat flow. The thermogravimetric analyses (TGA) and heat flow were recorded using a SETSYS (SETARAM, Caluire, France) analyzer module by heating the samples from room temperature to 800°C with a heating rate of 5 °C/min under 40 ml/min. flow of air.

Additionally, TGA was coupled with FT-IR spectroscopy in order to identify the evolved gases in each step simultaneously to the mass loss quantification. The inlet sidearm of the FT-IR cell is directly attached to the furnace tube of the TGA analyzer through a heated line, therefore, the gases evolved directly swept from the TGA to the IR cell. Then, the IR spectra (1 spectra/min) were recorded using a Nicolet Nexus AVATAR 360 IR spectrometer in the 400 - 4000 cm^{-1} range in 32 scans with a resolution of 4 cm^{-1}.

2.2.3. Infrared spectroscopy

Infrared spectroscopy provides quantitative and qualitative information about the molecular vibrations.

In our work, to qualitatively monitor the acidity of dried samples already intercalated with guest species such as pyridine, approximately 5 mg of the latter were thoroughly mixed with 95 mg of KBr, pressed (~10^7 Pa) into pellets (2 cm^2 area) and placed in the IR cell. The IR spectra were then recorded at room temperature on a Nicolet Nexus 5700 FT-IR spectrometer equipped with an MCT detector and an extended-KBr beam splitter in the 400 - 5500 cm^{-1} range in 128 scans with a resolution of 2 cm^{-1}.

2.2.4. Raman spectroscopy

Raman spectroscopy was used primarily to determine the vibrational fingerprints of the layered solids. Raman spectra were obtained at ambient conditions on a Raman microscope Horiba Jobin Yvon Labram 300. A green laser at 532 nm wavelength was focused on the sample through a 50x or 100x objectives at ca. 4mW.

Raman spectroscopy was also used in the presence of liquids as described below.

2.3. Intercalation experiments

Several organics were used for intercalation: n-alkylamines (butylamine (Aldrich Europe, 99%) and octylamine (Sigma Aldrich, 99%)), pyridine (Janssen Chimica, 99%) and alcohols (ethanol (Sigma Aldrich, > 96.9%), propanol (Carlo ERBA, 99 %), butanol (Alfa Aesar, 99.4%), hexanol (Sigma Aldrich, 98%), octanol (Fluoro Chem, 98%) and 2,5-hexanediol (Fluorochem, 98%). The intercalation process into protonated layered transition metal oxides was carried out in the following manner: intercalates were added either drop by drop or in larger quantities (0.2 - 1 ml) into 30 - 35 mg of the layered oxides at room temperature, then solids were analyzed daily during the first week, then later, once within two to three days. In order to ensure the intercalation process, the samples were kept with the liquid for one up to three months. Intercalation was characterized using Raman spectroscopy in the liquid phase. This step was achieved using a Raman immersion probe (In Photonics) that can be directly submerged in liquid solutions and allow for in-situ measurements. The latter is lined to the spectrometer via two optical fibers; the excitation one to direct and focus the monochromatic excitation source (green laser of 532 nm wavelength) to the sample and a

collecting fiber to collect the scattered light and direct it to the spectrometer to record and analyze the results. Rayleigh radiation is removed in the head of the probe before entering the collection fiber.

To optimize the best working procedure using the probe, several experiments were performed. After adding the sample into the intercalate, the solid was not detected by the probe anymore, therefore the intercalate was added into the sample.

After Raman characterization, samples were dried in air at 423K then characterized by powder X-ray diffraction and refined using Jana program to confirm the intercalation process and to examine its effects on the structure of the layered samples. Finally, TGA analyses were carried out to quantify the amount of intercalates inserted into the interlayers of the layered oxides following the procedure explained above.

With the case of alcohols and 2,5-hexanediol, the intercalation process was also monitored at higher temperatures (60 - 80 and 100°C). A quantity of 10 mmol of guest species were added to 0.10 mmol of layered oxides and stirred in an oil bath for 24 hours at 750 rpm using a round bottom flask at 60°C and a glass reactor vessel (Ace glass pressure tube, Sigma Aldrich) at higher temperatures (80 and 100°C). Then, all samples were washed using dichloromethane to be rapidly dehydrated then characterized by powder X-ray diffraction and Raman spectroscopy in the solid phase.

2.4. Catalytic test

Catalytic tests were performed to study the cyclization of 2,5-hexanediol over several solid acid catalysts such as $HNbMoO_6$, ZSM-5 (H-90, Si:Al = 40-45), Zeolite Beta (BEA, CP B/4E Si:Al = 12.5), Zeolite Y (NH_4-Y Si:Al = 2.6) and Niobium oxide ($Nb_2O_5.nH_2O$). $HNbMoO_6$ was synthesized in our lab using the procedure depicted above and used without any further treatment. The zeolites H-ZSM-5, H-beta and H-Y were purchased from Zeolyst and activated at 450°C for 6 hours before use under air flow followed by argon flux prior transfer over the reaction mixture. Niobium oxide ($Nb_2O_5.nH_2O$) was provided from Sigma Aldrich and was similarly activated at 250°C for 6 hours under air flow followed by Argon atmosphere before transferring to the reaction mixture.

The reaction was typically performed in a batch reactor by stirring 1g (8.46 mmol) of 2,5-hexanediol (Fluorochem, 98%) with 56 mg of catalyst at 750 rpm under reflux in absence of solvent in an oil bath at 120 °C for 15 - 60 minutes. During the reaction several aliquots

were collected at successive intervals to follow the evolution of the reaction. The reactants and products were analyzed by Gas chromatography (GC-Varian 3900) equipped with an FID detector and a 30 m HP-PLOT/Q column (573K, flow rate: 2.0 ml/min). After reaction, the samples were dried and their structural characterization was carried out by powder X-ray diffraction and Raman spectroscopy in the solid phase.

Additionally, the influence of several factors such as dilution, temperature and pressure on the reaction kinetics was examined.

1. To study the influence of water on the reaction kinetics, several H_2O:Diol ratios were introduced: 152 mg of H_2O (8.44 mmol, 1 equivalent compared to the diol), 457 mg (25.39 mmol, 3 equivalents), 1523 mg (84.62 mmol, 10 equivalents) or 14920 mg (828.88 mmol, 98 equivalents). Then, the reactions were carried out at 120 °C for 30 - 4080 minutes.

2. To monitor the effect of temperature, 1 g (8.46 mmol) of 2,5-hexanediol and 55.6 mg of $HNbMoO_6$ were stirred under reflux at 80, 100, 120 and 140°C for various time intervals (5 - 1440 min).

3. To examine the pressure effect, similar reactions were carried out in an autoclave purchased from PARR Instrument Company. A quantity of 2.025 g (17.13 mmol) of 2,5-hexanediol was stirred with 105 mg of $HNbMoO_6$ layered oxide for 90 minutes at 120 °C. During the reaction the pressure reached up to 5 bar. Note that, the experiment was repeated twice to confirm our results.

2.5. References

1 J. He, Q. J. Li, Y. Tang, P. Yang, A. Li, R. Li and H. Z. Li, *Appl. Catal. A Gen.*, 2012, **443–444**, 145–152.

2 M. R. Waller, T. K. Townsend, J. Zhao, E. M. Sabio, R. L. Chamousis, N. D. Browning and F. E. Osterloh, *Chem. Mater.*, 2012, **24**, 698–704.

3 R. E. Schaak and T. E. Mallouk, *Chem. Commun.*, 2002, **0**, 706–707.

4 V. D. Nithya, R. K. Selvan, D. Kalpana, L. Vasylechko and C. Sanjeeviraja, *Electrochim. Acta*, 2013, **109**, 720–731.

5 T. Saison, P. Gras, N. Chemin, C. Chanéac, O. Durupthy, V. Brezová, C. Colbeau-Justin and J. -P. Jolivet, *J. Phys. Chem. C*, 2013, **117**, 22656–22666.

6 G. Steciuk, Application de la précession des électrons en mode tomographie à l'étude de phases apériodiques et de films minces d'oxydes, Université de Caen Normandie, France.

7 Li-F. Hu, Y. Tang, J. He, K. Chen and W. Lv, *Russ. J. Phys. Chem. A.*, 2017, **91**, 511–516.

8 L.-F. Hu, R. Li, J. He, L. -g. Da, W. Lv and J. -s. Hu, *J. Nanophotonics*, 2015, **9**, 093041.

9 M. Kudo, H. Ohkawa, W. Sugimoto, N. Kumada, Z. Liu, O. Terasaki and Y. Sugahara, *Inorg. Chem.*, 2003, **42**, 4479–4484.

10 V. Petricek, M. Dusek and L. Palatinus, *Cryst. Mater.*, 2014, **229**, 345–352.

11 M. H. Rietveld, *J. Appl. Cryst.*, 1969, **2**, 65–71.

12 G. S. Pawley, *J. Appl. Cryst.*, 1981, **14**, 357–361.

13 A. Le Bail, H. Duroy and J. L. Fourquet, *Mat. Res. Bull.*, 1988, **23**, 447–452.

CHAPTER THREE

STRUCTURAL ANALYSIS AND INFLUENCE OF PROTONATION

In this Chapter we will focus on the comparison of the structural features of layered materials and their evolution upon acid treatments. For this purpose, known materials were compared to new solid oxides based on layered Aurivillius phases and characterized by a stair-like structure. Three main caracterization methods were utilized: powder X-ray diffraction, Raman spectroscopy and thermogravimetry.

3.1. $HNbMoO_6$, $HNbWO_6$ and $H_2W_2O_7$

3.1.1. Structural evolution upon protonation

The layered materials $LiNbMoO_6$, $LiNbWO_6$, Bi_2WO_6 and $Bi_2W_2O_9$ and their corresponding proton-exchanged forms $HNbMoO_6.xH_2O$, $HNbWO_6.xH_2O$, $H_2WO_4.H_2O$ and $H_2W_2O_7$ were first investigated by powder X-ray diffraction (PXRD). The structures of the starting materials are represented in Figure **3.1** [1, 2, 3, 4, 5].

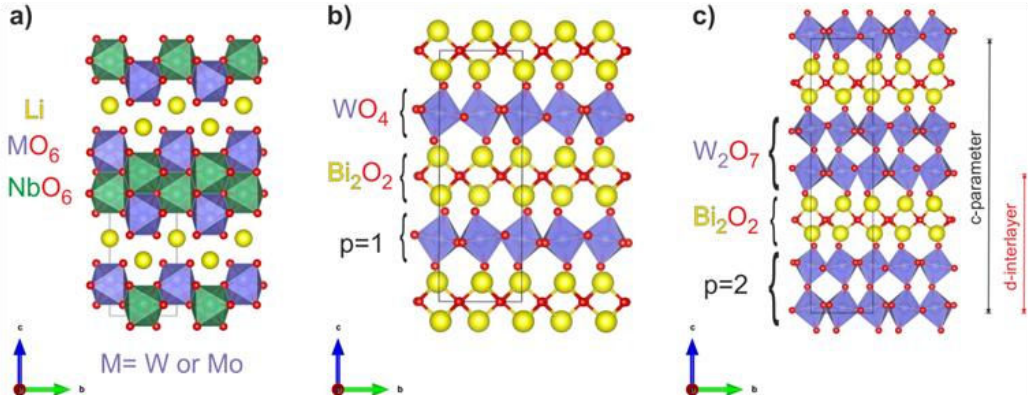

Figure 3.1: Crystal structure of (a) $LiNbMO_6$ (M = Mo, W), (b) Bi_2WO_6 and (c) $Bi_2W_2O_9$. The integer p corresponds to the number of layers (WO_4 or W_2O_7) intercalated between $Bi_2O_2^{2+}$ sheets in a crystal lattice. The spacing existing between two octahedral layers is noted as d-interlayer.

$LiNbMoO_6$ and $LiNbWO_6$ precursors crystallize in a tri-rutile structure (space group $P\text{-}42_1m$) formed of MO_6 (M = Mo, W) and NbO_6 octahedral slabs with lithium ions in the interlayer spaces and perpendicular to the c-axis [1, 6] (Figure **3.1-a**). Their PXRD patterns exhibit sharp and strong diffraction peaks, as shown in Figure **3.3**, which are characteristics of a well ordered layered structure. The most distinct ones are those situated at low 2θ° angle region (< 10°) attributed to (001) reflections and that at $2\theta \approx 27°$ ascribed to (110) in-plane diffraction. Lattice parameters for both solids, reported in Table **3.1**, are very similar and indexed on the basis of tetragonal cells (space group: $P\text{-}42_1m$). The c-parameter is here equal to the distance between two successive octahedral slabs (d-interlayer or interlayer spacing) along the stacking direction c. By modifying or inserting species in between the octahedral slabs, one expects to have a change in this interlayer spacing. Depending on how the insertion affects the stacking of the octahedral layers, the c-parameter will be either equal to the

interlayer spacing or a multiple of it. Conversely, if the structure inside the octahedral slabs is not affected by species insertion, a and b lattice parameters should stay unchanged.

Bi_2WO_6 and $Bi_2W_2O_9$ are members of the family of bismuth layered oxides known as Aurivillius phases [7, 8, 9] of general formula (Bi_2O_2) $(A_{p-1}B_pO_{3p+1})$ commonly described as the regular alternation of fluorine type $(Bi_2O_2)^{2+}$ and perovskite-like $(A_{p-1}B_pO_{3p+1})^{2-}$ slabs along the c-direction [10, 11]. None of these oxides contain an A cation, therefore, they can be respectively considered as p=1 and p=2 members of the family where the integer p corresponds to the number of layers of corner sharing BO_6 octahedra in the perovskite slabs [12, 13] (Figure **3.1-b** and **3.1-c**). Their PXRD profiles, Figure **3.4**, showed sharp and well defined intense peaks that are characteristic of a well ordered layered structures. All of the reflections were indexed on the basis of an orthorhombic cell with a space group Pna_{21} or $P2_1ab$ for $Bi_2W_2O_9$ and Bi_2WO_6 respectively (Table **3.1**). The difference in the c-parameter and the interlayer spacing correlates with the difference in the thickness (p=1 or p=2) of the perovskite slabs [14]. As for $LiNbMoO_6$ and $LiNbWO_6$, this parameter is expected to be a good indicator of any change occuring in the interlayer space (protonation, intercalation …).

Table 3.1: Lattice parameters of $LiNbMO_6$ (M = Mo, W) and $Bi_2W_xO_y$ with their proton exchanged phases. The d-interlayer is derived from the first peak encountered at lowest 2θ angle.

	Lattice parameters (Å)			
Compound	a	b	c	d-interlayer
$LiNbMoO_6$	4.6917(7)	4.6917(7)	9.243(2)	9.24
$HNbMoO_6.H_2O$	4.664(2)	4.664(2)	26.293(2)	13.15
$LiNbWO_6$	4.6831(3)	4.6831(3)	9.2792(6)	9.28
$HNbWO_6.0.5\ H_2O$	4.7157(9)	4.7157(9)	20.77(1)	10.39
$HNbWO_6.1.5\ H_2O$	4.733(2)	4.733(2)	25.47(3)	12.73
$Bi_2W_2O_9$	5.4346(3)	5.4137(1)	23.693(2)	11.85
$H_2W_2O_7$	5.197(2)	5.064(3)	18.32(1)	9.16
Bi_2WO_6	5.450(2)	5.445(2)	16.525(6)	8.26
$H_2WO_4.H_2O$	5.344(5)	5.241(4)	13.72(1)	6.86

After synthesis of the layered Li-based and Bi-based compounds, a subsequent protonation step is required in order to convert the as-made solids into their acidic forms. As expected, the PXRD patterns of protonated samples were strongly modified compared to their corresponding precursors. The shape of the peaks is much broader suggesting that the acid treatment has affected the crystallinity of the sample by decreasing the size of the diffracting domains. From the position of the peaks, we note a significant change in the c-parameter indicating the modification of the interlayer spacing.

For $HNbMoO_6.xH_2O$ and $HNbWO_6.xH_2O$, the interlayer spacing increased due to the replacement of Li^+ with H^+ and the simultaneous intercalation of water in the interlayer spacing in agreement with the literature [15]. The latter idea was illustrated with $HNbWO_6$ for which the interlayer spacing increased by ~ 2 Å when the amount of water is increased as represented in Table **3.1**. The TG analyses shown below also confirmed this. The proton exchange of Li-precursors is also accompanied by a transformation of the lattice from primitive to body-centered tetragonal related to a displacement of the adjacent $(M/Nb)O_6$ slabs by a (a + b)/2 translation as documented in the literature [1, 2], see Figure **3.2**. This explains the change in the indexation of the reflection peak encountered at low 2θ angle region (< 10°) from (001) for Li-precursors to (002) for the protonated phases.

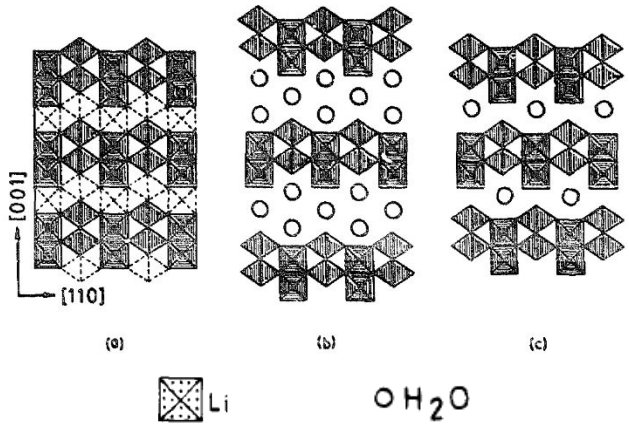

Figure 3.2: Schematic structure of (a) $LiNbWO_6$, (b) $HNbWO_6.1.5H_2O$ and (c) $HNbWO_6.0.5H_2O$ [2].

For $H_2W_2O_7$ and $H_2WO_4.H_2O$, an opposite change in the interlayer spacing was encountered with a decrease in the c-parameter and d-interlayer due to the selective leaching of $(Bi_2O_2)^{2+}$ layers by protons [3]. A structural change in the perovskite like slabs was observed upon acid treatment as evidenced by the shift in (200) and (020) reflections. Correspondingly,

a and b parameters decreased from those in $Bi_2W_2O_9$ and Bi_2WO_6 to that in the acid-treated sample [16].

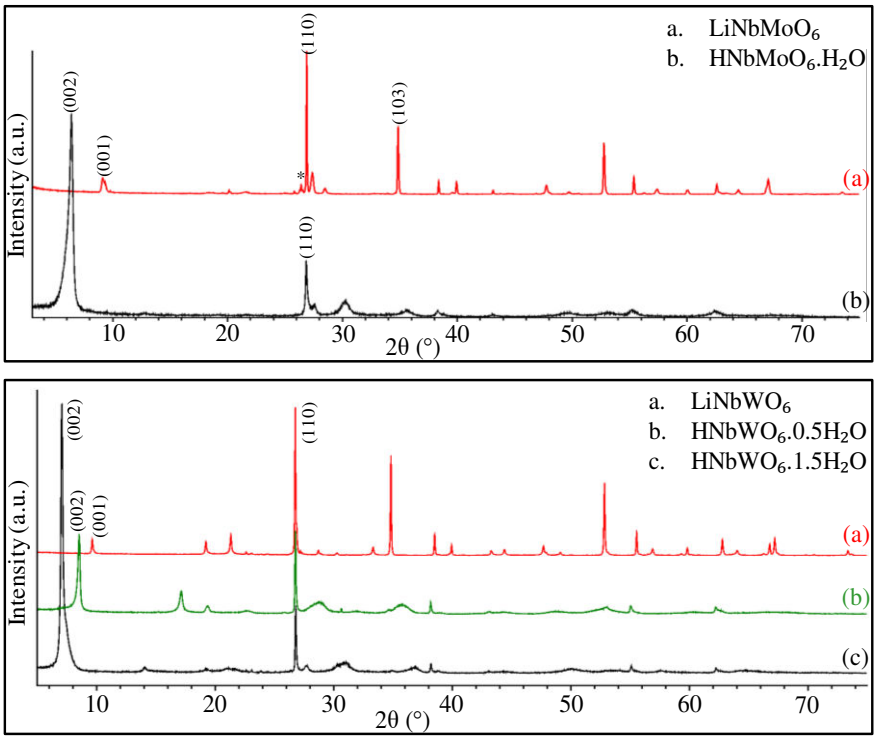

Figure 3.3: PXRD patterns of the Li-precursors and their acid treated samples. Asterisk denotes the presence of impurities.

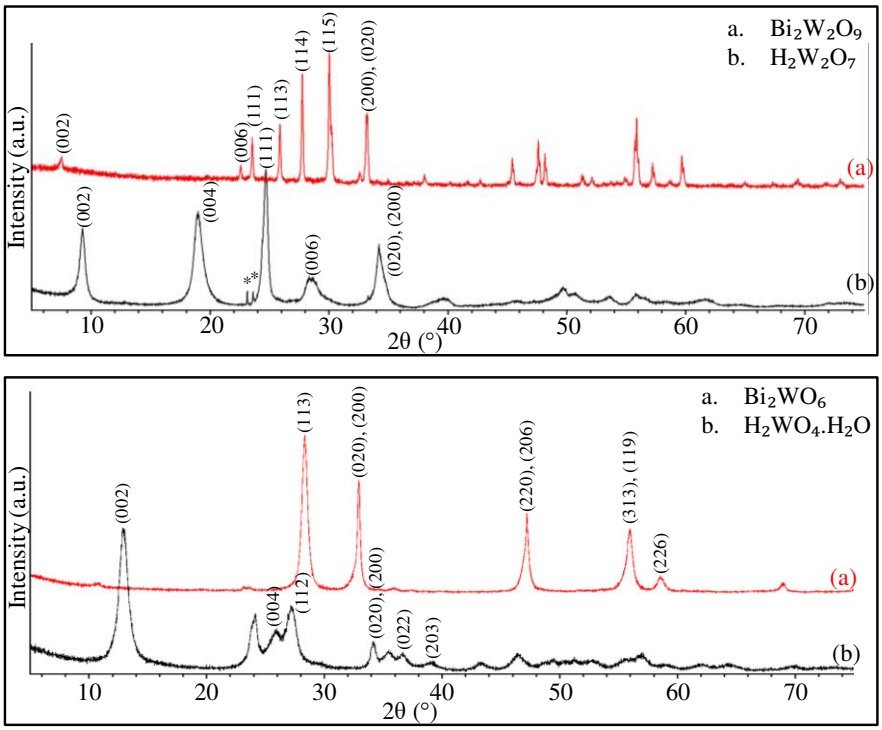

Figure 3.4: PXRD patterns of Bi-precursors and their acid treated samples. Asterisk denotes the presence of impurities.

The extent of hydration in all layered samples was quantified using thermogravimetric analysis. In case of protonated $LiNbMoO_6$, the TG curve, shown in Figure **3.5**, can be divided into two main regions: Region I: RT - 120°C and Region II: 120 - 480°C. The mass loss of 4.4% below 120°C with a maximum at 82°C in the dTG curve is associated to an endothermal peak at 83°C in the heat flow curve. It can be assigned to the desorption of water adsorbed on the surface. The mass loss of 4.4% with a maximum at 145°C and an endothermal peak at 148°C can be attributed to the release of water to form dehydrated $HNbMoO_6$. Taking into consideration the weight loss from room temperature till 480°C, the amount of water calculated is 1 mol/mol of the dehydrated sample. Therefore, protonated $HNbMoO_6$ can be expressed as follows: $HNbMoO_6.H_2O$.

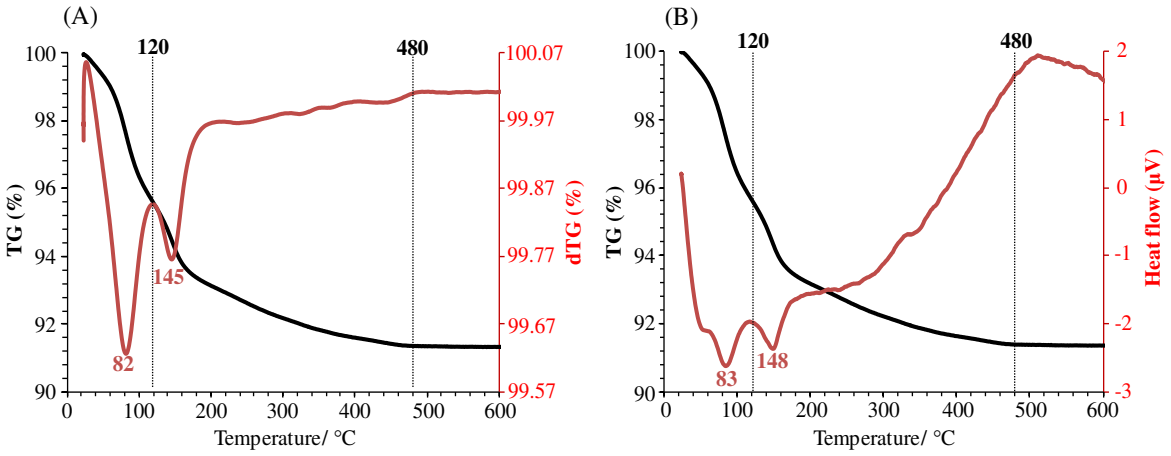

Figure 3.5: (A) TG-dTG and (B) TG-heat flow curves of $HNbMoO_6.H_2O$.

Similarly, $LiNbWO_6$ protonated forms should be formulated as follows: $HNbWO_6.0.5H_2O$ and $HNbWO_6.1.5H_2O$ based on the TG data represented in Figure **3.6** (parts A to D). Note that, $HNbWO_6.0.5H_2O$ and $HNbWO_6.1.5H_2O$ were formed depending on the water washing procedure to get rid of excess acid. In other words, as it is washed more, it is more likely to get $HNbWO_6.1.5H_2O$.

TG results indicated that hydrated $HNbWO_6$ loses water adsorbed on the surface (0.20 water molecule in part A and one water molecule per formula unit in part C) by 90°C. This was associated to an endothermic peak situated at 52 and 78°C as shown in parts B and D, respectively. In the range 67 - 200°C, dTG showed a maximum loss associated with an endothermic peak situated at 155 and 162°C, respectively. This was attributed to the loss of mildly adsorbed water and the calculated amounts were estimated to be equal to 0.30 mol/mol in part A and 0.5 mol/mol in part C. The formed anhydrous $HNbWO_6$ in the two cases are

stable up to 200°C, however on further heating the protonated forms loses hydroxyl protons to form $NbWO_{5.5}$ [2].

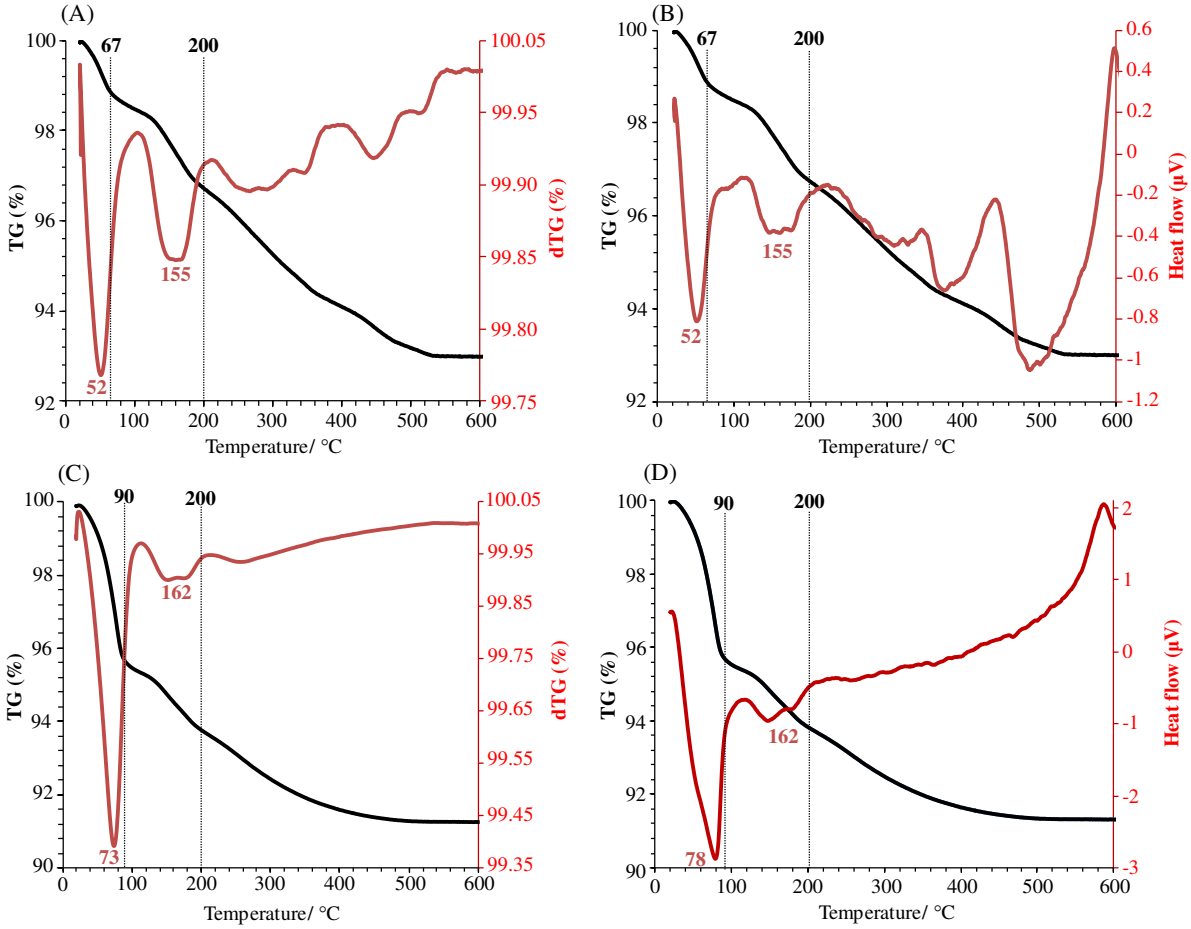

Figure 3.6: (A - C) TG-dTG and (B - D) TG-heat flow curves of $HNbWO_6.0.5H_2O$ and $HNbWO_6.1.5H_2O$ respectively.

For Protonated $Bi_2W_2O_9$ and Bi_2WO_6, thermogravimetric results are represented in Figure **3.7** and Figure **3.8** respectively.

The TG curve for acid-treated $Bi_2W_2O_9$, shown in Figure **3.7**, is divided into two main regions: Region I: < 120°C showed a small peak in the dTG curve corresponding to an endothermic peak in the heat flow curve situated at 66°C which was attributed to the loss of interlayer water to form dehydrated $H_2W_2O_7$ oxide. Region II: 120 - 450°C represented a strong peak in the dTG and heat flow curves situated at 293°C that is assigned to the dehydration of the layers to form WO_3 at the end of this region (at 450°C). This was previously illustrated in the literature by Kudo and co-workers [16]. Consequently, taking the first mass loss encountered in region I, the amount of interlayer water can be calculated and was estimated to be equal to 0.1 mol/mol of dehydrated sample. From the second mass loss

attributed to water of the structure and the remaining mass to WO_3, one can calculate the H_2O/WO_3 molar ratio and was estimated to be equal to 0.54 mol/mol. This value is consistent with the transformation of $H_2W_2O_7$ to $2WO_3 + H_2O$. Therefore, we can conclude that the composition of the acid treated sample is $H_2W_2O_7.0.1H_2O$.

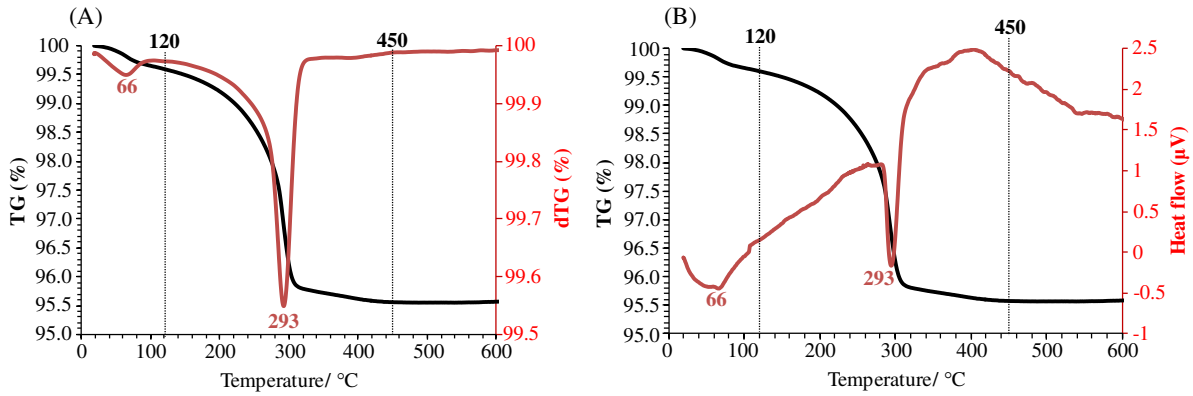

Figure 3.7: (A) TG-dTG and (B) TG-heat flow curves of acid-treated $Bi_2W_2O_9$

The TG curve for protonated Bi_2WO_6, Figure **3.8**, is divided into two regions: Region I: < 120°C showed a strong peak in the dTG curve and an endothermic one in the heat flow curve situated at 92 and 94°C, respectively, attributed to the loss of interlayer water to form dehydrated H_2WO_4 oxide. Region II: 120 - 450°C represented a broad peak in the dTG and heat flow curves situated at 207ºC and 195°C, respectively, that is assigned to the dehydration of the layers to form WO_3 at the end of this region (at 450°C). Therefore, taking into consideration the first mass loss encountered in region I, the amount of interlayer water can be calculated and was estimated to be equal to 1 mol/mol of dehydrated sample. From the second mass loss attributed to water of the structure and the remaining mass to WO_3, one can calculate H_2O/WO_3 molar ratio and was estimated to be equal to 0.80 mol/mol. This value is consistent with the transformation from H_2WO_4 to $WO_3 + H_2O$. Consequently, the protonated phases can be expressed as follows: $H_2WO_4.H_2O$.

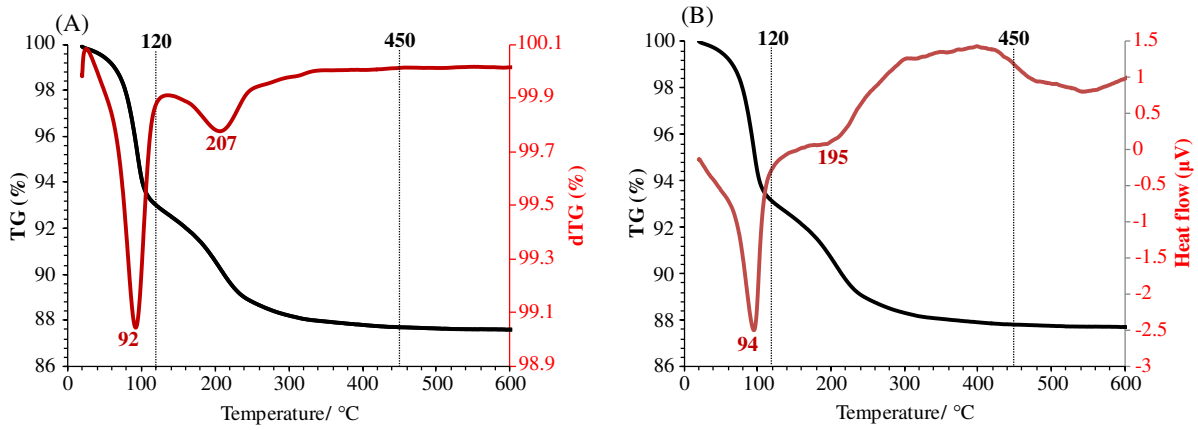

Figure 3.8: (A) TG-dTG and (B) TG-heat flow curves of $H_2WO_4.H_2O$.

3.1.2. Evolution of Raman spectra after protonation

Raman spectroscopy brings additional information on the various materials (Figure **3.9** and Figure **3.10**). The main Raman peaks and their assignments are listed in Table **3.2.**

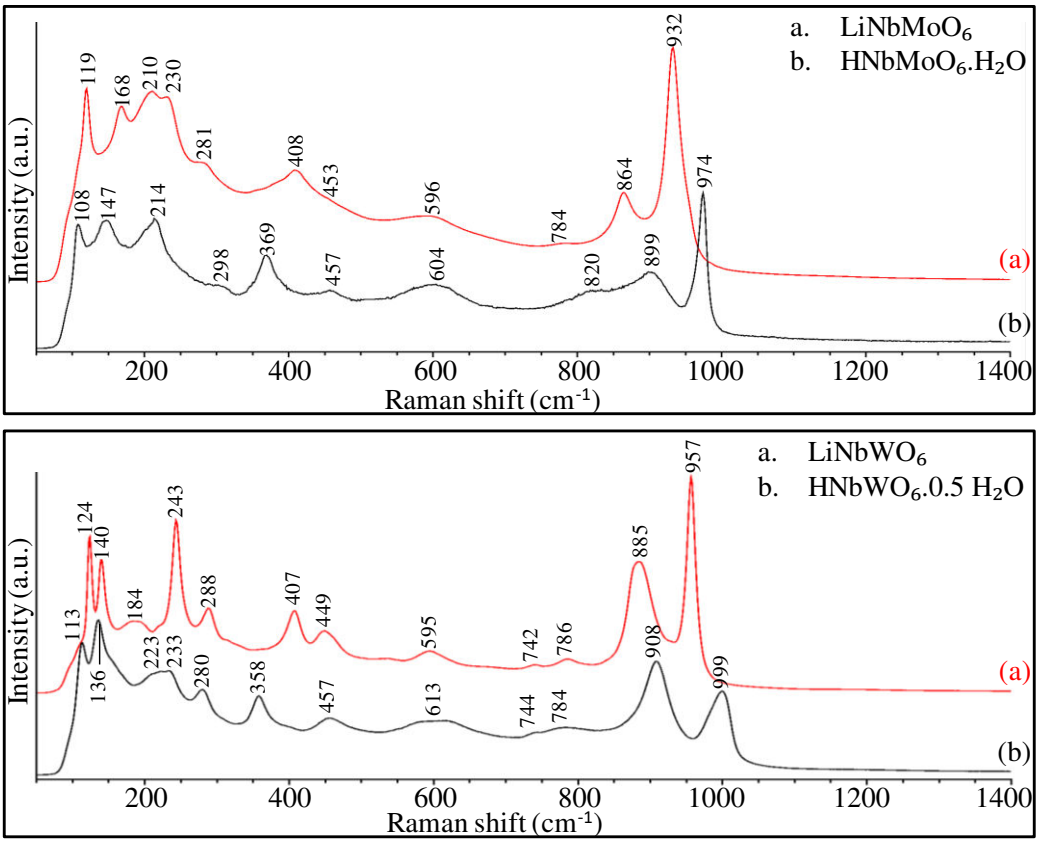

Figure 3.9: Raman spectra of $LiNbMO_6$ (M = Mo and W) and their protonated layered oxides.

$LiNbMoO_6$ and $LiNbWO_6$ mixed oxides show similar spectra with a clear distinction between the vibrations due to Nb and those due to Mo or W. Notably, the ν(Mo=O) or

ν(W=O) bands situated at 932 and 957 cm^{-1} for both $LiNbMoO_6$ and $LiNbWO_6$ respectively and the ν(Nb=O) bands at 864 and 885 cm^{-1} for $LiNbMoO_6$ and $LiNbWO_6$ respectively are clearly separated. Although both solids have a similar structure, the position of these latter ν(Nb=O) bands appears influenced by the surrounding metal [15].

The bands observed for both solids in the range (800 - 400 cm^{-1}) are assigned to ν(M-O) vibrations while those situated at lower Raman shifts (400 - 100 cm^{-1}) are attributed to the bending vibrations. These bands showed some differences between the two solids, either for the position or the relative intensities, notably the bands assigned to δ(O-Nb-O) and δ(NbO_6) at 230-210 and 168 cm^{-1} in $LiNbMoO_6$ and 243 and 184 cm^{-1} in $LiNbWO_6$, respectively.

When the cations of interlayer (Li^+) was exchanged with H^+ due to acid treatment, bands corresponding to the stretching vibration of Mo=O or W=O and Nb=O shifted to higher frequencies for both $HNbMoO_6$ and $HNbWO_6$ (ca. 30 cm^{-1}). By contrast the other bands were not strongly modified except for the bending δ(MO_6), δ(O-Nb-O) and δ(NbO_6) vibrations initially situated at (408, 230-210, 168 cm^{-1}) and (407, 243, 184 cm^{-1}) for $LiNbMoO_6$ and $LiNbWO_6$ respectively which shifted to (369, 214, 147 cm^{-1}) and (358, 233-223, 136 cm^{-1}) after protonation. This shows the impact of the interlayer cations on the framework of these materials.

Similarly, $Bi_2W_2O_9$ and Bi_2WO_6 and their acid-treated samples were characterized using Raman spectroscopy. As can be seen in Figure **3.10** and Table **3.2**, $Bi_2W_2O_9$ showed two bands at 854 and 800 cm^{-1}. This can be attributed to the presence of two apical oxygen atoms in the WO_6 octahedral within the perovskite-like layers in the latter oxide. Similarly, the asymmetric stretching WO_6 vibrations, ν_{as}(W-O-W), involving equatorial oxygen atoms are clearly separated at 741 and 697 cm^{-1} in $Bi_2W_2O_9$. Conversely, in the case of Bi_2WO_6, these two sets of bands are hardly separated at 818-792 and 722-702 cm^{-1}. The peaks at higher Raman shifts for $Bi_2W_2O_9$ compared to Bi_2WO_6 is likely due to the difference in the length of W-O bonds for the apical atoms [13]. Indeed the shortest W-O bond for the apical oxygen atoms is 1.79 Å for $Bi_2W_2O_9$ compared to 1.86 Å for Bi_2WO_6.

For both solids the $Bi_2O_2^{2+}$ layers are relatively similar. In view of the Bi-O distances greater than 2.1 Å, the (Bi-O) vibrations are expected below 500 cm^{-1} [17]. From the works of Gupta et al.[7] and Maczka et al.[13] the band at 416 cm^{-1} might be assigned to ν(Bi-O) while several bands below 330 cm^{-1} may be assigned to the bending modes of the WO_6 octahedra and $(Bi_2O_2)^{2+}$ layers. In particular the bands more intense at ca. 324 and 309-305 cm^{-1} are likely due to Bi-O vibrations.

Upon protonation, for both $Bi_2W_2O_9$ and Bi_2WO_6, the bands at ca. 416, 324 and 309-305 cm^{-1} disappeared, which confirms their assignments and indicates the complete protonation of the solids. Other changes were also observed upon protonation. For $Bi_2W_2O_9$, peaks attributed to ν(W=O) stretching vibrations have been blue shifted due to the formation of tungsten compounds with lower coordination numbers. In other words, as O/W ratio decreases, from 4.5 in $Bi_2W_2O_9$ to 3.5 in $H_2W_2O_7$, an upward spectral shift of the Raman bands was observed [18, 19]. Similarly, bands situated at 741 and 432 shifted to 806 and 459 cm^{-1} respectively. In addition to that, most of the bands become broader suggesting that the acid treatment had affected the crystallinity of the sample.

When Bi_2WO_6 is protonated, $H_2WO_4.H_2O$ was formed. In this case, a sharp peak centered at 955 cm^{-1} was observed which is attributed to ν(W=O) bonding since the structure of this oxide consists of layers of corner-shared WO_6 octahedra with alternate apical arrangements of W-OH_2 and W=O [20]. A broad band ν(W-O) is also observed at 675 cm^{-1}, this band is significantly affected by hydration and can be used to identify the hydration level of crystals [21, 22].

It should be noted that H_2WO_4 is not very stable in this state. Further dehydration, obtained for example by the use of full laser power yielded the quick formation of dehydrated WO_3. In this case, the characteristic intense bands were observed at 802, 708, 324 and 263 cm^{-1}. The intense peaks observed at 802 and 708 cm^{-1} correspond to the stretching vibrations of O-W-O, while those situated at lower frequency (324 and 263 cm^{-1}) corresponds to the bending vibration of W-O-W. Additionally, a small peak may remain at 950 cm^{-1}, in case of an incomplete dehydration of H_2WO_4 thus leaving a residual W=O. Consequently, the spectra of H_2WO_4 and WO_3 are totally different and can be readily distinguished.

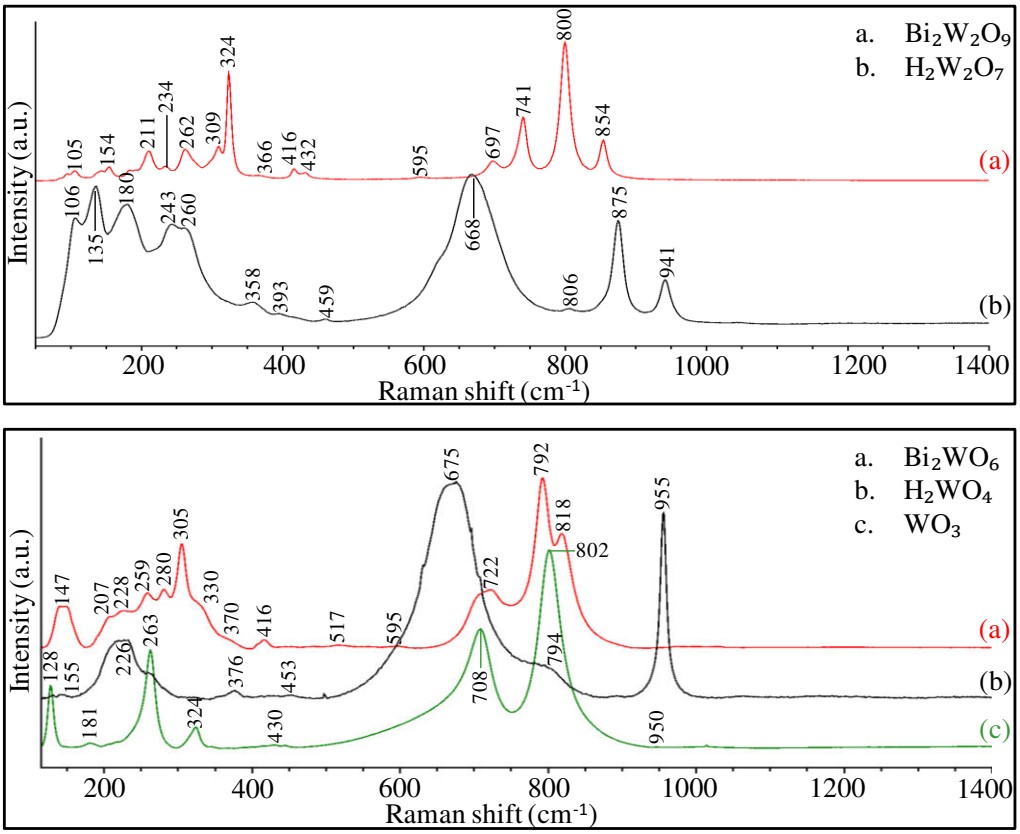

Figure 3.10: Raman spectra of $Bi_2W_xO_y$ and their protonated layered oxides.

Table 3.2: Detailed peak positions ($\Delta\nu/cm^{-1}$) and their assignments for all samples. The protonated samples are indicated in bold; M = (Mo or W). These assignments were tentatively made, based on the cited references. Notations were unified here between the samples for clarity

	Raman shift (cm^{-1})								
	$LiNbMoO_6$	**$HNbMoO_6$**	$LiNbWO_6$	**$HNbWO_6$**	$Bi_2W_2O_9$	**$H_2W_2O_7$**	Bi_2WO_6	**H_2WO_4**	**WO_3**
Reference	23	**23**	24	24	7, 13	**20**	13, 25	**20**	**20, 26**
ν(M = O)	932	**974**	957	**999**	854 - 800	**941 - 875**	818 - 792	**955**	**950**
ν(Nb = O)	864	**899**	885	**908**					
ν(M-O-M)	784	**820**	786 - 742	**784 - 744**	741 - 697	**806 - 668**	722	**794** **675**	**802** **708**
ν(Nb-O-M)	596	**604**	595	**613**					
ν(O-Nb-O)	453	**457**	449	**457**					
δ (MO_6)	408	**369**	407	**358**	432 - 366	**459 - 393 - 358**	370	**453 - 376**	**430**
δ(M-O-Nb)/ δ(M-O-M)	281	**298**	288	**280**	262	**260 - 243**	280 - 259		**324 - 263**
δ(O-Nb-O)	230 - 210	**214**	243	**233 - 223**					
δ(NbO_6)	168	**147**	184	**136**					
ν(Bi-O)					416		416		
δ(WO_6) + δ($Bi_2O_2^{2+}$)					324 - 309 - 234 - 211		330 - 305 - 228 - 207		

3.2. Novel Mixed oxides

All of the known solids presented in the previous section have the disadvantage of a fixed chemical composition which is not favourable for the modulation of the catalytic activity. Therefore, new mixed layered oxides constituted of both Nb and W transition metals should be formed which might provide us the possibility to investigate their catalytic behaviour in some acid catalyzed reactions. The feasibility of forming various compositions of Aurivillius phases is mostly due to the presence of pseudo-perovskite like layers as the cationic sites of the $(M_2O_2)^{2+}$ slabs are almost exclusively occupied by the Bi^{3+} cations [27, 28]. In the literature, Nb-based ($Bi_5Nb_3O_{15}$ [29, 30], $A^{2+}Bi_2Nb_2O_9$ with A = Ba, Sr, Ca ... [31]), W-based (Bi_2WO_6 [9, 32] $Bi_2W_2O_9$ [33]) and very few mixed Nb/W-based ($Bi_5TiNbWO_{15}$ [34], Bi-Nb-W-O [35]) compounds are reported. Considering these known phases, we had two options in our research for mixed Nb/W oxides: "Conventional" and "Stair-like" Aurivillius phases.

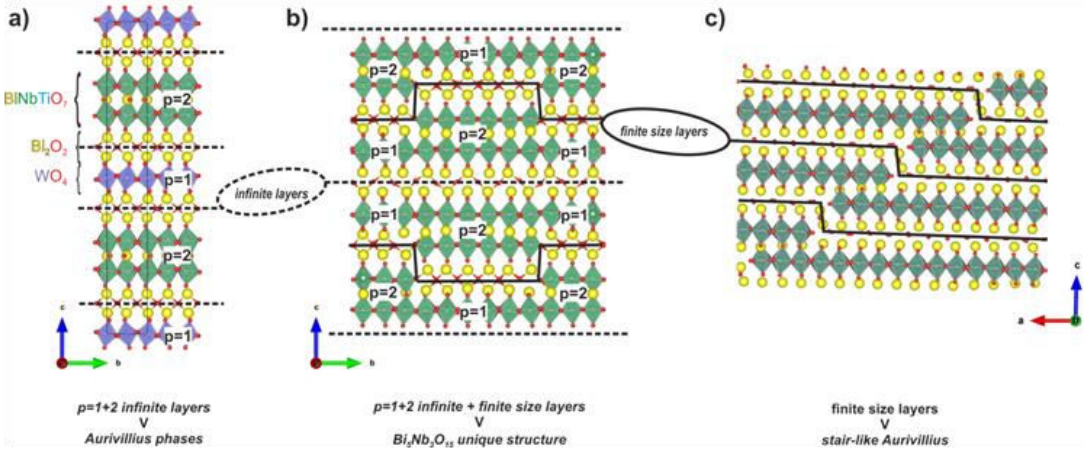

Figure 3.11: Schematic crystal structure of (a) $Bi_5TiNbWO_{15}$, an Aurivillius intergrowth with an alternation of continuous perovskite blocks of thickness p=1 and p=2, separated by $(Bi_2O_2)^{2+}$ layers (dotted line). (b) $Bi_5Nb_3O_{15}$, a compound characterized by a stacking sequence |p=1|p=2|p=2|p=1| and a periodic shear which induces the coexistence of continuous and discontinuous layers. (c) Example of a stair-like Aurivillius structure that is characterized by the presence of discontinuous layers only.

- *"Conventional" Aurivillius phases*

$Bi_5TiNbWO_{15}$ is an Aurivillius phase that possess two types of perovskite slabs with different thickness (p=1 and p=2) alternating regularly along the layers stacking direction (Figure **3.11-a**). The p=1 and p=2 components have the Bi_2WO_6 and Bi_3NbTiO_9 composition, respectively, which means that none of the perovskite slabs has actually a mixed Nb/W

composition but both Nb and W are still present in this phase [34]. Considering such "p=1+2" Aurivillius compounds, a modulation of the Nb/W ratio is expected assuming a hypothetic solid solution from $Bi_5Nb_3O_{15}$ (Figure **3.11-b**) to $Bi_5Ti_{1.5}W_{1.5}O_{15}$ passing by $Bi_5TiNbWO_{15}$ (Figure **3.12** possibility 1). In this case, having both Nb and W in a single phase can be only ensured with the presence of Ti. Exploring the pseudo-binary $A^{2+}Bi_2Nb_2O_9$ – $Bi_2W_2O_9$ (p=2 Aurivillius phases) might also be an alternative choice which necessitates the use of an alkaline-earth A^{2+} cations (Figure **3.12** possibility 2). The exploration of a possible solid solution based on these two possibilities was not considered in this work.

- *"Stair-like" Aurivillius phases*

During the PhD work of G. Steciuk at CRISMAT (2016 - Caen) [36], it was established that a series of layered compounds closely related to Aurivillius phases can be stabilized in the pseudo binary systems $Bi_5Nb_3O_{15}$ – $ABi_2Nb_2O_9$ [37, 38]. These compounds so-called "stair-like" Aurivillius phases (Figure **3.11-c**) offer a large compositional flexibility demonstrated for the $Bi_5Nb_3O_{15}$ – $ABi_2Nb_2O_9$ system (flexibility on the A site of the perovskite blocks) but not fully explored for the B site of the perovskite blocks in the $Bi_5Nb_3O_{15}$ – Bi_2WO_6 system [36] (Figure **3.12** possibility 3). Note that, in an earlier work [35], a stair like phase was already identified by transmission electron microscopy in the system Bi-Nb-W-O. We thus decided to investigate more this latter less explored system to stabilize new mixed Nb/W layered phase.

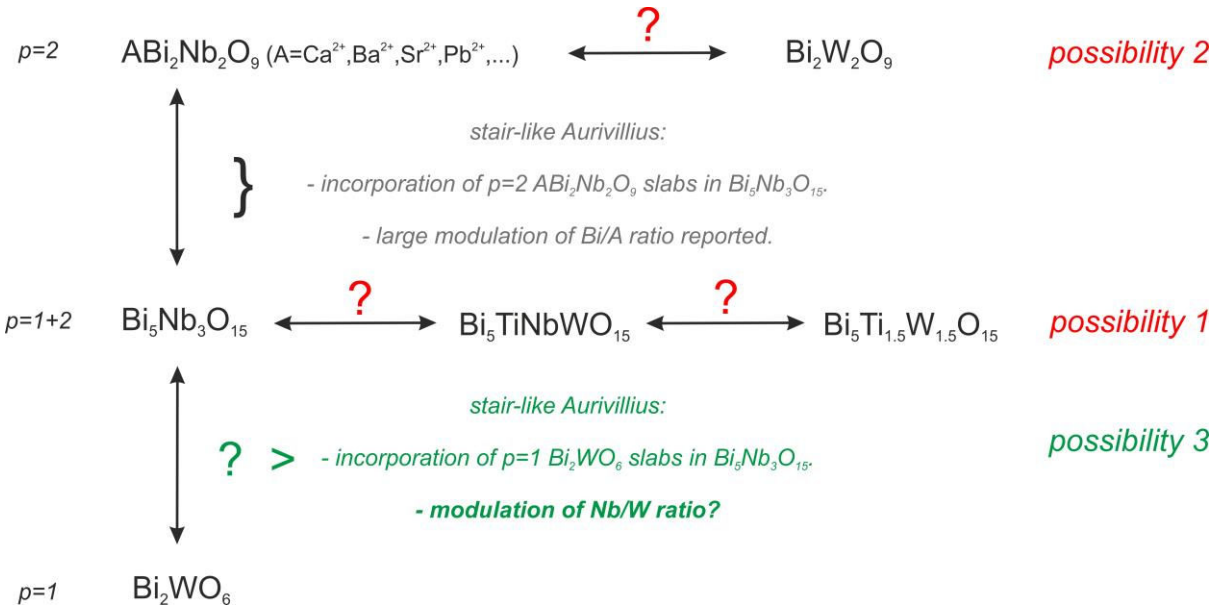

Figure 3.12: Considering the known Aurivillius related compounds (in black), 3 possibilities exist in order to form a series of mixed Nb/W compounds with an adjustable Nb/W ratio.

3.2.1. Structural characteristics of the new layered Aurivillius phases

A series of new mixed layered compounds containing both Nb and W were synthesized by exploring the pseudo binary system $Bi_5Nb_3O_{15}$ – Bi_2WO_6. Four compounds having a composition $Bi_{17}Nb_3W_6O_{51}$, $Bi_{11}Nb_3W_3O_{33}$, $Bi_9Nb_3W_2O_{27}$ and $Bi_7Nb_3WO_{21}$ with, respectively, Nb/W ratio 0.5, 1, 1.5 and 3 were synthesized. The powder X-ray diffraction patterns (PXRD) of the last three compounds (Figure **3.14-a**) confirm the formation of a single phase exhibiting the characteristics of the stair-like Aurivillius compounds [36]:

- Presence of a low intense peak encountered at low 2θ angle region (at ~ 14°)
- Two very close peaks exhibiting the highest intensities at 28-29°.

These three compounds possess a complex incommensurately modulated structure whose detailed structural analysis is beyond the scope of this work. Briefly, they all possess an average monoclinic cell with cell parameters a ~ b ~ c ~ $ap\sqrt{2}$ (ap stands for the lattice parameters of cubic perovskite) and a modulation vector in the form q = αa* + γc*. The values obtained from PXRD patterns are shown in Table **3.3**. The average unit cell shows some similarity with Aurivillius phases with a ≈ b ≈ 5.4 Å and c corresponding to the stacking direction. The structural analysis of the compounds $Bi_{11}Nb_3W_3O_{33}$, $Bi_9Nb_3W_2O_{27}$ and $Bi_7Nb_3WO_{21}$ (Figure **3.13**) was done by Rietveld refinement of neutron powder diffraction data using a structural model adapted from the one used for stair-like Aurivillius phases reported in the system $Bi_5Nb_3O_{15}$ – $ABi_2Nb_2O_9$ [37, 38].

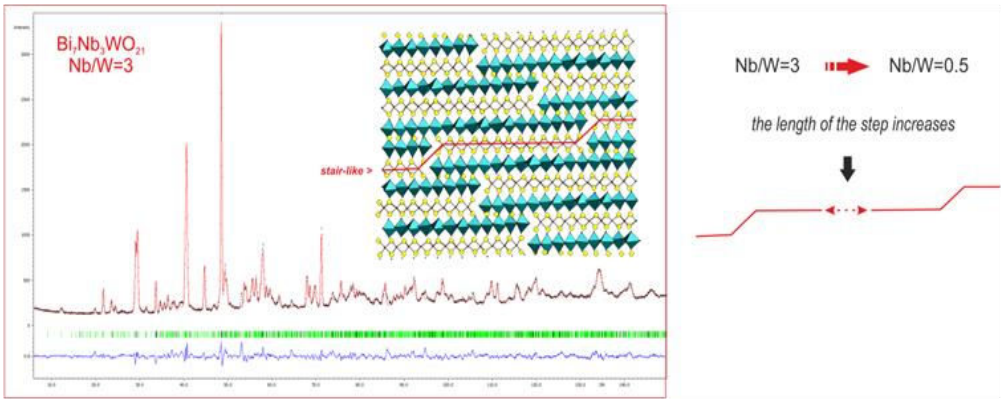

Figure 3.13: Structure of $Bi_7Nb_3WO_{21}$ as obtained from the neutron powder diffraction. The structural analysis of the new mixed Nb/W phases indicates that as the Nb/W ratio decreases the length of the layer increases.

These newly synthesized oxides are built up of Bi_2O_2 slabs and perovskite-like blocks, characteristics of Aurivillius phases as stated before. However, they exhibit a clear distinctive

structural feature: the stacking sequence of Bi_2O_2 slabs and octahedral layers are discontinuous, as shown in Figure **3.13**, due to the introduction of (100) shear planes leading to the formation of ”steps”. These oxides are thus designated as “stair-like Aurivillius phases” to distinguish them from the conventional Aurivillius phases exhibiting continuous layers.

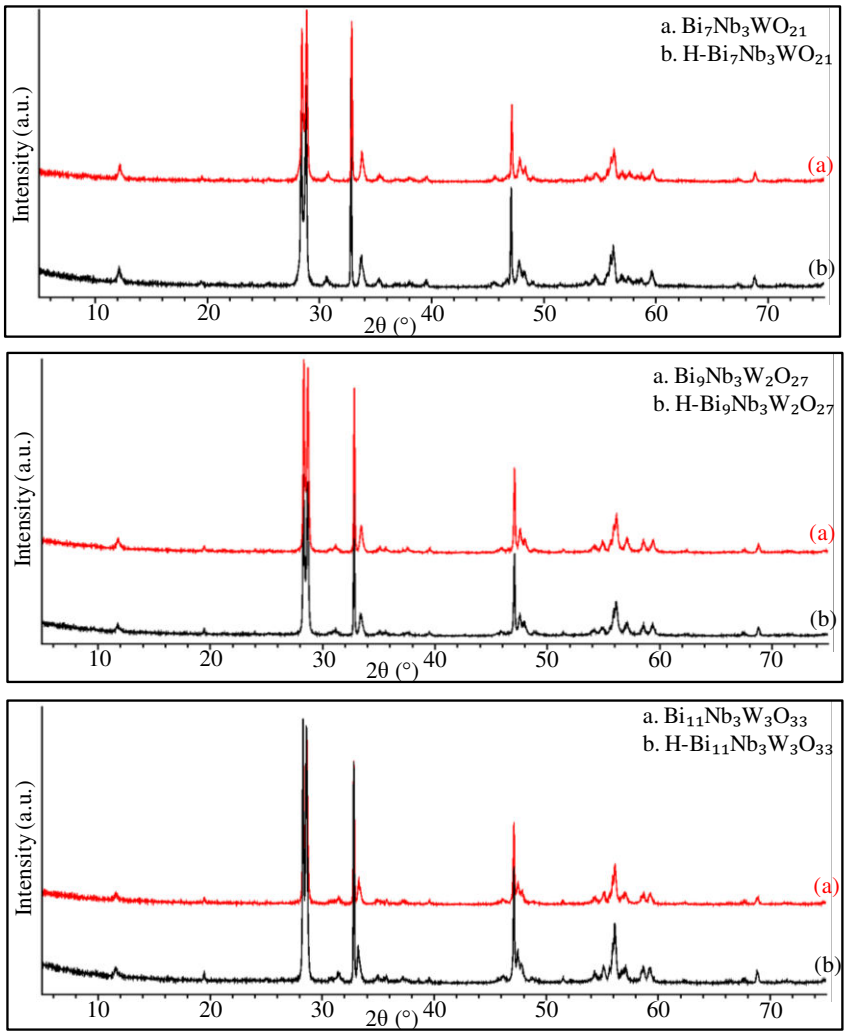

Figure 3.14: PXRD patterns of $Bi_xNb_yW_zO_n$ before and after protonation.

Table 3.3: Experimental data after XRD patterns refinement.

	Lattice parameters (Å) and components of the modulation vector q = αa* + γc*					
Compound	a	b	c	β [°]	α	γ
$Bi_7Nb_3WO_{21}$	5.4629(7)	5.4550(7)	5.3098(9)	91.155(8)	-0.0449(3)	0.2739(4)
$Bi_9Nb_3W_2O_{27}$	5.4588(8)	5.4537(7)	5.3546(9)	91.014(8)	-0.0320(4)	0.2850(4)
$Bi_{11}Nb_3W_3O_{33}$	5.451(1)	5.450(1)	5.375(1)	90.892(9)	-0.0263(4)	0.2932(3)
$Bi_{17}Nb_3W_6O_{51}$	5.466(3)	5.454(3)	16.38(2)	-	-	-

PXRD results for $Bi_{17}Nb_3W_6O_{51}$, Figure **3.15-a**, indicated that the peaks attributed to stair-like Aurivillius were not encountered; absence of peaks at low 2θº angle region and at 33°. While the presence of both Nb and W was confirmed by Energy Dispersive Spectrocopy (EDS) analyses performed in the TEM, only peaks similar to the Bi_2WO_6 layered oxide were observed. Actually only the strong anisotropy observed for most of the peaks could give a hint that $Bi_{17}Nb_3W_6O_{51}$ is different from Bi_2WO_6. Therefore, $Bi_{17}Nb_3W_6O_{51}$ was indexed on the basis of an orthorhombic cell (lattice parameters indicated in Table **3.3**) with a space group $P2_1ab$ as for Bi_2WO_6. Consequently, the structure of this sample is expected to be more or less similar to Bi_2WO_6 where, if present, the steps are far away from each other leading to a compound made of almost continuous layers (p=1). As the (Nb/W) ratio decreases, i.e. amount of tungsten increases, the structure of the newly found Nb/W layered oxides deviates from the stair-like Aurivillius to become more similar to the conventional Aurivillius ones.

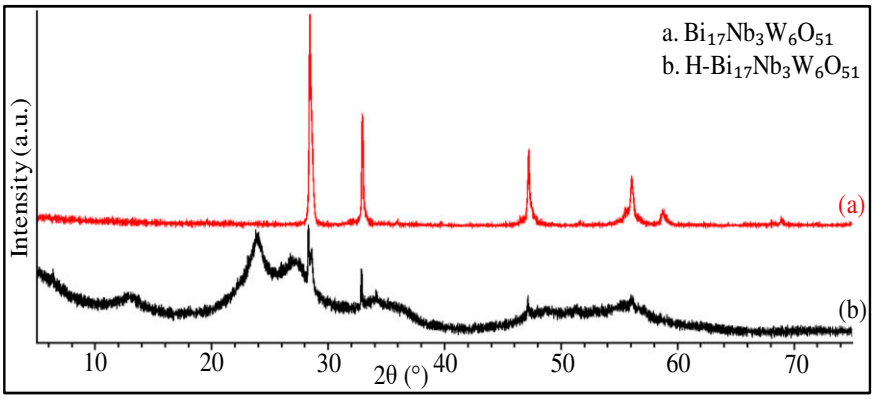

Figure 3.15: PXRD patterns of $Bi_{17}Nb_3W_6O_{51}$ before and after protonation.

3.2.2. Raman spectroscopy of new mixed layered oxides

The newly synthesized layered oxides were also studied by Raman spectroscopy. This will permit the investigation of the effect of different Nb/W compositions on the structure. The Raman spectra of $Bi_7Nb_3WO_{21}$, $Bi_9Nb_3W_2O_{27}$ and $Bi_{11}Nb_3W_3O_{33}$ layered oxides are shown in Figure **3.16.**

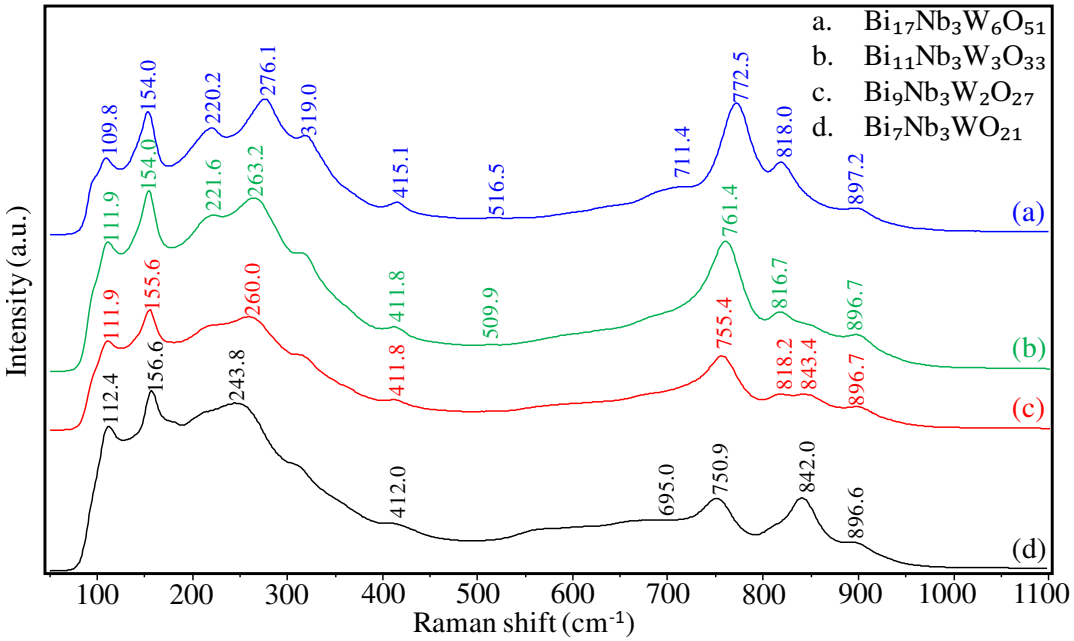

Figure 3.16: Raman spectra of $Bi_xNb_yW_zO_n$ layered oxides.

All the spectra showed similar features. Nevertheless, some differences can be seen depending on the Nb/W content. When the W relative amount decreased, the peaks at ca. 277 and 772 cm^{-1} shifted to lower Raman wavenumbers. This was accompanied by a broadening of the latter band towards lower wavenumbers by the development of bands at ca. 570 and 670 cm^{-1} and a decrease of the intensity at 772 cm^{-1}. In addition, it is noteworthy that the relative intensities of several peaks were also modified with the Nb/W ratio. The bands at 818 and 842 cm^{-1} in particular were largely modified, the band at 818 cm^{-1} decreased when W decreased while the band at 842 cm^{-1} increased. These bands were tentatively assigned in Table **3.4** based on the bands description in Table **3.2.** Similarly to $Bi_2W_2O_9$ and Bi_2WO_6, peaks observed at ca. 415 and 319 cm^{-1} might be attributed to the presence of $Bi_2O_2^{2+}$.

The spectra were curve-fitted for easier comparisons. The ratio of the band areas at 842/818 was correlated to that of the Nb/W ratio (Figure **3.18a**), confirming the assignments to ν(Nb-O) and ν(W-O) respectively. Interestingly, the band at 840 cm^{-1} was also related to the development of the band at 570 cm^{-1}, both evolving also with the band at 115 cm^{-1} (Figure **3.18b**). These bands must all be related to Nb-O vibrations. The bands at 900 and 670 cm^{-1} also appear to correlate but remained relatively constant vs. the Nb content. In view of their positions they could also be related to (Nb-O) vibrations. It is noteworthy that compounds based on $Bi_xNb_2O_9$ show their main bands in this region around 820-840 and 560 cm^{-1}. Compounds based on Nb_2O_6 units tend to show bands above 600 and 850-870 cm^{-1}. The bands at 840 and 570 cm^{-1} might thus tentatively be assigned to Nb-O vibrations for the p=2 zones where 2 niobium oxide layers are superimposed while the bands at 900 and 670 cm^{-1}

could be due to p=1 zones where niobium oxide appear as a single layer. Similarly the band at 818 cm^{-1} could be due to W-O vibrations for the p=2 zones where two tungsten oxide layers are superimposed. This band did not show any correlation with any other band. Nevertheless the bands at 772 and 277 cm^{-1} correlated and shifted with W/Nb ratio indicating a likely contribution of both Nb-O and W-O vibrations, notably in the superimposition zone.

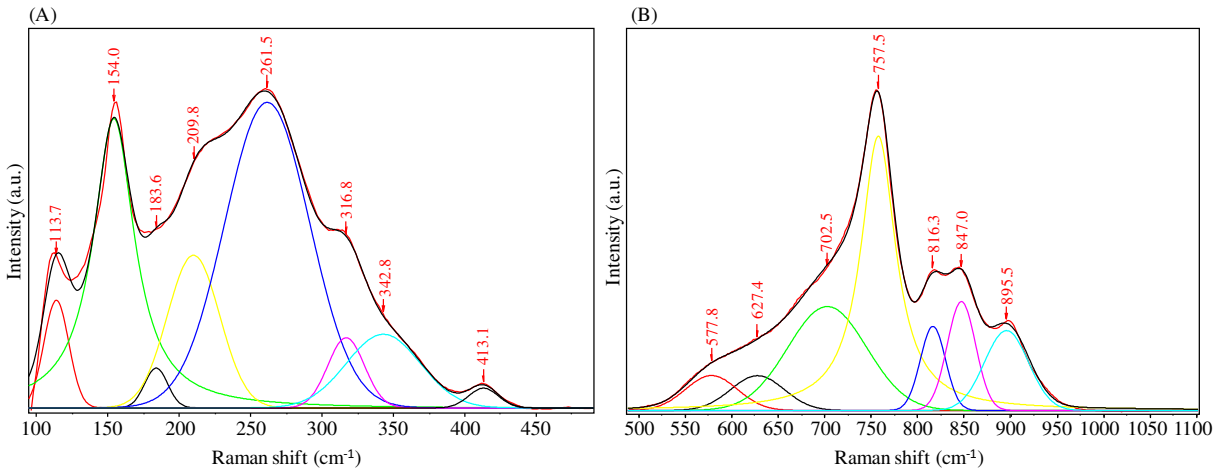

Figure 3.17: Curve fitting of the Raman spectra of $Bi_9Nb_3W_2O_{27}$ of various Raman peaks in the range 100 - 500 cm^{-1} (A) and 500 - 1100 cm^{-1} (B). Black curve is the curve fitted.

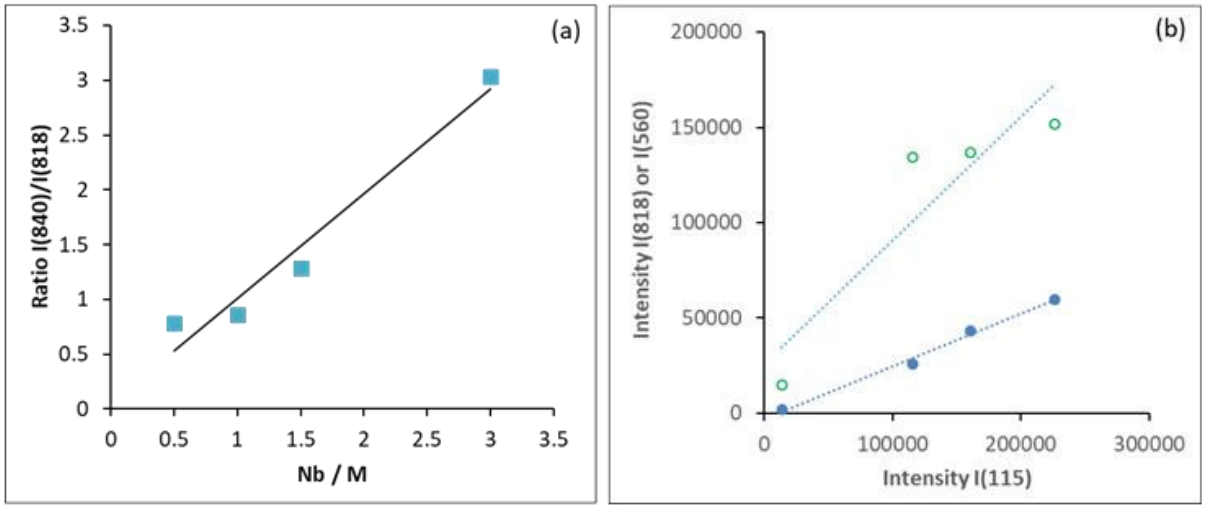

Figure 3.18: Evolution of the curve-fitted peaks for the different Nb/W solids. (a) Evolution of the ratio of the band intensities at ca. 840 and 818 cm^{-1}. (b) Evolution of the band intensities at ca. 840 (o) and 560 (•) cm^{-1} vs. the band at 115 cm^{-1}.

Table 3.4: Detailed Raman position ($\Delta\nu/cm^{-1}$) based on curve-fitting and their attribution for the mixed Nb/W Aurivillius-like compounds. Values in parentheses are not clearly visible on the original spectra.

	Raman shift (cm^{-1})			
	$Bi_7Nb_3WO_{21}$	$Bi_9Nb_3W_2O_{27}$	$Bi_{11}Nb_3W_3O_{33}$	$Bi_{17}Nb_3W_6O_{51}$
(Nb/W) ratio	3	1.5	1	0.5
ν(Nb=O) p=1	891	895	895	899
ν(Nb=O) p=2	842	847	848	(840)
ν(W-O-W) p=2	(810)	816	818	820
ν(W-O-W) p=1	753	757	761	772
ν(Nb-O-W)	600	627	628	638
ν(Nb-O-Nb) p=1	683	702	698	699
ν(Nb-O-Nb) p=2	557	578	587	(593)
ν(Bi-O)	414	413	413	416

3.2.3. Protonation of new mixed Nb/W layered oxides

The protonation procedure was carried out using several acids such as nitric acid, hydrochloric acid, phosphoric acid and sulfuric acid of several concentrations (12, 6, 3, 2 and 0.5 M). In some experiments, salts such as LiCl or KCl were added, since we assumed that by changing the Bi cations into Li^+ or K^+, respectively, the protonation process would be much easier. Then, after stirring the solids with one of the mentioned acids for several days either at room temperature or in an oil bath at 70 °C, washed with distilled water, centrifuged then dried, the powder was collected and characterized by PXRD. For instance, the powder X-ray diffraction patterns of the protonated stair-like Aurivillius represented in Figure **3.14-b**, were collected after stirring the Bi-precursors with 6M HCl for 1 week at room temperature. Results revealed that the protonated oxides still encounter a very small intense peak at low 2θ angle regions with two close peaks exhibiting the highest intensities at the same identical position to that of the Bi-precursors. Similarly, the other peaks were present at the same positions and no new peaks were encountered. Therefore, this revealed that the stair-like Aurivillius structure was maintained and that the protonation process was not successfully achieved. The same results were encountered either by changing the acids or the reaction

conditions, revealing the stability or rigidity of these layered oxides that might be attributed to its stair-like structure thus prohibiting reaching the Bi cations located between the octahedral W layers thus preventing exchanging process to take place and therefore their protonation.

In addition to the other oxides, the protonation of $Bi_{17}Nb_3W_6O_{51}$ was also examined. As mentioned above, due to the similarity of this layered oxide to the structure of Bi_2WO_6 we tried to use the same procedure of protonation implemented with the latter oxide to check its applicability. Therefore, $Bi_{17}Nb_3W_6O_{51}$ was stirred with 6 M hydrochloric acid for 6 days, exchanging the acid with a fresh one after 3 days. The sample was then dried and characterized by PXRD. Result represented in Figure **3.15-b** revealed several significant changes, first, the intense peaks that were initially present in the Bi-precursor decreased dramatically. Second, new broad peaks were encountered situated at 13, 24, 27, 35 and 56°. This indicated that the protonation process was successfully achieved and this was confirmed by EDS analyses performed in the TEM which showed that most of the grains are Bi-free. The protonation was much easier as the structure is constituted of continuous layers thus allowing facile exchange of the Bi located between the octahedral W layers into protons.

Similarly to PXRD patterns, Raman spectra before and after protonation, Figure **3.19** and Figure **3.20**, were also characterized.

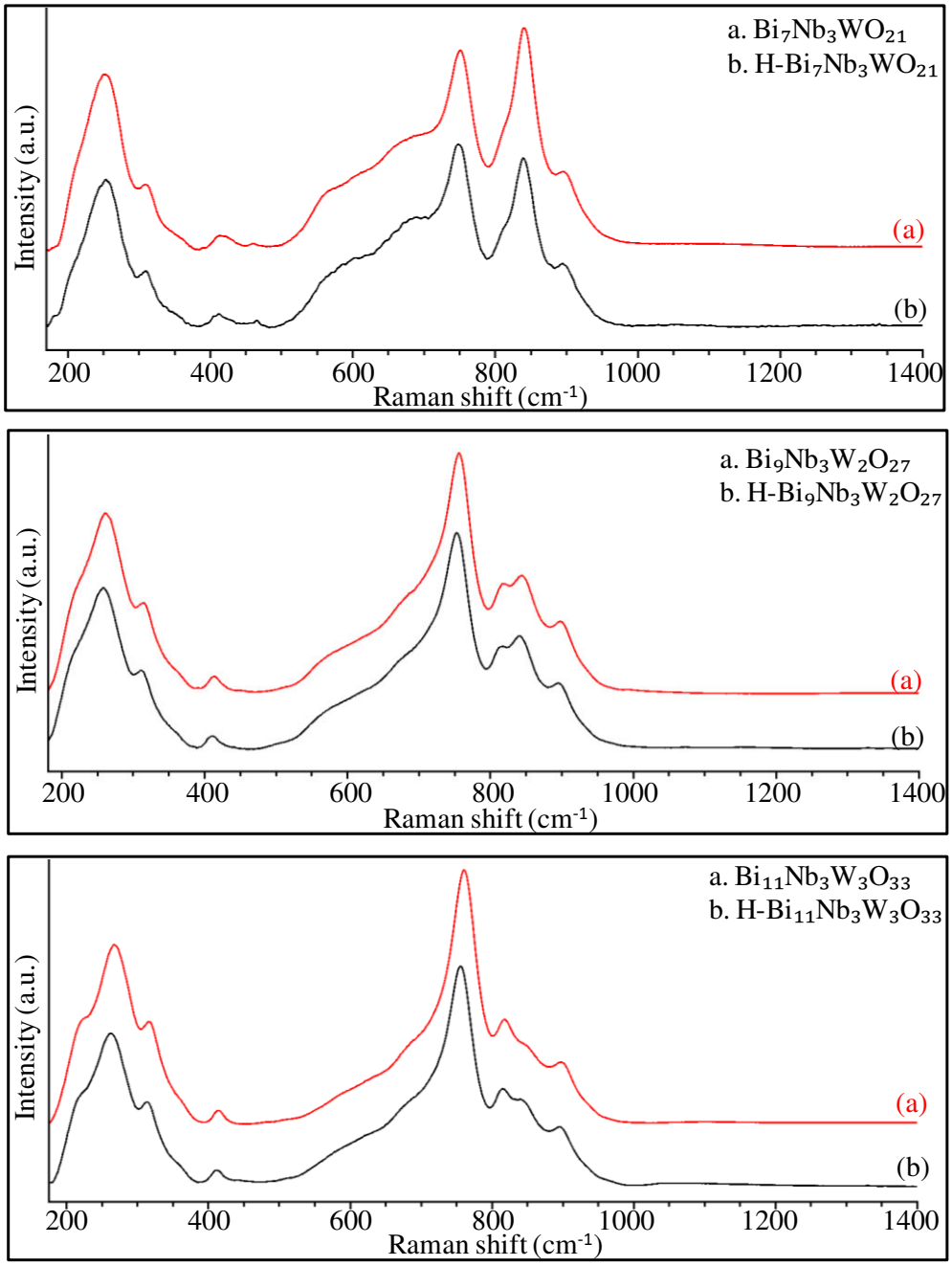

Figure 3.19: Raman spectra of $Bi_xNb_yW_zO_n$ before and after protonation.

In case of $Bi_7Nb_3WO_{21}$, $Bi_9Nb_3W_2O_{27}$ and $Bi_{11}Nb_3W_3O_{33}$, no changes were encountered in their Raman spectra after protonation confirming that the samples remain intact upon acid treatment.

However with $Bi_{17}Nb_3W_6O_{51}$, several changes were encountered. Band that is attributed to ν(Nb=O) shifted to higher wavenumbers, from 897 to 957 cm^{-1}. Those attributed to ν(W-O-W) and ν(Nb-O-Nb) situated at 818 and 772 cm^{-1} become broader and shifted to 809 and 762 cm^{-1}, respectively. Band situated at 276 cm^{-1} attributed to δ(W-O-W) decreased

in intensity and shifted to 269 cm^{-1}. These changes revealed that acid treatment affects both Nb and W sites.

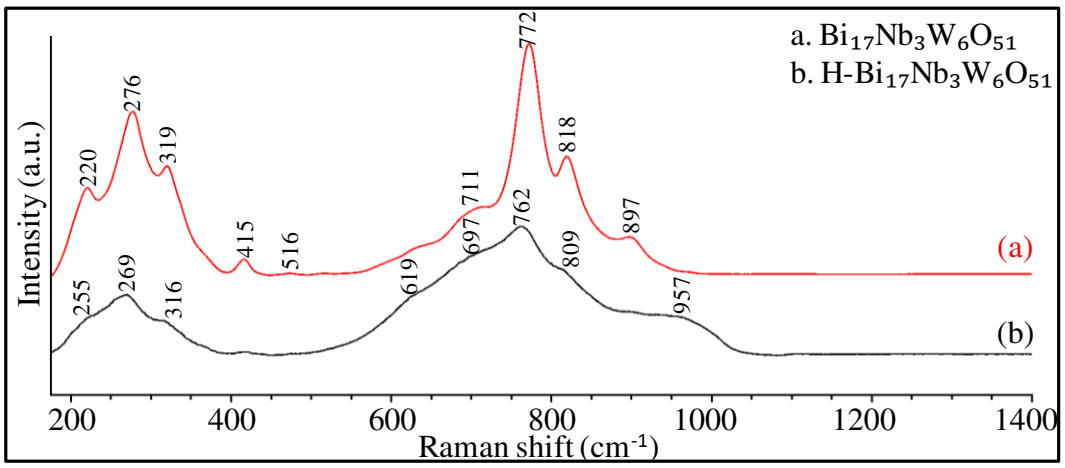

Figure 3.20: Raman spectra of $Bi_{17}Nb_3W_6O_{51}$ before and after protonation.

From the PXRD patterns and Raman spectra, one can conclude that only layered oxides with continuous layers can be successfully protonated and those with stair-like Aurivillius layered phases are very stable under acidic treatments.

3.3. Conclusion

This chapter was devoted to the synthesis and characterization of the solid layered materials. Several lamellar solids based on transition metals such as $LiNbMoO_6$, $LiNbWO_6$, $Bi_2W_2O_9$ and Bi_2WO_6 were successfully synthesized. Additionally, new series of mixed Nb/W were synthesized by exploring the compositions lying between $Bi_5Nb_3O_{15}$ (p=1+2) and Bi_2WO_6 (p=1), respectively. All samples were structurally characterized by powder diffraction techniques and Raman spectroscopy, notably the new Nb/W solids for the first time. To make the solids acidic and explore further their catalytic properties, the protonation process of all layered oxides was examined. $LiNbMoO_6$, $LiNbWO_6$, $Bi_2W_2O_9$ and Bi_2WO_6 were readily converted into their protonated forms by exchanging Li^+ or Bi^+ into protons and water of hydration. This was confirmed by PXRD and Raman spectroscopy since after protonation the PXRD patterns and Raman spectra were strongly modified. The water content in all samples was estimated from the TGA analysis.

Regarding the mixed Nb/W stair-like Aurivillius phases, the protonation process was unsuccessful. In these compounds, the Bi_2O_2 slabs and perovskite octahedral layers are discontinuous. The presence of "steps" seems to strongly enhance the stability of these layered oxides toward acidic treatments. However, with $Bi_{17}Nb_3W_6O_{51}$, since it exhibited a very similar structure to that of Bi_2WO_6, the sample was readily converted into its protonated form. The initial idea to go for totally new Nb/W compounds having a stair-like Aurivillius structure (Figure **3.12** possibility 3) turned out to be unsuitable for acid catalysis in view of their impossible protonation. In a future work, the synthesis of mixed Nb/W layered oxides based on known conventional Aurivillius phases (Figure **3.12** possibilities 1 and 2) shall be explored. This might provide insight about Aurivillius layered structures and their possible use as solid acid catalysts.

3.4. References

1 N. S. P. Bhuvanesh and J. Gopalakrishnan, *Inorg. Chem.*, 1995, **34**, 3760–3764.

2 V. Bhat and J. Gopalakrishnan, *Solid State Ionics*, 1988, **26**, 25–32.

3 R. E. Schaak and T. E. Mallouk, *Chem. Commun.*, 2002, **0**, 706–707.

4 T. Saison, P. Gras, N. Chemin, C. Chanéac, O. Durupthy, V. Brezová, C. Colbeau-Justin and J. P. Jolivet, *J. Phys. Chem. C*, 2013, **117**, 22656–22666.

5 D. Chen, L. Gao, A. Yasumori, K. Kuroda and Y. Sugahara, *Small*, 2008, **4**, 1813–1822.

6 P. Shen, H. T. Zhang, H. Liu, J. Y. Xin, L. F. Fei, X. G. Luo, R. Z. Ma and S. J. Zhang, *J. Mater. Chem. A*, 2015, **3**, 3456–3464.

7 H. C. Gupta, Archana and V. Luthra, *Physica B Condens Matter*, 2012, **407**, 477–484.

8 A. Kania, E. Talik, M. Szubka, W. Ryba-Romanowski, A. Niewiadomski, S. Miga and M. Pawlik, *J. Alloys Compd.*, 2016, **654**, 467–474.

9 V. D. Nithya, R. K. Selvan, D. Kalpana, L. Vasylechko and C. Sanjeeviraja, *Electrochim. Acta*, 2013, **109**, 720–731.

10 C. -M. Wang and J. -F. Wang, *J. Am. Ceram. Soc.*, 2008, **91**, 918–923.

11 H. Bernard, A. Lisińska-Czekaj, J. Dzik, K. Osińska and D. Czekaj, *Arch. Metall. Mater.*, 2011, **56**, 1137–1148.

12 M. Mączka, L. Macalik and S. Kojima, *J. Phys: Condens. Matter*, 2011, **23**, 405902.

13 M. Mączka, L. Macalik and J. Hanuza, *J. Raman Spectrosc.*, 2009, **40**, 2099–2103.

14 A. M. Abakumov, J. Hadermann, M. Batuk, H. D'Hondt, O. A. Tyablikov, M. G. Rozova, K. V. Pokholok, D. S. Filimonov, D. V. Sheptyakov, A. A. Tsirlin, D. Niermann, J. Hemberger, G. Van Tendeloo and E. V. Antipov, *Inorg. Chem.*, 2010, **49**, 9508–9516.

15 J. He, Q. J. Li, Y. Tang, P. Yang, A. Li, R. Li and H. Z. Li, *Appl. Catal. A: Gen.*, 2012, **443**–**444**, 145–152.

16 M. Kudo, H. Ohkawa, W. Sugimoto, N. Kumada, Z. Liu, O. Terasaki and Y. Sugahara, *Inorg. Chem.*, 2003, **42**, 4479–4484.

17 F. D. Hardcastle and I. E. Wachs, *J. Solid State Chem.*, 1992, **97**, 319–331.

18 T. Barré, L. Arurault and F. X. Sauvage, *Spectrochim. Acta Part A*, 2005, **61**, 551–557.

19 V. I. Tsaryuk and V. F. Zolin, *Spectrochim. Acta Part A*, 2001, **57**, 355–359.

20 B. Ingham, S. V. Chong and J. L. Tallon, *J. Phys. Chem. B*, 2005, **109**, 4936–4940.

21 A. Z. Sadek, H. Zheng, M. Breedon, V. Bansal, S. K. Bhargava, K. Latham, J. Zhu, L. Yu, Z. Hu, P. G. Spizzirri, W. Wlodarski and K. Kalantar-zadeh, *Langmuir*, 2009, **25**, 9545–9551.

22 C. Ng, C. Ye, Y. H. Ng and R. Amal, *Cryst. Growth Des.*, 2010, **10**, 3794–3801.

23 Li-F. Hu, Y. Tang, J. He, K. Chen and W. Lv, *Russ. J. Phys. Chem. A.*, 2017, **91**, 511–516.

24 Li.-F. Hu, R. Li, J. He, L.-g. Da, W. Lv and J.-s. Hu, *J. Nanophotonics*, 2015, **9**, 093041.

25 M. Maczka, J. Hanuza, W. Paraguassu, A. G. S. Filho, P. T. C. Freire and J. M. Filho, *Appl. Phys. Lett.*, 2008, **92**, 112911.

26 M. F. Daniel, B. Desbat, J. C. Lassegues, B. Gerand and M. Figlarz, *J. Solid State Chem.*, 1987, **67**, 235–247.

27 J. Tellier, P. Boullay, N. Créon and D. Mercurio, *Solid State Sci.*, 2005, **7**, 1025–1034.

28 J. Tellier, P. Boullay, M. Manier and D. Mercurio, *J. Solid State Chem.*, 2004, **177**, 1829–1837.

29 P. Boullay, L. Palatinus and N. Barrier, *Inorg. Chem.*, 2013, **52**, 6127–6135.

30 J. Gopalakrishnan, A. Ramanan, C. N. R. Rao, D. A. Jefferson and D. J. Smith, *J. Solid State Chem.*, 1984, **55**, 101–105.

31 Ismunandar, B. J. Kennedy, Gunawan and Marsongkohadi, *J. Solid State Chem.*, 1996, **126**, 135–141.

32 J. Li, Q. Shi, Y. Chen and M. Song, *Earth Environ. Sci.*, 2017, **100**, 012030.

33 A. Martínez-de la Cruz, S. O. Alfaro, L. M. Torres-Martínez and I. J. Ramírez, *J CERAM Process RES.*, 2008, **9**, 490–494.

34 A. Snedden, D. O. Charkin, V. A. Dolgikh and P. Lightfoot, *J. Solid State Chem.*, 2005, **178**, 180–184.

35 W. Zhou, *J. Solid State Chem.*, 2002, **163**, 479–483.

36 G. Steciuk, Application de la précession des électrons en mode tomographie à l ’étude de phases apériodiques et de films minces d’oxydes, Université de Caen Normandie, France.

37 G. Steciuk, P. Boullay, A. Pautrat, N. Barrier, V. Caignaert and L. Palatinus, *Inorg. Chem.*, 2016, **55**, 8881–8891.

38 G. Steciuk, N. Barrier, A. Pautrat and P. Boullay, *Inorg. Chem.*, 2018, **57**, 3107–3115.

CHAPTER FOUR

INTERCALATION AND ACIDITY

In this Chapter we will study the intercalation behaviour and the acidity of the protonated layered transition metal oxides directly in the liquid phase using Raman spectroscopy. Consequently, several compounds were incorporated into the protonated layered transition metal oxides, $HNbMoO_6$, $HNbWO_6$, $H_2W_2O_7$, H_2WO_4 and the protonated form of $Bi_{17}Nb_3W_6O_{51}$. Organic bases such as n-alkylamines (buylamine and octylamine) and pyridine were used as they will allow monitoring the acidity of the protonated layered oxides, while n-alcohols and 2,5-hexanediol were chosen as they are more closely related to the catalytic conversion that will be illustrtaed in chapter 5. The intercalation process was thus followed by Raman spectroscopy, X-ray diffraction and thermogravimetric analysis to determine the impact on the structure, to estimate quantitatively the amount of intercalates encountered in the interlayer regions and to evaluate the strength of the interactions between the layered oxides and the intercalates.

4.1. Intercalation of alkylamines and pyridine into known layered oxides

The intercalation behaviour of different layered transition metal oxides, $HNbMoO_6$, $HNbWO_6$, $H_2W_2O_7$ and H_2WO_4 was examined using nitrogen containing substrates such as n-alkylamines (butylamine and octylamine) and pyridine. These substrates are interesting as they are often used as intercalating molecules and also due to their basic character which in turn may allow monitoring acidity of the protonated layered oxides.

4.1.1. n-alkylamines intercalation into layered oxides

4.1.1.1. Influence on the structure

The intercalation process of butylamine and octylamine into the protonated layered metal oxides was evidenced using PXRD patterns and Raman spectroscopic data. The PXRD data of the various protonated layered solids interacting with n-alkylamines are described here. Lattice parameters are summarized in Table **4.1**. Note that the various protonated layered solids interacting with n-alkylamines were dried before the PXRD characterization.

Figure **4.1** and Figure **4.2** showed that upon n-alkylamines intercalation into $HNbMoO_6$ and $HNbWO_6$ layered oxides, sharp intense reflection peaks at low 2θ° angle regions can be clearly seen. The observed shift of these (00l) reflections towards lower 2θ values suggests that the intercalation process has modified the layered structure of the protonated phases by increasing the interlayer spacing between the metal oxide layers. The number of these (00l) reflections also increased as the carbon number of the n-alkyl chain increased. (hk0) reflections are scarce but still present. They are situated at the same position as for their respective protonated hydrated samples suggesting that the structure of the metal oxide layers has been preserved upon intercalation. The PXRD patterns are utterly dominated by the presence of (001) reflections with notably an absence of mixed (hkl) reflections as commonly observed upon intercalating long-carbon chain into layered compounds [1, 2]. In this context it is difficult to clearly identify the crystallographic structure of the intercalated compounds. For instance, lattice parameters are values that shall refer to a given space not unambiguously accessible based on these PXRD patterns. The only parameter that can be accessed here is the d(hkl) values that will, notably, provide an information on the evolution of the interlayer spacing between two inorganic sheets in the layered oxides. In the following, only this value will be given and discussed. The interlayer spacing of the intercalated

compounds is determined from the strongest reflection in the PXRD patterns, those situated at the lowest 2θ° angle region [3].

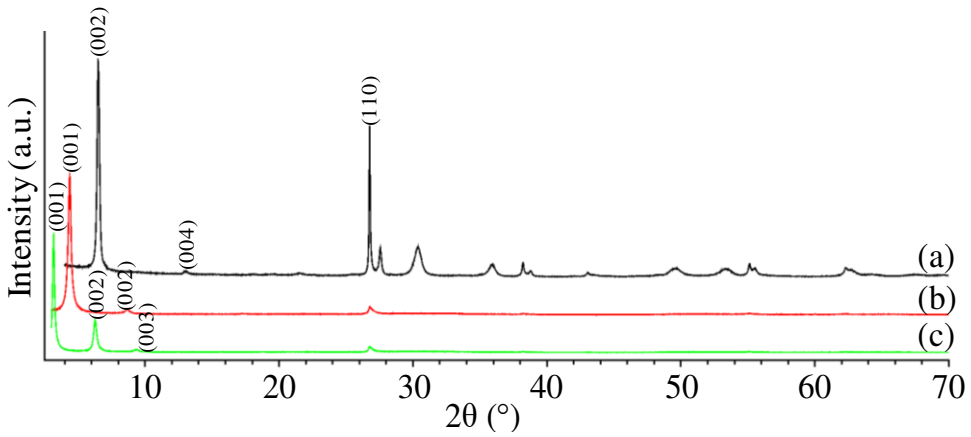

Figure 4.1: PXRD patterns of (a) $HNbMoO_6$ and after intercalation with (b) butylamine and (c) octylamine.

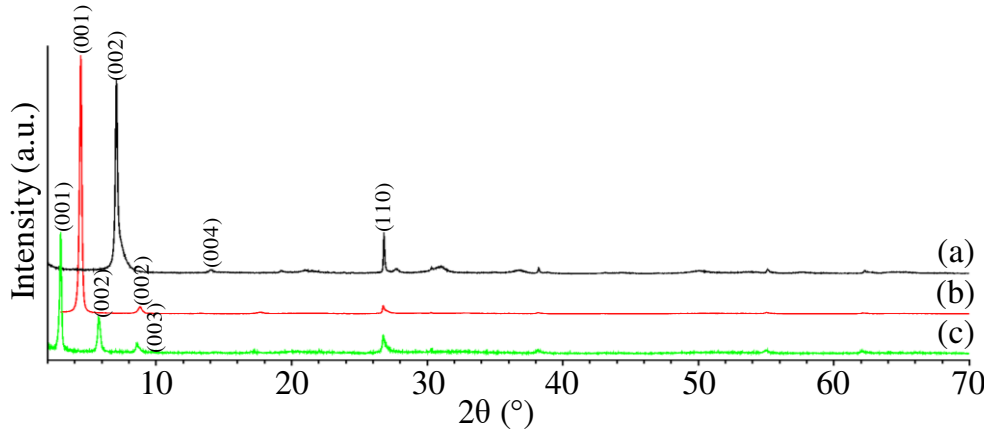

Figure 4.2: PXRD patterns of (a) $HNbWO_6$ and after intercalation with (a) butylamine and (c) octylamine.

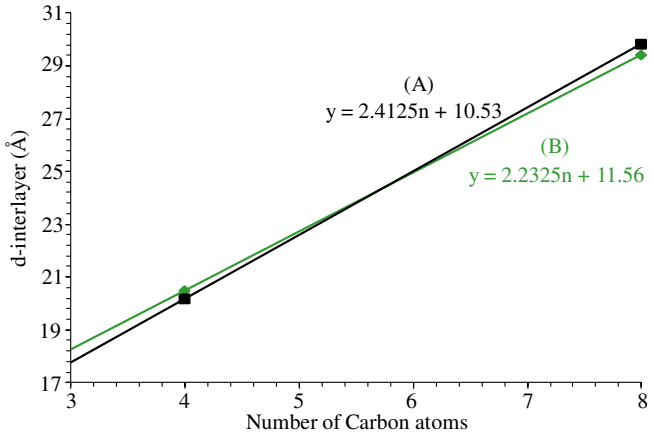

Figure 4.3: The d-interlayer spacing of (A) $HNbWO_6$ and (B) $HNbMoO_6$ intercalated with butylamine and octylamine as a function of the carbon number of the n-alkylamines.

It has been reported several times that the interlayer spacing linearly increases with the alkyl chain length (for even numbers) [1, 4]. Therefore, this was used to correlate with the interlayer though only two amines were used here. From these data, the layer configuration and geometry of the intercalation can be deduced. We tried to evaluate this by using a methodology similar to the one used by Chen et al. [2]

Figure **4.3** (A) and (B) represents the plots of d-interlayer spacing of $HNbMoO_6$ and $HNbWO_6$ intercalated with n-alkylamines as a function of number of carbon atoms n. Line equations are estimated to be d (Å) = 2.23n + 11.56 and d (Å) = 2.41n + 10.53 with $HNbMoO_6$ and $HNbWO_6$ respectively.

The increment per $-CH_2$ for a fully extended all trans alkyl chain is 1.27 Å [2]. When the slope value (k) is between 1.27 and 2.54 then n-alkyl chains intercalated might have a bilayer arrangement [4] and this is the case with both oxides as the slope was equal to 2.23 and 2.41. Therefore, in both oxides, n-alkyl chains have a bilayer arrangement with a tilt angle $\alpha = \sin^{-1}$ (slope/2.54) = 61 and 71° with $HNbMoO_6$ and $HNbWO_6$ respectively.

To estimate the thickness of the layered oxides layers, it is necessary to extrapolate the d-interlayer values at n = 1. According to the literature, the bond lengths of C-N and N-H in RNH_2 are 1.47 and 1.01 Å [5], respectively, therefore, the length (l_1) of a CH_3NH_2 molecule or $CH_3NH_3^+$ ion can be estimated as the sum (2.48 Å). Due to the bilayer arrangement and the tilt angle (61 and 71°), the contribution of the organic layers (CH_3NH_2 molecules or $CH_3NH_3^+$ ions) to the d-interlayer can be estimated as $h_o = 2l_1 \cdot \sin\alpha$ = 4.338 and 4.689 Å, respectively. Then the thickness of the inorganic layers (hi) can be calculated by subtracting ho from the d-interlayer values, i.e., hi = 13.79 - 4.338 = 9.452 or hi = 12.94 - 4.689 = 8.251 Å. The two values (9.452 or 8.251) are approximately double the thickness (4.1 Å) of the single-octahedral W–O layer. Therefore, we can conclude that upon n-alkylamine intercalation into $HNbMoO_6$ and $HNbWO_6$ layered oxides, their double octahedral layer was preserved.

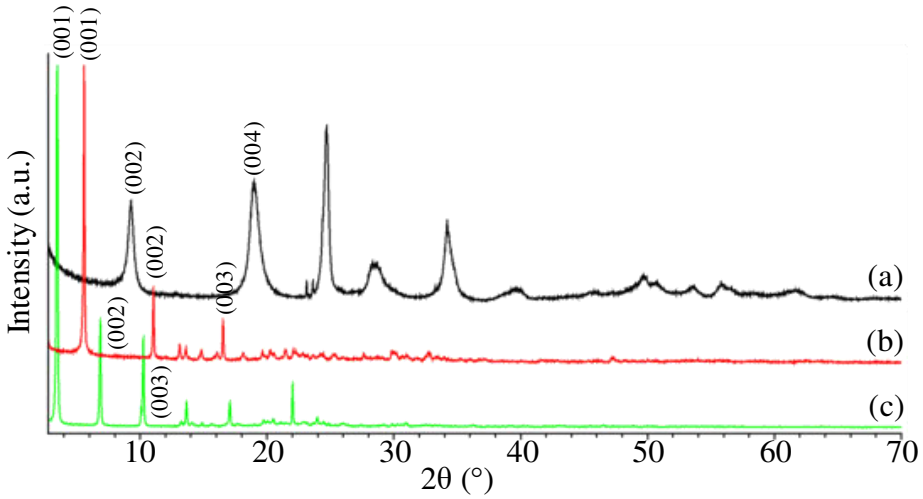

Figure 4.4: PXRD patterns of (a) parent $H_2W_2O_7$ before intercalation and (b) intercalation with butylamine and (c) octylamine.

In the case of $H_2W_2O_7$, its diffractions peaks disappeared upon adding butylamine and octylamine and a new series of strong (00l) reflections with sharp peaks were observed in the 2θ° angle region (3 - 20°), as shown in Figure **4.4** [2, 5]. Similarly to the results encountered with layered $HNbMoO_6$ and $HNbWO_6$, as the size of the alkyl chain increased, the number of diffraction peaks increased, from 4 to 8 when $H_2W_2O_7$ is intercalated with butylamine or octylamine respectively, indicating that the degree of long range order of the lamellar structure of the reaction products was enhanced. In this case a and b parameters were slightly modified while d-interlayer spacing increased from 9.16 Å to 16.20 or 26.04 Å upon butylamine or octylamine intercalation (results are represented in Table **4.1**).

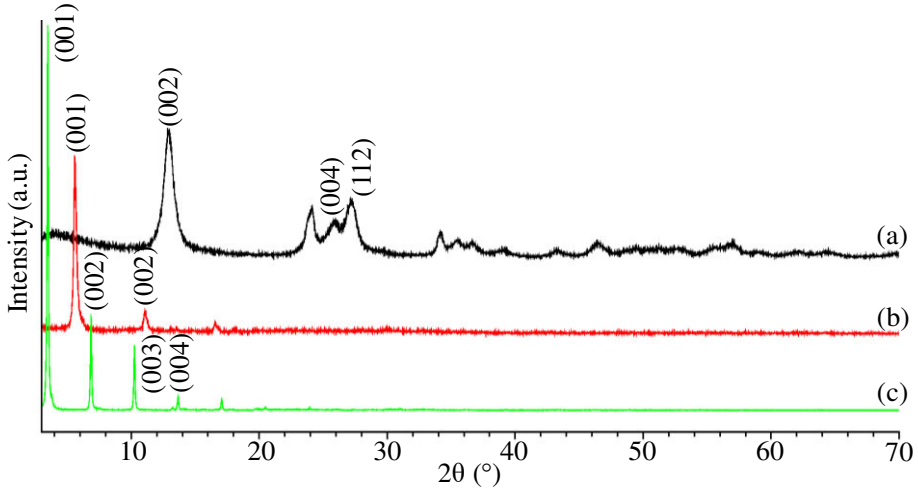

Figure 4.5: PXRD patterns of (a) parent $H_2WO_4.H_2O$ before intercalation and (b) after intercalation with butylamine and (c) octylamine.

Similarly to $H_2W_2O_7$, n-alkylamines intercalation into $H_2WO_4.H_2O$ layered oxide was also monitored (Figure **4.5**). Results revealed that with short chain n-alkylamine (butylamine), the intercalation process was successfully accomplished after three days; however, with octylamine, longer time (almost one month) was needed to complete the process. The resultant compounds were white in color in contrast to the yellow color of the parent oxide. Their PXRD patterns as indicated in Figure **4.5**, revealed the disappearance of diffraction peaks of the parent oxide and a new series of (00l) diffraction peaks in the 2θ° angle region (3 - 18°) were encountered. The latter was characterized by regular reduced intensities characteristic of an ordered layered structure [2]. As above, only the number of diffraction peaks increased with the number of carbon atoms of the n-alkyl chain. The intercalated n-alkylamines expanded the interlayer spacing of H_2WO_4 oxide along the c-axis as represented in the table.

To estimate the thickness of the layered oxides layers in $H_2W_2O_7$ and H_2WO_4 after n-alkylamines intercalation, the same procedure was followed as with $HNbMoO_6$ and $HNbWO_6$.

The line equations of the d-interlayer plots of $H_2W_2O_7$ and H_2WO_4 intercalated with n-alkylamines as a function of number of carbon atoms n are estimated to be d (Å) = 2.46n + 6.35 and d (Å) = 2.50n + 5.99 with $H_2W_2O_7$ and H_2WO_4 respectively. The values of the slope in both cases (2.46 and 2.50 Å) are in between 1.27 and 2.54 Å, indicating a bilayer arrangement of the n-alky chains with a tilt angle (75 and 80º) in $H_2W_2O_7$ and H_2WO_4, respectively. Then, the difference between the interlayer distance extrapolated from n = 1 (d_1 = 8.81 and 8.49 Å) and h_o = 4.790 and 4.884 Å calculated using the following formula $h_o = 2l_1.\sin\alpha$, was estimated to be equal to 4 or 3.6 Å with $H_2W_2O_7$ and H_2WO_4 layered oxides, respectively. The two values were close to the thickness of a single W-O octahedral layer, revealing that upon intercalation the double octahedral layer of $H_2W_2O_7$ dissociated into a single one.

Consequently, taking into consideration the d-interlayer of the dehydrated samples (10.8 [6], 10 [1], 9.10 [7] and 5.35 Å [2] for $HNbMoO_6$, $HNbWO_6$, $H_2W_2O_7$ and H_2WO_4 layered oxides, respectively), the interlayer spacing in all tested layered oxides encountered higher increase with octylamine in comparison to butylamine. This confirmed its relation with the carbon number of n-alkyl chain. Additionally, the d-interlayer spacing increase in all layered oxides with both butylamine and octylamine as shown in the table can be summarized in the

following order: $HNbMoO_6$ ≈ $HNbWO_6$ > $H_2W_2O_7$ ≈ H_2WO_4. In all cases, a bilayer organisation of the amine can be inferred.

Table 4.1: Interlayer spacing of protonated layered oxides before and after interaction with butylamine and octylamine.

	d-interlayer (Å)		
Compound	raw	+ butylamine	+ octylamine
$HNbMoO_6.H_2O$	13.15(1)	20.49(4)	28.6(1)
$HNbWO_6.1.5\ H_2O$	12.73(3)	20.18(3)	30.6(1)
$H_2W_2O_7.0.1\ H_2O$	9.16(1)	16.20(1)	26.04(1)
$H_2WO_4.H_2O$	6.86(1)	16.08(3)	26.06(1)

4.1.1.2. Quantification

TGA analysis coupled with IR was conducted in order to estimate the amount of intercalant in the interlayers and to evaluate the strength of interactions between the layered oxides and n-alkylamines.

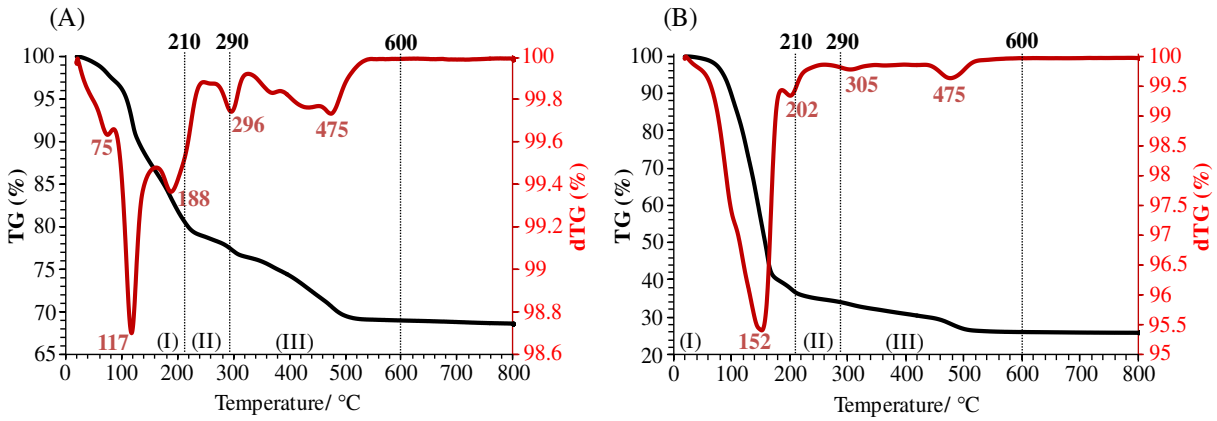

Figure 4.6: TG-dTG curves of $H_2W_2O_7$ after adsorption of (A) butylamine and (B) octylamine.

Figure **4.6** (A) and (B) represents the TG-dTG curves of butylamine and octylamine intercalated into $H_2W_2O_7$ layered oxides. The IR analysis of the evolved gases, allowed distinguishing between three regions. Region I: room temperature - 210°C, Region II: 210 -

290°C, Region III: 290 - 600°C. Beyond 600°C no mass loss was encountered as confirmed by the absence of peaks in the TG and dTG curves.

The highest mass loss encountered in Region I (20% with butylamine and 64% with octylamine) can be ascribed to the sole desorption of n-alkylamine molecules. A mass loss of 3.17 or 2.65% in Region II can be attributed to the desorption of remaining butylamine or octylamine, as well as desorption of structural water. Region III revealed a mass loss of 8.6 or 7.9% that can be assigned to the decomposition/oxidation of butylamine or octylamine. As a consequence, the total mass loss between room temperature and 600°C increased from 31% to 74% for $H_2W_2O_7$ intercalated with butylamine and octylamine.

The amount of n-alkylamines in each region were calculated in both cases from their respective mass losses and summarized in Table **4.2**. Results revealed that the highest amount of n-alkylamines was desorbed below 210°C. The total amount of amine intercalated into $H_2W_2O_7$ layered oxide calculated between room temperature and 600°C is approximately equal to 1.4 mol/mol of WO_3 in case of butylamine and 5 mol/mol of WO_3 in octylamine case.

Table 4.2: TGA results of n-alkylamines intercalated into $H_2W_2O_7$ layered oxides. Δm is the weight loss of n-alkylamine and Δn is the calculated amount of n-alkylamines per mol of the final product (WO_3 is formed at 600ºC) in each region.

		$H_2W_2O_7$ + butylamine		$H_2W_2O_7$ + octylamine	
Region	Temp. Range (°C)	Δm (g)	Δn (mol/mol)	Δm (g)	Δn (mol/mol)
I	RT - 210	6.17×10^{-3}	0.88	14.71×10^{-3}	4.40
II	210 - 290	1.02×10^{-3}	0.14	6.14×10^{-4}	0.18
III	290 - 600	2.76×10^{-3}	0.39	1.84×10^{-3}	0.55

Similarly, the butylamine and octylamine contents intercalated into $HNbMoO_6$ and $HNbWO_6$ layered oxides were determined using TGA as indicated in Figure **4.7** and Figure **4.8** respectively.

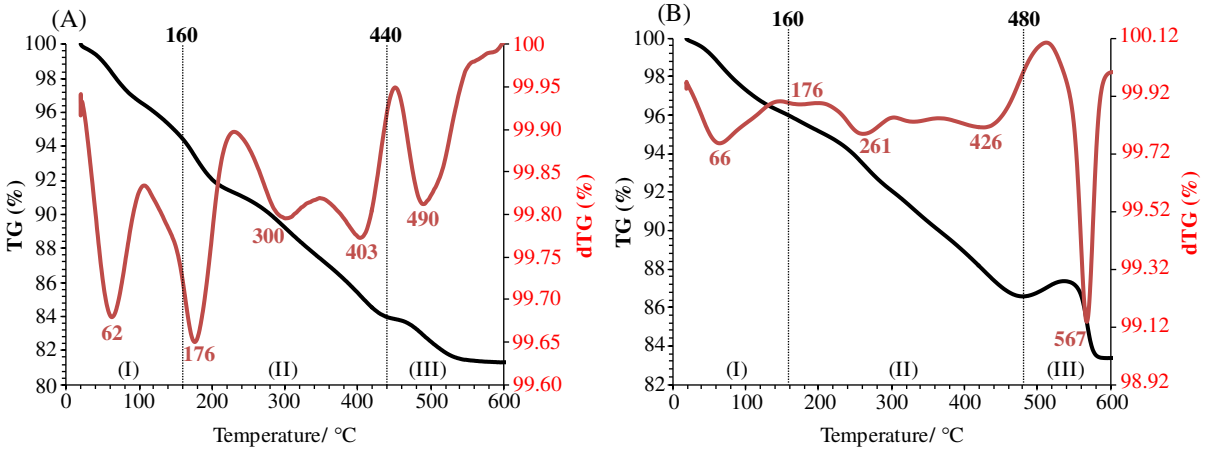

Figure 4.7: TG-dTG curves of butylamine intercalated into (A) $HNbMoO_6$ and (B) $HNbWO_6$.

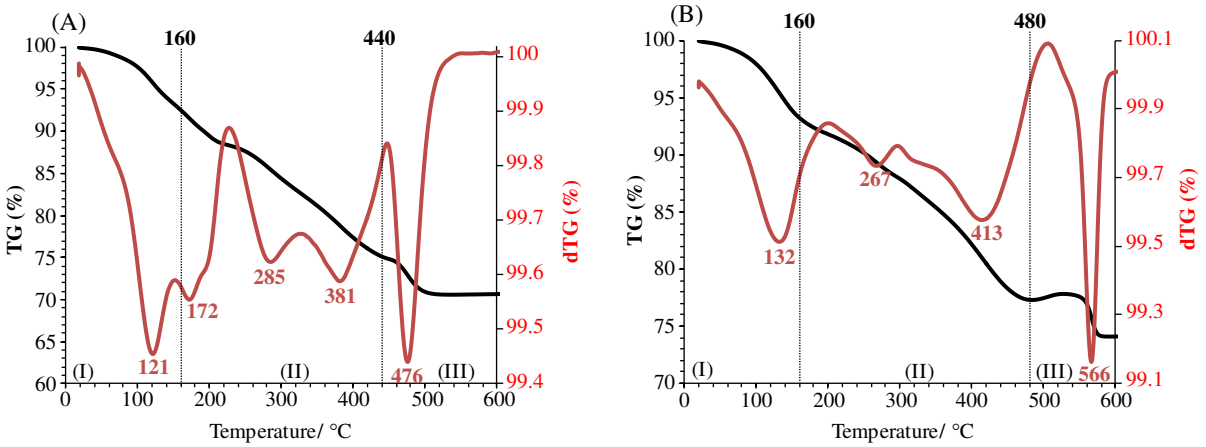

Figure 4.8: TG-dTG curves of octylamine intercalated into (A) $HNbMoO_6$ and (B) $HNbWO_6$.

TG curves of $HNbMoO_6$ and $HNbWO_6$ intercalated with butylamine and octylamine can be divided into three main regions. Region I attributed to desorption of water. Region II can be assigned to the release of n-alkylamines from the interlayers of the layered oxides through oxidation and Region III is probably due to the decomposition of the host solids.

As can been seen in Figure **4.7**, first, Regions (I, A) and (I, B) ranging between room temperature and 160°C, consists of dTG peaks situated at 62 and 66°C, attributed to the desorption of water. Second, Regions (II, A) (160 - 440°C) and (II, B) (160 - 480°C) exhibits several dTG peaks situated at (176, 300, 403°C) and (176, 261, 426°C) respectively, corresponding to the multi-desorption steps of incorporated amine in the interlayers. Third, Regions (III, A) (> 440°C) and (III, B) (> 480°C) consists of a strong dTG peak situated at 490 and 567°C respectively, which is probably due to the decomposition of the layered host solid. From the weight loss observed in Region I, the calculated water amount ranges between 1.0 to 1.5 mol of the dehydrated sample. From Region II, the amount of intercalated

butylamine was calculated and estimated to be equal to 0.48 mol/mol of dehydrated $HNbMoO_6$ and 0.55 mol/mol of dehydrated $HNbWO_6$.

Similar results were encountered in case of octylamine intercalated into $HNbMoO_6$ and $HNbWO_6$ layered oxides, as shown in Figure **4.8**. Therefore, the amount of octylamine intercalated was calculated by taking into account the weight loss in Regions (II, A) (160 - 440°C) and (II, B) (160 - 480°C), respectively, and estimated to be equal to 0.52 mol/mol of dehydrated $HNbMoO_6$ and 0.59 mol/ mol of dehydrated $HNbWO_6$.

Therefore, total removal of butylamine and octylamine were encountered at higher temperature with $H_2W_2O_7$ (at 600°C) in comparison with $HNbMoO_6$ (at 440°C) and $HNbWO_6$ (at 480°C) layered oxides and the amount of intercalated n-alkylamines into $H_2W_2O_7$ was much higher than with $HNbMoO_6$ and $HNbWO_6$ layered oxides. dTG data also revealed multi desorption maxima for n-alkylamines elimination from $H_2W_2O_7$ whereas, in case of $HNbMoO_6$ and $HNbWO_6$ layered oxides, lower desorption steps were encountered. Therefore, these results indicated that stronger interaction was evidenced between $H_2W_2O_7$ and amines than with $HNbMoO_6$ and $HNbWO_6$.

4.1.1.3. Spectroscopic characterization of intercalation

PXRD analysis as well as TG data revealed the successful intercalation of n-alkylamines into $H_2W_2O_7$, H_2WO_4, $HNbMoO_6$ and $HNbWO_6$ layered oxides. However, the specific interactions taking place between amines and layered oxides should be more specifically considered. Therefore, Raman spectroscopy in the liquid phase was utilized here as a tool to simultaneously monitor the structural changes encountered upon intercalating n-alkylamines and to evaluate the acidity of the protonated oxides.

Figure **4.9** and Figure **4.10** represent the Raman spectra of $HNbMoO_6$ and $HNbWO_6$ intercalated with butylamine and octylamine respectively. Upon adding the first few drops of either butylamine or octylamine into layered oxides, Raman spectroscopy detected several changes for the host solid. However, to ensure intercalation was complete, the host solids were left in solution for a longer time (up to one month).

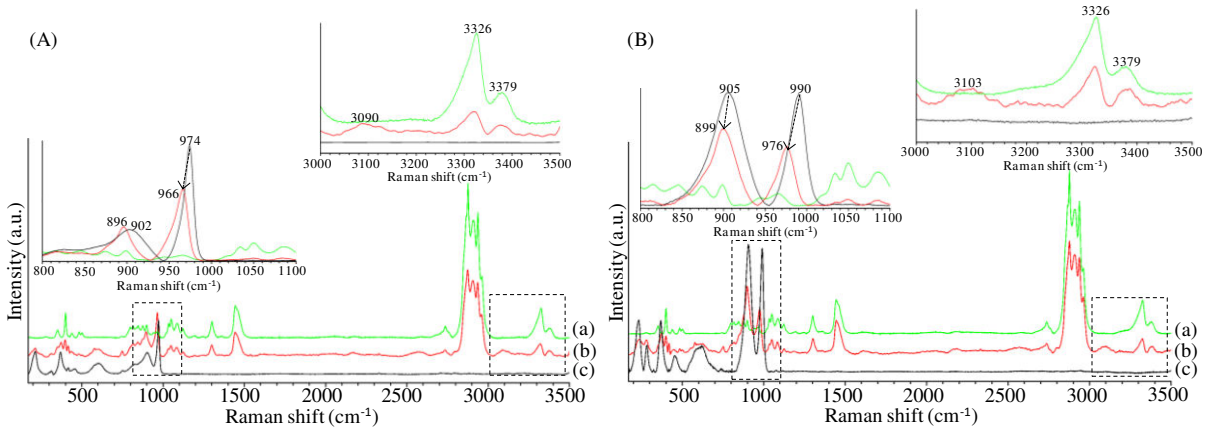

Figure 4.9: Full range Raman spectra (200 - 3500 cm^{-1}) of (a) butylamine, (b) Protonated sample + butylamine and (c) Protonated sample before intercalation for (A): $HNbMoO_6$ and (B) $HNbWO_6$. The insets show enlargements of the spectra in (800 - 1100 cm^{-1}) and (3000 - 3500 cm^{-1}) regions.

After adding butylamine, bands corresponding to M=O (M = Mo, W) and Nb=O shifted from 974 and 902 to 966 and 896 cm^{-1} in $HNbMoO_6$ case and from 990 and 905 to 976 and 899 cm^{-1} respectively in $HNbWO_6$ case (Figure). This indicates interaction between the amine and the M=O and Nb=O apical bonds from the lattice [9]. In parallel, bands of the amine also encountered some modifications around 3300 cm^{-1}, where NH_2 antisymmetric and symmetric ν(N-H) stretching bands at 3380 and 3325 cm^{-1} [10] decreased with the development of a band around (3080 - 3100 cm^{-1}) due to the protonation of the amine groups to form ammonium ions [11, 12]. This interaction guarantees the adsorption of n-alkylamines in the interlayer region of the protonated samples. This also implies that acidic sites are in the close vicinity of Mo(W)=O or Nb=O bonds.

In case of octylamine addition into $HNbMoO_6$ and $HNbWO_6$ layered oxides, similar results were encountered both at the level of the host solid and that of amine, as indicated in Figure **4.10**. Therefore, the bands of the layered samples situated at 972 and 904 cm^{-1} in case of $HNbMoO_6$ shifted to lower wavenumbers (964 and 892 cm^{-1}) after amine addition and that of $HNbWO_6$ shifted from 990 and 906 to 972 and 894 cm^{-1} respectively. In addition to that, pure amine bands situated at 3325 and 3380 cm^{-1} decreased in intensity and instead a band around (3080 - 3100 cm^{-1}) emerged. This similar behaviour confirms the intercalation of octylamine into the interlayers of the layered sample.

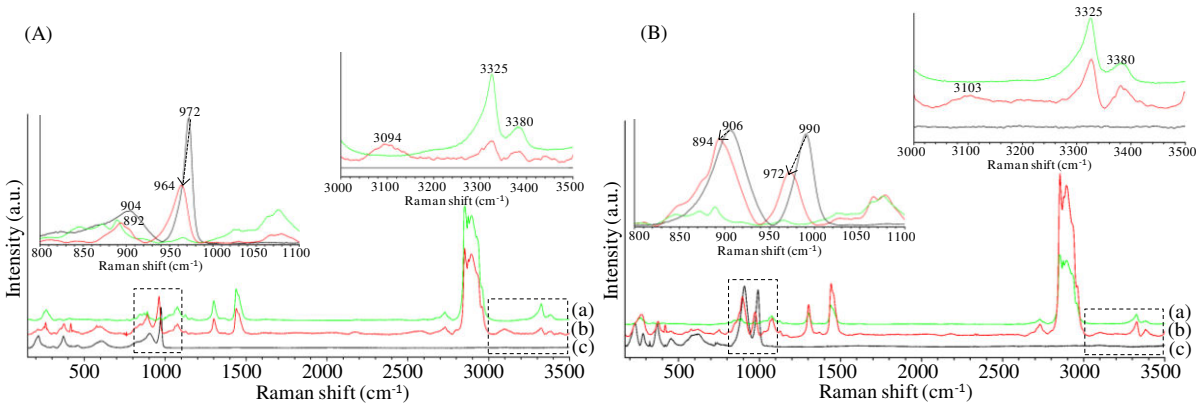

Figure 4.10: Full range Raman spectra (200 - 3500 cm^{-1}) of (a) octylamine, (b) Protonated sample + octylamine and (c) Protonated sample before intercalation for (A): $HNbMoO_6$ and (B) $HNbWO_6$. The insets show enlargements of the spectra in (800 - 1100 cm^{-1}) and (3000 - 3500 cm^{-1}) regions.

The interactions between $H_2W_2O_7$ and octylamine or butylamine were also characterized using Raman spectroscopy in the liquid phase. In contrast to the results encountered with $HNbMoO_6$ and $HNbWO_6$, upon intercalating butylamine and octylamine into $H_2W_2O_7$ layered oxide, the Raman spectra evolved progressively with time as shown in Figure **4.11** and Figure **4.12** respectively. In presence of butylamine, Figure **4.11**, the ν(W=O) band at 942 cm^{-1} decreased and shifted to 920 cm^{-1}. This occurred parallel to changes on the amine bands similar to those described above for $HNbMoO_6$ with some additional perturbations in the ν(C-H) bands. Figure **4.13** and Figure **4.14** showed that NH_2 antisymmetric and symmetric bands of pure butylamine (or octylamine) situated at 3380 and 3325 cm^{-1} decreased in intensity and a new band located at 3095 and 3097 cm^{-1} emerged respectively as a result of the protonation of the amine groups to form ammonium ions [11, 12]. This coherent changes imply that the amine interacts first with the apical W=O of $H_2W_2O_7$.

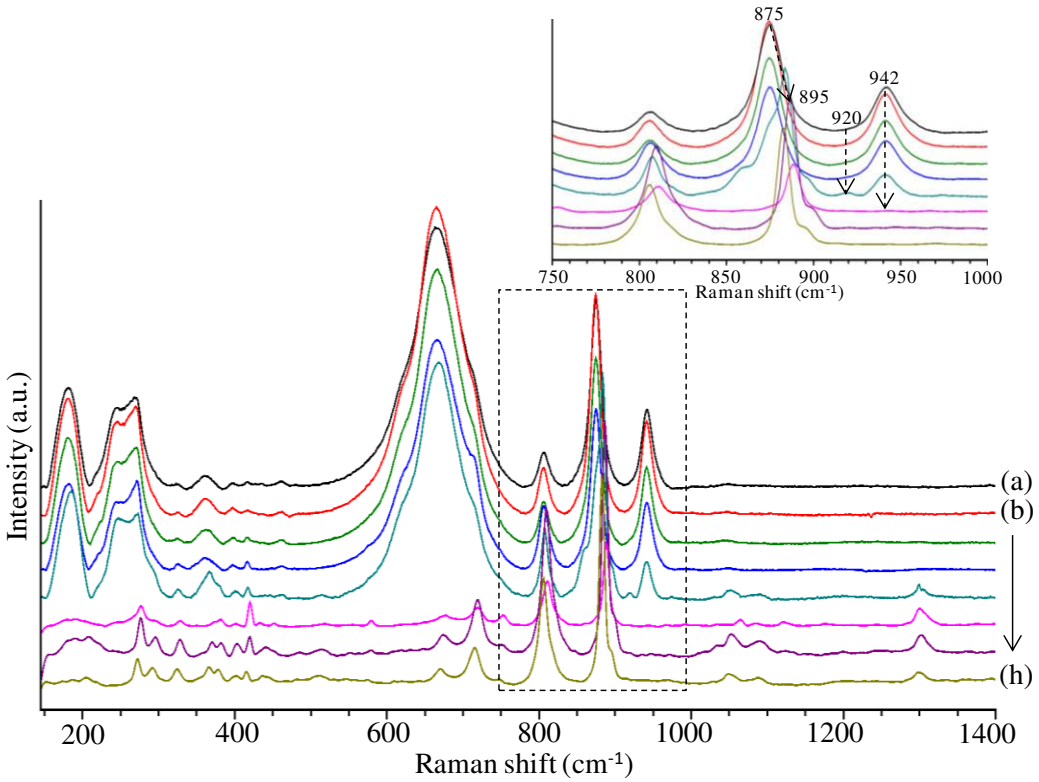

Figure 4.11: Raman spectra of butylamine intercalation on (a) $H_2W_2O_7$ and (b - h) evolution with time after adding butylamine. The inset shows the enlargement at (750 - 1000 cm^{-1}).

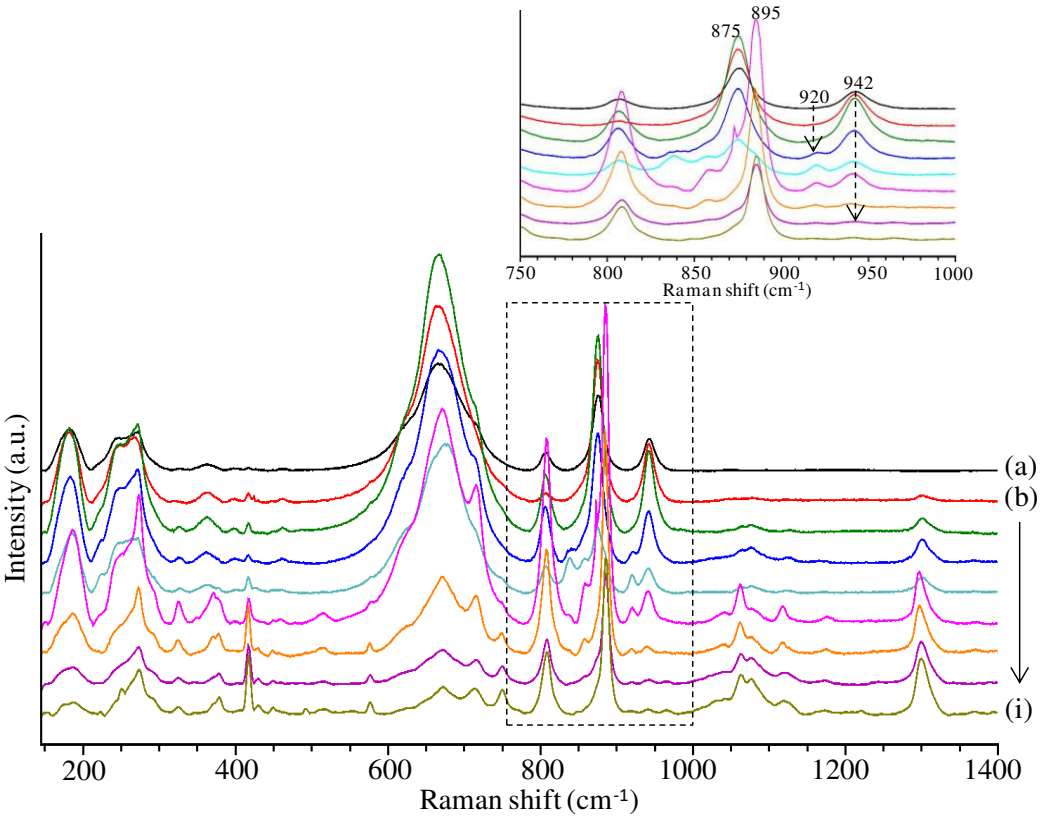

Figure 4.12: Raman spectra of octylamine intercalation on (a) $H_2W_2O_7$ and (b - i) evolution with time after adding octylamine. The inset shows the enlargement at (750 - 1000 cm^{-1}).

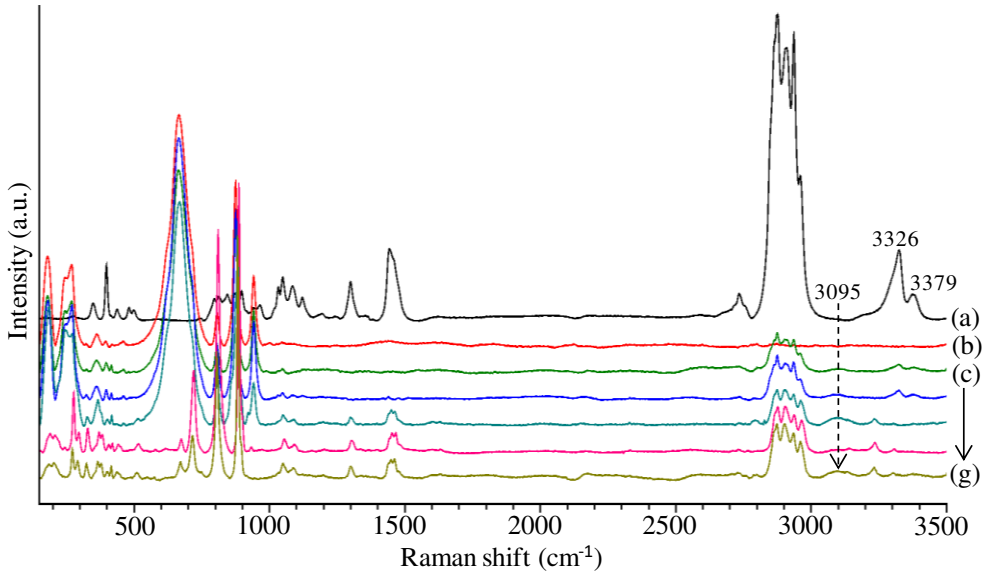

Figure 4.13: Full range Raman spectra (200 - 3500 cm^{-1}) of (a) butylamine, (b) $H_2W_2O_7$ and (c - g) evolution with time after adding butylamine.

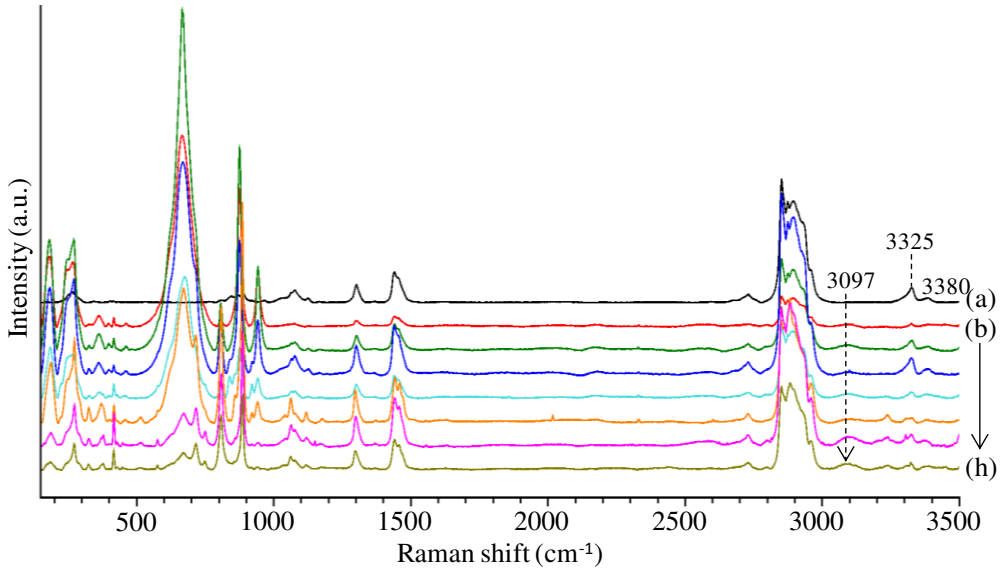

Figure 4.14: Full range Raman spectra (200 - 3500 cm^{-1}) of (a) octylamine and (b - h) evolution with time of $H_2W_2O_7$ after adding octylamine.

Then, the bands at 920 - 942 cm^{-1} progressively disappeared while the band at 875 shifted to 895 cm^{-1} and the broad band at 670 cm^{-1} decreased sharply. Meanwhile, new bands developed at 805, 714 and 268 cm^{-1}. This set of bands can be ascribed to the presence of WO_3 [13, 14, 15] while bands around 900 cm^{-1} may be found for WO_4 compounds [16, 17]. This development and the large modifications of the bands at 875 and 670 cm^{-1} indicated that $H_2W_2O_7$ is largely modified. Similar results were obtained with octylamine, Figure **4.12**.

Noteworthy, previous studies by Chen et al. [2,5] have proposed the possible dissolution-reorganization mechanism of the double octahedral W-O layers of $H_2W_2O_7$ upon reaction with n-alkylamines. After n-alkylamines intercalation in a first step, the interlayer water molecules may be released and react with surrounding n-alkylamines molecules forming highly alkaline solutions which induce the dissolution of the double-octahedral W-O layers. The dissolved species then recrystallize to form stackings of single W-O octahedral layers, hence mimicking the interaction between n-alkylamines and H_2WO_4 [2].

Consequently, the intercalation behaviour of n-alkylamines into H_2WO_4 was also examined. Upon adding the first few drops of either butylamine or octylamine, Raman spectra of H_2WO_4 layered oxide already indicated several changes. Nevertheless, the sample was kept in solution for almost one month to ascertain the process of intercalation. In case of butylamine, as indicated in Figure **4.15**, the peaks situated at 960, 670 and 238 cm^{-1} decreased dramatically, while new sets of peaks appeared at 887, 811, 756, 674, 326 and 297 cm^{-1} after adding the first few drops of butylamine. These peaks finally slightly shifted with time to lower wavenumbers as represented in Figure **4.15(c)** and they can be attributed to the presence of single W-O octahedral layers like for $H_2W_2O_7$. Simultaneously, the antisymmetric and symmetric (NH) bands of pure butylamine situated at 3379 and 3325 cm^{-1} decreased and a new peak at 3104 cm^{-1} emerged as represented in Figure **4.16**. Similar results were encountered in case of octylamine as can be seen in Figure **4.17** and Figure **4.18**. These results were similar to those encountered with $H_2W_2O_7$ intercalated with n-alkylamines as represented in Figure **4.19**. Therefore, one can conclude that the resultant compounds upon intercalating n-alkylamines into either $H_2W_2O_7$ or H_2WO_4 are the same, i.e. both are constructed of alternately stacking n-alkylammonium bilayers and of single octahedral (W-O) layers. As a consequence, these results can affirm more the process of dissolution-reorganization of double octahedral (W-O) layers in $H_2W_2O_7$ layered oxide into single ones.

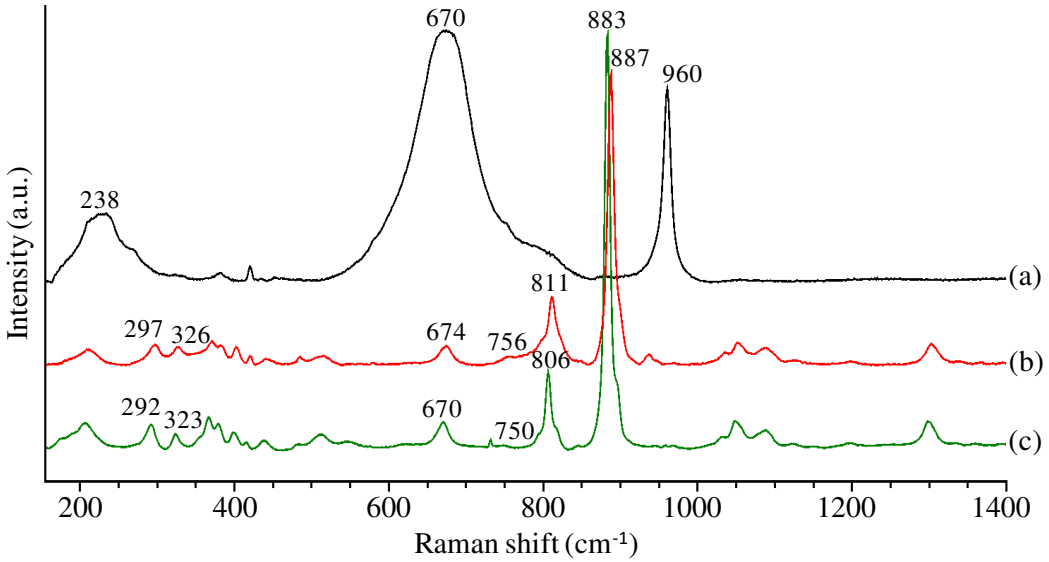

Figure 4.15: Raman spectra of butylamine intercalation on (a) H_2WO_4 and (b and c) evolution with time after adding butylamine. (b) after adding 4 drops of butylamine and (c) after 1 month of butylamine addition.

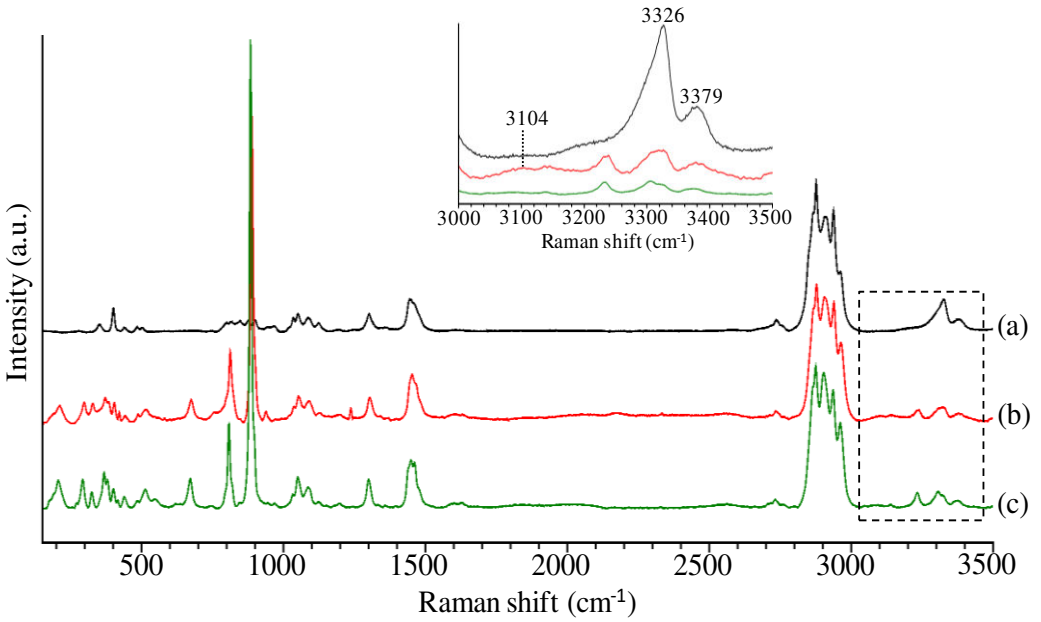

Figure 4.16: Full range Raman spectra (200 - 3500 cm^{-1}) of (a) butylamine and (b and c) evolution with time of H_2WO_4 after adding butylamine. The inset shows the enlargement at (3000 - 3500 cm^{-1}).

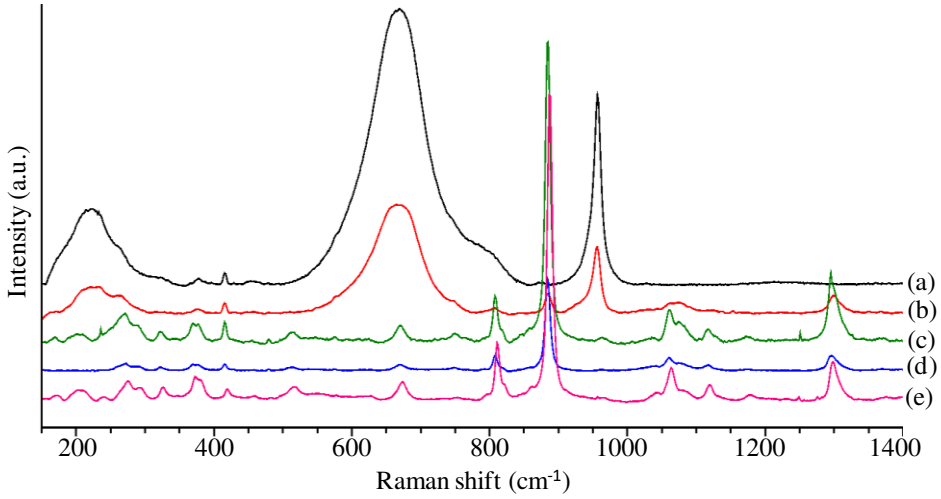

Figure 4.17: Raman spectra of octylamine intercalation on (a) H_2WO_4 and (b - e) evolution with time after adding octylamine.

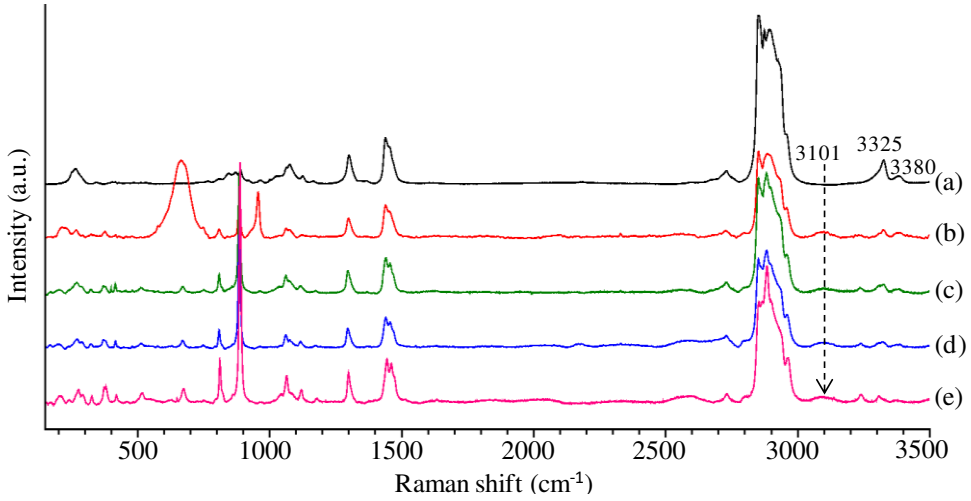

Figure 4.18: Full range Raman spectra (200 - 3500 cm^{-1}) of (a) octylamine and (b - e) evolution with time of H_2WO_4 after adding octylamine.

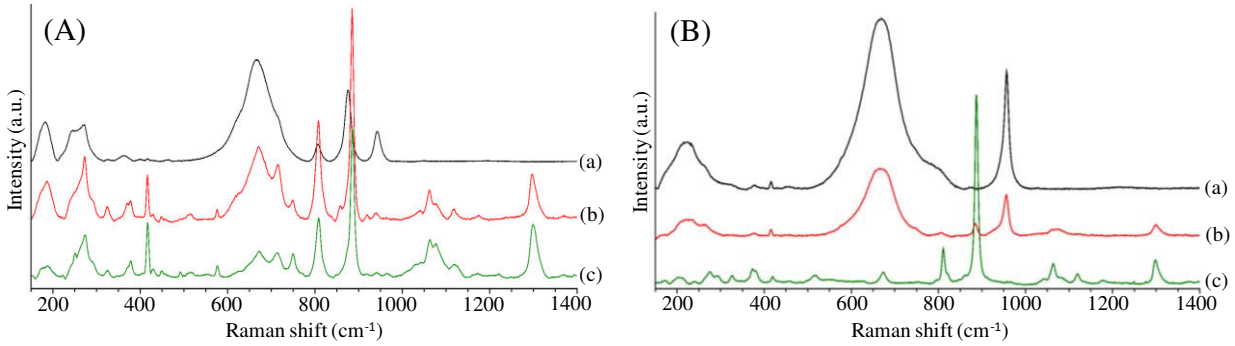

Figure 4.19: Raman spectra of (a) Protonated sample for (A) $H_2W_2O_7$ and (B) H_2WO_4, (b - c) protonated sample + octylamine at different time intervals.

4.1.2. Pyridine intercalation into layered oxides

In addition to n-alkylamines, pyridine was chosen since it is interesting due to its dual character, it can act as a cyclic intercalating molecule and it has been largely used as a basic molecular probe in Infrared spectroscopy (gas phase) to discriminate between different acidic sites [18, 19, 20]. However, the detailed characterization of the active sites has rarely been conducted in the liquid phase [21, 22, 23]. This part will be devoted to the simultaneous monitoring of pyridine intercalation as well as acidity of the layered oxides using Raman spectroscopy in the liquid phase. Dried samples were also characterized by PXRD and TGA to evaluate the extent of intercalation with pyridine.

4.1.2.1. Influence on the structure

Results above (Section 4.1.1) indicated that the intercalation of linear nitrogen containing compounds has been successfully achieved. However, pyridine is a bulkier molecule but it is a weaker base. Therefore, the influence of pyridine intercalation on the structure was examined using PXRD and TGA analysis was utilized to calculate the intercalated amount.

Figure **4.20** shows the PXRD patterns of the layered $HNbMoO_6$ and $HNbWO_6$ before and after intercalation.

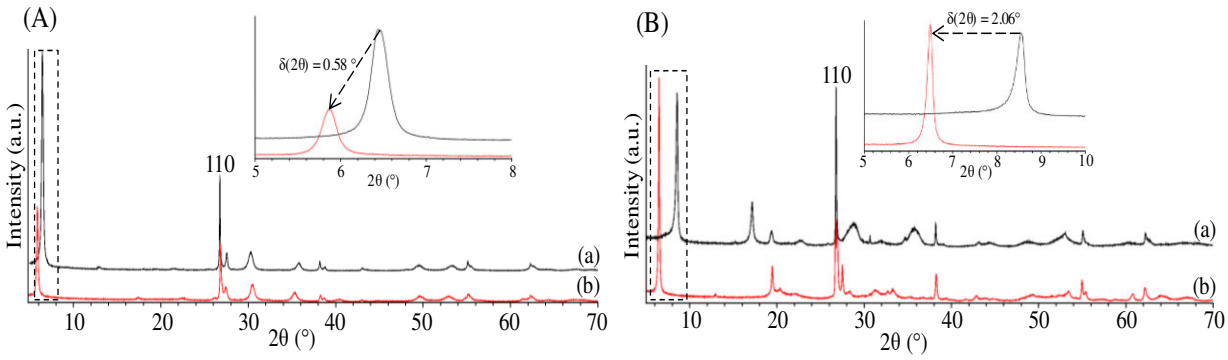

Figure 4.20: PXRD patterns of (A) $HNbMoO_6$ and (B) $HNbWO_6$, (a) before and (b) after intercalation with pyridine. The inset shows the enlargement at lower angles.

PXRD results revealed that immersion of pyridine into the protonated samples shifted the first peak into lower angles, from 6.40° to 5.89° for $HNbMoO_6$ and from 8.51° to 6.44° for $HNbWO_6$ corresponding to an increase in the interlayer spacing, as observed in Table **4.3**. Conversely, the diffraction peaks such as (110) corresponding to in-plane diffraction are

observed at the same position in both cases. This indicates that the structure of the metal oxide layer is preserved and that only the interlayer distance is expanded by the presence of pyridine. Given that the interlayer spacing of fully dehydrated sample is 10.8 Å for $HNbMoO_6$ [6] and 10 Å [1] for $HNbWO_6$ layered oxides, then the total expansion is estimated to be 4.3 Å and 3.7 Å respectively. Normally, a total net expansion of 5.8 or 3.3 Å is observed if pyridine is situated within the interlayers in a perpendicular or parallel orientation respectively [24, 25]. Therefore, with $HNbWO_6$ layered oxide, the total expansion of 3.7 Å could be due to a parallel orientation to the host layers, however, with $HNbMoO_6$ layered oxide, the expansion neither suggested a perpendicular nor a parallel orientation.

Table 4.3: Interlayer spacing for $HNbMoO_6$ and $HNbWO_6$ layered oxides before and after adding pyridine.

Compound	d-interlayer (Å)
$HNbMoO_6$	10.8(1)
$HNbMoO_6.H_2O$	13.15(1)
$HNbMoO_6$ + pyridine	15.06(1)
$HNbWO_6$	10(1)
$HNbWO_6.0.5H_2O$	10.39(1)
$HNbWO_6$ + pyridine	13.71(1)
$H_2WO_4.H_2O$	6.86(1)
$H_2WO_4.H_2O$ + pyridine	11.46(2)

In contrast to the results encountered with the latter mixed oxides, the intercalation of pyridine into $H_2W_2O_7$ layered oxide was not successfully achieved. This was confirmed by PXRD patterns, as indicated in Figure **4.21**, where no changes were observed after pyridine addition.

This was also the case when intercalation was carried out at higher temperature. When pyridine was added into $H_2W_2O_7$ layered oxide and heated in an oil bath at 80°C for 24 hours, no changes were observed in the PXRD pattern, Figure **4.21**, confirming the absence of intercalation.

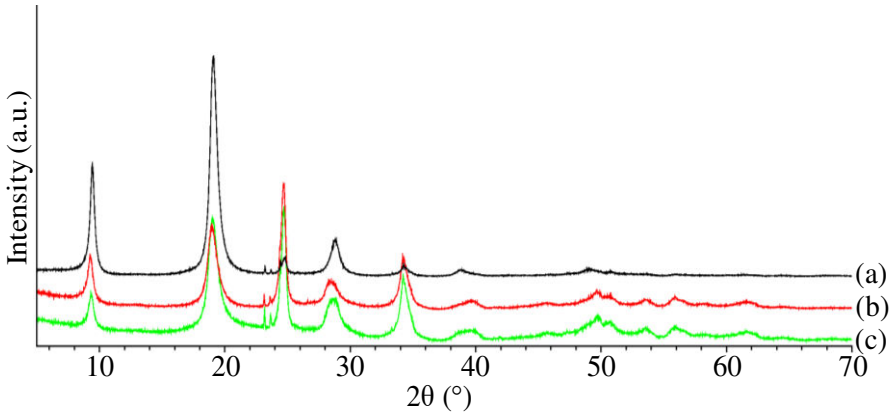

Figure 4.21: PXRD patterns of (a) $H_2W_2O_7$, (b) $H_2W_2O_7$ after pyridine addition at room temperature and (c) $H_2W_2O_7$ after pyridine addition at 80°C.

The intercalation of pyridine into H_2WO_4 was also examined. Powder X-ray diffraction patterns, represented in Figure **4.22**, revealed that (002) reflection peak shifted to lower wavenumber. A new peak was also found at 15.56° attributed to (004) reflection. As indicated in Table **4.3**, the increase in the interlayer spacing indicated that pyridine was successfully intercalated into the layered oxide.

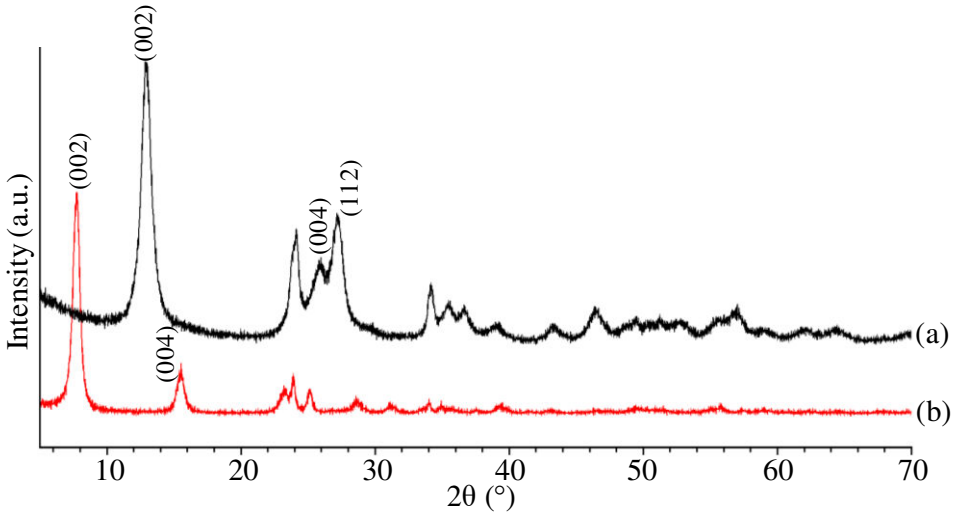

Figure 4.22: PXRD patterns of (a) $H_2WO_4.H_2O$ and (b) $H_2WO_4.H_2O$ after pyridine addition.

4.1.2.2. Quantification

The amount of pyridine intercalated into $HNbMoO_6$ and $HNbWO_6$ layered oxides was estimated using TG data coupled with FT-IR spectroscopy as shown in Figure **4.23** and Figure **4.24** respectively.

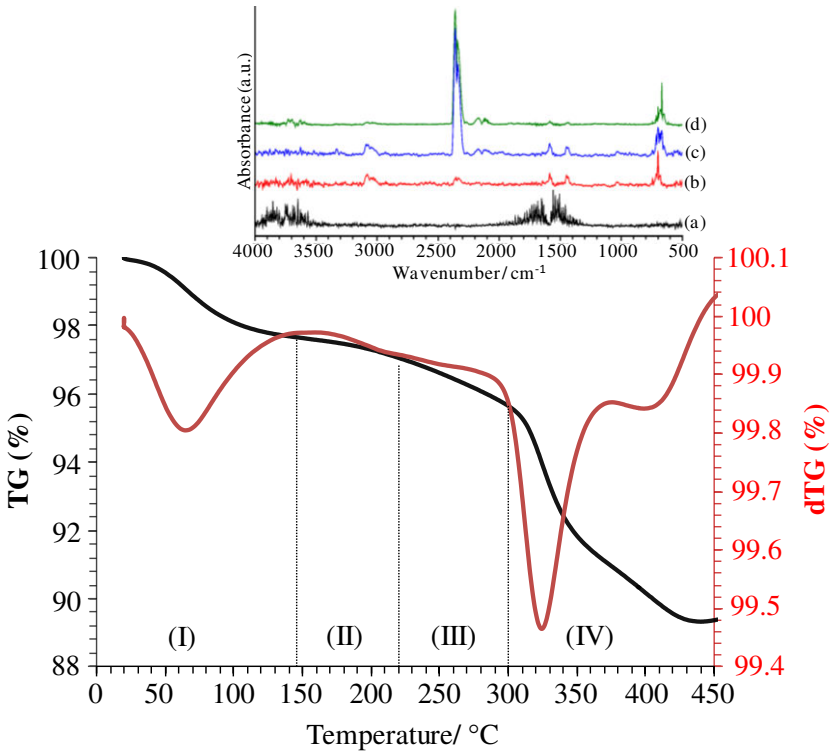

Figure 4.23: Thermogravimetric analysis for pyridine intercalated into $HNbMoO_6.H_2O$. The inset shows the FT-IR spectra measured for the volatile compounds at (a) 45, (b) 219, (c) 262 and (d) 332°C.

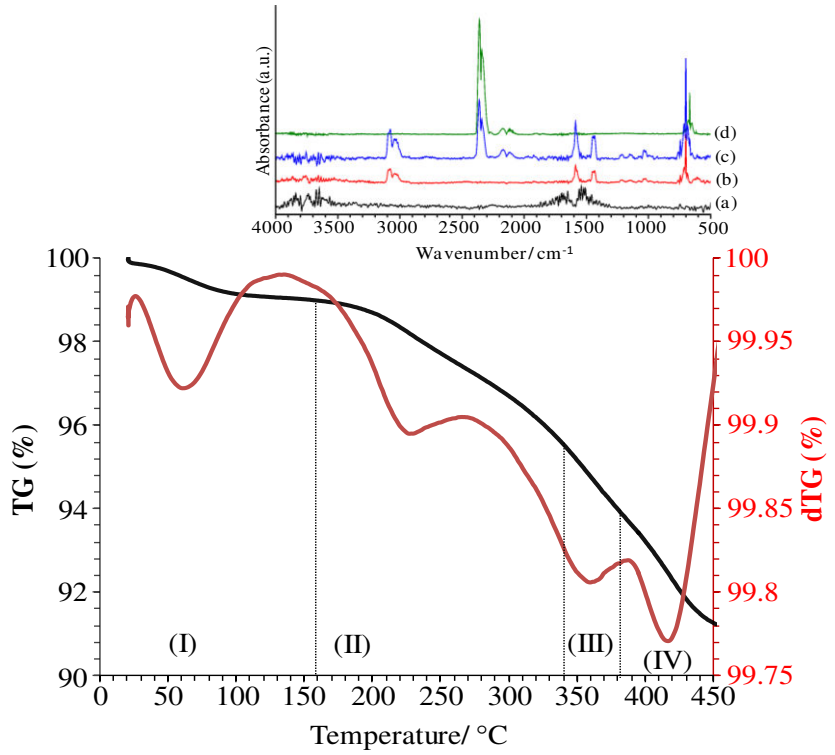

Figure 4.24: Thermogravimetric analysis for pyridine intercalated into $HNbWO_6.0.5H_2O$. The inset shows the FT-IR spectra measured for the volatile compounds at (a) 45, (b) 312, (c) 334 and (d) 420°C.

Using in-situ FT-IR data, four noticeable regions were observed in both cases. IR analysis identified in both cases in each region the evolved gas or gases as follows: water in Region I, pyridine in Region II, pyridine with carbon monoxide and carbon dioxide due to the initiation of pyridine decomposition in Region III and only carbon monoxide and carbon dioxide in Region IV. Similar results were previously encountered with Layered Titanates [24]. The limits were for Region I: 21 - 148°C, Region II: 148 - 220°C, Region III: 220 - 300°C and Region IV: 300 - 450°C in $HNbMoO_6$ case and Region I: 21 - 158°C, Region II: 158 - 341°C, Region III: 341 - 380°C and Region IV: 380 - 450°C in $HNbWO_6$ case, respectively. The layered structure of both samples was destroyed after region IV; this was confirmed by the powder X-ray diffraction data.

Table **4.4** reports the temperature ranges in each region along with their respective mass losses and calculated amounts. The highest amount of pyridine intercalated into $HNbMoO_6$ sample was desorbed in the range 300 - 440°C with a maximum dTG peak at 324°C as indicated in Figure **4.23**. In the case of $HNbWO_6$, the loses were more gradual but overall approximately similar amounts of pyridine were desorbed in the range (150 - 450°C). The easier decomposition of pyridine for $HNbMoO_6$ might indicate a more oxidizing nature compared to $HNbWO_6$.

Table 4.4: Thermogravimetric results of pyridine intercalated into $HNbMoO_6$ and $HNbWO_6$ layered oxides. Δm is the weight loss of water in Region I and of pyridine in Regions II, III and IV respectively. Δn is the calculated amount of water per mol of the dehydrated host oxide in Region I and of pyridine per mol of the dehydrated host oxide in Regions II, III and IV respectively.

	$HNbMoO_6$ + pyridine			$HNbWO_6$ + pyridine		
Region	Temp. Range (°C)	Δm (g)	Δn (mol/mol)	Temp. Range (°C)	Δm (g)	Δn (mol/mol)
I	RT - 148	4.67×10^{-4}	0.42	RT - 158	1.96×10^{-4}	0.23
II	148 - 220	1.17×10^{-4}	0.02	158 - 220	1.24×10^{-4}	0.03
				220 - 300	3.18×10^{-4}	0.08
				300 - 341	2.32×10^{-4}	0.06
III	220 - 300	2.78×10^{-4}	0.06	341 - 380	2.90×10^{-4}	0.07
IV	300 - 450	1.25×10^{-3}	0.26	380 - 450	5.23×10^{-4}	0.14
		$n_{\text{total pyridine (II+III+IV)}} = 0.34$			$n_{\text{total pyridine (II+III+IV)}} = 0.38$	

4.1.2.3. Spectroscopic characterization of intercalation

Raman spectroscopy was used in the liquid phase to monitor the acidic sites in the interlayers when they are accessible in the liquid phase.

By contrast to the results encountered with $HNbMoO_6$ and $HNbWO_6$ layered oxides, upon adding pyridine to $H_2W_2O_7$, no changes were encountered on the Raman spectra, Figure **4.25**. Bands due to $H_2W_2O_7$ and pyridine simply added to each other with no shift in the original bands of the host solid or appearance of new peaks. These results confirmed the absence of interaction or intercalation between pyridine and $H_2W_2O_7$ as was already observed with PXRD data. This also implies that eventual outer acidic sites located at the crystal surface and not in the interlayers are unable to protonate pyridine, either too weak or too scarce.

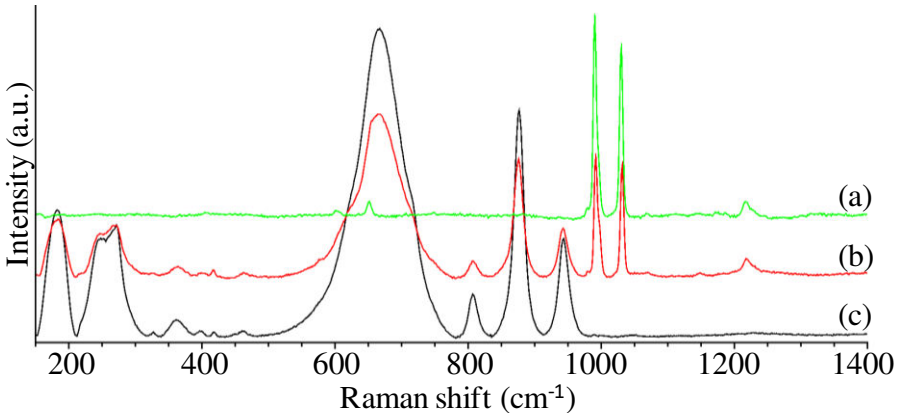

Figure 4.25: Raman spectra of (a) Pyridine, (b) $H_2W_2O_7$ + pyridine and (c) $H_2W_2O_7$.

Unlike $H_2W_2O_7$, changes are expected with Raman spectra upon adding pyridine into $HNbMoO_6$ and $HNbWO_6$ layered oxides as intercalation was already confirmed with PXRD analysis. Several modifications were indeed observed in the spectra of the host solids $HNbMoO_6$ and $HNbWO_6$ respectively (Figure **4.26**).

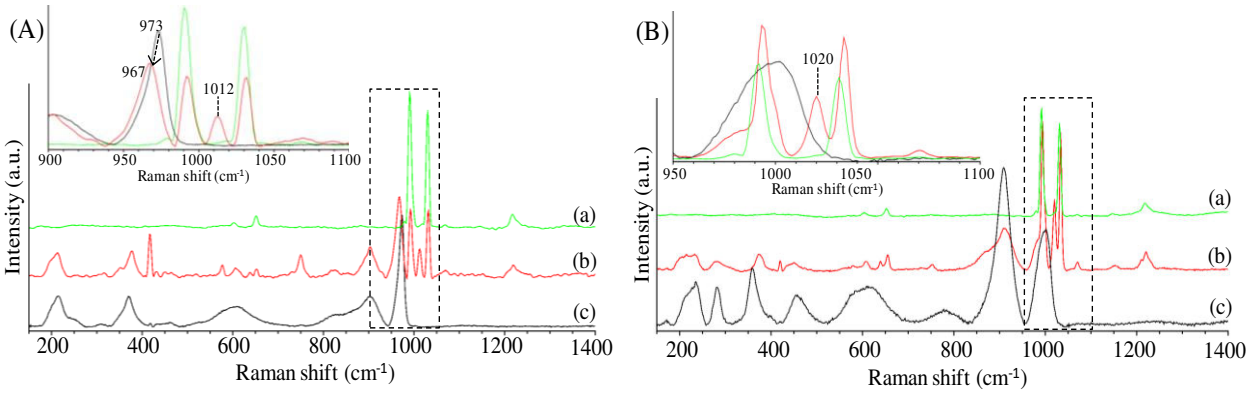

Figure 4.26: Raman spectra of (a) pyridine, (b) protonated sample + pyridine and (c) protonated sample for (A) $HNbMoO_6$ and in (B) $HNbWO_6$. The inset shows the enlargement in the region 800 - 1100 cm^{-1}.

Liquid pyridine is observed by Raman spectroscopy at 991 and 1031 cm^{-1}. These bands are due respectively to the ν_1 and ν_{12} modes of ring-breathing vibrations ν(CCN) [23]. They have been shown to shift depending on the acid sites coordinated to pyridine, notably the ν_1 mode which can shift from 990 to 1030 cm^{-1} depending on the material and the type of acidity, Brønsted or Lewis [22]. In presence of $HNbMoO_6$, in addition to the peaks due to liquid pyridine, new peaks developed at 1001 and 1012 cm^{-1}. In the case of $HNbWO_6$ these peaks were at ca. 1000 and 1020 cm^{-1}. Peaks around 996 - 1005 cm^{-1} were attributed to H-bonded pyridine by Ferwerda et al. [22] while Brønsted and Lewis acid sites should lead to bands respectively in the range 1006 - 1015 and 1016 - 1028 cm^{-1}. Nevertheless these boundaries are indicative and also depend on other aspects like the pyridine coverage on the surface. In view of the similar intrinsic characteristics of $HNbMoO_6$ and $HNbWO_6$, it is unlikely that they show a different type of acidity. Both are expected to show Brønsted acidity. To prove this, the pre-intercalated samples with pyridine were characterized using the IR spectroscopy. 5 % of the latter powdered samples were thoroughly mixed with 95 % KBr and pressed into pellets (20 mg, 2 cm^2 area), then their IR spectra, represented in Figure **4.27**, were recorded using a Nicolet Nexus 5700 spectrometer equipped with an MCT detector. Results revealed the presence of peaks situated at 1634, 1534 and 1486 cm^{-1}, respectively, attributed to the ring-stretching mode of pyridinium ions interacting with Brønsted acid sites [26]. In addition to that, another peak encountered at 1607 - 1609 cm^{-1} was observed that is associated to the ring-stretching mode of hydrogen-bonded pyridine [26]. However, bands at 1450 cm^{-1} due to pyridine interacting with Lewis acid sites did not exist in both cases.

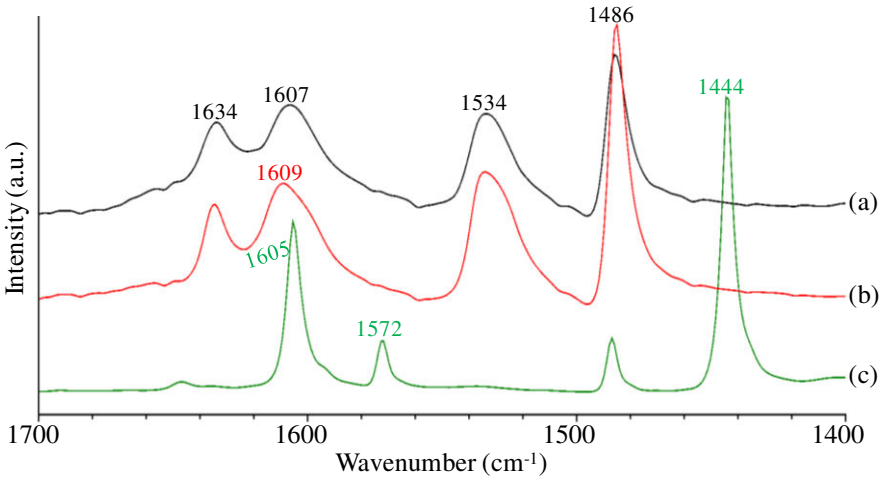

Figure 4.27: IR spectra of (a) $HNbMoO_6$ + pyridine, (b) $HNbWO_6$ + pyridine and (c) H_2WO_4 + pyridine.

Noteworthy, bands at ca. 1014 cm^{-1} were observed by Raman spectroscopy of pyridine for HY zeolite [22] and sulfated zirconia [27]. This could indicate a comparable acidity for $HNbMoO_6$ and a higher Brønsted acidity for $HNbWO_6$. Therefore, this methodology allows the direct titration of the acidic sites in the interlayer. In parallel to the development of this band, the stretching band of Mo=O shifted from 973 to 967 cm^{-1} and that of W=O from 991 to 981 cm^{-1} respectively (Figure **4.26**). Meanwhile it is noteworthy that no such shift was observed for the ν(Nb=O) vibration at ca. 900 cm^{-1}. Therefore, the stronger Brønsted acidity able to protonate pyridine can be found in the vicinity of W=O or Mo=O sites. Stronger acidic sites are thus more likely to be associated with the Mo(W)=O environment. By contrast, protons in the vicinity of Nb=O bonds are likely weaker and can only interact with stronger bases like alkylamines, inducing in that case the shift of the Nb=O bonds.

Similarly to $HNbMoO_6$ and $HNbWO_6$ layered oxides, adding pyridine into H_2WO_4 revealed several changes. As represented in Figure **4.28**, peaks at 959 and 675 were red shifted to 938 and 639 cm^{-1} respectively, with a simultaneous increase in the intensity of the former peak and decrease in the intensity of the latter one. The bands of liquid pyridine also shifted from 990 and 1031 to 993 and 1035 cm^{-1} respectively in addition to the presence of a new peak developed at 1015 cm^{-1} between the latter two. This can be attributed to the interaction between the pyridine and (W-O) from the lattice host. To determine whether pyridine interacted with available Brønsted or Lewis acidic sites, the sample was characterized by Fourier transform infrared spectroscopy. Results, represented in Figure **4.27**, revealed the presence a very strong IR band at 1444 cm^{-1} with a weak band at 1572 cm^{-1} attributed to pyridine adsorbed on Lewis acid sites [28]. A weak adsorption band at 1486 cm^{-1}

attributed to pyridinium ions interacting with Brønsted acid sites [28] was also observed. Consequently, since no evidence of bands at 1535 and 1635 cm^{-1} (characteristics of Brønsted acidity [26]) and stronger peaks due to Lewis acid sites were observed, therefore, almost all acidic sites are Lewis acid.

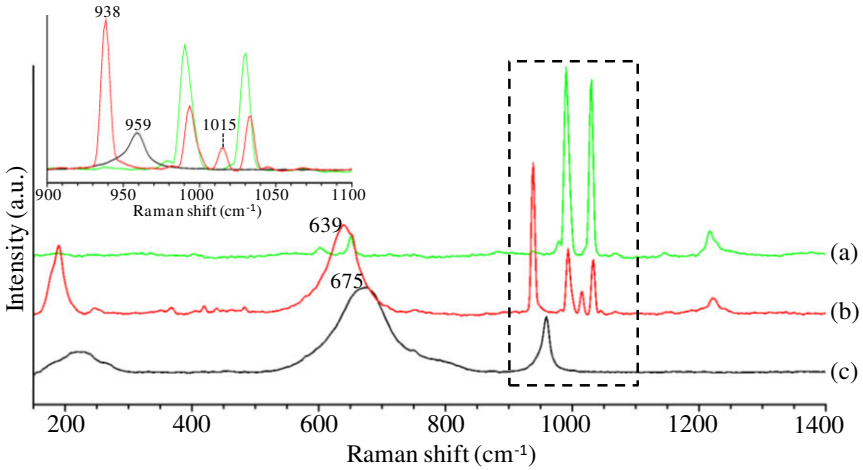

Figure 4.28: Raman spectra of (a) pyridine, (b) H_2WO_4 + pyridine and (c) H_2WO_4. Inset shows the enlargement in the region 900 - 1100 cm^{-1}.

As a conclusion, in view of the basicities of pyridine (pk_b = 8.82) and n-alkylamines (pk_b = 3.35-3.40), it can be inferred that the basicity of pyridine is not large enough to interact with $H_2W_2O_7$ acidic sites and thus cannot intercalate. Its protonic sites are thus weakly acidic. Conversely, the successful intercalation of pyridine into $HNbMoO_6$, $HNbWO_6$ and H_2WO_4 interlayers implies that their acid sites are thus sufficiently strong.

4.2. Novel Phases

Similar characterization methods were carried out with the newly synthesized mixed Nb/W layered oxides. However, among novel oxides, the protonated form of $Bi_{17}Nb_3W_6O_{51}$ (hereafter noted H-$Bi_{17}Nb_3W_6O_{51}$) is the only oxide studied here as it is the only sample that was successfully protonated as discussed previously in chapter three.

4.2.1. n-alkylamine intercalation

The intercalation of butylamine and octylamine into H-$Bi_{17}Nb_3W_6O_{51}$ layered oxide, was first characterized by Raman spectroscopy in the liquid phase. Then the samples were

dried and intercalation was monitored using PXRD analysis. Figure **4.29-32** represent the Raman spectra of H-$Bi_{17}Nb_3W_6O_{51}$ after adding butylamine and octylamine respectively.

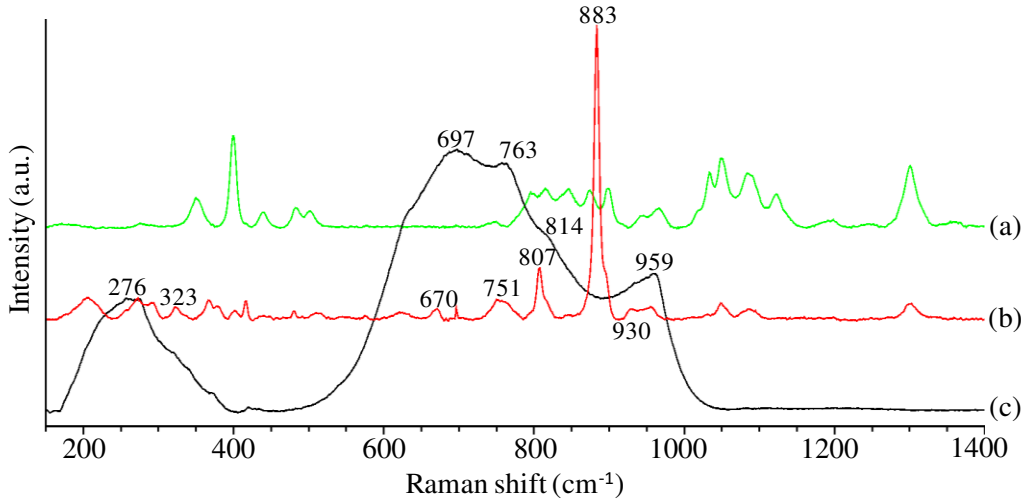

Figure 4.29: Raman spectra of (a) butylamine, (b) H-$Bi_{17}Nb_3W_6O_{51}$ + butylamine and (c) H-$Bi_{17}Nb_3W_6O_{51}$.

Upon adding butylamine into H-$Bi_{17}Nb_3W_6O_{51}$, several changes were encountered as represented in Figure **4.29**. Bands situated at 959, 814, 763, 697 and 276 cm^{-1} decreased dramatically and new peaks situated at 930, 883, 807, 751, 670, 323 and 272 cm^{-1} appeared. Simultaneously, the peaks of amine were also affected, Figure **4.30**, where peaks attributed to NH_2 antisymmetric and symmetric bands of pure butylamine situated at 3379 and 3326 cm^{-1} decreased in intensity and a new band located at 3090 cm^{-1} emerged. Similar results were encountered upon adding octylamine into H-$Bi_{17}Nb_3W_6O_{51}$, both at the level of the solid and at the level of octylamine (Figure **4.31** and Figure **4.32**).

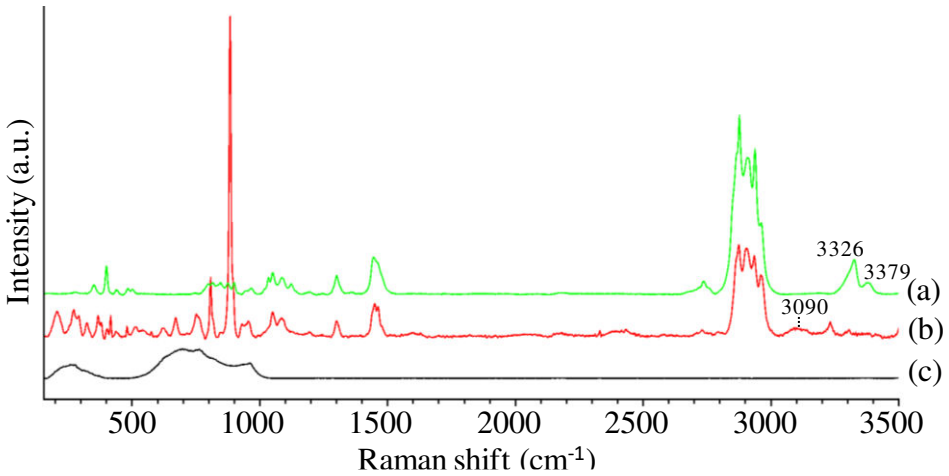

Figure 4.30: Full range Raman spectra (200 - 3500 cm^{-1}) of (a) butylamine, (b) H-$Bi_{17}Nb_3W_6O_{51}$ + butylamine and (c) H-$Bi_{17}Nb_3W_6O_{51}$.

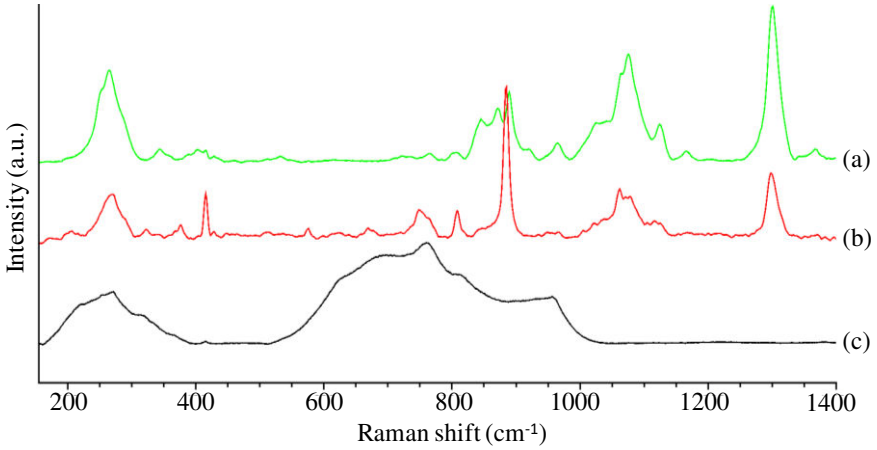

Figure 4.31: Raman spectra of (a) octylamine, (b) H-$Bi_{17}Nb_3W_6O_{51}$ + octylamine and (c) H-$Bi_{17}Nb_3W_6O_{51}$.

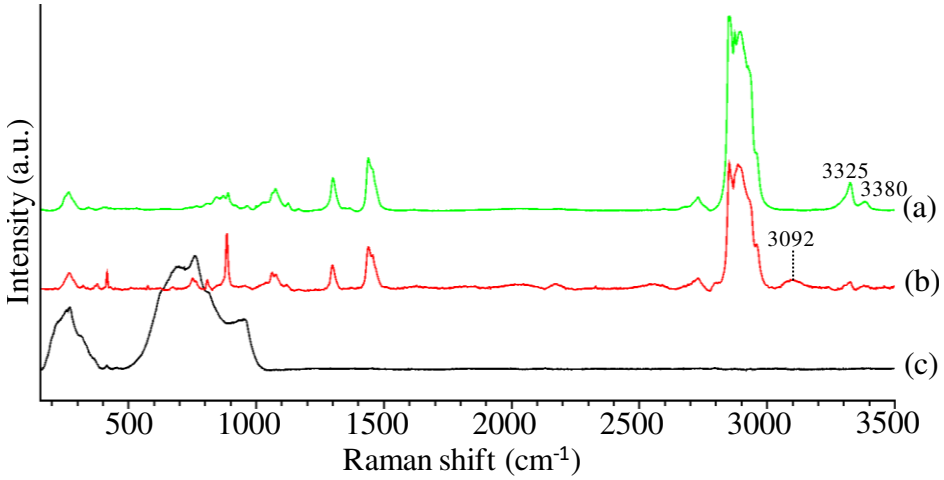

Figure 4.32: Full range Raman spectra (200 - 3500 cm^{-1}) of (a) octylamine, (b) H-$Bi_{17}Nb_3W_6O_{51}$ + octylamine and (c) H-$Bi_{17}Nb_3W_6O_{51}$.

When comparing the n-alkylamines intercalation results into the newly mixed (Nb/W) layered oxide with those of $H_2W_2O_7$ and H_2WO_4, similar results were achieved. All samples upon intercalation showed characteristic bands at approximately same wavenumber (883, 811, 323 and 272 cm^{-1}), Figure **4.33**. Additionally, the same behaviour was encountered with the amine bands. Consequently, one can deduce that upon intercalating n-alkylamines into the protonated H-$Bi_{17}Nb_3W_6O_{51}$ layered oxide, the resultant compound is constructed of alternating stacking n-alkylammonium bilayers and most importantly of single W-O octahedral layers.

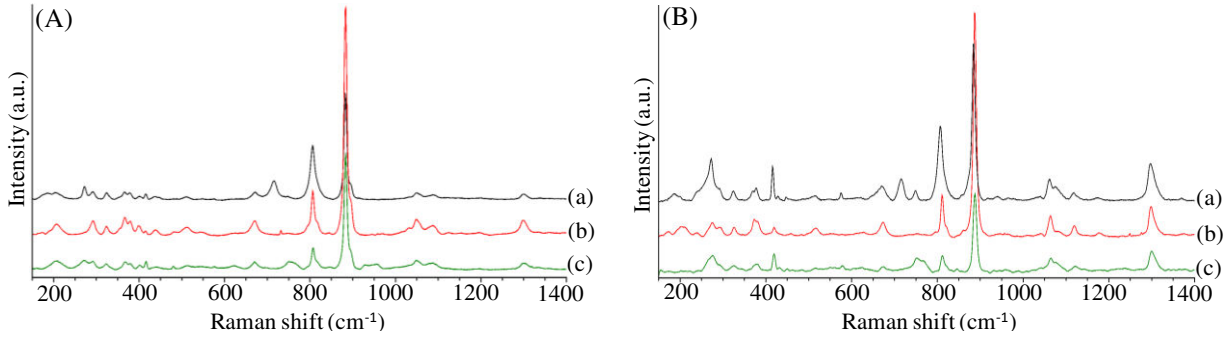

Figure 4.33: Raman spectra of (a) $H_2W_2O_7$, (b) H_2WO_4 and (c) H-$Bi_{17}Nb_3W_6O_{51}$ after (A) butylamine and (B) octylamine intercalation.

In addition to Raman spectroscopy, PXRD analysis was performed to monitor the structural changes of layered oxide upon n-alkylamines addition and also to confirm the process of intercalation.

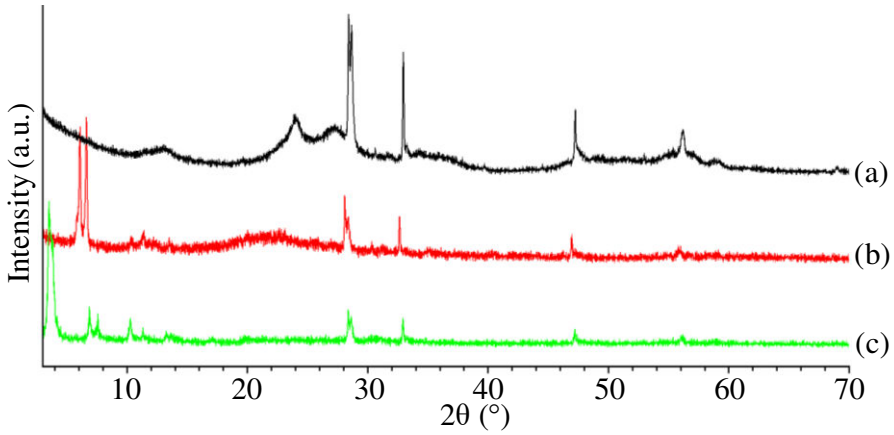

Figure 4.34: PXRD patterns of (a) parent H-$Bi_{17}Nb_3W_6O_{51}$ before intercalation and after intercalation with (b) butylamine and (c) octylamine.

Upon intercalating n-alkylamines into H-$Bi_{17}Nb_3W_6O_{51}$, several changes in the PXRD patterns were observed (Figure **4.34**). The broad peaks of the parent oxide situated at 13, 24 and 27º totally disappeared and the intense sharp peaks at 28-29, 32, 47 and 56º decreased in intensity. Additionally, two very close new intense peaks appeared at low 2θº angle regions. It suggests the intercalation of n-alkylamines into H-$Bi_{17}Nb_3W_6O_{51}$ layered oxide with the presence of two intercalates having a close but different interlayer d-spacing (Table **4.5**). The number of the latter diffraction peaks increased with the number of carbon atoms of the n-alkyl chain.

Table 4.5: Estimated interlayer spacing for H-$Bi_{17}Nb_3W_6O_{51}$ layered oxide before and after n-alkylamines intercalation.

Compound	d-interlayer (Å)
H-$Bi_{17}Nb_3W_6O_{51}$	6.74(2)
H-$Bi_{17}Nb_3W_6O_{51}$ + butylamine	Phase 1: 14.11(3) Phase 2: 12.98(3)
H-$Bi_{17}Nb_3W_6O_{51}$ + octylamine	Phase 1: 25.96(4) Phase 2: 23.83(5)

4.2.2. Pyridine intercalation

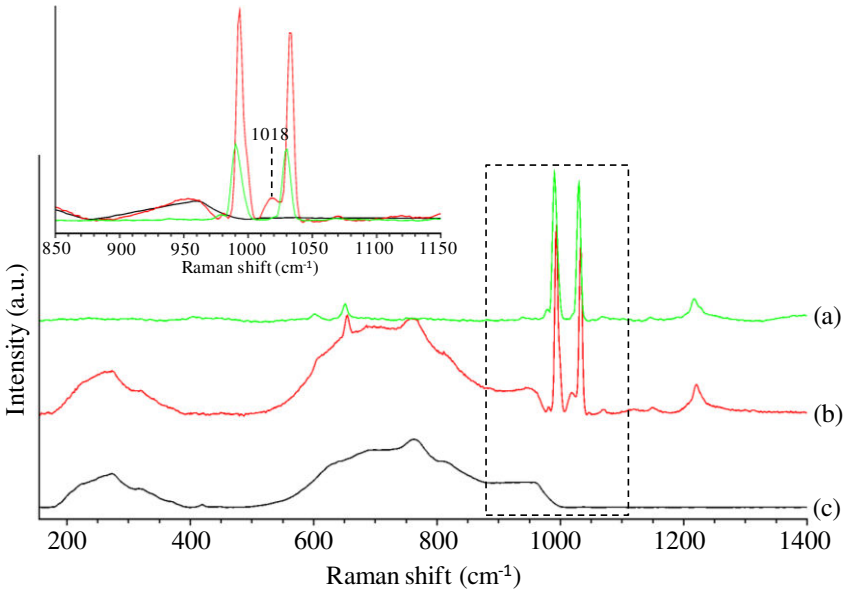

Figure 4.35: Raman spectra of (a) pyridine, (b) H-$Bi_{17}Nb_3W_6O_{51}$ + pyridine and (c) H-$Bi_{17}Nb_3W_6O_{51}$. Inset shows the enlargement in the region 850 - 1150 cm^{-1}.

To monitor the acidity of the newly protonated layered oxide; the intercalation process of pyridine was examined. Noteworthy, due to the similarity of the structure of $Bi_{17}Nb_3W_6O_{51}$ layered oxide to that of Bi_2WO_6, changes in the Raman spectra were expected. After adding a few drops of liquid pyridine into the parent oxide, the ν(W=O) band slightly shifted from 959 to 953 cm^{-1} (Figure **4.35**). Also, peaks of liquid pyridine shifted from 990 and 1031 to 993 and 1033 cm^{-1} respectively and a new one emerged between the peaks of pure liquid pyridine situated at 1018 cm^{-1}. To understand what type of acidity we encounter in this case, the pre-intercalated sample was characterized by FT-IR spectroscopy (Figure **4.36**). Results indicated the presence of a weak band at 1445 cm^{-1} attributed to pyridine adsorbed on Lewis acid sites [26, 28] however, strong IR bands situated at 1486, 1537 and 1634 cm^{-1} assigned to the ring-stretching modes of pyridinium ions interacting with Brønsted acid sites [26, 28] were encountered. Consequently, the FTIR data revealed that almost all acidic sites are attributed to the Brønsted acidity.

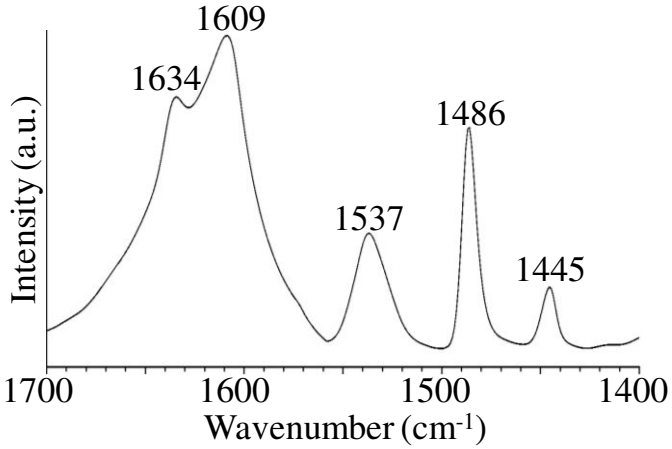

Figure 4.36: IR spectra of H-$Bi_{17}Nb_3W_6O_{51}$ + pyridine.

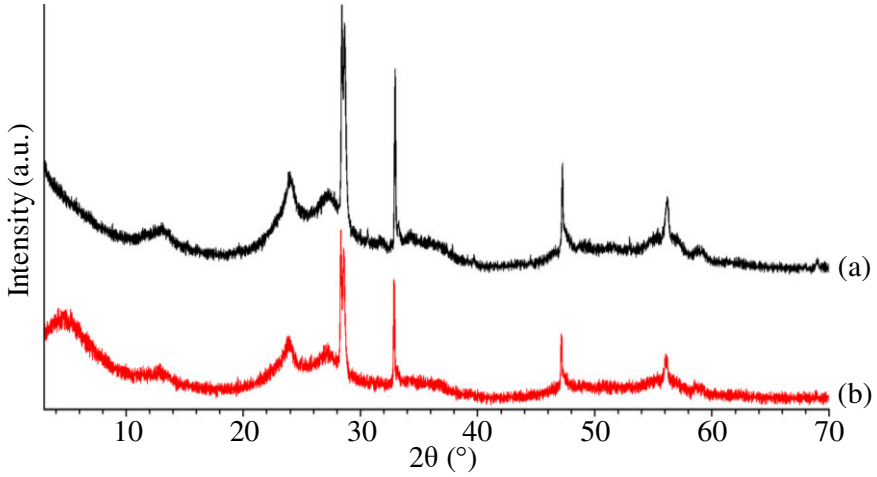

Figure 4.37: PXRD patterns of (a) parent H-$Bi_{17}Nb_3W_6O_{51}$ and (b) after pyridine addition.

PXRD patterns, represented in Figure **4.37**, indicated that upon adding pyridine into H-$Bi_{17}Nb_3W_6O_{51}$, most peaks were found at the same position. However, only one new peak at low 2θº angle region was observed situated at 4.82º associated with an increase in the d-interlayer spacing as confirmed in Table **4.6**. These results might indicate that the intercalation of pyridine into the interlayers was successfully achieved.

Table 4.6: Estimated interlayer spacing for H-$Bi_{17}Nb_3W_6O_{51}$ layered oxide before and after pyridine intercalation.

Compound	d-interlayer (Å)
H-$Bi_{17}Nb_3W_6O_{51}$	6.74(2)
H-$Bi_{17}Nb_3W_6O_{51}$ + pyridine	~15.4

4.3. Intercalation of biomass related compounds (n-alcohols and hexanediol) into layered oxides

This part will be devoted to the investigation of $HNbMoO_6$, $HNbWO_6$ and $H_2W_2O_7$ layered oxides intercalating with 2,5-hexanediol and primary n-alkyl alcohols with a chain length ranging between two to eight carbon atoms. These organic bases are interesting as they pave the way to understand the catalytic activity of all layered oxides for biomass conversion as will be discussed later in details in Chapter 5.

4.3.1. Intercalation monitoring at ambient temperature

4.3.1.1. Structural characterization

The intercalation process into layered oxides was monitored at room temperature using Raman spectroscopy in the liquid phase, where, n-alcohols and diols were added dropwise to the layered oxides and kept together for up to two months to examine the process of intercalation. After that, the samples were dried and characterized using powder X-ray diffraction to monitor the influence of organic bases intercalation on the structure of the

layered oxides. First we will go through PXRD results to investigate if intercalation had taken place, then we will examine the Raman spectroscopic results.

Figure **4.38**, Figure **4.39** and Figure **4.40** represent respectively the powder X-ray diffraction patterns of $HNbMoO_6$, $HNbWO_6$ and $H_2W_2O_7$ interacting with n-alcohols (n = 2, 3, 4, 6 and 8) and 2,5-hexanediol.

In case of $HNbMoO_6$ layered oxide, several modifications were encountered upon adding n-alcohols and diol, as indicated in Figure **4.38**. First, in case of short chain alcohols (ethanol, propanol, and butanol), their PXRD patterns revealed that the peak at low 2θ° angle region, attributed to (00l) reflection, was situated at similarly same position to that of the protonated hydrated layered oxide associated with a very slight increase in the interlayer spacing as indicated in Table **4.7**. In case of longer chain alcohols, the peak shifted to lower angles as the number of carbon atom in the alcohol chain increases. This was associated with an increase in the inyterlayer spacing.

Particularly, in case of octanol, PXRD pattern refinement revealed the presence of several sharp intense (00l) reflection peaks at low 2θ° angle regions characterized by regular reduced intensities that is characteristic of an ordered layered structure. This behaviour was similar to that encountered upon intercalating n-alkylamines into $HNbMoO_6$ as discussed at the beginning of this chapter, where upon intercalating long chain molecules into the layered oxides not only the interlayer spacing is increased but also the order of the layered structure is enhanced.

In all cases, (110) reflection peak situated at ≈ 27° remain unchanged indicating that no structural changes had taken place upon alcohol or diol intercalation. Therefore, these results revealed that with short chain alcohols a very low interlayer expansion had taken place, which becomes more significant with longer chain alcohols.

Table 4.7: Interlayer spacing for $HNbMoO_6$ before and after n-alcohols and diol intercalation at room temperature.

Compound	d-interlayer (Å)
$HNbMoO_6.H_2O$	13.15(1)
$HNbMoO_6.H_2O$ + ethanol	13.15(1)
$HNbMoO_6.H_2O$ + propanol	13.17(1)
$HNbMoO_6.H_2O$ + butanol	13.25(5)
$HNbMoO_6.H_2O$ + hexanol	Phase 1: 14.12(4) Phase 2: 15.03(3)
$HNbMoO_6.H_2O$ + octanol	27.25(5)
$HNbMoO_6.H_2O$ + 2,5-hexanediol	15.26(3)

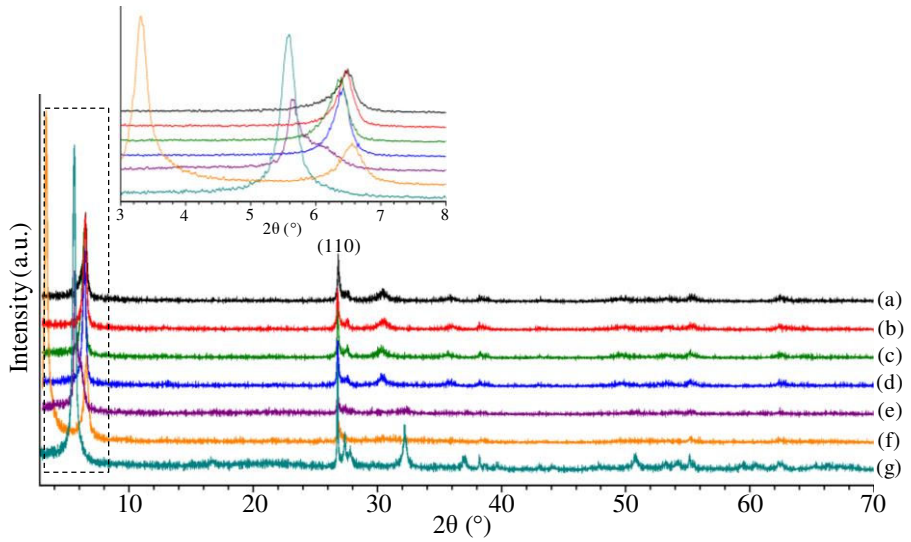

Figure 4.38: PXRD patterns of (a) parent hydrated $HNbMoO_6$ and after n-alcohol and diol intercalation at R.T.: (b) ethanol, (c) propanol, (d) butanol, (e) hexanol, (f) octanol and (g) 2,5-hexanediol. The inset shows the enlargement in the region: 3 - 8°.

For $HNbWO_6$ layered oxide, upon adding ethanol, (001) reflection peak of the hydrated parent oxide shifted very slightly (from 7.05 to 6.98°), however with propanol, butanol and hexanol, two peaks at low 2θ° angle regions were observed, as represented in Figure **4.39**. The first peak was situated at a similar position as that of the parent $HNbWO_6$

layered oxide and the second one was situated at lower positions. The latter shifted to lower angles as the length of the alcohol chain increases and it is characterized by a moderate intensity in case of propanol and butanol or a very low intensity with hexanol.

The partial intercalation or its absence might be attributed to the difference between the kinetic diameter of n-alcohol molecules and the gallery height of the layered oxide. He et al. [29] indeed previously reported that the esterification process of n-butanol into $HNbWO_6$ layered oxide showed lower activity than $HNbMoO_6$ since the kinetic diameter of n-butanol molecules (0.50 nm) is close to the gallery height of layered $HNbWO_6$ (value calculated here: 0.496 nm) which limits the diffusion into the interlayer region and might hamper the complete intercalation. Nevertheless, a peak at lower angles was sometimes observed revealing successful intercalation. This might be due to the effect of time i.e. as the intercalates are kept for a long period with the layered oxide, they will be more susceptible to sweep into the interlayers thus inducing the shift of the peak and therefore increasing the interlayer spacing. In case of octanol, the presence of reflection peaks at low 2θ° angle regions attributed to (00l) reflections revealed similar behaviour as encountered with $HNbMoO_6$ layered oxide. Note that, He et al. [29] reported that the value of gallery height is 0.496 nm.

On the contrary, in case of hexanediol, even after keeping it for a long time (up to two months), (001) reflection peak did not shift at all, indicating that no intercalation had taken place. This might be due to the structure of 2,5-hexanediol, as it contains two OH groups and it is not a linear alkyl chain as the other tested alcohols, thus hindering its capability to squeeze into the interlayers of the layered oxide.

The d-interlayer spacing of $HNbWO_6$ layered oxide after adding n-alcohols and 2,5-hexanediol were estimated by LeBail fitting of the PXRD patterns (Table **4.8**).

Table 4.8: Interlayer spacing for $HNbWO_6$ before and after n-alcohols and diol intercalation at room temperature.

Compound	d-interlayer (Å)
$HNbWO_6.1.5\ H_2O$	12.73(3)
$HNbWO_6.1.5\ H_2O$ + ethanol	12.78(1)
$HNbWO_6.1.5\ H_2O$ + propanol	Phase 1: 12.83(3) Phase 2: 13.71(3)
$HNbWO_6.1.5\ H_2O$ + butanol	Phase 1: 12.87(2) Phase 2: 14.22(2)
$HNbWO_6.1.5\ H_2O$ + hexanol	Phase 1: 12.79(2) Phase 2: 21.47(2)
$HNbWO_6.1.5\ H_2O$ + octanol	26.05(3)
$HNbWO_6.1.5\ H_2O$ + 2,5-hexanediol	12.81(1)

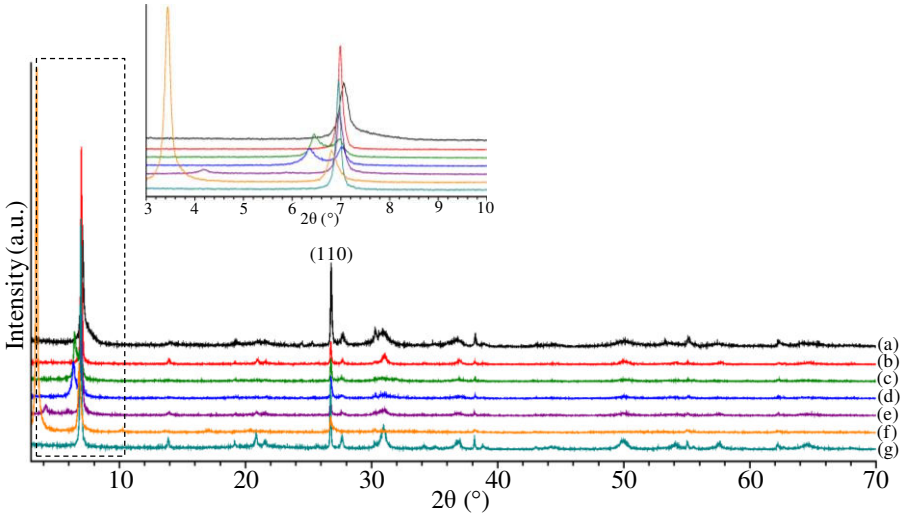

Figure 4.39: PXRD patterns of (a) parent hydrated $HNbWO_6$ and after n-alcohol and diol intercalation at R.T.: (b) ethanol, (c) propanol, (d) butanol, (e) hexanol, (f) octanol and (g) 2,5-hexanediol. The inset shows the enlargement in the region: 3 - 10 °.

In contrast to the latter results, neither n-alcohols nor 2,5-hexanediol were able to intercalate into the interlayer region of $H_2W_2O_7$ layered oxide, since the same PXRD patterns, indicated in Figure **4.40**, were encountered before and after the guest species addition. Neither

any of the PXRD diffraction peaks shifted to lower or higher wavenumbers, nor any new peaks were observed.

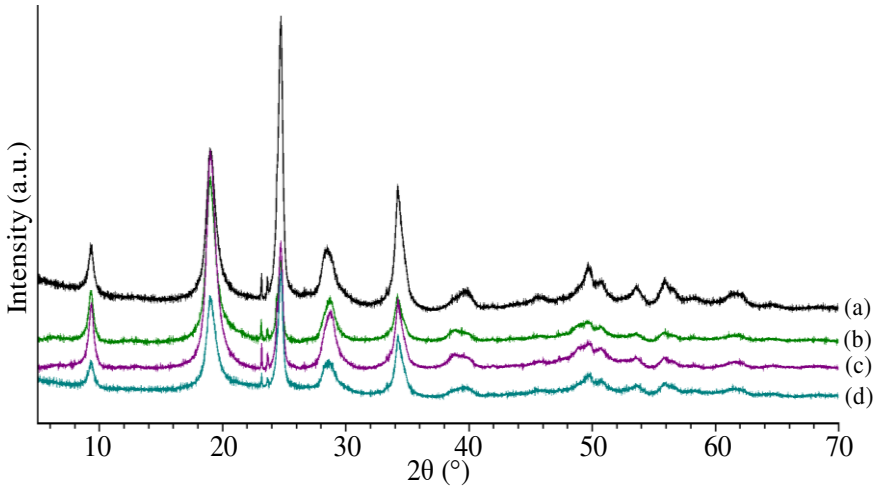

Figure 4.40: PXRD patterns of (a) parent $H_2W_2O_7$ and after n-alcohol and diol intercalation at R.T.: (b) propanol, (c) hexanol and (d) hexanediol.

4.3.2. Intercalation monitoring at higher temperatures

As the extent of intercalation was not significant at ambient temperature in both cases ($HNbMoO_6$ and $HNbWO_6$ layered oxides) due to the small increase in the d-interlayer spacing or due to the presence of more than one peak at low 2θ° angle regions, therefore, the process of intercalation will be examined at higher temperatures: at 60, 80 and 100°C.

The guest species were reacted with the host layered oxides for 24 hours at 60 - 80 or 100°C in an oil bath, then the resultant compounds were dried and characterized using powder X-ray diffraction and then by Raman spectroscopy in the solid Phase.

4.3.2.1. Structural characterization of $HNbMoO_6$

As indicated in Figure **4.41**, upon adding the guest species into the host solid at 60°C, only one peak at low 2θ° angle region was encountered for all alcohols. This peak shifted to lower angles as the number of carbon atoms of the alcohol chain increases and therefore d-interlayer spacing increases (Table **4.9**). In this case the shift in the (001) reflection peak was much higher than those achieved at ambient temperature. Therefore, higher temperature facilitates the penetration of n-alcohols into the interlayer region of $HNbMoO_6$. At the same time, no structural changes were observed for the a and b parameters. Noteworthy, in case of octanol there was no presence of several sharp intense peaks at low 2θ° angle regions as

previously illustrated, this might be attributed to the lower intercalation amount as it was kept for a shorter time which did not induce the enhancement in the order of the layered structure or due to the effect of temperature (the vibrational motion inhibits the ordering of the structure).

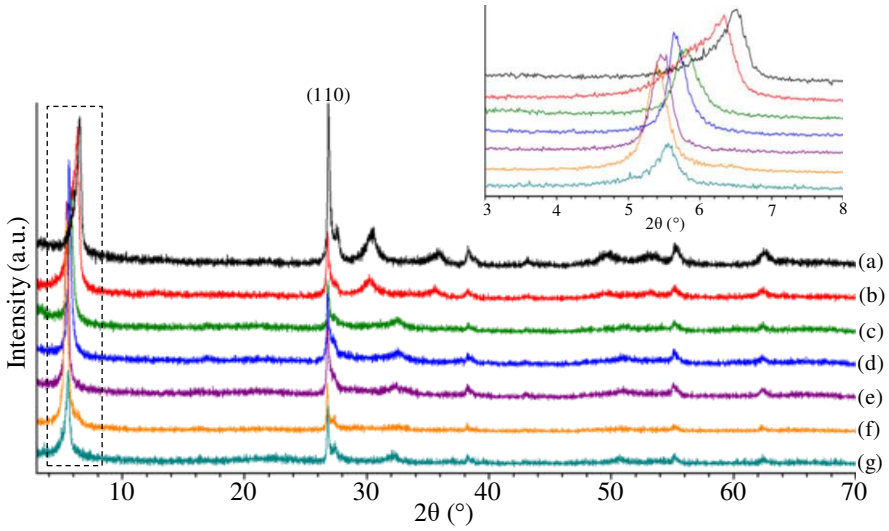

Figure 4.41: PXRD patterns of (a) parent $HNbMoO_6$ and after alcohol and diol addition at 60°C: (b) ethanol, (c) propanol, (d) butanol, (e) hexanol, (f) octanol and (g) 2,5-hexanediol. The inset shows the enlargement in the region: 3 - 8 °.

Table 4.9: Interlayer spacing for $HNbMoO_6$ before and after n-alcohols and diol intercalation at 60°C.

Compound	d-interlayer (Å)
$HNbMoO_6.H_2O$	13.81(5)
$HNbMoO_6.H_2O$ + ethanol	14.08(6)
$HNbMoO_6.H_2O$ + propanol	15.5(3)
$HNbMoO_6.H_2O$ + butanol	15.89(6)
$HNbMoO_6.H_2O$ + hexanol	16.35(5)
$HNbMoO_6.H_2O$ + octanol	16.5(2)
$HNbMoO_6.H_2O$ + 2,5-hexanediol	16.02(7)

Similar experimental procedures and characterization methods were carried out to monitor and evaluate the intercalation process into layered oxides at 80 and 100°C. With these two cases not all alcohols were examined, only the extreme ones (lowest and highest

alcohol chains, propanol and octanol) were involved. 2,5-hexanediol intercalation was also monitored.

Adding n-alcohols and hexanediol into $HNbMoO_6$ layered oxide at 80 and 100°C, shifted the (001) diffraction peak to lower angles confirming the process of intercalation. In case of propanol, the interlayer spacing increase was similar at all temperatures. However, with octanol and 2,5-hexanediol, the latter parameter increases with temperature. This revealed that short chain alcohols can be totally intercalated already at low temperatures, in the contrary, with longer chain alcohols, higher temperature is required. In all cases (110) diffraction peak did not encounter any significant shift suggesting that upon intercalation no major structural changes occurred.

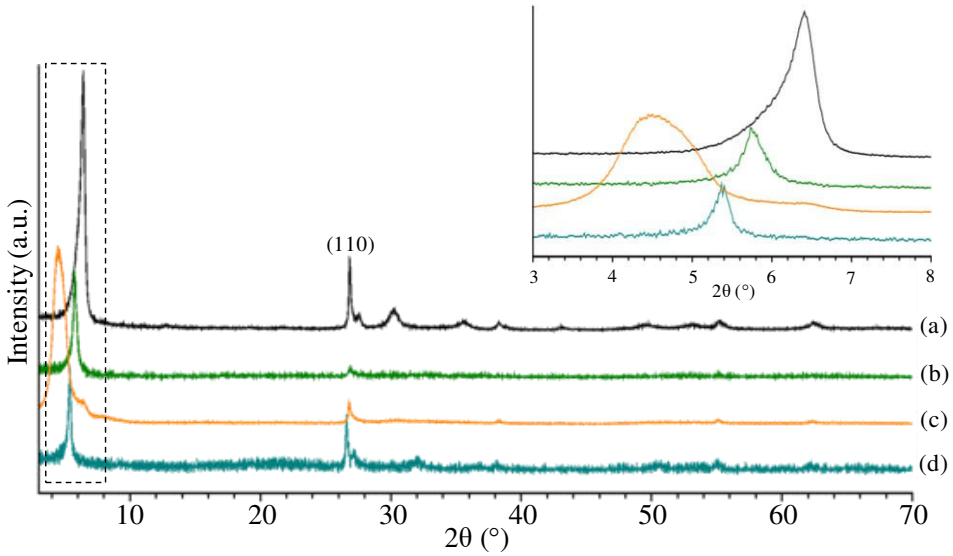

Figure 4.42: PXRD patterns of (a) parent $HNbMoO_6$ and after n-alcohols and diol addition at 80°C: (b) propanol, (c) octanol and (d) hexanediol. The inset shows the enlargement of the region 3 - 8 °.

Table 4.10: Interlayer spacing for $HNbMoO_6$ before and after n-alcohols and diol intercalation at 80°C.

Compound	d-interlayer (Å)
$HNbMoO_6.H_2O$	13.98(3)
$HNbMoO_6.H_2O$ + propanol	15.6(2)
$HNbMoO_6.H_2O$ + octanol	19.4(2)
$HNbMoO_6.H_2O$ + 2,5-hexanediol	16.2(5)

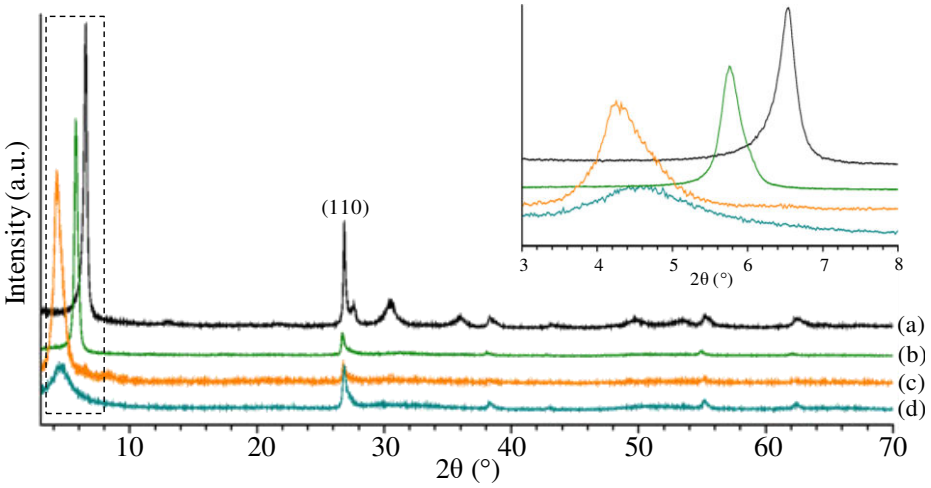

Figure 4.43: PXRD patterns of (a) parent $HNbMoO_6$ and after n-alcohols and diol addition at 100°C: (b) propanol, (c) octanol and (d) hexanediol. The inset shows the enlargement of the region 3 - 8 °.

Table 4.11: Interlayer spacing for $HNbMoO_6$ before and after n-alcohols and diol intercalation at 100°C.

Compound	d-interlayer (Å)
$HNbMoO_6.H_2O$	13.71(3)
$HNbMoO_6.H_2O$ + propanol	15.55(3)
$HNbMoO_6.H_2O$ + octanol	21.3(2)
$HNbMoO_6.H_2O$ + 2,5-hexanediol	19.5(2)

4.3.2.2. Structural monitoring of $HNbWO_6$

The intercalation of n-alcohols and 2,5-hexanediol into $HNbWO_6$ layered oxide at the three temperatures was also examined. The PXRD patterns after intercalation at 60, 80 and 100°C are represented in Figure **4.44**, Figure **4.45** and Figure **4.46** respectively.

At 60°C, powder X-ray diffraction patterns of $HNbWO_6$ after intercalate addition, Figure **4.44**, show that in case of ethanol and propanol, the (001) diffraction peak shifted to lower positions associated with an increase in the interlayer spacing (Table **4.12**). In case of butanol, two peaks were observed, one is situated at higher $2\theta^o$ value with respect to that of

the parent oxide probably due to the dehydration of the sample since its position is similar to that of the anhydrous $HNbWO_6$ and the other peak is shifted to lower 2θ° value inducing increase in the interlayer spacing. With hexanol, several peaks were encountered, one observed at higher 2θ° value similar to the one encountered with the anhydrous $HNbWO_6$, another one at same position to that of the hydrated parent oxide and two others at lower 2θ° values revealing that the intercalates are intercalated differently in the interlayer space giving rise to two interlayer spacing. With octanol and hexanediol no intercalation was observed as the (001) peak remained at the same position to that of the parent layered oxide. As previously, (110) diffraction peak indicated no change in its position revealing no structural changes upon ethanol and propanol intercalation.

Consequently, the complete intercalation of propanol is clearly eased by the higher temperature. However, this remains insufficient with longer chain alcohols for which the kinetic diameter may be greater than the actual gallery height of the layered oxide.

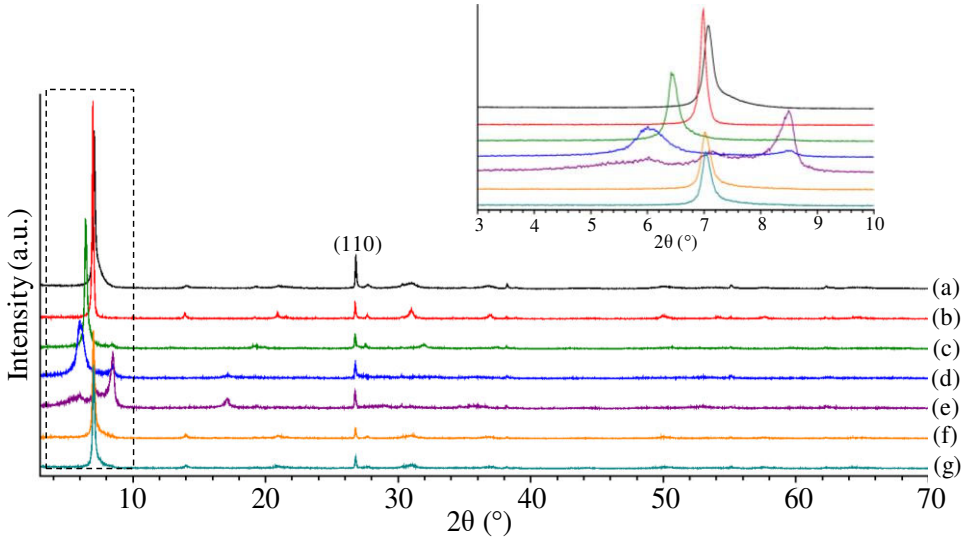

Figure 4.44: PXRD patterns of (a) parent $HNbWO_6$ and after alcohol and diol addition at 60°C: (b) ethanol, (c) propanol, (d) butanol, (e) hexanol, (f) octanol and (g) hexanediol. The inset shows the enlargement of the region 3 - 10 °.

Table 4.12: Interlayer spacing for $HNbWO_6$ layered oxides upon intercalating n-alcohols and 2,5-hexanediol at 60°C.

Compound	d-interlayer (Å)
$HNbWO_6.1.5\ H_2O$	12.71(4)
$HNbWO_6.\ 1.5\ H_2O$ + ethanol	12.80(1)
$HNbWO_6.1.5\ H_2O$ + propanol	13.95(3)
$HNbWO_6.1.5\ H_2O$ + butanol	Phase 1: 10.48(4) Phase 2: 14.34(4)
$HNbWO_6.1.5\ H_2O$ + hexanol	Phase 1: 10.47(2) Phase 2: 12.37(8) Phase 3: 14.5(2) Phase 4: 16.26(5)
$HNbWO_6.1.5\ H_2O$ + octanol	12.77(3)
$HNbWO_6.1.5\ H_2O$ + 2,5-hexanediol	12.78(2)

The intercalation process was also monitored at higher temperatures, at 80 and 100°C and similarly to $HNbMoO_6$, in this part only the extreme alcohol cases were examined (propanol and octanol). 2,5-hexanediol was only monitored at 100°C.

PXRD patterns results revealed that after adding octanol into the layered oxide, either at 80 or 100°C, or 2,5-hexanediol at 100ºC, a very slight shift in the (001) diffraction peak was encountered, similarly to the results at 60°C. Therefore, increasing temperature was not sufficient to facilitate the intercalation process of either octanol or 2,5-hexanediol. However, with propanol as temperature increases, (001) diffraction peak shifted to lower position associated to a higher increase in the interlayer spacing (Table **4.13** and Table **4.14**). Therefore, in this case increasing the temperature only facilitates the intercalation of short chain alcohols into the interlayer regions. Additionally, (110) diffraction peak did not shift at all as was observed with all other cases revealing the preservation of the tetragonal structure.

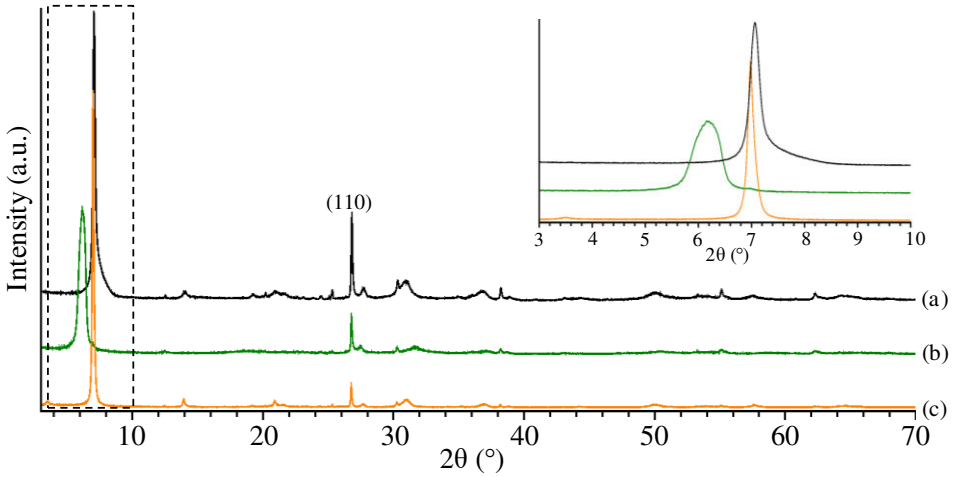

Figure 4.45: PXRD patterns of (a) parent $HNbWO_6$ and after alcohol addition at 80°C: (b) propanol and (c) octanol. The inset shows the enlargement of the region 3 - 10 °.

Table 4.13: Interlayer spacing for $HNbWO_6$ layered oxides upon intercalating propanol and octanol at 80°C.

Compound	d-interlayer (Å)
$HNbWO_6.1.5\ H_2O$	12.78(2)
$HNbWO_6.1.5\ H_2O$ + propanol	14.56(3)
$HNbWO_6.1.5\ H_2O$ + octanol	12.78(1)

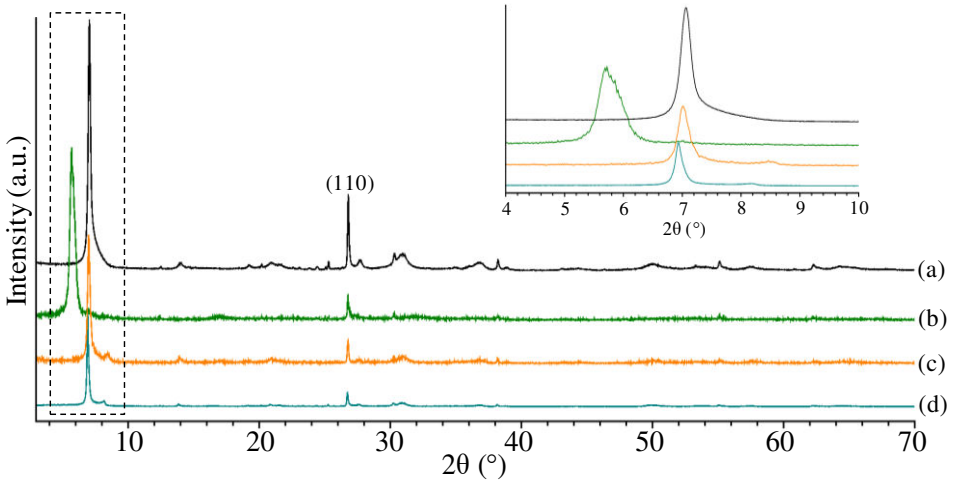

Figure 4.46: PXRD patterns of (a) parent $HNbWO_6$ and after alcohol addition at 100°C: (b) propanol, (c) octanol and (d) 2,5-hexanediol. The inset shows the enlargement of the region 4 - 10 °.

Table 4.14: Interlayer spacing for $HNbWO_6$ layered oxides upon intercalating propanol, octanol and 2,5-hexanediol at 100°C.

Compound	d-interlayer (Å)
$HNbWO_6.1.5\ H_2O$	12.79(2)
$HNbWO_6.1.5\ H_2O$ + propanol	15.58(5)
$HNbWO_6.1.5\ H_2O$ + octanol	12.74(3)
$HNbWO_6.1.5\ H_2O$ + 2,5-hexanediol	12.81(1)

4.3.2.3. Structural monitoring of $H_2W_2O_7$

With $H_2W_2O_7$ layered oxide, no intercalation had taken place either with n-alcohols or 2,5-hexanediol at 60, 80 or 100°C, since identical powder X-ray diffraction patterns were observed. This implies that the outer acidic sites are either too weak or too scarce to allow intercalation.

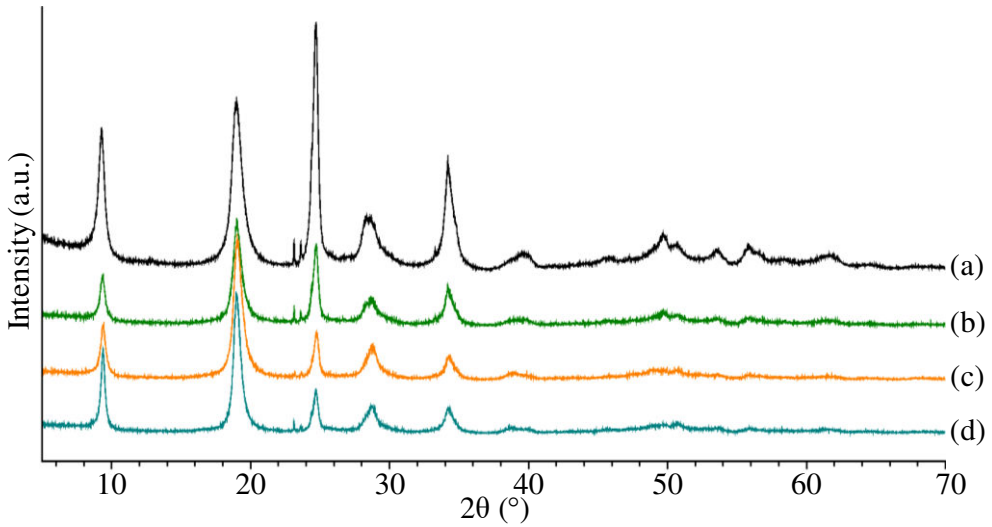

Figure 4.47: PXRD patterns of (a) parent $H_2W_2O_7$ and after alcohol and diol addition at 60°C: (b) propanol, (c) octanol, and (d) hexanediol.

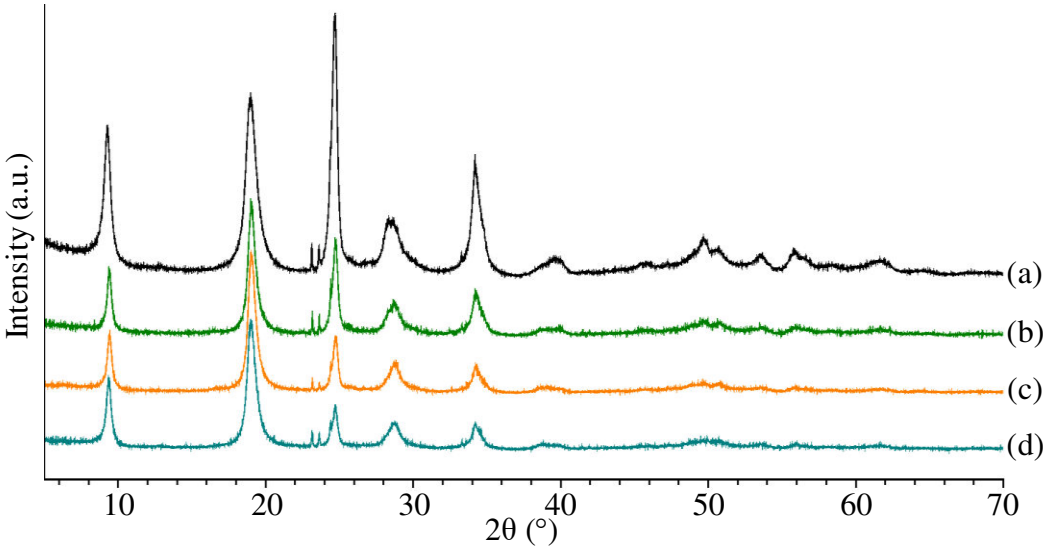

Figure 4.48: PXRD patterns of (a) parent $H_2W_2O_7$ and after alcohol and diol addition at 80°C: (b) propanol, (c) octanol, and (d) hexanediol.

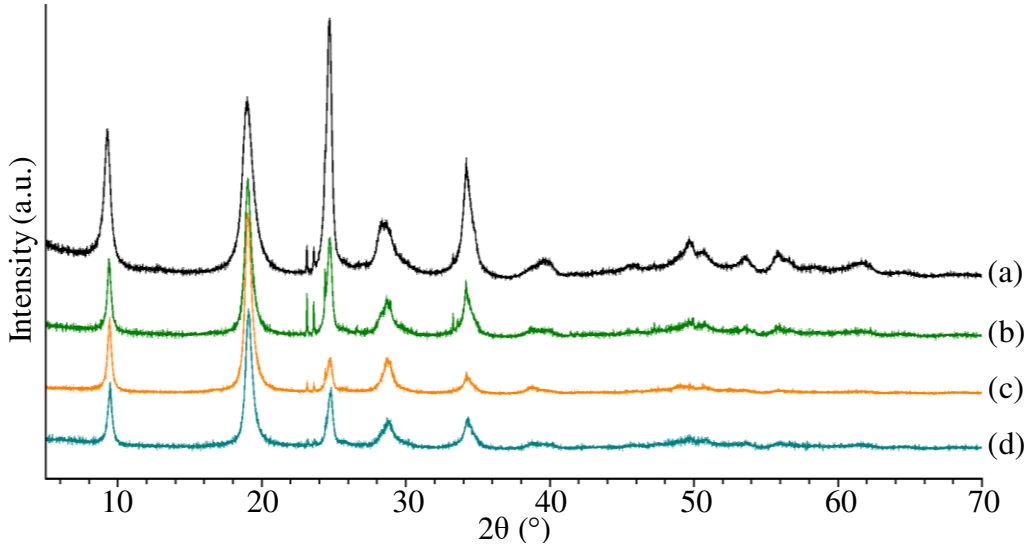

Figure 4.49: PXRD patterns of (a) parent $H_2W_2O_7$ and after alcohol and diol addition at 100°C: (b) propanol, (c) octanol, and (d) hexanediol.

4.3.3. Spectroscopic characterization

Raman spectroscopy in the liquid phase was utilized to monitor and examine the interaction between the guest species (n-alcohols and 2,5-hexanediol) and the host layered oxides ($HNbMoO_6$ and $HNbWO_6$) at room temperature. This technique was also utilized upon adding the guest species into the host layered oxides at higher temperatures, however, since only peaks of liquid were present and no information could be deduced from the solid, the

samples were dried and then Raman in the solid phase was used to characterize the spectra of the intercalated layered oxide.

Figure **4.50** and Figure **4.51**, represents the Raman spectra of $HNbMoO_6$ and $HNbWO_6$ respectively upon adding n-alcohols and 2,5-hexanediol at room temperature. Results revealed that after introducing the guest species into either $HNbMoO_6$ or $HNbWO_6$ layered oxides, a very slight shift in the M=O (M = Mo, W) and Nb=O peak was encountered.

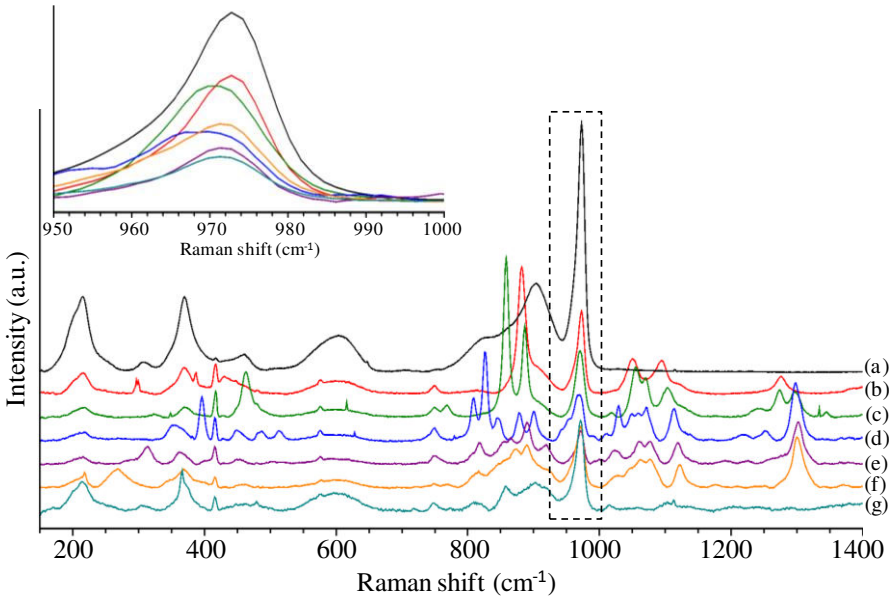

Figure 4.50: Raman spectra of (a) parent $HNbMoO_6$ and after alcohol and diol addition at R.T.: (b) ethanol, (c) propanol, (d) butanol, (e) hexanol, (f) octanol and (g) hexanediol. The inset shows the enlargement of the region 950 - 1000 cm^{-1}.

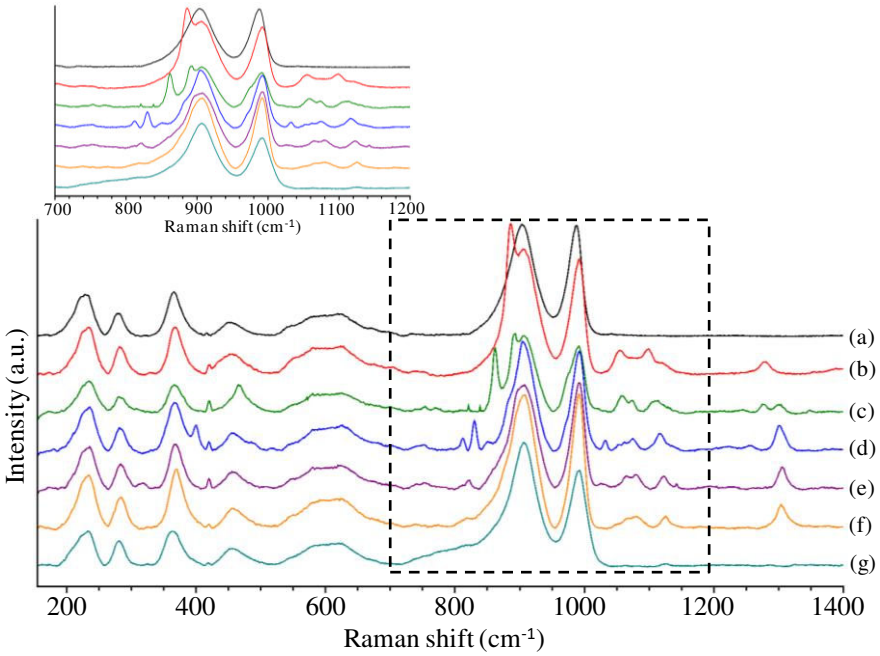

Figure 4.51: Raman spectra of (a) parent $HNbWO_6$ and after alcohol and diol addition at R.T.: (b) ethanol, (c) propanol, (d) butanol, (e) hexanol, (f) octanol and (g) hexanediol. The inset shows the enlargement of the region 700 - 1200 cm^{-1}.

In case of $H_2W_2O_7$ layered oxides, results are represented in Figure **4.52**, no changes were encountered upon adding either n-alcohols or hexanediol. Besides, peaks of the alcohols could hardly be observed. This confirms the PXRD results that no intercalation had taken place.

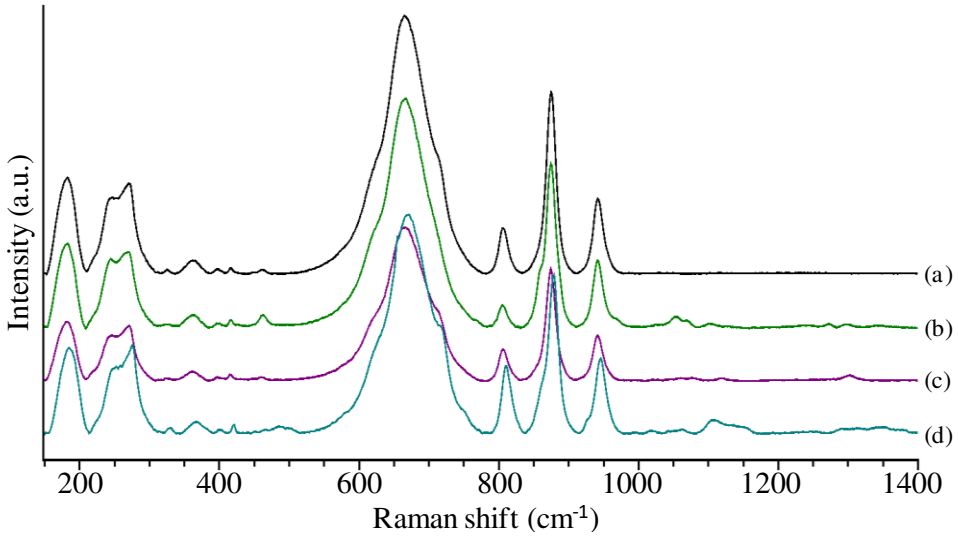

Figure 4.52: Raman spectra of (a) parent $H_2W_2O_7$ and after alcohol and diol addition at R.T.: (b) propanol, (c) hexanol and (d) hexanediol.

The Raman spectra of the resultant powdered samples after n-alcohols and hexanediol addition into $HNbMoO_6$ layered oxide at 60, 80 and 100ºC, were investigated using Raman spectroscopy in the solid phase and results are represented in Figure **4.53**, Figure **4.54** and Figure **4.55**.

Results represented in Figure **4.53**, revealed that adding the guest species into $HNbMoO_6$ layered oxides at 60ºC shifted the (Mo=O) peak into higher wavenumbers (for example in case of ethanol and propanol, the peak shifted from 972 to 984 and 985 cm^{-1} respectively). With hexanediol, two bands for (Mo=O) were more clearly observed at 979 and 1000 cm^{-1}. Two slightly different adsorption sites are likely present. In addition to that, the massif around 800 cm^{-1} was largely modified with a broadening and shift to lower wavenumbers. This must be largely due to the strong perturbation of the ν(Nb=O). Therefore, these results can confirm the interaction between M=O and Nb=O with the OH group from the added guest species.

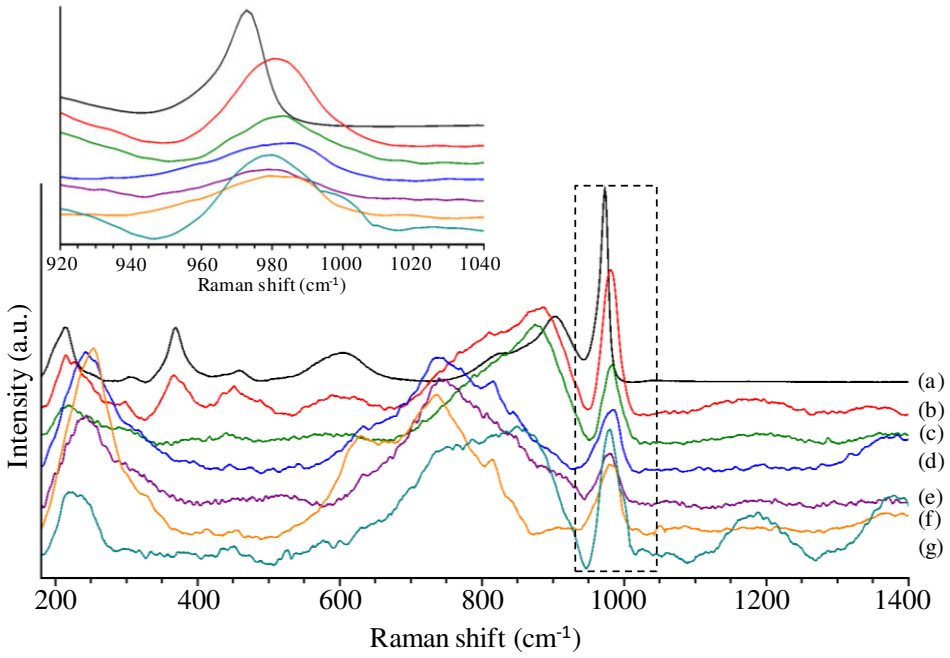

Figure 4.53: Raman spectra of (a) parent $HNbMoO_6$ heated at 60ºC and after alcohol and diol intercalation at 60°C: (b) ethanol, (c) propanol, (d) butanol, (e) hexanol, (f) octanol and (g) hexanediol. The inset shows the enlargement of the region 920 - 1040 cm^{-1}.

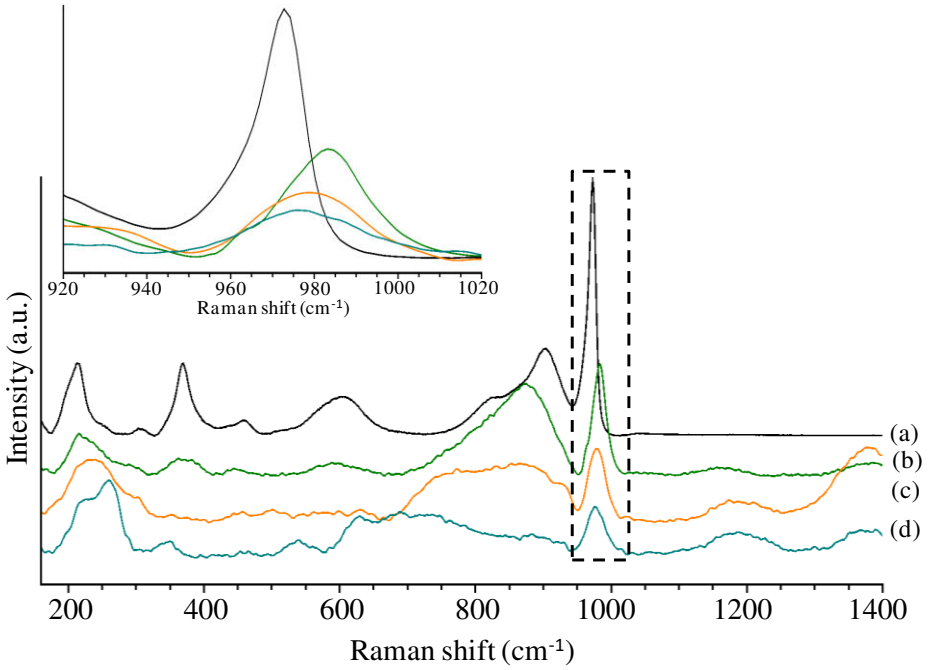

Figure 4.54: Raman spectra of (a) parent $HNbMoO_6$ heated at 80ºC and after alcohol and diol intercalation at 80°C: (b) propanol, (c) octanol and (d) hexanediol. The inset shows the enlargement of the region 920 - 1020 cm^{-1}.

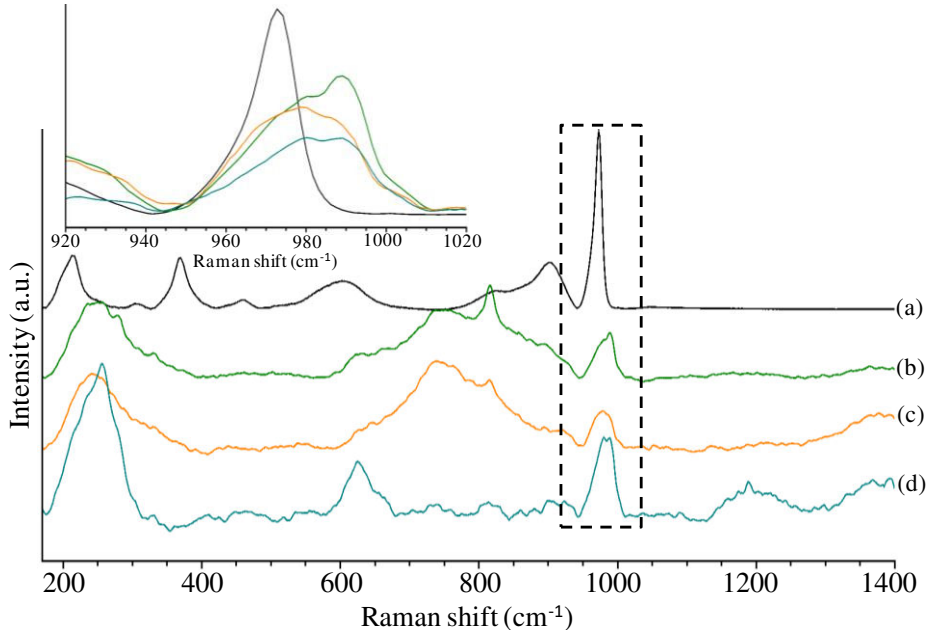

Figure 4.55: Raman spectra of (a) parent $HNbMoO_6$ heated at 100ºC and after alcohol and diol intercalation at 100°C: (b) propanol, (c) octanol and (d) hexanediol. The inset shows the enlargement of the region 920 - 1020 cm^{-1}.

Upon adding the guest species into $HNbMoO_6$ at 80 and 100ºC, similar results were encountered. (Mo=O) shifted to higher wavenumber upon alcohol and diol addition. Two peaks seem present around 980 and 990 cm^{-1} for all n-alcohols, but in presence of the diol

they were more clearly distinguished. The band at 800 cm^{-1} also broadened and shifted to lower wavenumber as already seen with propanol. This noticeable adsorption process guarantees the adsorption of alcohols into the interlayer region.

4.4. Conclusions

In this chapter the intercalation process of N-containing substrates (n-alkylamines and pyridine) was extensively studied and characterized in details for the transition metal layered oxides ($HNbMoO_6$, $HNbWO_6$, $H_2W_2O_7$ and $H_2WO_4.H_2O$) and for the newly synthesized mixed Nb/W oxides. The intercalation of n-alcohols into $HNbMoO_6$, $HNbWO_6$ and $H_2W_2O_7$ layered oxides was also investigated. Powder X-ray diffraction and TGA analysis confirmed the intercalation process while Raman spectroscopy provided information regarding the interaction between the host layered oxides and the guest species.

All examined layered oxides were able to intercalate n-alkylamines. PXRD results indicated that not only the interlayer spacing increased with the number of carbon of n-alkyl chains but also the order of the layered structure enhanced. Raman spectroscopy showed the perturbations of n-alkylamines bands and of the layered solids. For $HNbMoO_6$ and $HNbWO_6$ layered oxides, both (Nb=O) and (Mo,W=O) bonds were affected. For H_2WO_4 and H-$Bi_{17}Nb_3W_6O_{51}$, (W=O) was affected. For $H_2W_2O_7$ and H_2WO_4, the intercalation of n-alkylamines induces the perturbation of the (W=O) bond but this mainly accompanied by a reorganization-dissolution of the double octahedral layers into singles ones.

Pyridine intercalation was also examined since its weaker basicity allows distinguishing between the acidity of the various layered oxides. $H_2W_2O_7$ did not encounter any change in its powder X-ray diffraction pattern or Raman spectra revealing no successful intercalation due to its lower acidity. However, for all other layered oxides, the powder X-ray diffraction results indicated an increase in the interlayer spacing confirming the intercalation process. Raman spectroscopy showed the perturbations in the (M=O) bands and the appearance of a new peak between the bands of the liquid pyridine. For $HNbMoO_6$ and $HNbWO_6$ layered oxides, only (Mo=O) or (W=O) were affected indicating their close location to the protonic acidic sites.

To understand more the catalytic activity of the layered oxides, n-alcohols and diol intercalation was monitored. $H_2W_2O_7$ was not able to intercalate any of the alcohols or diol (no change in the PXRD patterns or Raman spectra). Short chain alcohols were intercalated into $HNbMoO_6$ and $HNbWO_6$ layered oxides, however, longer chain alcohols and diol were fully intercalated into $HNbMoO_6$ while partial or no intercalation was encountered with $HNbWO_6$. This is likely due to the difference in the gallery height. Moreover, powder X-ray results indicated that as increasing temperatures facilitates the intercalation process. Raman

spectroscopy showed that (Mo=O) shifted to higher wavenumber in all cases, also it split into two bands with 2,5-hexanediol due to the presence of two OH functional groups.

4.5. References

1 V. Bhat and J. Gopalakrishnan, *Solid State Ionics*, 1988, **26**, 25–32.

2 D. Chen, T. Li, L. Yin, X. Hou, X. Yu, Y. Zhang, B. Fan, H. Wang, X. Li, R. Zhang, T. Hou, H. Lu, H. Xu, J. Sun and L. Gao, *Mater. Chem. Phys.*, 2011, **125**, 838–845.

3 S. V. Chong, B. Ingham and J. L. Tallon, *Curr. Appl. Phys.*, 2004, **4**, 197–201.

4 G. Lagaly, *Angew. Chemie Int. Ed. English*, 1976, **15**, 575–586.

5 D. Chen and Y. Sugahara, *Chem. Mater.*, 2007, **19**, 1808–1815.

6 C. Tagusagawa, A. Takagaki, S. Hayashi and K. Domen, *J. Am. Chem. Soc.*, 2008, **130**, 7230–7231.

7 R. E. Schaak and T. E. Mallouk, *Chem. Commun.*, 2002, **0**, 706–707.

8 V. Bhat and J. Gopalakrishnan, *J. Solid State Chem.*, 1986, **63**, 278–283.

9 Y. Jing, Q. Pan, Z. Cheng, X. Dong and Y. Xiang, *Mater. Sci. Eng. B Solid-State Mater. Adv. Technol.*, 2007, **138**, 55–59.

10 J. J. C. Teixeira-Dias, L. A. E. Batista de Carvalho, A. M. Amorim da Costa, I. M. S. Lampreia and E. F. G. Barbosa, *Spectrochim. Acta*, 1986, **42**, 589–597.

11 S. Shoval and S. Yariv, *Clays Clays Miner.*, 1979, **27**, 29–38.

12 A. L. Garcia-Ponce, L. Moreno-Real and A. Jiménéz López, *J. Solid State Chem.*, 1990, **87**, 20–28.

13 M. F. Daniel, B. Desbat, J. C. Lassegues, B. Gerand and M. Figlarz, *J. Solid State Chem.*, 1987, **67**, 235–247.

14 M. Boulova and G. Lucazeau, *J. Solid State Chem.*, 2002, **167**, 425–434.

15 S. Vidya, S. Solomon and J. K. Thomas, *J. Mater. Sci. Mater. Electron.*, 2015, **26**, 3243–3255.

16 J. Hanuza, M. Mączka and J. H., van der Maas, *J. Solid State Chem.*, 1995, **117**, 177–188.

17 F. D. Hardcastle and I. E. Wachs, *J. Raman Spectrosc.*, 1995, **26**, 397–405.

18 G. Busca, *Catal. Today*, 1998, **41**, 191–206.

19 G. Busca, *Phys. Chem. Chem. Phys.*, 1999, **1**, 723–736.

20 J. A. Lercher, C. Gründling and G. Eder-Mirth, *Catal. Today*, 1996, **27**, 353–376.

21 P. J. Hendra, I. D. M. Turner, E. J. Loader and M. Stacey, *J. Phys. Chem.*, 1974, **78**, 300–304.

22 R. Ferwerda, J. H. van der Maas and P. J. Hendra, *Vib. Spectrosc.*, 1994, **7**, 37–47.

23 P. J. Hendra, J. R. Horder and E. J. Loader, *J. Chem. Soc. A*, 1971, **0**, 1766–1770.

24 T. Sasaki, F. Izumi and M. Watanabe, *Chem. Mater.*, 1996, **8**, 777–782.

25 D. A. Odink, K. Song and S. M. Kauzlarich, *Chem. Mater.*, 1992, **4**, 906–911.

26 Y. Morita, S. Furusato, A. Takagaki, S. Hayashi, R. Kikuchi and S. T. Oyama, *ChemSusChem*, 2014, **7**, 748–752.

27 M. I. Zaki and A. A. M. Ali, *Colloids Surf A Physicochem Eng Asp.*, 1996, **119**, 39–50.

28 T. Barzetti, E. Selli, D. Moscotti and L. Forni, *J. Chem. Soc., Faraday Trans.*, 1996, **92**, 1401–1407.

29 J. He, Q. J. Li, Y. Tang, P. Yang, A. Li, R. Li and H. Z. Li, *Appl. Catal. A Gen.*, 2012, **443**–**444**, 145–152.

CHAPTER FIVE

DEVELOPMENT OF A TEST REACTION AND RELATION WITH INTERCALATION

This chapter will be devoted to the characterization of the catalytic activity of the layered oxides ($HNbMoO_6$, $HNbWO_6$ and $H_2W_2O_7$) in comparison with other compounds. For this purpose, a new test reaction was developed, the conversion of 2,5-hexanediol into 2,5-dimethyltetrahydrofuran. This reaction was tested in various reaction conditions and the activity of the layered materials was compared to that of common solid acid catalysts, zeolites (H-ZSM-5, H-Beta and H-Y) and Niobic acid. The catalytic performance has been confronted to the structural features of the materials, notably their intercalation behaviour monitored by powder X-ray diffraction and Raman spectroscopy.

5.1. Hexanediol cyclization: a novel test reaction

The potential use of a novel test reaction for layered materials, the cyclodehydration of 2,5-hexanediol, was examined at different reaction conditions (temperature, pressure and various amounts of water). All the results related to catalytic activity were obtained with the assistance of Dr. Moussa Zaarour, a researcher at LCS on the Oxylac Project.

5.1.1. General features and influence of reaction parameters

5.1.1.1. Catalytic conversion over various solid acid catalysts at 120°C

The cyclodehydration reaction of 2,5-hexanediol into both cis- and trans-2,5-dimethyltetrahydrofuran in the liquid phase, Figure **5.1**, was examined using several solid acid catalysts (catalyst/diol ratio = 0.05).

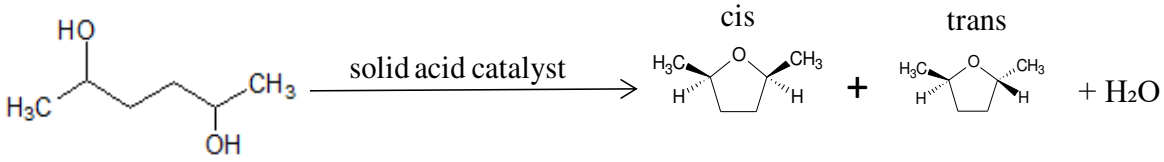

Figure 5.1: Cyclodehydration of 2,5-hexanediol into 2,5-dimethyltetrahydrofuran.

Note that whenever 2,5-dimethyltetrahydrofuran was formed, Gas Chromatography always showed two consecutive peaks attributed to the cis and trans isomers. Both isomers were always obtained with similar ratios. Therefore, in all the following results, selectivity will be given considering the sum of both cis and trans isomers.

First of all, it should be noted that, without any catalyst no reaction occurred upon heating 2,5-hexanediol at 120°C for 24 hours. Gas chromatography did not show neither the desired product (2,5-dimethyltetrahydrofuran) nor any other secondary products. Therefore, the catalytic activity was examined for several catalysts ($HNbMoO_6$, Nb_2O_5 and different zeolites).

In case of $HNbMoO_6$ layered oxide, a fast consumption was observed from the very beginning of the reaction (15% after 5 minutes), then the conversion increased till it reached 50% after 15 minutes and 95% after 60, 100 and 150 minutes (Figure **5.3(A)** and Table **5.1**). This high catalytic activity was associated with a high selectivity, where 88% of the desired product (cis and trans 2,5-dimethyltetrahydrofuran) was achieved after 15 minutes. Then

selectivity increased and reached 95% after 60 minutes and remained constant beyond this time (Figure **5.3(B)**).

In liquid phase, the leaching of active species can occur. Therefore, in order to verify that the catalytic activity of $HNbMoO_6$ was truly heterogeneous, 2,5-hexanediol was reacted over $HNbMoO_6$ for 15 minutes at 120°C followed by extraction of the catalyst and heating the reaction mixture for prolonged period (Figure **5.2**). After 15 minutes in presence of $HNbMoO_6$, the conversion reached 47% with 92% selectivity. From this point and the catalyst withdrawal, no further formation of product was observed beyond this time, conversion was maintained at 47%, thus indicating that the catalyst stays intact in its solid form and no dissociation had taken place during the reaction process.

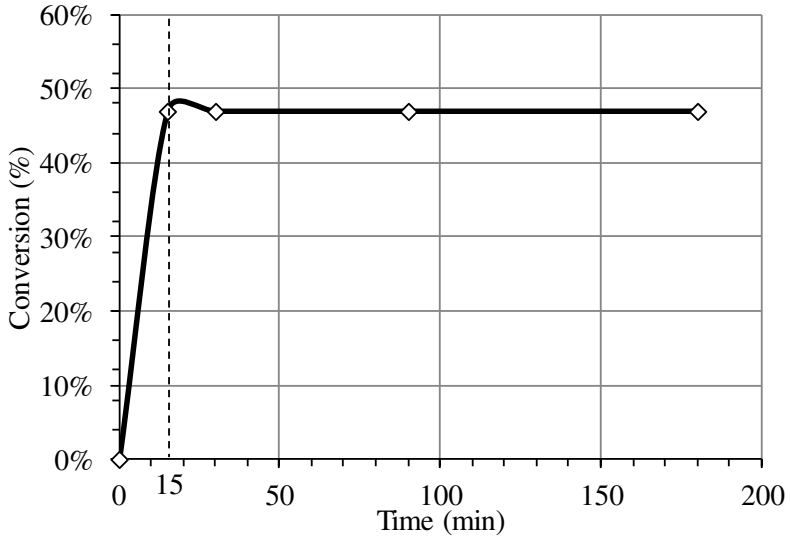

Figure 5.2: Conversion of 2,5-hexanediol over layered $HNbMoO_6$ catalyst at 120°C as a function of time before and after catalyst extraction.

The activity of $HNbMoO_6$ layered oxide was compared with Niobium oxide (Nb_2O_5) and several commercial zeolites (H-Y, H-Beta and H-ZSM-5, where H- stands for protonated zeolites). Noteworthy, all these catalysts were activated before utilization as mentioned in the experimental part. The cyclodehydration results of 2,5-hexanediol at 120ºC under solvent free conditions using a variety of solid acid catalysts are represented in Figure **5.3** and Table **5.1**.

Results indicated that with Nb_2O_5 no products were formed (neither the desired product nor any other secondary products). However, H-Y zeolite revealed the lowest activity (17% after 60 minutes with no additional conversion after 150 minutes). A slightly higher, but still moderate conversion was achieved with H-ZSM-5 (23% after 60 minutes that remained

constant after 150 minutes). On the contrary, a relatively high conversion was encountered with H-Beta zeolite (61% after 60 minutes that increased and reached to 96% after 150 minutes). Consequently, the order of the active catalysts can be represented as follows: $HNbMoO_6$ > H-Beta > H-ZSM-5 > H-Y > Nb_2O_5. In addition to that, all active catalysts showed high selectivity. H-Beta and H-Y zeolites exhibited 100% selectivity, whereas, H-ZSM-5 showed 82% selectivity from the beginning till the end of the reaction. Therefore, the selectivity can be represented in the following order: H-Beta (100%) = H-Y (100%) > $HNbMoO_6$ (95%) > H-ZSM-5 (82%).

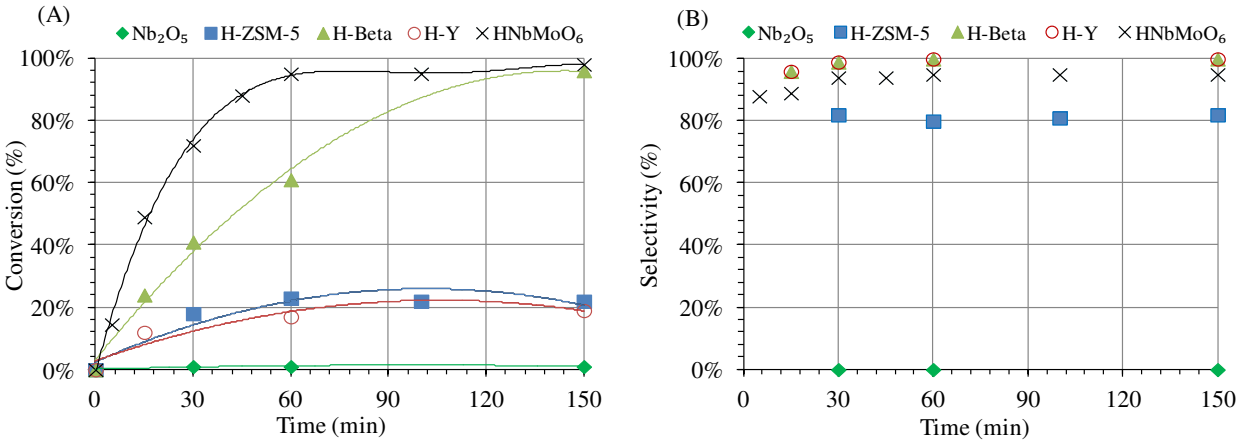

Figure 5.3: (A) Catalytic conversion and (B) selectivity of 2,5-hexanediol at 120°C as a function of time over various solid acid catalysts.

Table 5.1: Conversion of 2,5-hexanediol and selectivity after 60 minutes towards formation of 2,5-dimethyltetrahydrofuran using various solid acid catalysts.

Catalyst	Conversion	Selectivity	Yield
$HNbMoO_6$	95%	95%	90%
[b]H-Beta	61%	100%	61%
[b]H-ZSM-5	23%	82%	19%
[b]H-Y	17%	100%	17%
[c]Nb_2O_5	1%	0%	0%

Reaction conditions: m(hexane-2,5-diol) = 1 g, m(catalyst) = 55.6 mg, T = 120°C, t = 60 min. Catalysts activated for 6h at [b] 550°C, [c] 250°C.

Therefore, results displayed the effectiveness of this test to evaluate the catalytic activity of several solid acid catalysts as only the desired product was formed, dimethyltetrahydrofuran with a very high selectivity.

5.1.1.2. Influence of temperature and pressure

The performance of $HNbMoO_6$ layered oxide was evaluated at different reaction temperatures (80, 100, 120 and 140°C). Results represented in Figure **5.4** and Figure **5.5**, revealed that conversion rapidly increased at 140 and 120°C, 81% and almost total conversion (95%) was achieved after 30 and 60 minutes, respectively. However, at lower temperatures, conversion steadily increased till it reached 95% after 210 and 2640 minutes at 100 and 80°C, respectively. Additionally, high selectivities (85 to 100%) were measured at all temperatures and were maintained even at high conversion.

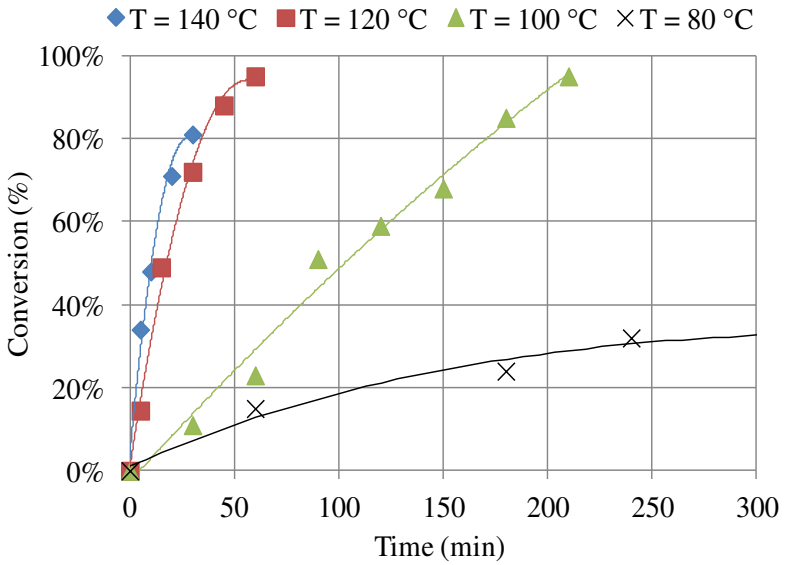

Figure 5.4: Conversion of 2,5-hexanediol as a function of elapsed time at different reaction temperatures.

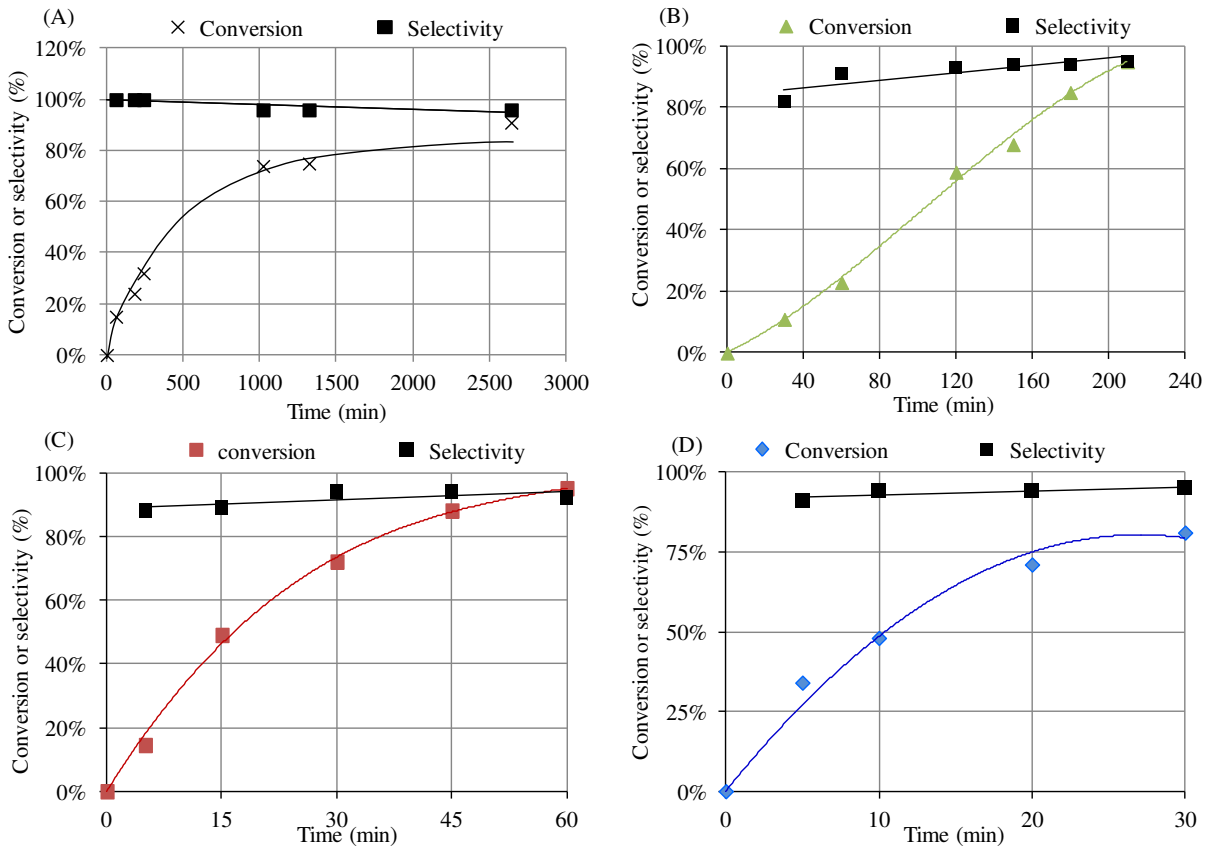

Figure 5.5: Conversion of 2,5-hexanediol and selectivity towards 2,5-dimethyltetrahydrofuran over $HNbMoO_6$ at (A) 80, (B) 100, (C) 120 and (D) 140°C respectively.

50% conversion of the desired product, represented in Table **5.2,** was achieved after 520 minutes upon heating the diol with $HNbMoO_6$ layered oxide at 80°C. Then, as temperature increased to 100, 120 and 140°C, the time required decreased to 110, 18 and 10 min., respectively. In addition to that, the selectivity towards the formation of the desired product was high and similar at all temperatures (ranging between 90 - 94%).

Table 5.2: Time required to convert 50% of 2,5-hexanediol over $HNbMoO_6$ at various temperatures and selectivity towards formation of 2,5-dimethyltetrahydrofuran at this time.

Temperature (°C)	t½ (min)	Selectivity at t½ (%)
80	520	90
100	110	93
120	18	92
140	10	94

Initial rate constants were evaluated from the slope of the initial linear part at each temperature (data taken until 70%). The activation energy for 2,5-hexanediol cyclodehydration over $HNbMoO_6$ was then estimated from the Arrhenius plot shown in Figure **5.6**. The calculated activation energy was 78.5 $kJ.mol^{-1}$. It is smaller than that reported for the cyclodehydration of 1,4-butanediol over $HNbMoO_6$ (99 $kJ.mol^{-1}$) [1] which can be explained by the stabilization of the partially positive secondary carbon holding the protonated hydroxide by the terminal CH_3 located at α-position.

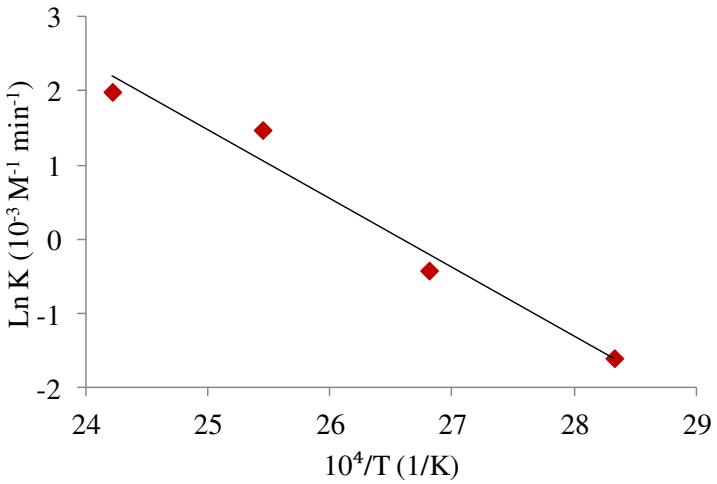

Figure 5.6: Arrhenius plot for cyclodehydration of 2,5-hexanediol over $HNbMoO_6$ (Ln k = 24.6 - $\frac{9247}{T}$).

The reaction of $HNbMoO_6$ layered oxide with 2,5-hexanediol at 120ºC was also monitored under autogenous pressure using an autoclave.

After heating $HNbMoO_6$ layered oxide and 2,5-hexanediol at 120 ºC for 1 hour and a half in the autoclave under solvent free conditions, the formed product was collected and analyzed by gas chromatography. Results revealed 100% conversion with a very high selectivity (97%). The experiment was repeated twice and identical results were encountered. Consequently, performing reactions at higher pressure induces total conversion, which was not achieved before under atmospheric pressure.

5.1.2. Influence of water

To examine the influence of water on the catalytic activity of layered $HNbMoO_6$, several batches with different H_2O/Diol ratios of 1, 3, 10 and 98 were heated at 120°C for 30 - 4080 minutes. Figure **5.7** and Figure **5.8** showed that upon increasing water amounts, conversion decreased. This might be due to the blocking of active sites in the interlayer

gallery by water molecules. For example, the time required to achieve 50% conversion increased from 18 to 100, 350, 600 and 1400 minutes as H_2O/Diol ratio increased from 0 to 1, 3, 10 and 98 molar ratio respectively (Table **5.3**). Up to a H_2O/Diol molar ratio of 10, the selectivity was similar to that obtained in solvent free conditions. On the contrary, it decreased in the presence of huge excess of water (98 equivalent) where unidentified secondary products were formed.

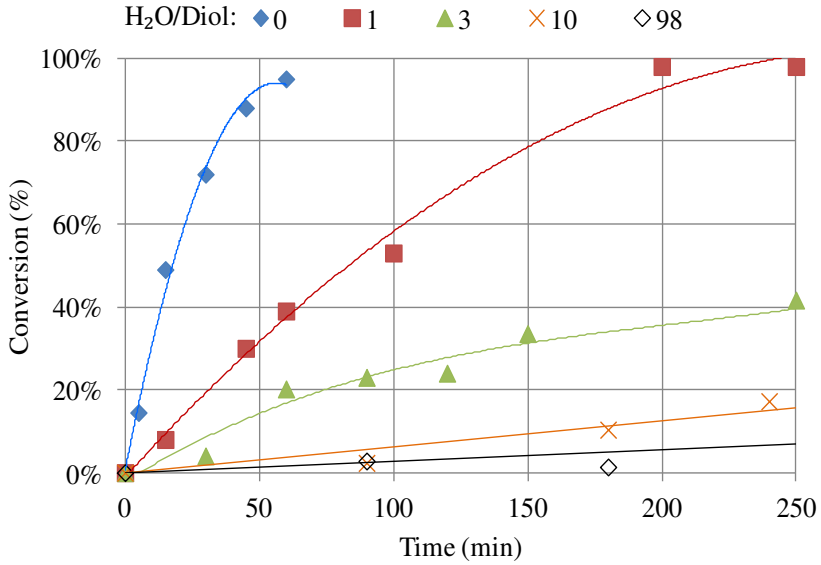

Figure 5.7: Conversion of 2,5-hexanediol at 120°C as a function of time in the presence of $HNbMoO_6$ at different H_2O/Diol ratio.

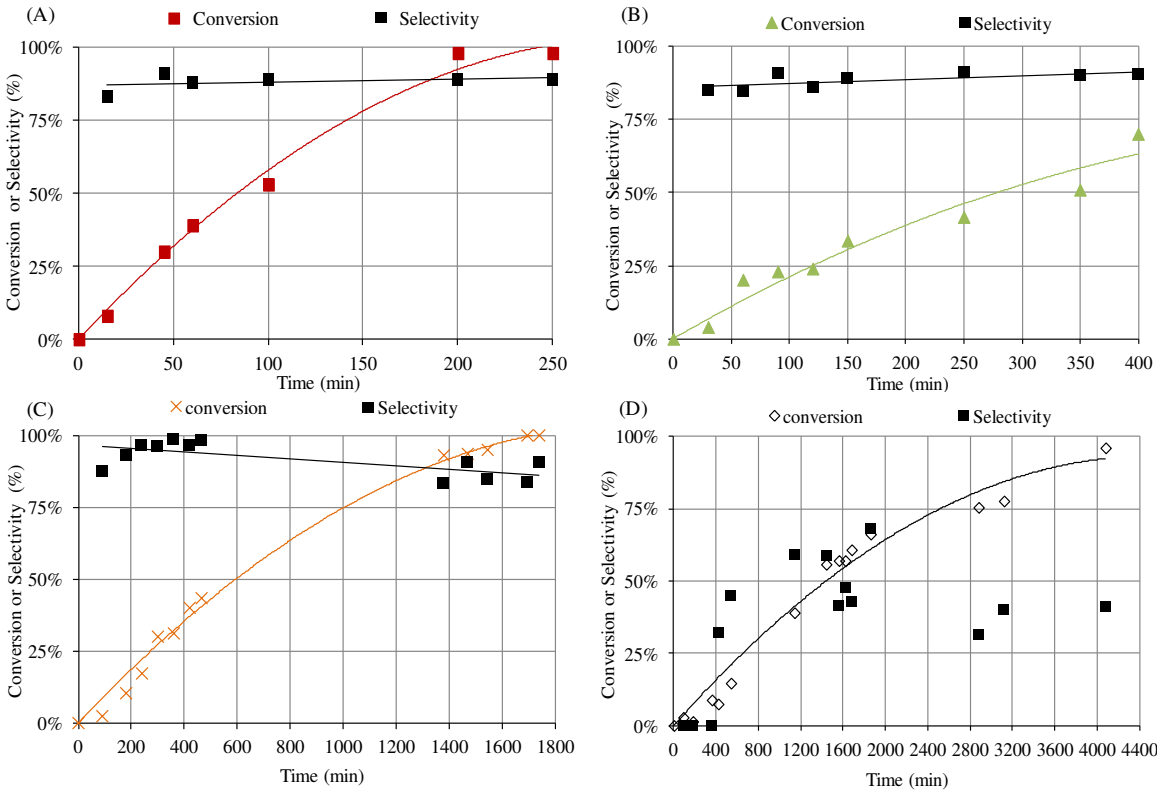

Figure 5.8: Conversion of 2,5-hexanediol and selectivity formation of 2,5-dimethyltetrahydrofuran using $HNbMoO_6$ at 120°C as a function of time with different H_2O/Diol ratio: (A) 1, (B) 3, (C) 10 and (D) 98.

Table 5.3: Time required to convert 50% of 2,5-hexanediol over $HNbMoO_6$ and selectivity towards formation of 2,5-dimethyltetrahydrofuran at different H_2O/Diol ratio at T = 120°C.

H_2O/Diol[a]	T½ (min)	Selectivity at T½ (%)
0	18 min	92%
1	100 min	89%
3	350 min	90%
10	600 min[b]	90%[b]
98	1400 min	59%

[a]Molar ratio. [b]Values are estimated from the trend curves.

5.1.3. Reaction mechanism

Sergi and co-workers [2] proposed that the intramolecular cyclization of 2,5-hexanediol is most energetically favourable via an SN2 nucleophilic substitution of a protonated hydroxyl group. The reaction is initiated by protonating hydroxyl group at the C2 or C5 position. This step can be achieved by the acidic sites available within the interlayer gallery of the layered oxides such as $HNbMoO_6$ layered catalyst. Then the carbocation formed in step (I) can follow two different pathways, as represented in Scheme **5.1**. In pathway (A), the lone pair of the non-protonated hydroxyl group attacks the carbon atom with the protonated -OH and simultaneously giving rise to cyclic ether (2,5-dimethyltetrahydrofuran) with one water molecule. In pathway (B), proton at position C3 or C6 attacks the carbon atom with the protonated hydroxyl group and simultaneously eliminating water and forming the alkene derivative.

With the catalysts tested, the selectivity to cyclic ether was always very high. For instance, with $HNbMoO_6$ layered oxide, high selectivity exceeding 90% was achieved. This result was not affected neither by increasing temperature as indicated in Table **5.2** nor in presence of water ≤ 10 equivalents as indicated in Table **5.3**. This indicates that pathway A is favoured. With higher H_2O/Diol molar ratio (98 equivalents), the selectivity to cyclic ether decreased to 59% since water is a protic solvent that favours pathway (B) thus leading to secondary products (alkene derivatives).

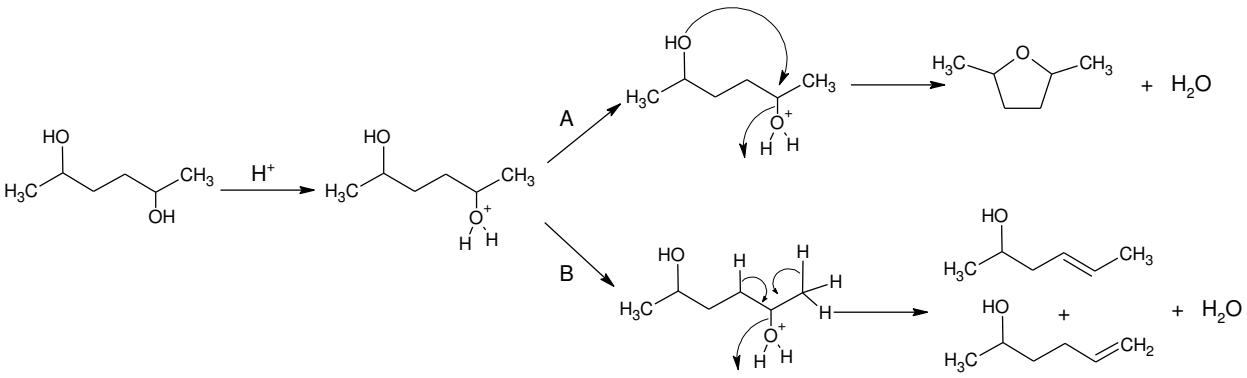

Scheme 5.1: Acid catalyzed cyclization of 2,5-hexanediol.

5.1.4. Operando Raman characterization of $HNbMoO_6$ layered oxide at 100°C

The cyclization process of 2,5-hexanediol was characterized during the reaction using Raman spectroscopy in the liquid phase by submerging the Raman immersion probe in the solution. In these conditions, the liquid could only be analysed, not the solid catalyst. To have sufficient time for the spectra acquisitions, the temperature was lowered at 100°C. Noteworthy, for longer reaction times, the spectra were less resolved and required longer scanning periods. Therefore, they should rather be considered as the average data over the acquisition time.

Results represented in Figure **5.9**, revealed the progressive disappearance of peaks situated at 750, 820 and 860 cm^{-1} (denoted by red triangles), with a simultaneous appearance of two bands at 805 and 880 cm^{-1} (denoted by green circles) after 30 and 60 minutes, respectively. The latter two bands increased in intensity as indicated in Figure **5.9(b)**. This set of bands can be ascribed to the presence of 2,5-dimethyltetrahydrofuran as reported by Shurvell et. al. [3]. The ratio of the product to the starting material, displayed in Figure **5.9(c)**, was estimated by calculating the ratio of the band at 800 cm^{-1} over the band situated at 820 cm^{-1}. The ratio increased sharply up to 90 minutes, then beyond this value, a further increase was encountered, but more slowly, until it becomes stable. This indicated that mostly all of the starting material was consumed during the initial stages of the reaction.

Results obtained were coherent with the conversion data represented in Figure **5.5** part (B). After 20 minutes, only peaks of 2,5-hexanediol were observed since conversion was lower than 10%. After 30 minutes, as conversion slightly increased, new peaks situated at 810 and 880 cm^{-1} attributed to 2,5-dimethyltetrahydrofuran was observed. Beyond this time, they increased in intensity until they became predominant after 180 minutes as conversion reached 85%. These changes occurred with a simultaneous decrease in the peaks of 2,5-hexanediol at 500, 750, 820, 860 and 950 cm^{-1}.

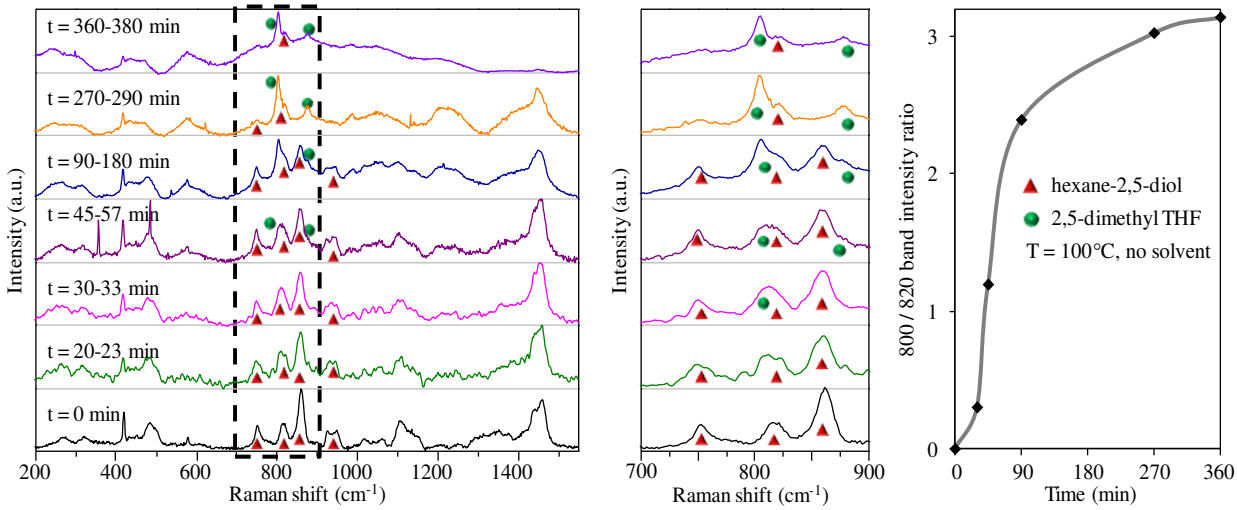

Figure 5.9: (a) Evolution of the Raman spectra of the reaction mixture upon heating at 100°C in absence of solvent. t_1= beginning of spectral recording, t_2= end of spectral recording, the stirring was stopped between t_1 and t_2. (b) Zoom in the region 700 - 900 cm^{-1}. Triangles refer to bands of 2,5-hexanediol, circles refer to bands of 2,5-dimethyltetrahydrofuran. (c) Ratio of the band intensities at 800/820 cm^{-1} versus time at middle of spectral recording ((t_1+t_2)/2)).

5.2. Comparison between intercalation and reactivity

5.2.1. Influence of the reaction on the structural and vibrational features

To examine the structural and vibrational features of the layered $HNbMoO_6$ during the catalytic reaction investigated at 120°C, samples were collected at successive intervals, dried then characterized using powder X-ray diffraction and Raman spectroscopy.

Powder X-ray diffraction results represented in Figure **5.10**, indicated that the reaction of the layered oxide with diol take place progressively with a coexistence of two different phases in the early stage of the reaction. The first phase (Phase 1) possesses an interlayer spacing relatively close to the parent $HNbMoO_6$ that decreases proportionally with time until it is undetectable after 150 minutes. The second phase (Phase 2) exhibits a higher interlayer spacing which is the only one detectable at 150 minutes. The evolution of the peaks intensities characterizing these two phases are represented in Figure **5.11**. The (110) peak situated at ≈ 27° did not shift at all indicating that the catalyst structure remained intact during reaction. This peak was used as a reference to estimate the zero shift of the PXRD patterns and obtain the evolution of the interlayer spacing with time for phases 1 and 2 (see Figure **5.11**). These results first indicate that the highest catalytic activity of the layered oxide can be attributed to

the facile intercalation of substrates within the interlayer gallery of the layered catalyst. This is consistent with previous results illustrated by Takagaki et al., who showed that layered $HNbMoO_6$ can intercalate water, alcohols and ketones resulting in a high catalytic activity for acid-catalyzed reactions such as Friedel-Crafts alkylation of benzyl alcohol [4], acetalization [4, 5], esterification of lactic acid [6] and hydrolysis of ethyl lactate [6] and by Domen and co-workers who studied extensively several acid catalyzed reactions and showed that layered $HNbMoO_6$ exhibited remarkable catalytic activity for the hydrolysis of saccharides such as sucrose and cellobiose into glucose [4, 6] due to its ability to intercalate substrates within the interlayer gallery.

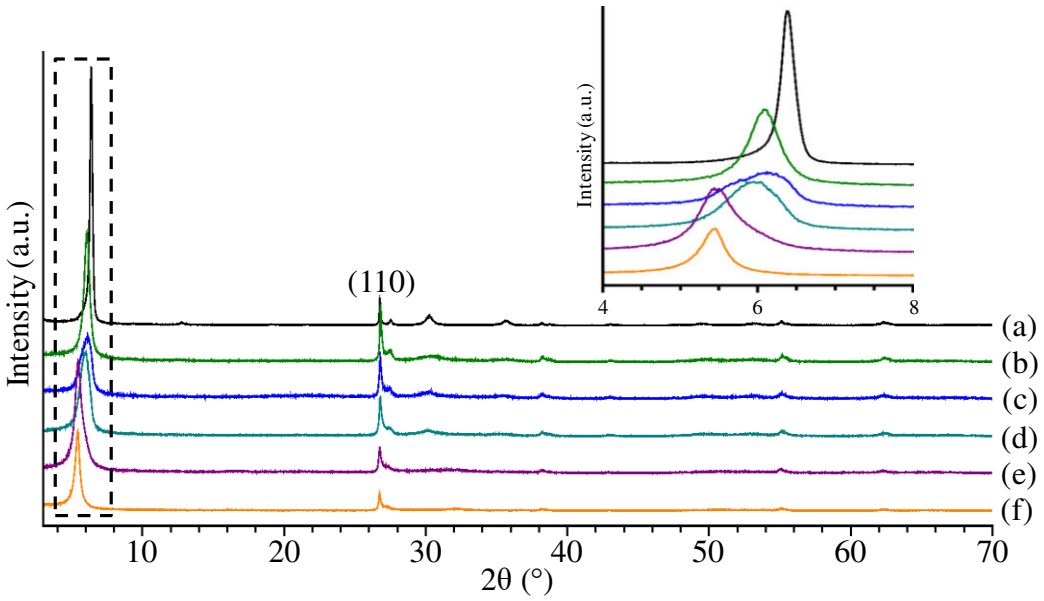

Figure 5.10: Evolution of PXRD patterns of $HNbMoO_6$ during cyclization of 2,5-hexanediol at 120°C after (a) 0 min., (b) 15 min., (c) 30 min., (d) 45 min. (e) 60 min. and (f) 150 min. Inset shows the enlargement in the region 4 - 8 °.

	d-interlayer (Å)		
Time (min)	Initial	Phase 1	Phase 2
0	13.84(4)		
15		14.86(2)	-
30		14.50(3)	15.75(6)
45		14.76(3)	15.75(5)
60		14.73(7)	16.19(2)
150		-	16.45(6)

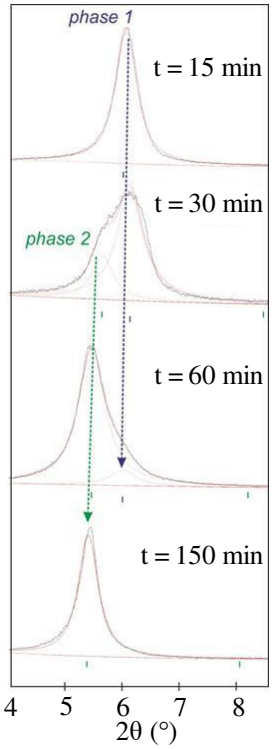

Figure 5.11: Evolution of d-interlayer spacing (Å) of $HNbMoO_6$ after diol reaction at 120°C at successive intervals.

The latter results confirmed the process of intercalation, however, the interaction between the added substrate and $HNbMoO_6$ layered oxide needs to be defined. Therefore, Raman spectroscopy was used to monitor the structural changes upon diol intercalation. Figure **5.12** represented the Raman spectra of $HNbMoO_6$ collected at successive intervals during reaction at 120°C. Results revealed similar patterns of the layered catalyst from the beginning till the end of the reaction, i.e. no degradation of any peak or formation of others, indicating the retention of the catalyst structure and confirming the powder X-ray diffraction results. Taking a closer look on each spectrum, several peaks shifted from their initial position. For example, the stretching vibration of (Mo=O) shifted by 9 cm^{-1}. Raman bands of mixed Nb-O-Mo species also shifted. The stretching vibration of (Nb-O-Mo) initially situated at 604 cm^{-1} was shifted by 13 cm^{-1}. A significant displacement in the stretching vibration of (Nb=O) and (O-Nb-O) was observed from 903 to 880 cm^{-1} and from 461 to 451 cm^{-1} respectively. Consequently, these results confirm the interaction between the metal of the layered oxide and the OH from the guest species.

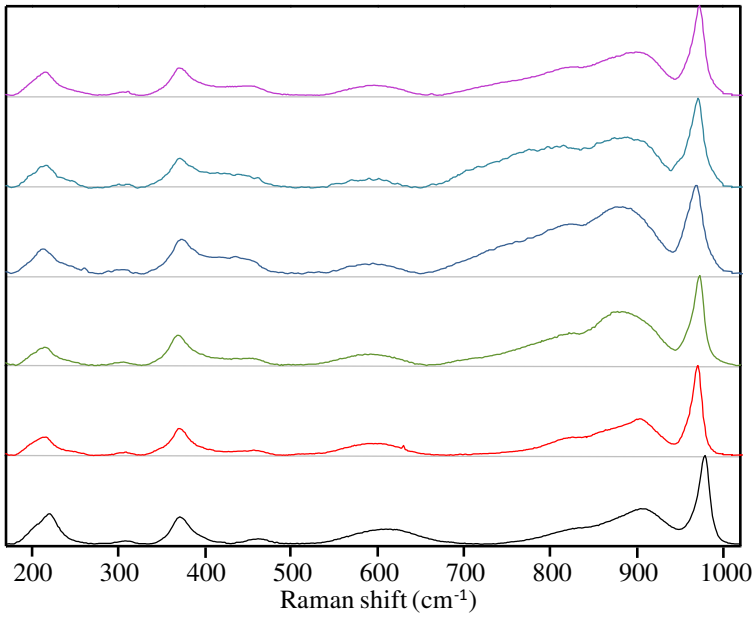

Figure 5.12: Raman spectra of (a) $HNbMoO_6$ heated at 120ºC and after reaction with 2,5-hexanediol at 120°C at successive intervals (b) 5 min., (c) 15 min., (d) 30 min., (e) 45 min. and (f) 60 min.

Table 5.4: Raman spectra of $HNbMoO_6$ collected at successive intervals during reaction at 120°C.

	Raman shift (cm^{-1})							
Time (min)	ν (Mo=O)	ν(Nb=O)	ν(Mo-O-Mo)	ν(Nb-O-Mo)	ν(O-Nb-O)	δ(MoO_6)	δ(Mo-O-Nb)	δ(O-Nb-O)
0	978	903	818	604	461	371	305	219
5	971	904	818	598	456	371	308	216
15	972	887	816	591	453	368	305	214
30	969	883	814	596	451	374	304	213
45	971	880	814	595	452	371	305	216
60	973	899	814	596	455	370	311	215

5.2.2. Influence of the reaction conditions on the structural and vibrational parameters

To examine the influence of water or pressure on the catalyst structure, at the end of each reaction, samples were collected, dried using dichloromethane under hood and characterized using powder X-ray diffraction to monitor the process of intercalation and by Raman spectroscopy to investigate the structural changes occurring at the level of the layered catalyst.

Figure **5.13** and Table **5.5** represent the powder X-ray diffraction patterns of $HNbMoO_6$ layered oxide and their d-interlayer spacing after reaction with different Diol/H_2O ratio. Results revealed that in presence of water in the reaction, two phases are present: the major one corresponds to a slight shift in the (001) diffraction peak, from its initial position situated at 6.37° to 5.93, 6.33, 5.90 and 6.26° with (Diol/H_2O) molar ratio of 1:1, 1:3, 1:10 and 1:98 respectively associated to a slight increase in the interlayer spacing a indicated in the table. In all cases, this shift was lower than those encountered under solvent free conditions. A minor phase was also present characterized by higher interlayer spacing. These results could be attributed to the blocking of the active sites in the interlayer gallery by water molecules, thus inhibiting the process of intercalation of 2,5-hexanediol and therefore, lower conversion would be expected and this was confirmed by our results. In addition to that, (110) diffraction peak did not shift at all in all cases, confirming that the layered catalyst structure remained intact in the presence of water.

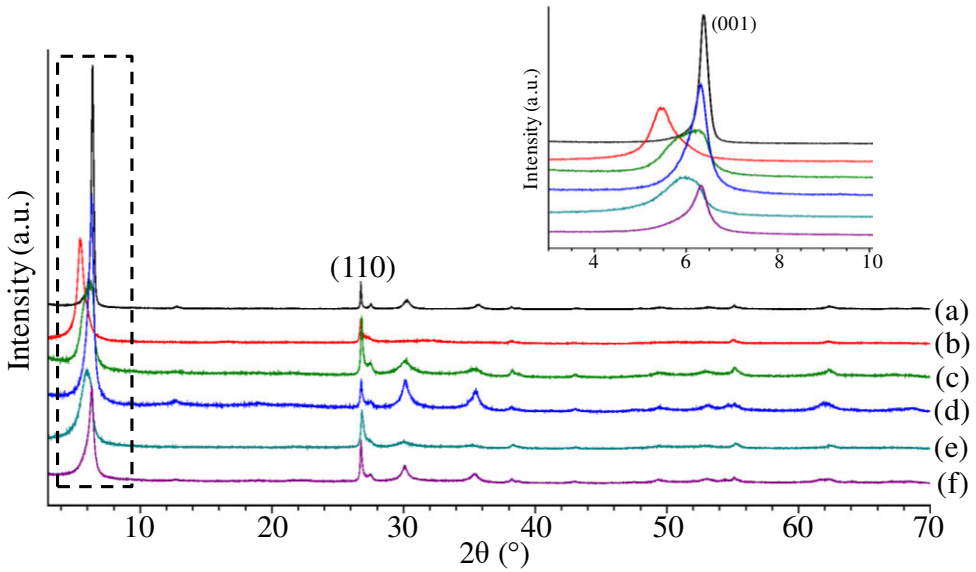

Figure 5.13: PXRD patterns of (a) parent $HNbMoO_6$ layered oxide and after reaction with several Diol/H_2O molar ratios; (b) 1:0, (c) 1:1, (d) 1:3, (e) 1:10 and (f) 1:98. Inset shows the enlargement in the region 3 - 10 °.

Table 5.5: Evolution of d-interlayer spacing of protonated layered $HNbMoO_6$ after reaction with various Diol/H_2O ratio at 120°C.

mol Diol / mol H_2O	Time (min.)	Conversion (%)	d-interlayer (Å)
1:0	0		13.84(4)
1:0	60	95	16.19(2) / 14.73(7)*
1:1	150	76	14.52(3) / 15.92(5)*
1:3	400	70	14.16(3) / 15.71(4)*
1:10	1740	100	14.94(3) / 16.44(8)*
1:98	360	9	14.26(1)
1:98	3120	78	14.11(2) / 15.41(3)*

* minority phase.

Raman spectra with their band assignments are displayed in Figure **5.14** and Table **5.6**. Results revealed several modifications. (Mo=O) stretching vibration exhibited a shift ranging between 4 to 9 cm^{-1}. By contrast to (Mo=O), (Nb=O) stretching vibration situated at 903 cm^{-1} was highly influenced by the presence of water. (Nb=O) shifted by 16 cm^{-1} at Diol/H_2O molar ratio of 1:10 and by 32 and 29 cm^{-1} at Diol/H_2O molar ratio of 1:1 and 1:98 respectively. In addition to that, the broadening of this peak increases with increasing water molecules. For

(O-Nb-O) stretching vibration, the highest shift (9 cm^{-1}) was encountered at Diol/H_2O, 1:98. For (Nb-O-Mo) stretching vibrations, the highest shift (19 cm^{-1}) was encountered at Diol/H_2O molar ratio of 1:1. However, lower shift was displayed upon increasing water indicating its weak effect on these two bands. Therefore, only (Nb=O) and (O-Nb-O) stretching vibrations were highly affected by increasing water amounts.

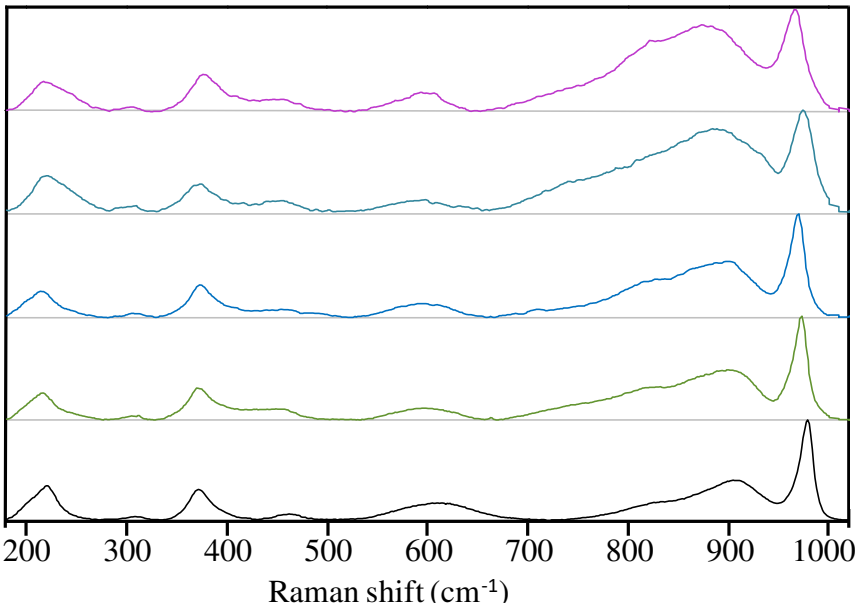

Figure 5.14: Raman spectra of parent $HNbMoO_6$ (a) heated at 120ºC and collected at the end of the reaction (T = 120°C) with different Diol/H_2O ratio: (c) 1:1, (d) 1:3 (d), (e) 1:10 and (f) 1:98.

Table 5.6: Raman band assignments of $HNbMoO_6$ layered catalyst after reaction with different H_2O/Diol molar ratios.

		Raman shift (cm^{-1})							
H_2O/Diol	Time (min)	ν (Mo=O)	ν(Nb=O)	ν(Mo-O-Mo)	ν(Nb-O-Mo)	ν(O-Nb-O)	δ(MoO_6)	δ(Mo-O-Nb)	δ(O-Nb-O)
0		978	903	818	604	461	371	305	219
1	150	972	871	816	582	453	374	308	218
3	400	969	900	818	592	457	374	305	213
10	1740	974	887	817	597	459	373	308	219
98	3120	966	874	822	595	452	376	305	217

Similarly, after performing the catalytic reaction under autogeneous pressure (ca. 5 bar), the layered oxide was collected at the end, dried and characterized using powder X-ray diffraction. Figure **5.15**, indicated that upon reacting $HNbMoO_6$ with diol for 90 minutes, (001) diffraction peak shifted to lower angle (~ 4.4 °) associated to an increase in the interlayer spacing to ~ 20 Å (Table **5.7**). This increase was higher than that encountered upon heating $HNbMoO_6$ with diol under atmospheric pressure for 150 minutes (16.45 Å), as shown in Figure **5.15(b)**. This revealed that higher pressure facilitates the intercalation process of 2,5-hexanediol into the interlayer gallery, resulting in lower (001) position and higher increase in the basal spacing, consequently achieving higher conversion. In addition to that, (110) diffraction peak was situated at the same identical position before and after reaction, indicating that no change in the ($NbMoO_6$) layers was encountered.

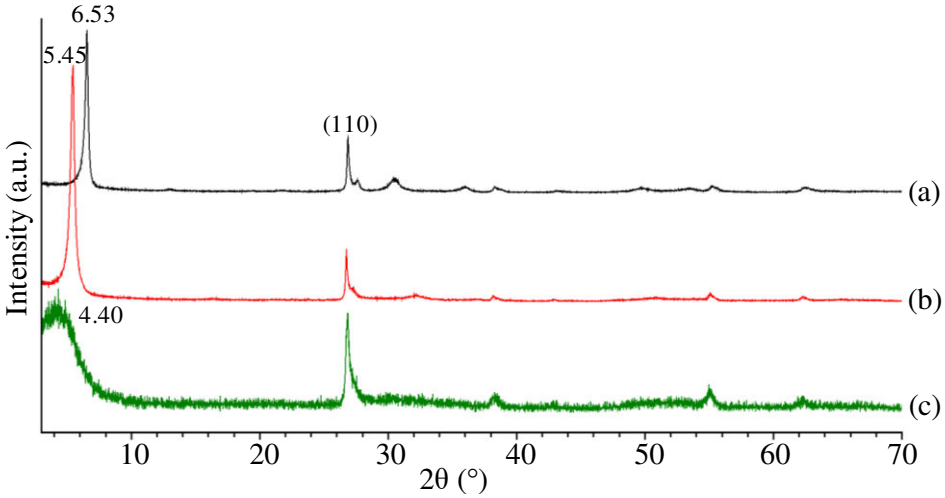

Figure 5.15: PXRD patterns of parent $HNbMoO_6$ (a) and (b) $HNbMoO_6$ reacted with 2,5-hexanediol at 120°C under atmospheric pressure after 150 min and (c) under pressure after 90 min.

Table 5.7: Evolution of d-interlayer spacing (Å) of $HNbMoO_6$ layered oxide after reaction with diol at different pressures.

Pressure	Time (min)	d-interlayer
	0	13.84(4)
Atmospheric	150	16.45(6)
ca. 5 bar	90	20.0(9)*

* high uncertainty due to the very broad peak observed at low angle.

5.2.3. Comparison between Layered metal oxide ($HNbMoO_6$, $HNbWO_6$ and $H_2W_2O_7$)

$HNbMoO_6$ exhibited the highest catalytic activity among the reference solid acid catalysts. The catalytic conversion of 2,5-hexanediol was also tested using other layered oxides based on transition metals such as $HNbWO_6$ and $H_2W_2O_7$. The results will be compared with those obtained with $HNbMoO_6$. The catalysts were characterized using powder X-ray diffraction and Raman spectroscopy to follow the changes due to the reaction.

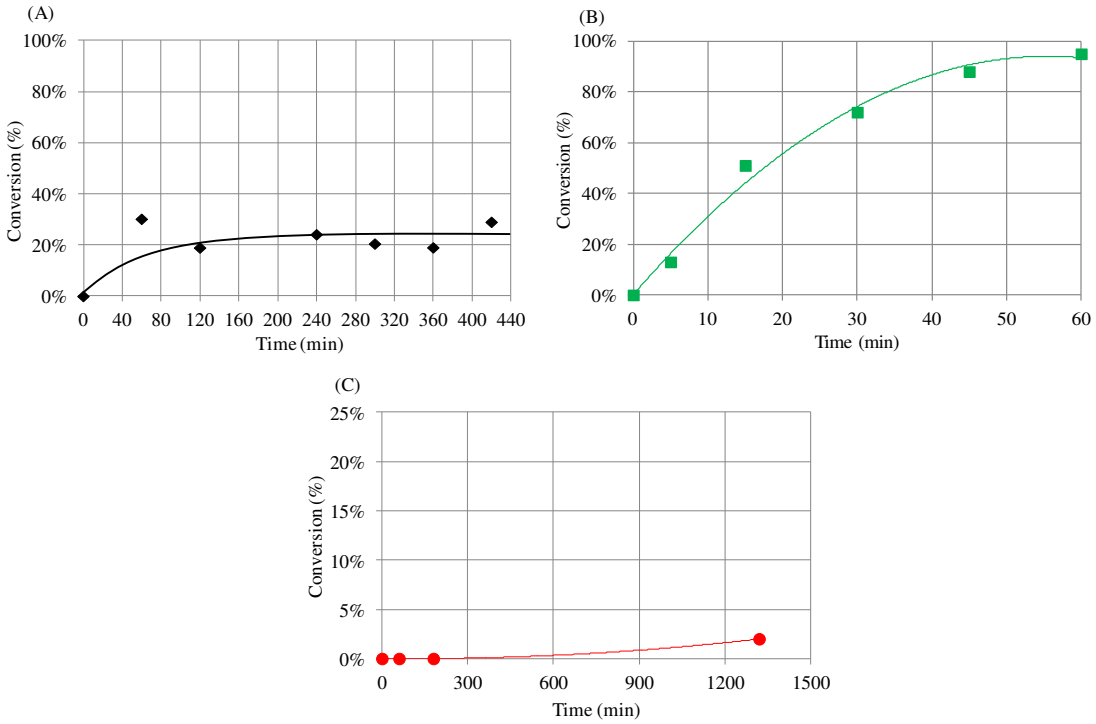

Figure 5.16: Conversion of 2,5-hexanediol at 120°C as a function of time with (A) $HNbWO_6$, (B) $HNbMoO_6$ and (C) $H_2W_2O_7$ layered catalyst.

The cyclodehydration of 2,5-hexanediol using $HNbMoO_6$, was performed at 120°C under solvent free conditions and reported in section 5.1. Compared with the high conversion (95%) and high selectivity (95%), $HNbWO_6$ only indicated a low conversion (around 25%) after 7 hours of reaction (Figure **5.16**) with a very low selectivity (lower than 30%). However, with $H_2W_2O_7$, no reaction had taken place; only 2% conversion after 22 hours was achieved. Therefore, the order of the catalysts activity for 2,5-hexanediol conversion can be represented as follows: $HNbMoO_6 > HNbWO_6 > H_2W_2O_7$.

To understand this significant difference, the structural features of the layered catalysts were characterized using powder X-ray diffraction to monitor the intercalation process. With $HNbMoO_6$ catalyst, powder was collected at successive intervals during the reaction; dried using dichloromethane, however, with $HNbWO_6$ and $H_2W_2O_7$, since only a slight or no difference in conversion between successive intervals, the latter two samples were only collected at the end of the reaction, dried then characterized. Figure **5.17**, represents the PXRD patterns of the layered catalysts collected at the beginning and at the end of the reaction.

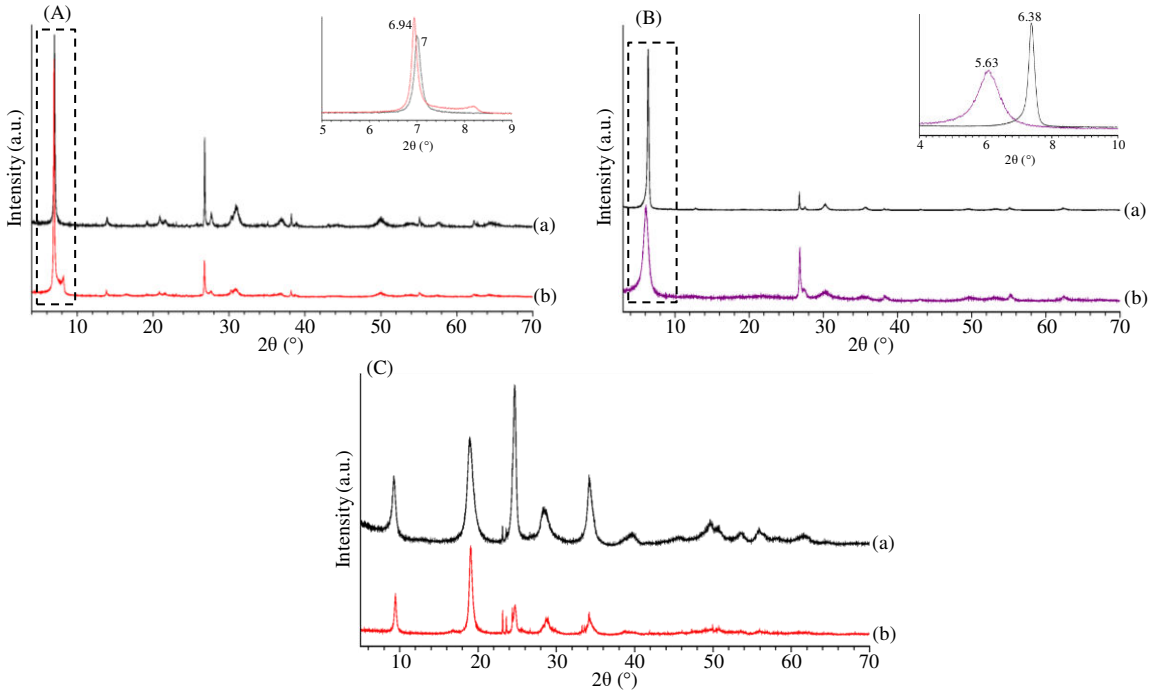

Figure 5.17: PXRD patterns of (A) $HNbWO_6$, (B) $HNbMoO_6$ and (C) $H_2W_2O_7$ at (a) time = 0 min. and (b) after 60 min in part B and 24 hrs in parts A and C. The insets in parts (A) and (B) show the enlargement in the range 5 - 9 ° and 4 - 10 ° respectively.

Results revealed that with $HNbMoO_6$ layered oxide, after 60 minutes reaction, (001) diffraction peak shifted from 6.38 to 5.63° respectively; however with $HNbWO_6$ after 24 hours reaction a very slight shift in the (001) diffraction peak was observed (from 7 to 6.94°, respectively). This indicated that higher intercalation took place with $HNbMoO_6$ than with $HNbWO_6$ layered oxide. This could be attribute to the smaller gallery height of $HNbWO_6$ (0.496 nm) than that of $HNbMoO_6$ (0.553 nm) [7], therefore intercalation of 2,5-hexanediol into the interlayer gallery of layered $HNbWO_6$ will be more difficult thus diminishing the conversion. It is also possible that the 25% conversion achieved with this catalyst may be due to the acidic sites present on the surface and not inside the interlayers. In case of $H_2W_2O_7$ layered oxide, PXRD patterns did not show any significant change, only peak situated at 25° decreased in intensity revealing that the intercalation or interaction did not take place since the protons are too weak or too scarce, as discussed previously in Chapter 4, therefore resulting in no catalytic conversion.

Consequently, our results emphasize that intercalation is a key factor for any catalytic reaction and can greatly affect the catalytic activity of the layered catalysts. Therefore, the intercalation process will be the preliminary step to permit the successful catalytic reaction.

In addition to that, to monitor the interaction between $HNbWO_6$ and $H_2W_2O_7$ with 2,5-hexanediol, samples at the end of the reaction were characterized by Raman spectroscopy and their spectra were compared with their initial ones.

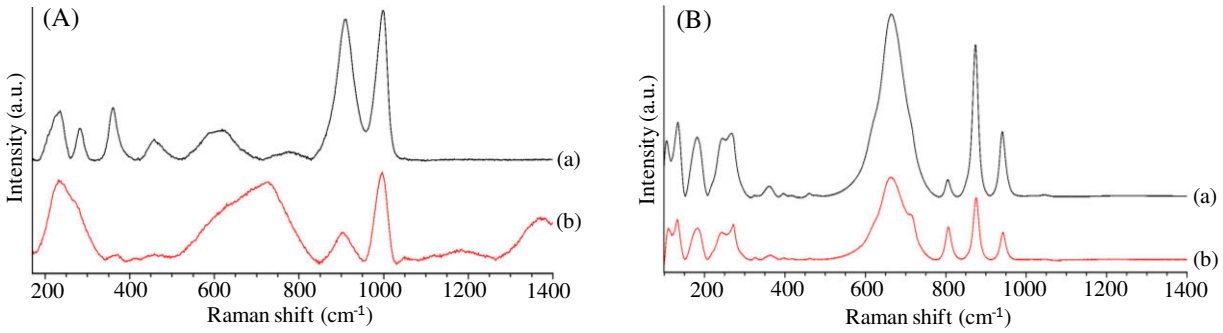

Figure 5.18: Raman spectra of (A) $HNbWO_6$ and (B) $H_2W_2O_7$ before reaction (a) and after 24 hours reaction at 120°C (b).

Results represented in Figure **5.18**, revealed that $H_2W_2O_7$ layered oxide remained intact indicating no interaction with 2,5-hexanediol. With $HNbWO_6$ upon 24 hours reaction, (W=O) remained at approximately the same position similarly to (Nb=O). The latter only broadened and decreased in intensity. This was accompanied by the development of a band at

723 cm^{-1}. Compared to $HNbMoO_6$, these results only indicate a partial interaction with the niobate sites. This might confirm that the reaction took place on the outer surface and not in the interlayers.

5.3. Conclusion

In this chapter the catalytic activity of various solid acid catalysts was evaluated by investigating the cyclization of 2,5-hexanediol into 2,5-dimethymtetrahydrofuran. This reaction proved to be efficient test reaction, able to discriminate between solid acid catalysts and notably among layered materials.

The reaction was studied for various reaction parameters, such as temperature and pressure. It was also tested in presence of various amounts of water. In this case, even though Raman spectroscopy and powder X-ray diffraction pattern results revealed the stability of $HNbMoO_6$ layered oxide in presence of water, the conversion and selectivity decreased. This could be attributed to the poisoning of the active sites with water. Nevertheless, several aspects are contradictory with this assumption: the stability of the $HNbMoO_6$ in presence of water as indicated by the reproducible uptake measured by TGA after hydration, the progressive decrease of the conversion when water content is increased in the reaction mixture, the absence of indication of an irreversible poisoning and the absence of change on the catalyst measured by PXRD and Raman spectroscopy. All these aspects rather indicate that the catalytic activity is decreased due to the dilution of the reactant and the competitive adsorption of water and the diol at the catalyst surface.

For this reaction, $HNbMoO_6$ layered oxide revealed the highest catalytic activity and selectivity much more than Nb_2O_5, several commercial zeolites and other transition metals based layered catalysts ($HNbWO_6$ and $H_2W_2O_7$). It is noteworthy that unlike conventional catalysts, the catalytic activity develops without any activation steps, which also confirms that the presence of some water is not detrimental to the catalytic activity. This was attributed to several important factors. Obviously, the acidity plays an important role. The acidity of $HNbMoO_6$ and $HNbWO_6$ are greater than $H_2W_2O_7$ which is completely inactive. Nevertheless, although the acidity of $HNbMoO_6$ appears slightly weaker than that of $HNbWO_6$ (based on the spectroscopic displacement of the pyridinium band), its catalytic activity is much larger than $HNbWO_6$. $HNbMoO_6$ is characterized by its great ability to intercalate several substrates within its interlayer region which is a key preliminary step of any catalytic reaction on such types of solids. This proved to be more efficient in this solid than in the other solid tested $HNbWO_6$ and $H_2W_2O_7$. This could be due to the higher gallery height than $HNbWO_6$ and the related ability to accommodate specific geometries of the molecule inserted.

5.4. References

1 A. Takagaki, *Catal. Sci. Technol.*, 2016, **6**, 791–799.

2 S. Ruiz-Barragan, J. R. Arino and M. Shig, *Phys.Chem.Chem.Phys.,* 2016, **18**, 32438–32447.

3 H. F. Shurvell and M. C. Southby, *Vib. Spectrosc.*, 1997, **15**, 137–146.

4 A. Takagaki, C. Tagusagawa and K. Domen, *Chem. Commun.*, 2008, **0**, 5363–5365.

5 C. Tagusagawa, A. Takagaki, S. Hayashi and K. Domen, *J. Am. Chem. Soc.*, 2008, **130**, 7230–7231.

6 A. Takagaki, C. Tagusagawa, S. Hayashi, M. Hara and K. Domen, *Energy Environ. Sci.*, 2010, **3**, 82–93.

7 J. He, Q. J. Li, Y. Tang, P. Yang, A. Li, R. Li and H. Z. Li, *Appl. Catal. A Gen.*, 2012, **443**–**444**, 145–152.

GENERAL CONCLUSIONS AND PERSPECTIVES

This work aimed to evaluate the potential of layered materials as catalysts and notably for biomass conversion processes. Consequently, several known lamellar or layered compounds based on transition metal oxides such as $HNbMoO_6$, $HNbWO_6$, H_2WO_4 and $H_2W_2O_7$ have been studied as well as a new type of solid acid catalysts based on mixed Nb and W metal oxides and characterized by a stair-like Aurivillius structure. The characterization methods for such materials have also been extensively explored by Raman spectroscopy notably.

Li- ($LiNbMoO_6$ and $LiNbWO_6$) and Bi-precursors ($Bi_2W_2O_9$ and Bi_2WO_6) were synthesized using solid state synthesis as reported in the literature. Additionally, new series of solids based on Nb and W ($Bi_7Nb_3WO_{21}$, $Bi_9Nb_3W_2O_{27}$, $Bi_{11}Nb_3W_3O_{33}$ and $Bi_{17}Nb_3W_6O_{51}$) were successfully synthesized by exploring the compositions lying between $Bi_5Nb_3O_{15}$ and Bi_2WO_6. These solids are based on discontinuous layers denoted as "steps" of Bi_2O_2 and perovskite octahedral slabs. All samples, including the new phases for the first time, were structurally characterized using PXRD and Raman spectroscopy of the solids. Raman spectroscopy helped distinguishing between the W and Nb sites and also between the sites on single inorganic layers or on steps made of double layers.

In order to obtain acidic solids, samples were converted into their protonated forms by exchanging the Li^+ or Bi^+ ions using either hydrochloric or nitric acid, respectively. PXRD patterns and Raman spectra were strongly modified and confirmed the protonation. The water content in all samples was estimated from the TGA analysis.

Conversely, the new mixed (Nb/W) layered oxides ($Bi_7Nb_3WO_{21}$, $Bi_9Nb_3W_2O_{27}$ and $Bi_{11}Nb_3W_3O_{33}$) could not be protonated even after several protonation procedures, as indicated by both PXRD and Raman spectroscopy. This can be attributed to the stability of these layered oxides on the step-like structure. On the contrary, the solid with the smallest stair-like structure, $Bi_{17}Nb_3W_6O_{51}$, which shares structural similarity with Bi_2WO_6, was readily protonated.

A second aspect of the work concerned the intercalation process for all the protonated samples. This interesting property, characteristic of layered compounds, was extensively monitored using several organic bases such as pyridine, n-alkylamines (butylamine and octylamine), n-alcohols and 2,5-hexanediol.

To simultaneously monitor the acidity and intercalation of the layered oxides, N-containing bases were used. Intercalation of n-alkylamines occurred into all protonated

layered oxides as confirmed by PXRD patterns and Raman spectra in the liquid phase. The interlayer spacing increased with the alkyl chain length, but this also induced an enhancement of the ordering of the layered structure. Additionally, depending on the solid, the impact on the structure differed: the double octahedral slabs of $HNbMoO_6$ and $HNbWO_6$ were preserved, while, in the case of $H_2W_2O_7$, double slabs underwent a dissolution-reorganization mechanism. Raman spectroscopy showed that all sites interacted with the amine group confirming their acidity by the possible protonation of the amine.

As a basic probe, pyridine was also utilized due to its weaker basicity. Raman spectroscopy was well-suited for the study of layered materials as it allowed the monitoring of the acidity during intercalation. The intercalation of pyridine was not detected in the case of $H_2W_2O_7$, appearing thus only mildly acidic. Conversely, all other oxides ($HNbMoO_6$ and $HNbWO_6$, H_2WO_4 and H-$Bi_{17}Nb_3W_6O_{51}$) were able to intercalate pyridine. Their PXRD patterns indeed indicated the increase of the interlayer spacing and their Raman spectra showed the perturbations either on (W=O) or (Mo=O) as well as the development of a new peak around 1015 cm^{-1} between the bands of the liquid pyridine. $HNbMoO_6$, $HNbWO_6$, and H-$Bi_{17}Nb_3W_6O_{51}$ were shown to possess Brønsted acidity while H_2WO_4 only showed Lewis acidity. Unlike the intercalation with the n-alkylamines, niobium sites appeared mildly affected by pyridine which is closer to either (W=O) or (Mo=O).

Intercalation of alcohols into the acidic layered oxides was also studied in order to gain insight for their catalytic activity. n-alcohols and 2,5-hexanediol intercalation was thus carried out for $HNbMoO_6$, $HNbWO_6$ and $H_2W_2O_7$ at room temperature and higher temperatures. With $H_2W_2O_7$, no intercalation had taken place from 25 to 100 °C. With $HNbMoO_6$, the intercalation process of short and long chain alcohols was successfully achieved, however with $HNbWO_6$, only short chain alcohols were intercalated and long chain alcohols showed either partial or no intercalation. At higher temperatures, the extent of intercalation increased for $HNbMoO_6$ as indicated by the increase in the interlayer spacing. However with $HNbWO_6$, the increase only concerned short chain alcohols. This can be partly due to the difference in the gallery height between these two samples and thus to the geometry of intercalation, but also to the acidity. In the optimal case of $HNbMoO_6$, hexanediol and octanol were able to induce the largest interlayer expansion. This has a direct impact on the catalytic activity.

The third main aspect of this work concerned the evaluation of the catalytic behaviour of layered materials. The catalytic activity of layered $HNbMoO_6$, $HNbWO_6$ and $H_2W_2O_7$ was

monitored through a novel test reaction: the cyclo-dehydration of 2,5-hexanediol into 2,5-dimethyltetrahydrofuran. These results were compared to other solid acid catalysts such as niobium oxide and different zeolites. Among all the solids tested (conventional solid acid catalysts and other layered oxides), $HNbMoO_6$ showed the highest catalytic activity. Besides, it should be noted that unlike conventional catalysts, layered materials were used without any activation step (heat treatment) prior to reaction. This high catalytic activity can be attributed to the facile intercalation of substrates within the interlayer gallery of the layered catalyst. The low acidity of $H_2W_2O_7$ was not sufficient to develop catalytic activity. $HNbWO_6$ is strikingly less active than $HNbMoO_6$. This lower activity is consistent with the low intercalation capability of $HNbWO_6$ for higher alcohols, due to its lower gallery height than $HNbMoO_6$ and different geometry of intercalation.

The catalytic conversion was examined for different reaction parameters (temperature, pressure and various amounts of water). Pressure and temperature had a beneficial impact on the catalytic activity. In presence of water, $HNbMoO_6$ did not deactivate showing its stability. Nevertheless, the addition of water diminishes the conversion and selectivity by the dilution of the reactant and the competitive adsorption of water and the diol at the catalyst surface.

Therefore, our work shows the importance of the comprehensive study of layered solids through intercalation, acidity and catalytic activity measurements. Notably, Raman spectroscopy proved useful for the study of the solids in condition of intercalation or reaction, as well as to discriminate between different solid acids. Among transition layered metal oxides, mixed oxides containing Nb and (Mo or W) have the potential to act as acidic catalysts in various conversions including biomass processes. Besides, 2,5-hexanediol cyclo-dehydration can act as a new catalytic test, efficient to evaluate various solids including layered materials.

Nevertheless, this work also paves the way for future studies.

Regarding the materials, $HNbMoO_6$ proved to be the most interesting layered solid tested. The large difference with $HNbWO_6$ raises questions on the role of the metals involved. This could be investigated in the same manner for other layered transition metal oxides based on different couples of transition metals such as Nb and Ti or Ta and (Mo or W). The influence of the relative amounts of each metal in the structure also deserves specific studies. Obviously, this is difficult to achieve with fixed compositions like that of $HNbMoO_6$. This

had also been one of the objectives of the study carried out here when the new solid phases based on the stair-like Aurivillius structures have been characterized. Different Nb/W ratios were successfully obtained, but these structures proved to be impossible to protonate. This new result is structurally interesting as it highlights the importance of the "steps" or "stairs" to stabilize the structure, but this also implies that these new materials are useless for acid catalysis, except possibly for the protonated form of $Bi_{17}Nb_3W_6O_{51}$ which deserves further studies. Nevertheless, the possible use of the bismuth phases could also be tested for non acidic catalysis or even for photocatalysis. Alternatively, the pseudo-binary $A^{2+}Bi_2Nb_2O_9$ – $Bi_2W_2O_9$ (p=2 Aurivillius phases) could be explored. These phases, which do not hold stair-like structures, might be easier to protonate and thus act as solid acid catalysts. The study of the equivalent solids in the Nb/Mo system is also necessary for comparison with $HNbMoO_6$. Additionally, as nanosheets can be readily formed from protonated layered oxides, it could be worth studying their catalytic activity, notably to precise more clearly the difference between $HNbMoO_6$ and $HNbWO_6$.

Intercalation proves to be a key step in the activity of layered materials. To evaluate the potential of the selected materials for other conversions, it would be interesting to determine the extent of intercalation using bulkier intercalants, e.g. carbohydrates or molecules with more than one cyclic ring. For this, the combined study by PXRD, TGA and Raman spectroscopy is really meaningful including when it brings additional information on the accessible acidity.

The catalytic test developed here shows many advantages (e.g. simplicity, very low amounts of by-products, low temperature, ability to discriminate between similar solids). To determine to what extent it could be applied to "mimic" biomass conversion processes, it will be necessary to confront data on various different catalysts with the rankings obtained on the same solids for other relevant processes like carbohydrates conversions.

New studies are also required to evolve towards more extensive *operando* characterization. Although Raman spectroscopy proved to characterize the evolutions of the solid during intercalation or reaction steps, it was not possible to fully follow the solid in the liquid during the reaction, probably because of the dispersion of the catalyst when immersed and thus the low solid concentration in front of the probe. This should be tackled, possibly by modifying the reactor configuration, and gathering the catalyst in a dedicated recipient.

Future works could also envision alternative types of reactions. Many processes often involve both acidic and metallic functions. Layered materials have the capability to host

various types of compounds. This was shown here for the reagent or for basic probes but this could also be the case for supported metals. In this case, selective access to the different reaction sites could be forecasted depending on the layer expansion.

Layered materials have a role to play as catalysts, notably as acidic catalysts. Besides, new questions also arise regarding their characterization. It is thus expected that such studies will improve their understanding and applicability.

ANNEX I

RESUME DE LA THESE

Caractérisation des matériaux lamellaires ou nanostructurés à base d'oxydes de métaux de transition pour la catalyse en phase liquide.

Le texte ci-après est un résumé détaillé de la thèse en français. Par souci de brièveté, il ne reprend qu'une partie des arguments développés dans la thèse. Le lecteur est donc invité à se référer préférentiellement au texte initial en anglais.

1. Introduction et objectifs de la thèse

La découverte du pétrole brut au 19ème siècle a créé une source de carburant liquide peu coûteuse qui a contribué à industrialiser le monde et à améliorer le niveau de vie [1]. Les matières premières non renouvelables telles que le charbon, le pétrole et le gaz naturel sont donc utilisées pour produire de l'électricité, de la chaleur et des carburants de transport, ainsi qu'une vaste majorité de produits chimiques de valeur [2, 3].

Cependant, la demande de pétrole devrait augmenter en raison principalement de la forte augmentation de la population et de la forte croissance économique dans le monde entier. Par ailleurs, l'utilisation des combustibles fossiles contribue largement aux émissions de gaz à effet de serre tels que le CO_2 et le CH_4 [4, 5]. La recherche de sources d'énergie alternatives telles que les énergies éolienne, solaire, nucléaire et de la biomasse présente donc un grand intérêt.

Comparée aux autres sources d'énergie renouvelables, la biomasse composée principalement de végétaux et de matières végétales [6, 7, 8] est considérée comme une matière première potentielle pour la production de liquides combustibles et de produits chimiques, car c'est la seule source de carbone disponible sur la planète, avec une production annuelle abondante [9], une large distribution dans le monde entier et a un faible impact sur l'environnement en raison de ses émissions de gaz à effet de serre neutres ou neutres si une production efficace est développée [10, 11]. Cependant, son utilisation reste encore marginale car les processus de conversion de la biomasse n'ont pas été développés ou optimisés, principalement en raison de sa diversité, de sa complexité et de sa forte teneur en oxygène [12].

Parmi les procédés envisageables, des réactions en plusieurs étapes sont souvent nécessaires, avec notamment le recours à des catalyseurs acides.

Au cours du siècle dernier, des catalyseurs acides homogènes tels que les acides chlorhydrique et sulfurique ont été largement utilisés, leur solubilité élevée favorisant l'accessibilité totale des sites acides dans le milieu réactionnel [13]. Cependant, leur toxicité et leur corrosivité [14], ainsi que les difficultés rencontrées lors de la tentative de séparation de ces catalyseurs du milieu réactionnel [9], ont amené les chercheurs à envisager leur remplacement par des processus de catalyse hétérogène que ce soit pour la conversion du pétrôle ou pour les processus de conversion de la biomasse.

De nombreux catalyseurs ont déjà été proposés dans la littérature pour convertir la biomasse souvent basés sur leur efficacité pour d'autres conversions connexes. Les zéolithes [14], les acides supportés [13], les hétéropolyanions [15], les oxydes métalliques [15] comme l'acide niobique ou les oxydes de tungstène ou titane, les résines échangeuses d'ions [15] ont ainsi été rapportées.

Par exemple, Aghaziarati et ses collaborateurs [16] ont révélé l'activité catalytique d'H-ZSM-5 dans la production de tétrahydrofurane par déshydratation du 1,4-butanediol. Takagaki et ses collaborateurs [17] ont montré que les résines Amberlyst 15, Nafion NR-50 et Nafion SAC-13 peuvent catalyser l'hydrolyse de disaccharides tels que le maltose, le saccharose, le cellobiose et l'amidon à 80 ºC. De plus, Du et al. [18] a révélé l'utilisation de catalyseurs WO_3/MoO_3 dans la déshydratation du glucose en 5-HMF. Li et ses collaborateurs [19] ont étudié la bonne activité catalytique de MoO_3/ZrO_2 pour l'estérification de l'acide acétique avec de l'éthanol et l'hydrolyse de l'acétate d'éthyle dans un excès d'eau.

Ces divers catalyseurs peuvent se révéler très actifs mais ils présentent également des limitations intrinsèques qui peuvent limiter leur applicabilité. Par exemple, dans le cas de zéolithes, la régénération est compliquée par la formation de coke et de goudron pendant la majeure partie du processus de pyrolyse et, par conséquent, de la désactivation de leur activité catalytique [20]. Les résines acides ou échangeuses d'ions manquent de stabilité dans les réactions hydrothermales, la présence d'eau diminue l'accessibilité des réactifs aux sites acides, ce qui réduit leur utilisation du fait des larges teneurs en eau des charges issues de la biomasse [21]. Par conséquent, les catalyseurs utilisés doivent être stables en solution aqueuse ou polaire.

Par conséquent, le développement de nouveaux types de catalyseurs solides acides présentant une activité catalytique, une sélectivité et une stabilité élevées dans les milieux aqueux reste nécessaire. Les matériaux lamellaires ou stratifiés sont des candidats prometteurs du fait de leur stabilité, d'une acidité proche de celle des oxydes conventionnels, liée aux métaux de transition permettant d'ajuster leur force et leur nombre de sites acides [22]. De plus, les composés lamellaires présentent une caractéristique unique, leur structure en couches, qui permet d'envisager l'intercalation réversible de molécules [23]. Ainsi des anions, des complexes et des produits chimiques organiques peuvent être accommodés dans l'espace interlamellaire.

Les composés lamellaires ont été utilisés depuis les débuts de l'industrie pétrochimique dans le domaine de la catalyse [24, 25]. Quelques études ont commencé à envisager leur utilisation dans les procédés de conversion de la biomasse. Par exemple, le $HNbMoO_6$ en couches présente une activité catalytique remarquable pour l'hydrolyse de saccharides tels que le sucrose, l'amidon et le cellobiose en glucose [17, 26], pour l'alkylation de Friedel-Crafts de l'alcool benzylique et l'estérification d'acides carboxyliques [17], l'acétalisation de la cyclohexanone [27], l'alkylation de Friedel-Crafts de l'anisole, du toluène ou du benzène [28, 29] comme démontré par Domen et al. Tagusagawa et al. [29] ont également montré que les couches de $HNbMoO_6$ ont une activité catalytique supérieure pour l'alkylation du toluène par rapport aux autres catalyseurs testés, tel que les nanofeuillets de $HNbMoO_6$.

Néanmoins, ces composés méritent des études spécifiques, pour évaluer leur potentiel mais également pour la caractérisation de leur acidité ou pour comprendre le rôle du processus d'intercalation dans l'activité catalytique. Ces caractérisations, celle de l'acidité notamment, ont souvent été menées en phase gazeuse; Cependant, la caractérisation en phase liquide, est nécessaire, car la plupart des processus de conversion de la biomasse se déroulent en milieu liquide ou en présence d'eau.

Plusieurs aspects liés à la valorisation de la biomasse ont été étudiés dans le chapitre 1 et mettent en évidence des opportunités et contraintes qui indiquent le besoin de catalyseurs adaptés. Il est évident que plusieurs des catalyseurs existants, tels que les zéolithes ou les oxydes, conservent un potentiel important pour l'une ou l'autre des transformations envisageables. Néanmoins, la recherche de matériaux alternatifs capables de résister aux conditions de réaction spécifiques requises reste un enjeu important. Il a été démontré que les matériaux lamellaires présentent plusieurs caractéristiques qui pourraient être appliquées de manière intéressante à ces conversions de biomasse. Les solides existants, mais également les nouveaux matériaux, devraient être étudiés de manière plus approfondie dans ce contexte. Les

données développées ici montrent que, pour ces matériaux, la compréhension du processus d'intercalation est un aspect important de leur activité.

Un autre aspect lié au développement de ces nouveaux catalyseurs est la caractérisation de ces matériaux (lamellaires), en particulier directement en phase liquide, où l'intercalation et la réaction se déroulent. Actuellement, la caractérisation des sites acides effectuée par adsorption en phase gazeuse montre ses limites et dans le cas de matériaux en couches, le contrôle direct de l'acidité en phase liquide serait bénéfique. De même, l'interaction de la molécule d'intercalation ou des réactifs avec les solides lamellaires nécessite des études spécifiques qui pourraient être fournies par spectroscopies vibrationnelles, et par Raman en particulier.

Enfin, on peut noter qu'il existe peu de réactions-test simplifiées disponibles dans la littérature pour reproduire les processus liés aux conversions de la biomasse alors que de nombreux tests standard ont été développés au fil des ans pour l'étude des composés à base de pétrole. De tels tests pourraient cependant être intéressants, notamment pour l'évaluation de matériaux en couches.

Par conséquent, ces trois aspects liés au développement et à la compréhension des matériaux lamellaires seront au centre de ce travail de thèse.

Alors que le deuxième chapitre présente rapidement les méthodes utilisées ici, le troisième chapitre est consacré à la caractérisation structurale par spectroscopie Raman (phase solide) et analyse DRX des matériaux lamellaires à base d'oxydes de métaux de transition utilisés dans la thèse : $LiNbMoO_6$, $LiNbWO_6$, Bi_2WO_6 et $Bi_2W_2O_9$ avant protonation et après modification par traitement acide. Ces oxydes lamellaires connus ont également été comparés aux solides nouvellement synthétisés qui sont basés sur des oxydes de métaux de transition Nb et W de type similaire aux phases d'Aurivillius avec une structure en forme d'escalier. La protonation de ces derniers oxydes sera également étudiée.

Dans le quatrième chapitre, le processus d'intercalation des oxydes lamellaires protonés ($HNbMoO_6$, $HNbWO_6$, H_2WO_4, $H_2W_2O_7$ et $H\text{-}Bi_{17}Nb_3W_6O_{51}$) a été étude de manière approfondie en utilisant plusieurs bases organiques telles que la pyridine, les n-alkylamines (butylamine et l'octylamine), des alcools linéaires et le 2,5-hexanediol. La pyridine et les n-alkylamines ont été utilisées pour caractériser l'acidité des matériaux tandis que l'intercalation des n-alcools et diol permet de mieux comprendre l'activité catalytique évaluée dans le chapitre suivant. Pour caractériser le processus d'intercalation, nous avons

utilisé plusieurs techniques: la spectroscopie Raman en phase liquide, l'analyse DRX et la thermogravimétrie. Ils permettent d'examiner les nteractions entre les sondes et les oxydes lamellaires, d'estimer quantitativement la quantité de molécules sonde intercalées et de comparer la force acide de tous les oxydes testés.

Dans le cinquième chapitre, une nouvelle réaction-test (cyclisation du 2,5-hexanediol en 2,5-diméthyltétrahydrofurane) a été développée. L'activité catalytique de $HNbMoO_6$, $HNbWO_6$ et $H_2W_2O_7$ a été comparée à celle d'autres catalyseurs solides acides plus classiques tels que Nb_2O_5 et plusieurs zéolithes. Cette réaction-test a également été étudiée dans différentes conditions de réaction et avec différents rapports diol/H_2O pour examiner la stabilité du catalyseur. Finalement, les catalyseurs ont été caractérisés par spectroscopie Raman et DRX afin de corréler le processus d'intercalation avec celui de l'activité catalytique.

2. Partie expérimentale

2.1. Synthèse de précurseurs d'oxydes métalliques

a. $LiNbMoO_6$ et $LiNbWO_6$: Les oxydes $LiNbMoO_6$ et $LiNbWO_6$ ont été synthétisés par réaction à l'état solide. Une quantité stœchiométrique de 0,5 mole de Li_2CO_3, 0,5 mole de Nb_2O_5 et 1 mole de WO_3/MoO_3 a été mélangée puis calcinée sous air à 1023/853K pendant 72/24 h avec un broyage intermédiaire.

b. $Bi_2W_2O_9$ et Bi_2WO_6: $Bi_2W_2O_9$ a été synthétisé par voie solide. Une quantité stœchiométrique de trioxyde de bismuth et de trioxyde de tungstène a été mélangée, broyée en une poudre fine, comprimée en pastilles, placée dans un creuset en porcelaine puis chauffée à 1023K pendant 20 h sous air pour obtenir 5 grammes de poudre de tungstate de bismuth jaunâtre.

Pour Bi_2WO_6, les quantités stœchiométriques de solutions de bismuth et de tungstate de sodium ont été obtenues en dissolvant 0,472 g de $Bi(NO_3)_3.5H_2O$ dans 50 ml d'acide nitrique et 1,39 g de $Na_2WO_4.2H_2O$ dans 50 ml d'eau distillée. Ensuite, 15 ml de chaque solution ont été mélangés dans un réacteur en téflon et chauffés dans un four à micro-ondes à 473 K pendant 4 h. Enfin, le solide a été centrifugé, lavé à l'eau distillée puis séché à l'air pour obtenir 1 gramme de poudre jaune pâle.

c. Nouveaux oxydes mixtes ($Bi_xNb_yW_zO_n$): Des oxydes lamellaires de bismuth de formule générale $Bi_{2p}A_{n-p}B_nO_{3(n+p)}$ tels que $Bi_7Nb_3WO_{21}$, $Bi_9Nb_3W_2O_{27}$, $Bi_{11}Nb_3W_3O_{33}$ et

$Bi_{17}Nb_3W_6O_{51}$ ont été synthétisés par réaction à l'état solide. Comme décrit par Steciuk et al. [30], des quantités stœchiométriques des précurseurs de Bi_2O_3, WO_3 et Nb_2O_5 de départ avec des rapports de cations Bi:W:Nb de 7:3:1, 9:3:2, 11:3:3 et 17:3:6 ont été mélangées, compactées sous forme de pastilles (3 tonnes.cm^{-2}), placés sur une plaque de platine dans un creuset en alumine puis calcinés dans un four tubulaire sous air à 1323K pendant 24 h pour obtenir les phases cristallisées.

2.2. Protonation de tous les échantillons en couches

a. $LiNbMoO_6$ et $LiNbWO_6$: $HNbMoO_6$ et $HNbWO_6$ ont été obtenus en agitant 1 g des précurseurs de lithium dans 100 ml de solution d'acide 2M (HNO_3) à température ambiante pendant 3 jours, en renouvellant l'acide une fois. Après 3 jours d'agitation, les produits ont été lavés à l'eau distillée puis séchés à l'air à 423K.

b. $Bi_2W_2O_9$ et Bi_2WO_6: $Bi_2W_2O_9$ et Bi_2WO_6 ont été mis en suspension dans une solution de HCl à une concentration de 6 M et agités à température ambiante pendant 72 h. Après 3 jours d'agitation, le mélange a été centrifugé une fois et le surnageant acide a été jeté. Les solides résultants ont été remis en suspension dans de l'acide frais, agités pendant 72 h supplémentaires, puis centrifugés et lavés à l'eau distillée avant d'être séchés à l'air à 423K.

c. Nouveaux oxydes mixtes ($Bi_xNb_yW_zO_n$): La protonation des nouveaux oxydes en couches a été étudiée ici pour la première fois. Par conséquent, pour atteindre cet objectif, plusieurs essais ont été réalisés avec différents acides (HCl, HNO_3, H_2SO_4 et H_3PO_4) de concentrations différentes et agités pendant 2 à 7 jours soit à température ambiante, soit dans un bain d'huile à 70 °C.

2.3. Techniques de caractérisation

2.3.1. Diffraction des rayons X

Tous les oxydes en couches ont été analysés qualitativement par diffraction des rayons X sur poudre (DRX) à température ambiante sur un diffractomètre PANalytical X'Pert Pro fonctionnant à 45 KV et 20 mA avec une irradiation au CuKα, λ = 1,54060 Å, comme source de rayons X. Tous les diffractogrammes ont été enregistrés sur une gamme allant de 3 à 70° (2θ) et un pas de 0,017°. Les affinements de structure ont été effectués en utilisant un programme cristallographique, JANA 2006 [31].

2.3.2. Analyse par thermogravimétrie-Infrarouge (TG-IR)

Les analyses thermogravimétriques (TGA) ont été enregistrés à l'aide d'un module d'analyse SETSYS (SETARAM, Caluire). Les échantillons ont été chauffés de la température ambiante jusqu'à 800 °C à 5 °C/min sous 40 ml/min d'air. En outre, le TGA a été couplé à la spectroscopie FT-IR, afin de quantifier simultanément la perte de masse et d'identifier avec précision le gaz dégagé à chaque étape. Les spectres infrarouges (1 spectre/minute) ont été enregistrés à l'aide d'un spectromètre infrarouge Nicolet Nexus AVATAR 360 sur une gamme allant de 400 à 4000 cm^{-1} en 32 scans avec une résolution de 4 cm^{-1}.

2.3.3. Spectroscopie Raman

La spectroscopie Raman a été d'abord utilisée pour déterminer les empreintes spectrales des solides lamellaires. Les spectres Raman ont été obtenus en conditions ambiantes sur un microscope Raman Horiba Jobin Yvon Labram 300. Un laser vert à une longueur d'onde de 532 nm a été concentré sur l'échantillon via un objectif 50x, correspondant à environ 4mW sur l'échantillon.

La spectroscopie Raman a également été utilisée en présence de liquides, comme décrit ci-dessous.

2.4. Expériences d'intercalation

Le processus d'intercalation des n-alkylamines (butylamine et octylamine), de la pyridine, des n-alcools et du 2,5-hexanediol dans les oxydes de métaux de transition lamellaires protonés a été réalisé en ajoutant le liquide à intercaler soit goutte à goutte, soit en quantités plus importantes (0,2 à 1 ml) pour 30 à 35 mg de solide à température ambiante. Puis les solides ont été analysés quotidiennement pendant la première semaine, au-delà, une fois tous les deux ou trois jours en utilisant la spectroscopie Raman en phase liquide. Cette étape a été réalisée à l'aide d'une sonde Raman (In Photonics) pouvant être directement immergée dans des solutions liquides et permettant des mesures in situ. Après caractérisation Raman, les échantillons ont été séchés, puis caractérisés par diffraction des rayons X et analyses TG pour confirmer le processus d'intercalation et quantifier la quantité de molécule intercalée dans les régions interlamellaires.

2.5. Test Catalytique

La cyclisation du 2,5-hexanediol sur les oxydes lamellaires et d'autres catalyseurs acides solides classiques (H-ZSM-5, zéolite bêta, zéolite Y et Oxyde de niobium) a été

examinée. Les zéolithes (H-ZSM-5, H-bêta et H-Y) et l'acide niobique ont été activés à 450 °C et 250 °C, respectivement, pendant 6 h avant utilisation sous flux d'air, suivies d'un flux d'argon avant transfert sur le mélange réactionnel.

La réaction a été réalisée en agitant 1 g de 2,5-hexanediol avec 56 mg de catalyseur au reflux en l'absence de solvant dans un bain d'huile à 120°C pendant 15 à 60 minutes. Au cours de la réaction, plusieurs échantillons ont été collectés à des intervalles successifs. Ensuite, les réactifs et les produits ont été analysés par chromatographie en phase gazeuse (GC-Varian 3900) équipée d'un détecteur FID et d'une colonne HP-PLOT/Q de 30 m (573K, débit: 2,0 ml/min). Après séchage, la caractérisation structurale des échantillons a été réalisée par diffraction des rayons X et spectroscopie Raman en phase solide.

De plus, l'influence de plusieurs facteurs tels que la pression, la température (80, 100, 120 ou 140°C) et le facteur de dilution (rapports molaires Diol:H_2O utilisés 1:1, 1:3, 1:10 et 1:98) sur la cinétique de la réaction a été examinée.

3. Analyse structurale et influence de la protonation

3.1. $HNbMoO_6$, $HNbWO_6$ and $H_2W_2O_7$

3.1.1. Evolution structurale lors de la protonation

Les précurseurs Li- et Bi- et les formes protonées correspondantes $HNbMoO_6$, $HNbWO_6$, $H_2W_2O_7$ et H_2WO_4 ont d'abord été caractérisés par diffraction des rayons X sur poudre (DRX). Leurs paramètres de réseau sont représentés dans le Tableau **A.1**.

Les précurseurs de Li cristallisent dans une structure tri-rutile formée de pavés octaédriques de NbO_6 et de MoO_6 incluant les ions Li^+ dans la couche intermédiaire. Leurs diagrammes DRX (Figure **A.1**) possèdent des pics de diffraction fins et intenses, caractéristiques d'une structure en couches bien ordonnée. Les plus significatifs sont ceux situés à $2\theta^o < 10^o$ attribué à la diffraction dans le plan (001) et celui à $2\theta \approx 27°$ attribué à la diffraction dans le plan (110). Leurs paramètres de réseau sont très similaires et indexés sur la base d'une maille tétragonale (groupe d'espace: P-421m).

Bi_2WO_6 et $Bi_2W_2O_9$ sont considérés comme les membres p=1 et p=2 de la famille des oxydes lamellaires au bismuth ne possédant pas de cations A, appelés phases d'Aurivillius déficientes en cations, de formule générale $(Bi_2O_2)(A_{p-1}B_pO_{3p+1})$ où p correspond au nombre

entier de feuillets d'octaèdres BO_6 liés par un sommet dans les couches pérovskite. Leurs profils de diffraction X, Figure **A.2**, montrent des pics intenses et bien définis, caractéristiques d'une structure lamellaire bien ordonnée, indexés à partir d'une cellule orthorhombique de groupe d'espace Pna_{21} ou $P2_1ab$ pour $Bi_2W_2O_9$ et Bi_2WO_6 respectivement. L'espacement entre les couches est lié à la différence d'épaisseur (p=1 ou p=2) des couches pérovskite, mais comme pour $LiNbMoO_6$ et $LiNbWO_6$, ce paramètre est un bon indicateur de tout changement survenant dans l'espace interlamellaire.

Lors de la protonation, la forme des pics DRX est beaucoup plus large, ce qui suggère que le traitement acide a affecté la cristallinité de l'échantillon en réduisant la taille des domaines de diffraction. À partir de la position des pics, on note un changement significatif dans le paramètre c indiquant la modification de l'espacement entre les couches.

Pour $HNbMoO_6.H_2O$ et $HNbWO_6.1.5H_2O$, l'espacement entre les couches a augmenté en raison du remplacement de Li^+ par H^+ et de l'intercalation simultanée de l'eau. L'échange protonique induit la transformation du réseau tétragonal primitif en un réseau tétragonal centré suite à la translation des feuillets adjacents $(M/Nb)O_6$ d'un facteur (a+b)/2.

Pour $H_2W_2O_7$ et $H_2WO_4.H_2O$, on observe un changement opposé, avec une diminution du paramètre c et de l'espacement entre les couches due à la lixiviation sélective de couches de $(Bi_2O_2)^{2+}$ par des protons. Lors du traitement acide, on a observé un changement structural dans les feuillets de type pérovskite, comme indiqué par le décalage dans les réflexions (200) et (020) et une diminution des paramètres a et b.

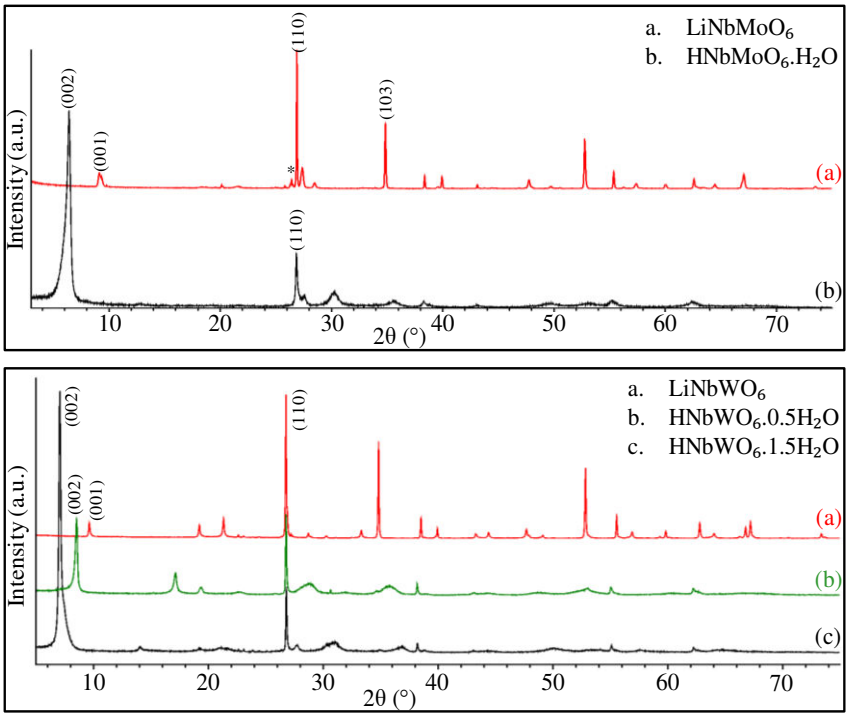

Figure A.1: DRX des précurseurs de Li et des formes protonées correspondantes. L'astérisque indique la présence d'impuretés.

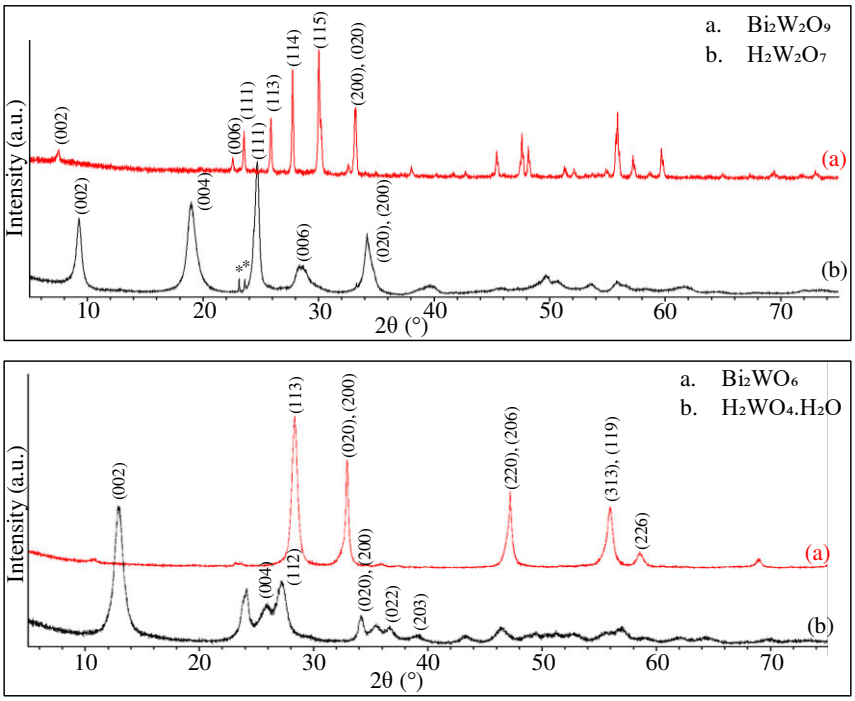

Figure A.2: DRX des précurseurs de Bi et des formes protonées correspondantes. L'astérisque indique la présence d'impuretés.

Tableau A.1**:** Paramètres de réseau de $LiNbMO_6$ (M = Mo, W) et $Bi_2W_xO_y$ et des phases protonées. La distance inter-lamellaire d est déterminée d'après le pic situé à l'angle 2θº <10º.

	Paramètres de réseau (Å)			
Composé	a	b	c	d-interlamellaire
$LiNbMoO_6$	4.6917(7)	4.6917(7)	9.243(2)	9.24
$HNbMoO_6.H_2O$	4.664(2)	4.664(2)	26.293(2)	13.15
$LiNbWO_6$	4.6831(3)	4.6831(3)	9.2792(6)	9.28
$HNbWO_6.0.5\ H_2O$	4.7157(9)	4.7157(9)	20.77(1)	10.39
$HNbWO_6.1.5\ H_2O$	4.733(2)	4.733(2)	25.47(3)	12.73
$Bi_2W_2O_9$	5.4346(3)	5.4137(1)	23.693(2)	11.85
$H_2W_2O_7$	5.197(2)	5.064(3)	18.32(1)	9.16
Bi_2WO_6	5.450(2)	5.445(2)	16.525(6)	8.26
$H_2WO_4.H_2O$	5.344(5)	5.241(4)	13.72(1)	6.86

L'ATG a également été utilisée pour évaluer le degré d'hydratation des divers composés.

3.1.2. Evolution des spectres Raman après la protonation

Les échantillons ont également été caractérisés par spectroscopie Raman afin de disposer d'informations supplémentaires sur les différents oxydes. Les oxydes mixtes $LiNbMoO_6$ et $LiNbWO_6$ présentent des spectres similaires (Figure **A.3**), avec une distinction nette entre les vibrations dues à Nb et celles dues aux bandes Mo ou W. ν(Mo=O) ou ν(W=O) situées à 932 et 957 cm^{-1} pour $LiNbMoO_6$ et $LiNbWO_6$ respectivement et les bandes ν(Nb=O) à 864 et 885 cm^{-1} pour $LiNbMoO_6$ et $LiNbWO_6$ respectivement sont clairement séparées. De plus, les bandes observées pour les deux solides sur une gamme (800 - 400 cm^{-1}) correspondent aux vibrations ν(MO) et celles situées au nombre d'onde inférieur (400 - 100 cm^{-1}) attribuées aux vibrations de déformation de MO ou MO_6 ont montré quelques différences entre les deux solides, que ce soit pour la position ou les intensités relatives.

Après échange des cations de la couche intermédiaire (Li^+) par H^+, les bandes correspondant aux vibrations d'élongation de Mo=O et W=O ainsi que Nb=O ont été décalées

vers des fréquences plus élevées pour $HNbMoO_6$ et $HNbWO_6$. En revanche, les autres bandes n'ont pas été fortement modifiées, à l'exception des vibrations de déformation $\delta(MO_6)$, δ(O-Nb-O) et $\delta(NbO_6)$ initialement situées à (408, 230-210, 168 cm^{-1}) et (407, 243, 184 cm^{-1}) pour $LiNbMoO_6$ et $LiNbWO_6$ respectivement, qui sont passés à (369, 214, 147 cm^{-1}) et (358, 233-223, 136 cm^{-1}) après protonation. Cela montre l'impact des cations interlamellaires sur la structure de ces matériaux.

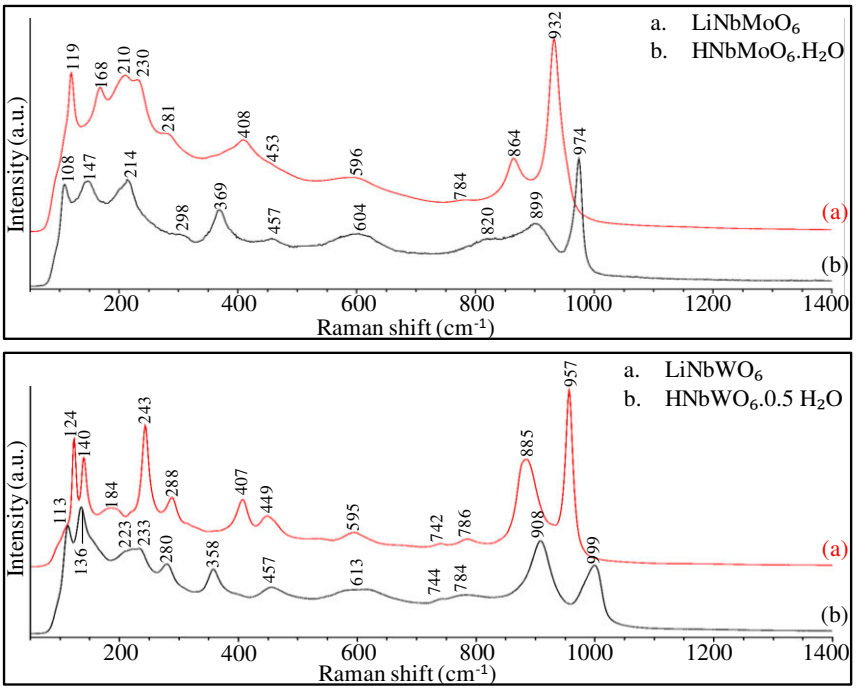

Figure A.3: Spectres Raman de $LiNbMO_6$ (M = Mo et W) et des formes protonées.

De manière similaire, $Bi_2W_2O_9$ et Bi_2WO_6 et leurs formes protonées ont été caractérisés par spectroscopie Raman. Comme on peut le voir sur la Figure **A.4** et le Tableau **A.2**. $Bi_2W_2O_9$ montre deux bandes à 800 et 854 cm^{-1}. Ceci peut être attribué à la présence de deux atomes d'oxygène apicaux dans l'octaèdre WO_6 des couches pérovskite. De même, les vibrations asymétriques WO_6, ν_{as} (W-O-W), impliquant des atomes d'oxygène équatoriaux sont clairement séparées à 697 et 741 cm^{-1}. Inversement, dans le cas de Bi_2WO_6, ces deux ensembles de bandes sont difficilement séparés à 792-818 et 702-722 cm^{-1}. Cette différence est probablement due à la différence de longueur des liaisons W-O des atomes apicaux. Les bandes situées dans la gamme 440 - 200 cm^{-1} pour les deux oxydes sont attribuées aux modes de déformation des octaèdres WO_6 et aux liaisons Bi-O des couches $(Bi_2O_2)^{2+}$ et montrent quelques différences entre elles.

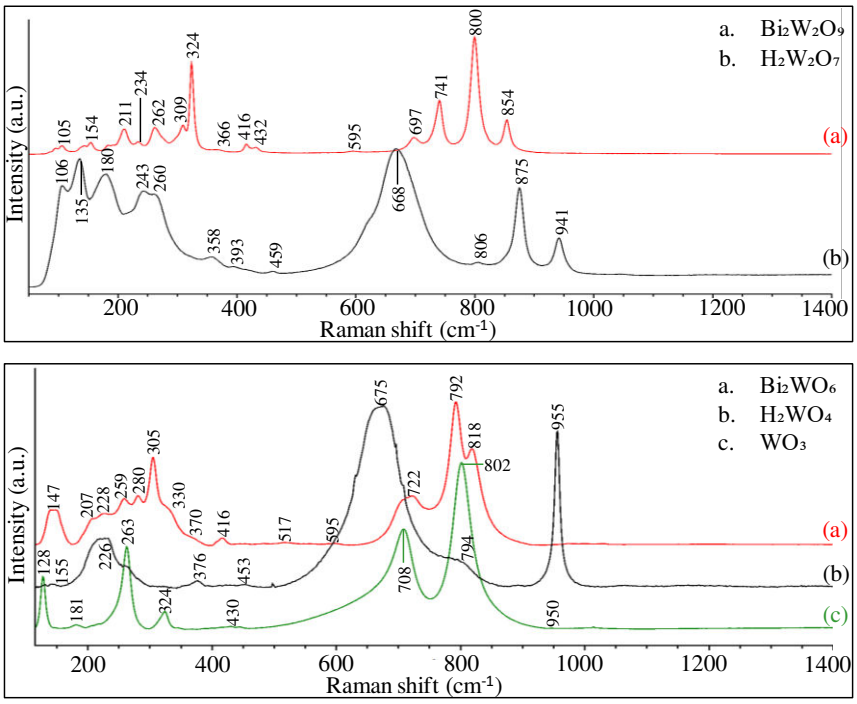

Figure A.4: Spectres Raman de $Bi_2W_xO_y$ et leurs oxydes lamellaires protonés.

Lors de la protonation, pour $Bi_2W_2O_9$, les pics attribués aux vibrations d'étirement W=O sont décalés à une fréquence inférieure en raison de la formation de composés de tungstène avec des nombres de coordination plus faibles. De même, les bandes situées à 741, 432, 324 et 234 cm^{-1} sont passées respectivement à 806, 459, 358 et 243 cm^{-1}. Au contraire, la bande rencontrée en 697 est passée à 688 cm^{-1}, tandis que celle attribuée aux vibrations d'élongation et déformation (Bi-O) à 416, 324 and 309-305 cm^{-1} ont totalement disparu en raison de la lixiviation des feuillets $Bi_2O_2^{2+}$.

Lorsque Bi_2WO_6 est protoné, $H_2WO_4.H_2O$ est formé. Dans ce cas, un pic intense centré à 955 cm^{-1} a été observé, ce qui est attribué à la liaison ν(W=O). Une large bande ν(W-O) est également observée à 675 cm^{-1}. Cette bande est significativement affectée par l'hydratation et peut être utilisée pour identifier le niveau d'hydratation des cristaux. Par exemple, si ce pic apparaît sous la forme d'un doublet, le matériau peut être identifié comme étant $WO_3.2H_2O$.

Il convient de noter que H_2WO_4 n'est pas très stable dans cet état. Une déshydratation supplémentaire, obtenue par exemple par l'utilisation d'une puissance laser plus élevée, a permis la formation rapide de WO_3 déshydraté. Dans ce cas, des bandes intenses caractéristiques sont observées à 802, 708 attribuées aux vibrations d'élongation ν(O-W-O) et les bandes à 324 et 263 cm^{-1} correspondant aux vibrations de déformation de W-O-W.

Tableau A.2**:** Positions des bandes Raman ($\Delta\nu/cm^{-1}$) et attributions. Les échantillons protonés sont indiqués en gras; M = (Mo ou W). Ces attributions ont été faites sur la base des références citées. Pour clarifier, les notations ont été unifiées entre les échantillons.

	Déplacement Raman (cm^{-1})								
	$LiNbMoO_6$	**$HNbMoO_6$**	$LiNbWO_6$	**$HNbWO_6$**	$Bi_2W_2O_9$	**$H_2W_2O_7$**	Bi_2WO_6	**H_2WO_4**	**WO_3**
Reference	32	32	33	33	34, 35	36	35, 37	36	36, 38
ν(M = O)	932	**974**	957	**999**	854 - 800	**941 - 875**	818 - 792	**955**	**950**
ν(Nb = O)	864	**899**	885	**908**					
ν(M-O-M)	784	**820**	786 - 742	**784 - 744**	741 - 697	**806 - 668**	722	**794** **675**	**802** **708**
ν(Nb-O-M)	596	**604**	595	**613**					
ν(O-Nb-O)	453	**457**	449	**457**					
δ (MO_6)	408	**369**	407	**358**	432 - 366	**459 - 393 - 358**	370	**453 - 376**	**430**
δ(M-O-Nb)/ δ(M-O-M)	281	**298**	288	**280**	262	**260 - 243**	280 - 259		**324 - 263**
δ(O-Nb-O)	230 - 210	**214**	243	**233 - 223**					
δ(NbO_6)	168	**147**	184	**136**					
ν(Bi-O)					416		416		
δ(WO_6) + δ($Bi_2O_2^{2+}$)					324 - 309 - 234 - 211		330 - 305 - 228 - 207		

3.2. Nouveaux oxydes mixtes

Tous les solides connus présentés dans la section précédente présentent l'inconvénient d'une composition chimique fixe qui n'est pas favorable à une modulation de l'activité catalytique. Par conséquent, il est intéressant d'étudier de nouveaux oxydes en couches mixtes constitués à la fois de métaux de transition Nb et W, ce qui peut affecter à la fois la quantité de sites acides et la force de l'acide.

Au cours des travaux de G. Steciuk [30], une série de nouveaux composés multicouches à base de métaux de transition Nb et W et étroitement apparentés aux phases d'Aurivillius, tels que $Bi_{17}Nb_3W_6O_{51}$, $Bi_{11}Nb_3W_3O_{33}$, $Bi_9Nb_3W_2O_{27}$ et $Bi_7Nb_3WO_{21}$, ont été synthétisés. Pour comprendre leurs caractéristiques structurales et leurs caractéristiques vibrationnelles, les échantillons nouvellement synthétisés ont été caractérisés par PXRD et spectroscopie Raman.

$Bi_{11}Nb_3W_3O_{33}$, $Bi_9Nb_3W_2O_{27}$ et $Bi_7Nb_3WO_{21}$ sont caractérisées par une séquence d'empilement de feuillets Bi_2O_2 et de couches octaédriques discontinues en raison de l'introduction de plans de cisaillement (100) menant à la formation de marches, comme l'indique la Figure **A.5**. Ces oxydes sont donc désignés par le terme de phase d'"Aurivillius en escalier" pour les distinguer des phases conventionnelles d'Aurivillius ne présentant que des couches continues.

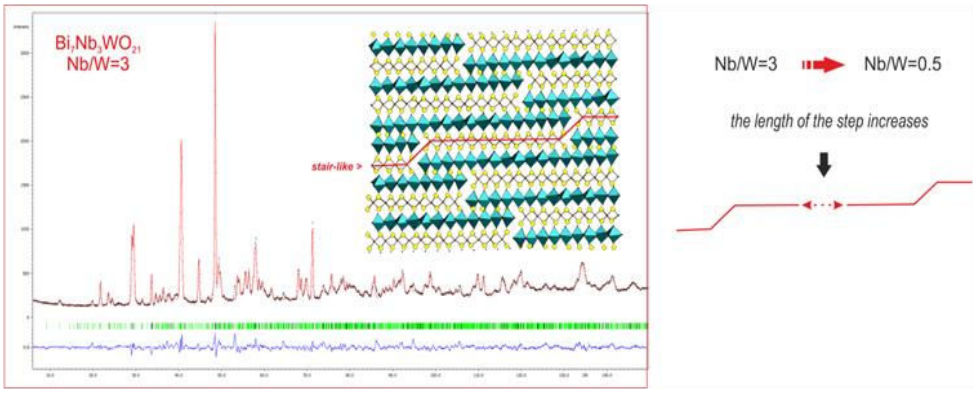

Figure A.5: Structure de $Bi_7Nb_3WO_{21}$ obtenue à partir de la diffraction de neutrons sur poudre. L'analyse structurale des nouvelles phases mixtes Nb/W indique que la longueur de la couche augmente lorsque le rapport Nb/W diminue.

La Figure **A.6(A-a)** pour $Bi_7Nb_3WO_{21}$ est représentative des diagrammes obtenus également pour $Bi_{11}Nb_3W_3O_{33}$ et $Bi_9Nb_3W_2O_{27}$. Elle indique la présence d'un pic à bas angle (2θº environ égal à 14°) et de deux pics très proches présentant les intensités les plus élevées à 28-29° caractéristiques d'un composé d'Aurivillius. Ces oxydes en couches possèdent une

maille monoclinique avec les paramètres de maille a ~ b ~ c ~ ap√2 (ap représente le paramètre de maille pour une pérovskite cubique) et un vecteur de modulation de la forme q = αa* + γc*. Les valeurs sont présentées dans le Tableau **A.3.**

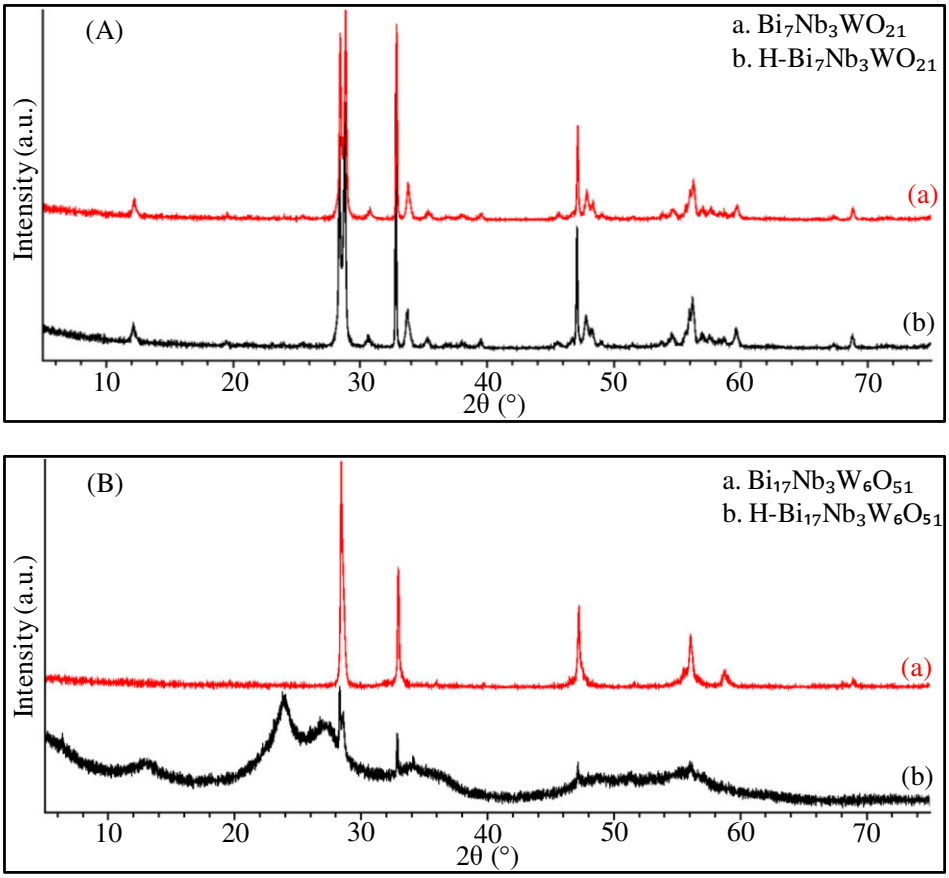

Figure A.6: DRX de $Bi_xNb_yW_zO_n$ avant et après la protonation.

Dans le cas de $Bi_{17}Nb_3W_6O_{51}$, la structure est différente de celle des trois autres composés. La Figure **A.6(B-a)** indique que les pics attribués aux phases d'Aurivillius en escalier ne sont pas présents; on observe ainsi l'absence de pics pour 2θº ~ 33 ° et des pics similaires à ceux de l'oxyde lamellaire de Bi_2WO_6. En fait, seule la forte anisotropie observée pour la plupart des pics pourrait donner à penser que $Bi_{17}Nb_3W_6O_{51}$ est différent de Bi_2WO_6. Par conséquent, $Bi_{17}Nb_3W_6O_{51}$ a été indexé sur la base d'une maille orthorhombique (paramètres de réseau indiqués dans le Tableau **A.3**) avec un groupe d'espace $P2_1ab$ comme pour Bi_2WO_6. Par conséquent, la structure de cet échantillon se rapproche de celle de Bi_2WO_6 où, si elles sont présentes, les marches sont éloignées les unes des autres, ce qui donne un composé constitué de couches presque continues (p=1). Lorsque le rapport (Nb/W) diminue, c'est-à-dire que la quantité de tungstène augmente, la structure des oxydes lamellaires Nb/W récemment découverts s'écarte donc de celle de phases en escalier pour se rapprocher des phases d'Aurivillius conventionnelles.

Tableau A.3: Données expérimentales après affinement des modèles de DRX.

	Paramètres de réseau (Å) et composantes du vecteur de modulation $q = \alpha a^* + \gamma c^*$					
Composé	a	b	c	β [°]	α	γ
$Bi_7Nb_3WO_{21}$	5.4629(7)	5.4550(7)	5.3098(9)	91.155(8)	-0.0449(3)	0.2739(4)
$Bi_9Nb_3W_2O_{27}$	5.4588(8)	5.4537(7)	5.3546(9)	91.014(8)	-0.0320(4)	0.2850(4)
$Bi_{11}Nb_3W_3O_{33}$	5.451(1)	5.450(1)	5.375(1)	90.892(9)	-0.0263(4)	0.2932(3)
$Bi_{17}Nb_3W_6O_{51}$	5.466(3)	5.454(3)	16.38(2)	-	-	-

Après leur synthèse, une étape de protonation a été effectuée afin de rendre les solides acides. Cette étape a été réalisée pour la première fois pour tous ces échantillons. Après avoir essayé différentes procédures il apparaît que la protonation de $Bi_{11}Nb_3W_3O_{33}$, $Bi_9Nb_3W_2O_{27}$ et $Bi_7Nb_3WO_{21}$ n'a pu être effectuée comme le montre la Figure **A.6(A-b)**, leur diagramme DRX restant inchangé.

Cependant, dans le cas de $Bi_{17}Nb_3W_6O_{51}$, en raison de la similitude avec Bi_2WO_6, le processus de protonation a été réalisé avec succès. Cela a été confirmé par les DRX (Figure **A.6(B-b)**). Le résultat a été confirmé par des analyses EDS réalisées dans le MET, qui ont montré que la plupart des grains ne contiennent pas de Bismuth. Par conséquent, la protonation est dans ce cas beaucoup plus facile du fait de la structure constituée de couches quasi continues, permettant ainsi un échange facile du Bi situé entre les couches W octaédriques en protons.

Parallèlement, l'étude de l'effet de différents rapports Nb/W sur la structure a été réalisée par spectroscopie Raman. Les spectres Raman des oxydes en couches $Bi_7Nb_3WO_{21}$, $Bi_9Nb_3W_2O_{27}$, $Bi_{11}Nb_3W_3O_{33}$ et $Bi_{17}Nb_3W_6O_{51}$ sont représentés dans la Figure **A.7**.

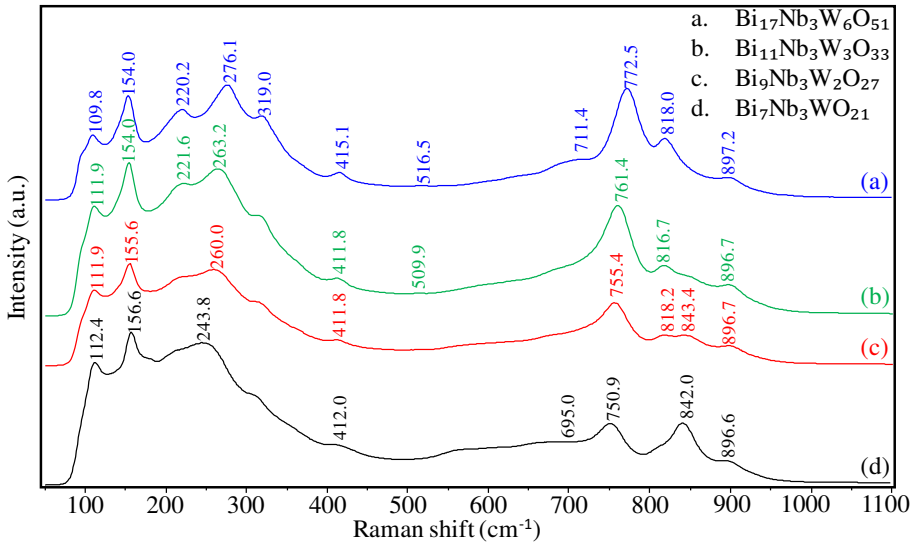

Figure A.7: Spectres Raman des oxydes $Bi_xNb_yW_zO_n$.

Tous les spectres présentent des caractéristiques similaires. Néanmoins, certaines différences peuvent être observées en fonction du rapport Nb/W. Lorsque la quantité relative de W diminué, les pics à environ 277 et 772 cm^{-1} sont décalés vers les bas déplacements Raman. Ceci s'accompagne d'un élargissement de la bande à 277 cm^{-1} vers les bas nombres d'ondes, du développement de bandes à environ 570 et 670 cm^{-1} et d'une diminution de l'intensité à 772 cm^{-1}. Par ailleurs, on observe la modification des intensités relatives de plusieurs pics avec le rapport Nb/W. Les bandes à 818 et 842 cm^{-1} en particulier ont été largement modifiées, la bande à 818 cm^{-1} a diminué lorsque W a diminué, tandis que celle à 842 cm^{-1} a augmenté. De la même manière que pour $Bi_2W_2O_9$ et Bi_2WO_6, les pics observés à env. 415 et 319 cm^{-1} pourraient être attribués à la présence de $Bi_2O_2^{2+}$.

Les spectres ont été déconvolués pour faciliter les comparaisons. Le rapport des zones de bande à 842/818 est corrélé à celui du rapport Nb/W, confirmant les assignations respectives à ν (Nb-O) et ν (W-O). La bande à 840 cm^{-1} est également liée au développement de la bande à 570 cm^{-1}. Ces bandes doivent donc être liées aux vibrations Nb-O. Les bandes à 900 et 670 cm^{-1} semblent également corrélées mais restent relativement constantes par rapport à la teneur en Nb. Compte tenu de leurs positions, elles pourraient également être liées aux vibrations (Nb-O). Il est à noter que les composés à base de $Bi_xNb_2O_9$ montrent leurs bandes principales dans cette région autour de 820-840 et 560 cm^{-1}. Les composés basés sur des unités Nb_2O_6 ont tendance à montrer des bandes supérieures à 600 et 850-870 cm^{-1}. Les bandes à 840 et 570 cm^{-1} pourraient ainsi être attribuées aux vibrations Nb-O pour les zones p=2 où 2 couches d'oxyde de niobium se superposent, tandis que les bandes à 900 et 670 cm^{-1} pourraient être dues à des zones p=1 où l'oxyde de niobium apparaît comme une seule couche.

De même, la bande à 818 cm^{-1} pourrait être due à des vibrations W-O pour les zones p=2 où deux couches d'oxyde de tungstène sont superposées. Cette bande n'a montré aucune corrélation avec aucune autre bande. Néanmoins, les bandes à 772 et 277 cm^{-1} sont corrélées et décalées avec le rapport W/Nb, ce qui indique une contribution probable des vibrations Nb-O et W-O, notamment dans la zone de superposition. Sur ces bases, une attribution des bandes Raman a donc pu être proposée pour la première fois pour ces nouveaux matériaux.

4. Intercalation et Acidité

4.1. Intercalation d'alkylamines et de pyridine en oxydes en couches connus

4.1.1. Intercalation de n-alkylamine

4.1.1.1. Caractérisation structurale

Les capacités d'intercalation des différents oxydes de métaux de transition , $HNbMoO_6$, $HNbWO_6$, $H_2W_2O_7$ et H_2WO_4 ontété examinées à l'aide de substrats contenant de l'azote, tels que des n-alkylamines et de la pyridine, et mis en évidence par diffraction des rayons X et spectroscopie Raman.

On voit sur la Figure **A.8** que lors de l'intercalation des n-alkylamines dans $HNbMoO_6.H_2O$ et $HNbWO_6.1.5H_2O$, des pics de diffraction intenses et fins dans des régions à bas angle sont clairement visibles. Ces réflexions sont de type (00l) et leur nombre augmente avec l'augmentation du nombre de carbone de la chaîne n-alkyle, ce qui indique une augmentation de l'ordre à longue distance. De plus, des pics de diffraction de type (hk0) sont également présents, (110) se situant au même endroit que celui des solides hydratés protonés correspondant, indiquant que la structure tétragonale est préservée lors de l'intercalation. L'espacement entre les couches a augmenté de 13,15 à 20,49 et 28,6 Å pour $HNbMoO_6$ et de 12,73 à 20,18 et 30,6 Å pour $HNbWO_6$ après intercalation de butylamine et d'octylamine, respectivement.

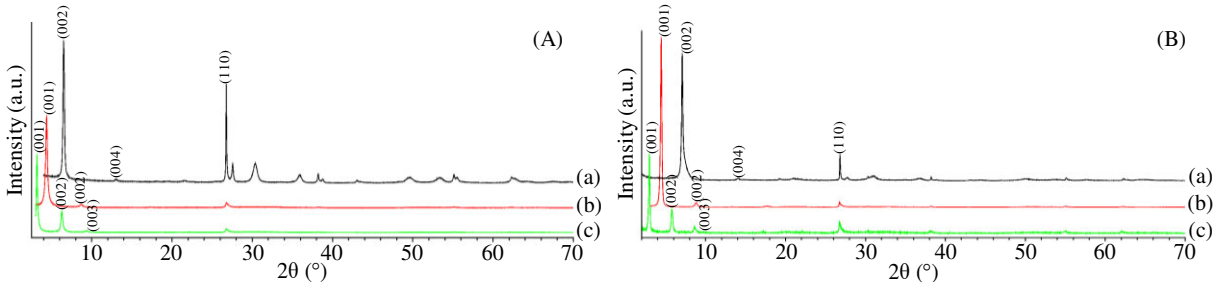

Figure A.8: DRX de (a) l'échantillon protoné pour (A) $HNbMoO_6$ et (B) $HNbWO_6$ avant intercalation et après intercalation avec de la butylamine (b) et de l'octylamine (c).

De manière similaire, avec $H_2W_2O_7$ et $H_2WO_4.H_2O$, (Figure **A.9)**, les pics de diffraction du solide disparaissent lors de l'ajout de butylamine et d'octylamine et une nouvelle série de réflexions fortes (00l) avec des pics bien définis est observée aux bas angles La distance interlamellaire augmente ainsi de 9,16 Å pour $H_2W_2O_7$ à 16,20 ou 26,04 Å et de 6,86 Å à 16,08 et 26,06 Å lors de l'ajout de butylamine ou d'octylamine respectivement.

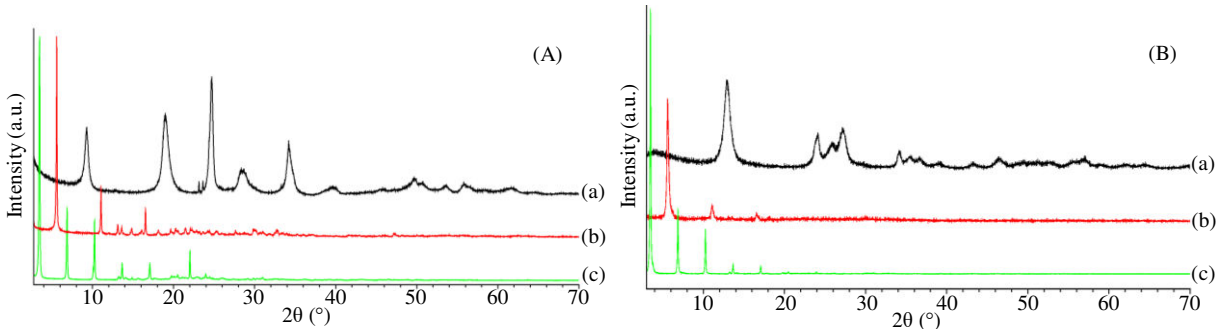

Figure A.9: DRX de (a) l'échantillon protoné pour (A) $H_2W_2O_7$ et (B) $H_2WO_4.H_2O$ avant intercalation et après intercalation avec de la butylamine (b) et de l'octylamine (c).

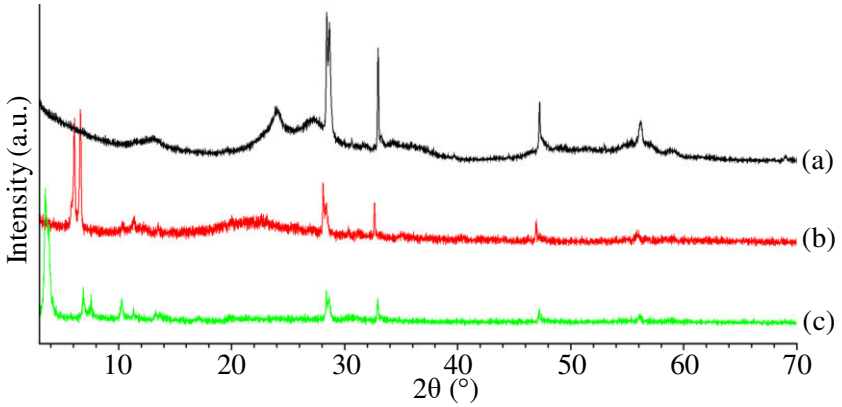

Figure A.10: DRX de H-$Bi_{17}Nb_3W_6O_{51}$ avant intercalation (a) et après intercalation avec la butylamine (b) et l'octylamine (c).

Lors de l'intercalation des n-alkylamines dans H-$Bi_{17}Nb_3W_6O_{51}$, plusieurs changements dans les diffractogrammes ont été observés (Figure **A.10**). Les larges bandes de

l'oxyde d'origine situées à 13, 24 et 27° ont totalement disparu et les bandes intenses présentes à 28, 32, 47 et 56° ont diminué en intensité. En outre, deux nouveaux pics intenses très proches apparaissent dans des régions à angle bas. Ceci suggère que les n-alkylamines sont intercalées dans l'oxyde en couches H-$Bi_{17}Nb_3W_6O_{51}$ avec la co-existence de deux intercalations différentes pour deux espacements d de l'intercouche.

4.1.1.2. Quantification

Pour quantifier la quantité d'amine intercalée dans les oxydes, on a utilisé la thermogravimétrie couplée à l'IR.

La plus grande quantité de n-alkylamines est désorbée en dessous de 210 °C. La quantité totale intercalée dans $H_2W_2O_7$ calculée entre la température ambiante et 600 °C est approximativement égale à 1,4 mole/mole et 5 mole/mole d'échantillon déshydraté dans le cas de la butylamine et de l'octylamine, respectivement.

De même, la quantité de n-alkylamines intercalée entre les couches de $HNbMoO_6$ et $HNbWO_6$ a été évaluée à 0,52 mole/mole de $HNbMoO_6$ déshydraté et à 0,59 mole/mole de $HNbWO_6$ déshydraté pour le butylamine et à 0,48 mole/mole de $HNbMoO_6$ déshydraté et à 0,5 mol/mol de $HNbWO_6$ déshydraté pour l'octylamine.

4.1.1.3. Caractérisation spectroscopique

La spectroscopie Raman en phase liquide a été utilisée pour surveiller simultanément les changements structuraux rencontrés lors de l'intercalation des n-alkylamines et pour évaluer l'acidité des oxydes protonés.

Après addition de butylamine, les bandes correspondant à M=O (M=Mo, W) et Nb=O sont passées respectivement de 974 et 902 à 966 et 896 cm^{-1} dans le $HNbMoO_6$ et de 990 et 905 à 976 et 899 cm^{-1} dans $HNbWO_6$ (Figure **A.11**). Cela indique une interaction entre l'amine et les liaisons apicales M=O et Nb=O du réseau. En parallèle, les bandes de l'amine ont également subi des modifications autour de 3300 cm^{-1}, où des bandes d'élongation NH_2 antisymétriques et symétriques ν(NH) à 3380 et 3325 cm^{-1} ont diminué avec le développement d'une bande autour de (3080 - 3100 cm^{-1}) en raison de la protonation des groupes amine pour former des ions ammonium. Cette interaction garantit l'adsorption des alkylamines dans la région interlamellaire des échantillons protonés. Cela implique également que les sites acides se trouvent à proximité immédiate des liaisons Mo(W)=O ou Nb=O. Des résultats similaires ont été observés lors de l'intercalation d'octylamine.

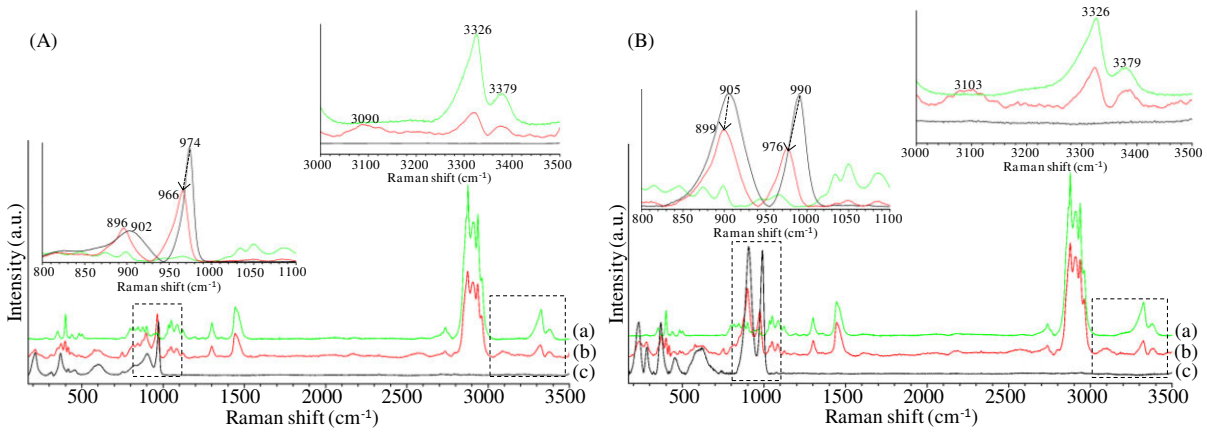

Figure A.11: Spectres Raman (200 - 3500 cm^{-1}) de (a) butylamine, (b) solide + butylamine et (c) solide pour (A): $HNbMoO_6$ et (B) $HNbWO_6$, avant et après intercalation. Les inserts montrent des agrandissements du spectre entre (800 - 1100 cm^{-1}).

L'interaction entre $H_2W_2O_7$ et l'octylamine ou la butylamine montre des résultats différents de ceux de $HNbMoO_6$ et $HNbWO_6$. Les spectres Raman de $H_2W_2O_7$ évoluent progressivement avec le temps après l'intercalation de la butylamine, comme illustré à la Figure **A.12**. La bande ν(W=O) à 942 cm^{-1} diminue et se déplace à 920 cm^{-1}. Parallèlement les bandes antisymétriques et symétriques de NH_2 de butylamine pure situées à 3380 et 3325 cm^{-1} diminuent en intensité et une nouvelle bande située à 3095 cm^{-1} apparaît suite à la protonation des groupes amine pour former des ions ammonium. Ces changements cohérents impliquent que l'amine interagit d'abord avec le W apical de $H_2W_2O_7$.

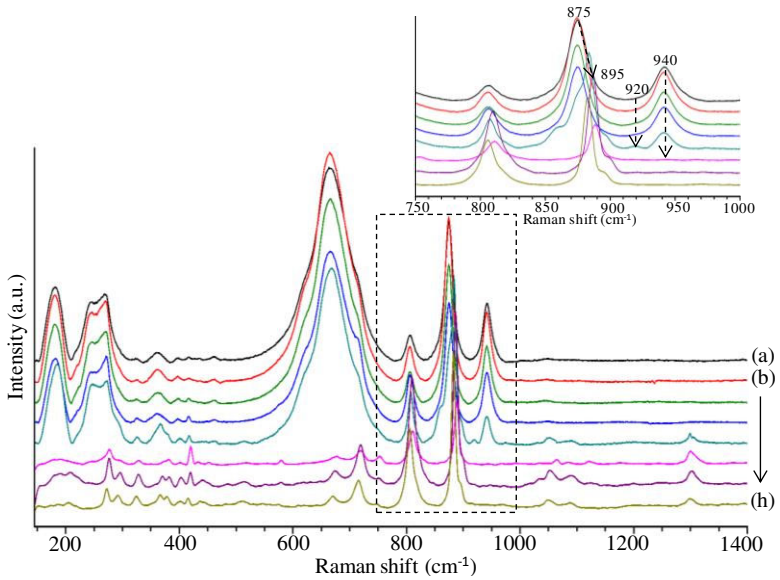

Figure A.12: Evolution progressive avec le temps des spectres Raman de (a) $H_2W_2O_7$ et (b - h) après addition de butylamine. L'encart montre l'agrandissement à (750 - 1000 cm^{-1}).

Dans un deuxième temps, les bandes à 920 - 942 cm^{-1} disparaissent progressivement tandis que la bande passe de 875 à 895 cm^{-1} et que la bande large à 670 cm^{-1} diminue fortement. Parallèlement, de nouvelles bandes se sont développées à 805, 714 et 268 cm^{-1}. Cet ensemble de bandes peut être attribué à la présence de WO_3, alors que des bandes à environ 900 cm^{-1} peuvent être trouvées pour les composés basés sur WO_4. Des résultats similaires ont été obtenus avec l'octylamine. On peut noter que des études antérieures de Chen et al.[39, 40] ont proposé un mécanisme de dissolution-réorganisation des couches W-O octaédriques doubles de $H_2W_2O_7$ lors de la réaction avec des n-alkylamines. Après intercalation de n-alkylamine dans une première étape, les molécules d'eau intercalaires peuvent être libérées et réagir avec les molécules de n-alkylamine environnantes en formant des solutions hautement alcalines qui induisent la dissolution des couches W-O à double octaèdre. Les espèces dissoutes recristallisent ensuite pour former des empilements de couches octaédriques W-O uniques, de façon similaire à ce qui a été observé pour l'interaction entre les n-alkylamines et H_2WO_4.

Le comportement d'intercalation des n-alkylamines dans H_2WO_4 a également été examiné, car ce dernier oxyde est constitué uniquement de feuillets octaédriques simples (W-O). Des résultats similaires à ceux rencontrés avec $H_2W_2O_7$ ont été obtenus. Par conséquent, on peut conclure que les composés résultants lors de l'intercalation de n-alkylamines dans $H_2W_2O_7$ ou H_2WO_4 sont identiques, c'est-à-dire qu'ils sont tous deux construits en empilant alternativement des bicouches de n-alkylammonium et une seule couche octaédrique (W-O).

De plus, l'intercalation des n-alkylamines dans le nouvel oxyde mixte (Nb/W) ($H-Bi_{17}Nb_3W_6O_{51}$) a également été examinée. Des résultats comparables à ceux de $H_2W_2O_7$ et H_2WO_4 ont été obtenus, tant au niveau des bandes du solide que des bandes liées aux alkylamines.

4.1.2. Intercalation de pyridine

4.1.2.1. Caractérisation structurale

En plus des n-alkylamines, la pyridine a été choisie en raison de sa double fonction de molécule intercalante et comme sonde moléculaire basique pour discriminer entre les différents sites acides. Cependant, la caractérisation détaillée des sites actifs a rarement été conduite en phase liquide, ce qui a été fait dans ce travail enutilisant la spectroscopie Raman en phase liquide.

Les échantillons ont été séchés et caractérisés par DRX afin de surveiller simultanément l'intercalation et les changements structuraux. La Figure **A.13** montre que

l'immersion des échantillons protonés dans la pyridine entraîne un décalage du premier pic vers les bas angles, passant de 6,40° à 5,89° pour $HNbMoO_6$ et de 8,51° à 6,44° pour $HNbWO_6$, ce qui correspond à une augmentation de l'écartement de l'espace interlamellaire de 13,15 à 15,06Å et de 10,39 à 13,71 Å pour $HNbMoO_6$ et $HNbWO_6$ respectivement. Inversement, des pics de diffraction (110) sont observés à la même position dans les deux cas, ce qui indique que la structure tétragonale est préservée et que les couches ne sont dilatées que par la présence de pyridine.

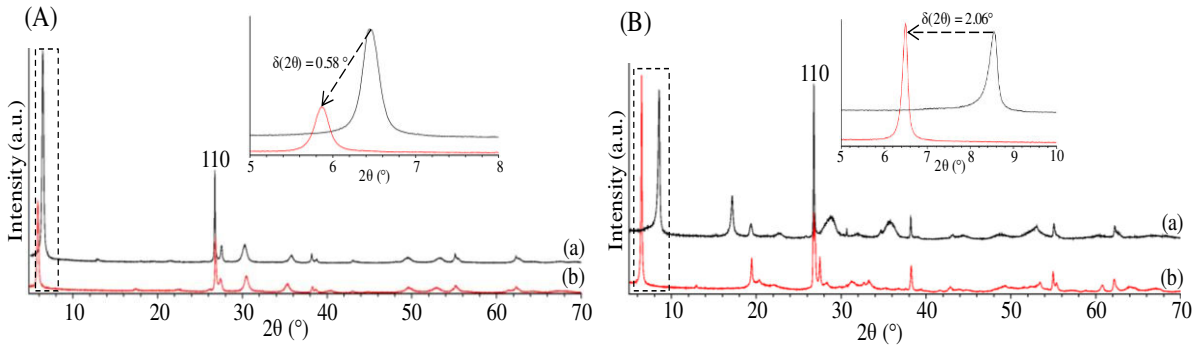

Figure A.13: DRX de (A) $HNbMoO_6$ et (B) $HNbWO_6$, (a) avant et (b) après intercalation avec de la pyridine. L'encart montre l'agrandissement aux bas angles.

Dans le cas de H_2WO_4 et $H\text{-}Bi_{17}Nb_3W_6O_{51}$, l'intercalation de pyridine a également été confirmée par l'augmentation de l'espacement entre les couches. Contrairement aux résultats obtenus avec ces derniers oxydes mixtes, l'intercalation de la pyridine dans l'oxyde lamellaire de $H_2W_2O_7$ n'a pas été possible.

La thermogravimétrie a été utilisée pour quantifier les quantités de pyridine adsorbées pour $HNbMoO_6$ et $HNbWO_6$. Ces résultats ne montrent cependant pas de différence majeure entre ces solides.

4.1.2.2. Caractérisation spectroscopique

Contrairement aux résultats obtenus avec les oxydes lamellaires $HNbMoO_6$ et $HNbWO_6$, lors de l'ajout de pyridine à $H_2W_2O_7$, aucun changement n'a été observé sur les spectres Raman. Les bandes dues à $H_2W_2O_7$ et à la pyridine se sont simplement ajoutées les unes aux autres, sans décalage dans les bandes d'origine du solide hôte ni apparition de nouveaux pics. Ces résultats ont confirmé l'absence d'interaction entre la pyridine et $H_2W_2O_7$. Cela implique également que les éventuels sites acides extérieurs situés à la surface des cristaux ne sont pas en mesure de protoner la pyridine, car trop faibles ou trop peu nombreux.

Lors de l'intercalation de $HNbMoO_6$ et $HNbWO_6$ avec de la pyridine, plusieurs modifications ont été observées au niveau des solides et de l'intercalant (Figure **A.14**). La pyridine liquide est observée par spectroscopie Raman à 991 et 1031 cm^{-1}. Ces bandes sont dûes respectivement aux modes ν1 et ν12 des vibrations ν(CCN). Il a été démontré qu'elles se déplaçaient en fonction des sites acides coordonnés à la pyridine, notamment le mode ν1, qui peut passer de 990 à 1030 cm^{-1} en fonction du matériau et du type d'acidité, Brønsted ou Lewis. En présence de $HNbMoO_6$, en plus des pics dûs à la pyridine liquide, de nouveaux pics se sont développés à 1001 et 1012 cm^{-1}. Dans le cas de $HNbWO_6$, ces pics étaient à environ 1000 et 1020 cm^{-1}. Les pics à 996 - 1005 cm^{-1} ont été attribués à la pyridine en liaison Hydrogène par Ferwerda et al.[41] tandis que les sites acides de Brønsted et de Lewis devraient conduire à des bandes comprises respectivement entre 1006 et 1015 et entre 1016 et 1028 cm^{-1}. Compte tenu des caractéristiques intrinsèques similaires de $HNbMoO_6$ et $HNbWO_6$, il est peu probable qu'ils présentent un type d'acidité différent. Les deux devraient présenter de l'acidité de Brønsted. De plus, la bande d'élongation de Mo=O est passée de 973 à 967 cm^{-1} et celle de W=O de 991 à 981 cm^{-1}. Dans le même temps, il est à noter qu'aucun changement de ce type n'a été observé pour la vibration (Nb=O) à env. 900 cm^{-1}. Par conséquent, la plus forte acidité de Brønsted capable de protoner la pyridine peut être trouvée au voisinage des sites W=O ou Mo=O. Les sites acides forts sont donc plus susceptibles d'être associés à l'environnement Mo(W)=O. En revanche, les protons situés au voisinage des liaisons Nb=O sont probablement plus faibles et ne peuvent interagir qu'avec des bases plus fortes telles que les alkylamines, qui a induit le déplacement des bandes Nb=O.

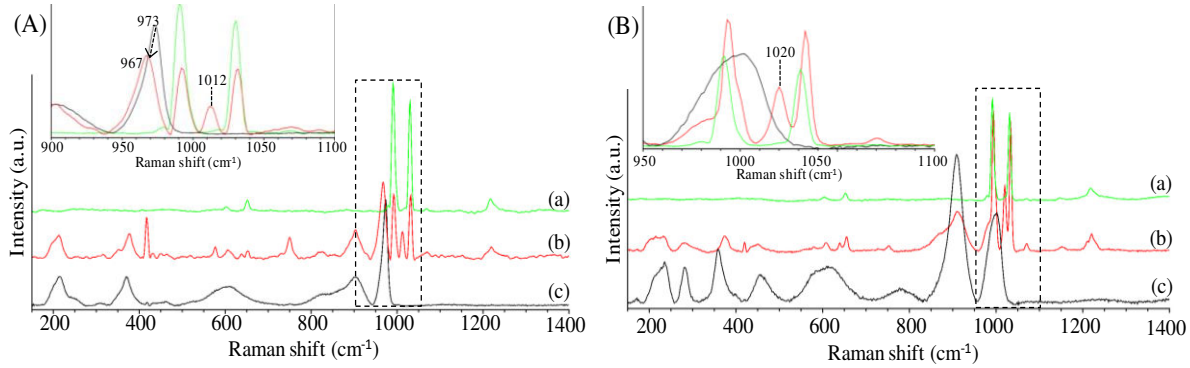

Figure A.14: Spectres Raman de (a) pyridine, (b) solide protoné + pyridine et (c) solide protoné. L'encart montre l'agrandissement dans la région 800 - 1100 cm^{-1}. L'échantillon protoné dans (A) est $HNbMoO_6$ et dans (B) est $HNbWO_6$.

De manière similaire aux oxydes lamellaires $HNbMoO_6$ et $HNbWO_6$, l'ajout de pyridine dans H_2WO_4 a révélé plusieurs modifications. Les pics à 959 et 675 ont été décalés

vers 938 et 639 cm^{-1}. Les bandes de pyridine liquide sont également passées de 990 et 1031 à 993 et 1035 cm^{-1}, en plus de la présence d'un nouveau pic développé à 1015 cm^{-1} entre les deux dernières, ce qui peut être attribué à l'acidité de Lewis. Ces résultats peuvent indiquer l'interaction entre la pyridine et les bandes (W-O) du solide.

4.2. Intercalation des n-alcools et hexanediol

L'intercalation des n-alcools et du 2,5-hexanediol dans les oxydes lamellaires de $HNbMoO_6$, $HNbWO_6$ et $H_2W_2O_7$ à des températures variables a également été examinée à l'aide de la spectroscopie Raman en phase liquide ou solide lorsque l'intercalation a été réalisée à la température ambiante ou à des températures plus élevées. Ces bases organiques sont intéressantes car elles ouvrent la voie à la compréhension de l'activité catalytique avec ce type de réactifs.

4.2.1. Caractérisation de l'intercalation à température ambiante

4.2.1.1. Caractérisation structurale

Les échantillons ont d'abord été caractérisés par des PXRD afin d'étudier le processus d'intercalation. Ensuite, les résultats spectroscopiques Raman, destinés à caractériser l'interaction entre les solide-adsorbant, ont été examinés.

Lors de l'ajout de n-alcools et de 2,5-hexanediol au sein des couches de $HNbMoO_6$ et $HNbWO_6$ à température ambiante, plusieurs modifications des diffractogrammes ont été constatées. Avec $HNbMoO_6$, les diffractogrammes en présence d'alcools à chaîne courte (éthanol, propanol et butanol) montrent une très légère augmentation de l'espacement entre les couches comparativement à l'oxyde hydraté protoné. En présence d'alcools à chaîne plus longue, l'espacement entre les couches augmente avec la chaîne carbonée.

Avec $HNbWO_6$, seul l'éthanol est en mesure d'être complètement intercalé (les DRX montrent un seul pic dans la région à bas angle, inférieur à celui de l'oxyde parent). Toutefois, avec le propanol, le butanol et l'hexanol, deux pics sont observés, l'un à la même position que celle de l'oxyde parent et l'autre à la position la plus basse, indiquant une intercalation partielle. Dans le cas de l'octanol, plusieurs pics intenses, attribués à des réflexions (00l) sont observés. Au contraire, avec le 2,5-hexanediol, aucune intercalation n'a eu lieu.

A l'inverse, ni les n-alcools ni le 2,5-hexanediol ne peuvent s'intercaler dans la structure de $H_2W_2O_7$.

Le processus d'intercalation a également été examiné à des températures plus élevées: 60, 80 et 100°C afin d'examiner les variations induites pour $HNbMoO_6$ et $HNbWO_6$.

Dans le cas d'$HNbMoO_6$ à 60°C, l'intercalation de tous les alcools montre un seul pic aux angles < 10 °. Ce pic se décale vers les bas angles à mesure que le nombre d'atomes de carbone de la chaîne alcool augmente, associé à une augmentation de l'espacement entre les couches. Dans ce cas, le décalage du pic de réflexion (001) était beaucoup plus élevé que ceux obtenus à la température ambiante. Par conséquent, une température plus élevée facilite la pénétration des alcools dans la région interlamellaire de $HNbMoO_6$ sans autre changement structural car. Le décalage s'amplifie avec la température (à 80 et 100ºC) pour le propanol, l'octanol et le 2,5-hexanediol, indiquant une intercalation plus importante.

Avec $HNbWO_6$, après ajout d'éthanol et de propanol à 60°C, le pic de diffraction (001) a été décalé vers les bas angles, indiquant une augmentation de l'espacement entre les couches. Pour le butanol et l'hexanol, on observe deux pics comme à température ambiante mais le pic à bas angle est décalé indiquant un espacement plus important entre les couches. Avec l'octanol et l'hexanediol, aucune intercalation n'a été observée. Par conséquent, on peut supposer que des températures plus élevées peuvent faciliter le processus d'intercalation des alcools à chaîne courte dans les régions intercouches. Cependant, cela reste insuffisant pour les alcools à chaîne longue, induisant soit une intercalation partielle comme dans le cas du butanol et de l'hexanol, soit aucune intercalation comme dans le cas de l'octanol et du 2,5-hexanediol. Des résultats similaires ont été obtenus avec le propanol, l'octanol et le 2,5-hexanediol à 80 et 100ºC, l'intercalation du propanol augmentant avec la température alors qu'elle n'intervient pas dans le cas de l'octanol et du 2,5-hexanediol.

L'intercalation partielle ou son absence pourrait être attribuée à la différence entre le diamètre cinétique des molécules de n-alcool et la distance interlamellaire des oxydes [42].

Tableau A.4: Distance inter lamellaire des $HNbMoO_6$ et $HNbWO_6$ après intercalation avec des n-alcools et du 2,5-hexanediol à 100ºC.

Compound	d-interlayer (Å)
$HNbMoO_6.H_2O$	13.71(3)
$HNbMoO_6.H_2O$ + propanol	15.55(3)
$HNbMoO_6.H_2O$ + octanol	21.3(2)
$HNbMoO_6.H_2O$ + 2,5-hexanediol	19.5(2)
$HNbWO_6.1.5H_2O$	12.79(2)
$HNbWO_6.1.5H_2O$ + propanol	15.58(5)
$HNbWO_6.1.5H_2O$ + octanol	12.74(3)
$HNbWO_6.1.5H_2O$ + 2,5-hexanediol	12.81(1)

Avec $H_2W_2O_7$, aucune intercalation n'a eu lieu ni avec les n-alcools ni avec le 2,5-hexanediol à 60, 80 ou 100°C. Cela implique que les sites acides extérieurs sont trop faibles ou trop rares pour permettre leur intercalation.

4.2.1.2. Caractérisation spectroscopique

La spectroscopie Raman en phase liquide a également été utilisée pour caractériser l'interaction entre les alcools et les oxydes ($HNbMoO_6$ et $HNbWO_6$).

Aucun changement n'est observé en Raman lors de l'ajout de n-alcools ou d'hexanediol à $H_2W_2O_7$ et les bandes des alcools sont difficilement observables. Ceci confirme les résultats de la DRX indiquant qu'aucune intercalation n'a lieu pour ce solide.

Les spectres Raman de $HNbMoO_6$ et $HNbWO_6$ ont révélé que lors de l'ajout de n-alcools ou de 2,5-hexanediol à la température ambiante, un très léger décalage du pic M=O (M=Mo, W) et Nb=O a été observé. Cette technique a également été utilisés lors des intercalations dans le $HNbMoO_6$ à des températures plus élevées; toutefois, seuls les pics de liquide étant présents et aucune information ne pouvant être déduite concernant le solide, les échantillons ont été finalement séchés et caractérisés par spectroscopie Raman de la phase solide.

Les résultats révèlent que l'ajout d'alcool au $HNbMoO_6$ à 60°C entraîne un déplacement de la bande (Mo=O) vers le haut (dans le cas de l'éthanol et du propanol, il passe

de 972 à 984 et 985 cm^{-1} respectivement). Avec l'hexanediol, 2 pics de (Mo=O) ont été observés à 979 et 1000 cm^{-1}. Cela pourrait être attribué à l'interaction différenciée des deux fonctions alcool. En plus de cela, un élargissement de (Nb=O) avec un décalage vers les nombres d'ondes inférieurs a été observé. Par conséquent, ces résultats peuvent confirmer l'interaction entre M=O et Nb=O avec le groupe OH de l'espèce intecalée. Des résultats similaires ont été obtenus lors de l'ajout d'alcool à $HNbMoO_6$ à 80 et 100ºC. (Mo=O) s'est déplacé vers des nombres d'onde plus élevés lors de l'addition d'alcool et de diol. Cela garantit donc l'adsorption des alcools dans la région interlamellaire.

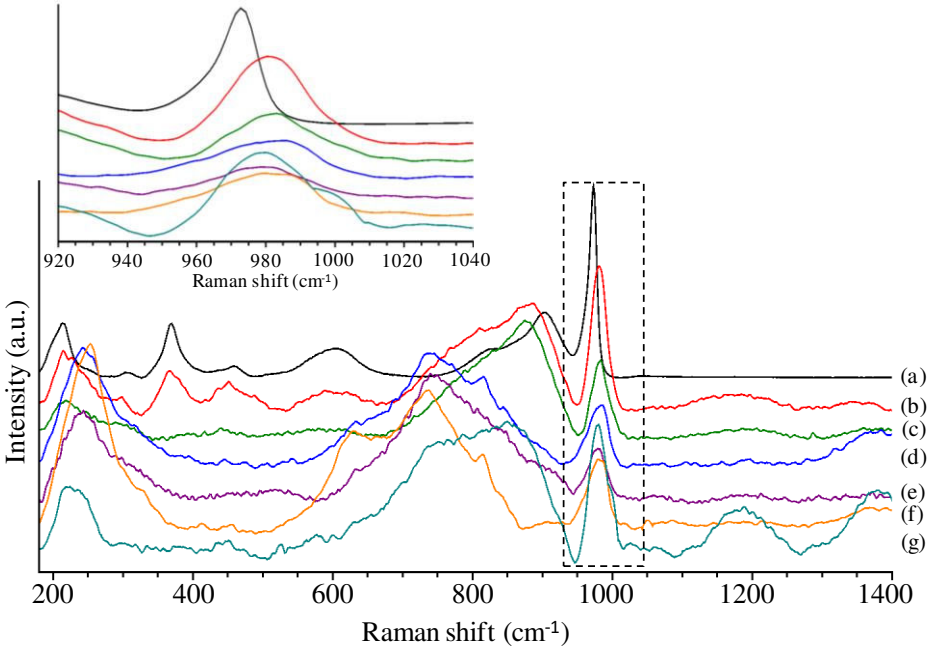

Figure A.15: Spectres Raman de (a) $HNbMoO_6$ parent chauffé à 60ºC et après intercalation d'alcool et de diols à 60°C: (b) éthanol, (c) propanol, (d) butanol, (e) hexanol, (f) octanol et (g) l'hexanediol. L'encart montre l'agrandissement de la région 920 - 1040 cm^{-1}.

5. Développement d'une réaction test et relation avec l'intercalation

5.1. Cyclisation de l'hexanediol: une nouvelle réaction test

5.1.1. Caractéristiques générales et influence des paramètres de réaction

5.1.1.1 Conversion catalytique sur divers catalyseurs acides solides à 120°C.

La cyclodéshydratation du 2,5-hexanediol en phase liquide, en cis et en trans-2,5-diméthyltétrahydrofurane, a été examinée en présence de divers catalyseurs solides acides (rapport catalyseur/diol = 0,05) (Figure **A.16**).

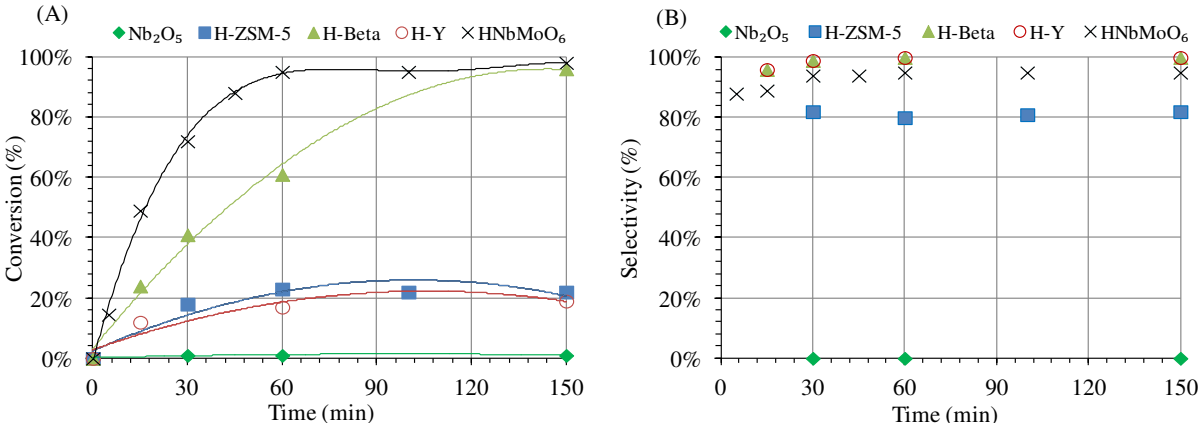

Figure A.16: (A) Conversion catalytique et (B) sélectivité du 2,5-hexanediol à 120°C en fonction du temps sur divers catalyseurs acides solides.

En l'absence de catalyseur, aucune activité n'est observée. Dans le cas de $HNbMoO_6$, on observe une consommation rapide du réactif dès le début de la réaction (15% après 5 minutes), puis la conversion augmente jusqu'à atteindre 50% après 15 minutes et 95% après 60 minutes. Inversement Nb_2O_5 est quasiment inactif. Parmi les zéolithes, H-Y a révélé l'activité la plus faible (17% après 30 minutes sans conversion supplémentaire après 150 minutes). H-ZSM-5 a permis une conversion légèrement plus élevée, mais toujours modérée (23% après 60 minutes et conversion constante après 150 minutes). Au contraire, une conversion relativement élevée a été observée avec la zéolite H-beta (61% après 60 minutes, puis 96% après 150 minutes). Par conséquent, l'ordre des catalyseurs actifs peut être représenté comme suit: $HNbMoO_6$ > H-Beta > H-ZSM-5 > H-Y > Nb_2O_5.

De plus, tous les catalyseurs actifs présentent une sélectivité élevée. Avec $HNbMoO_6$, la sélectivité est de 94% après 60 minutes. Les zéolithes H-Beta et H-Y montrent une

sélectivité de 100%, alors que H-ZSM-5 présente une sélectivité de 82% du début à la fin de la réaction. Par conséquent, la sélectivité peut être représentée dans l'ordre suivant: H-Bêta (100%) = H-Y (100%)> $HNbMoO_6$ (92%)> ZSM-5 (82%).

L'activité catalytique la plus élevée a été obtenue avec $HNbMoO_6$, en raison de sa capacité d'intercalation. Ceci est confirmé par les résultats de diffraction des rayons X sur les solides en cours de réaction (Figure **A.17**), qui indiquent une augmentation de l'espacement entre les couches après réaction.

	d-interlayer (Å)		
Time (min)	Initial	Phase 1	Phase 2
0	13.84(4)		
15		14.86(2)	-
30		14.50(3)	15.75(6)
45		14.76(3)	15.75(5)
60		14.73(7)	16.19(2)
150		-	16.45(6)

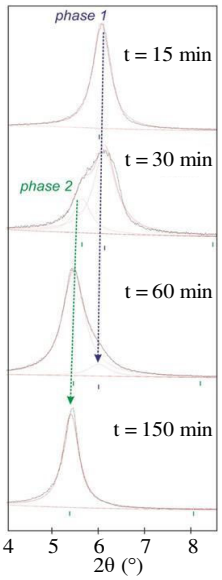

Figure A.17: Evolution de l'espacement inter-couches (Å) de HNbMoO6 après réaction du diol à 120°C à intervalles successifs.

5.1.1.2. Influence de la température et de la pression

Les performances de $HNbMoO_6$ ont été évaluées à différentes températures (80, 100, 120 et 140 °C). Les résultats montrent que la conversion augmente rapidement à 140 et 120 °C, pour atteindre une conversion presque totale (95%) après 30 et 60 minutes, respectivement. Cependant, à des températures plus basses, la conversion augmente régulièrement et on trouve 95% après 210 et 2640 minutes à 100 et 80 °C, respectivement. La sélectivité est élevée (85 à 100%) à toutes les températures et elle se maintient même à conversion élevée.

L'énergie d'activation pour la cyclodéshydratation du 2,5-hexanediol sur $HNbMoO_6$ a été estimée à 78,5 $kJ.mol^{-1}$.

Pour examiner l'influence de la pression, la réaction de $HNbMoO_6$ avec du 2,5-hexanediol à 120°C a été réalisée à l'aide d'un autoclave pendant 1 heure et demie. Les

résultats ont révélé une conversion de 100% avec une sélectivité très élevée (97%). Par conséquent, la réalisation de réactions à des pressions plus élevées induit une conversion totale, qui n'était pas atteinte auparavant sous pression atmosphérique. Ceci est dû à une intercalation plus élevée, confirmée par les résultats de diffraction DRX, où la distance interlamellaire passe de 16,45 Å à pression atmosphérique à 20 Å après réaction en autoclave (P~5 bar), ce qui révèle donc un accès plus facile aux sites actifs.

5.1.2. Influence de l'eau

Pour examiner l'influence de l'eau sur l'activité catalytique de $HNbMoO_6$, plusieurs lots avec différents rapports H_2O/Diol de 1, 3, 10 et 98 ont été chauffés à 120 °C pendant 30 à 4080 minutes. Les résultats représentés Figure **A.18** montrent que lors de l'augmentation des quantités d'eau, la conversion diminue. Cela pourrait être dû au blocage de sites actifs par des molécules d'eau. La sélectivité reste similaire à celle obtenue dans des conditions sans solvant pour des rapports molaires H_2O/Diol de 1, 3 et 10. Au contraire, cette dernière diminue en présence d'un énorme excès d'eau (98 équivalents) où des produits secondaires non identifiés sont formés.

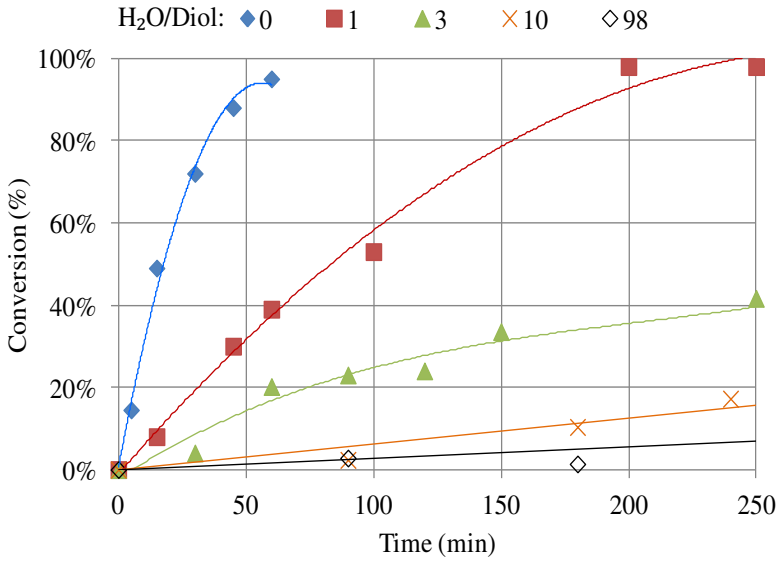

Figure A.18: Conversion du 2,5-hexanediol à 120°C en fonction du temps en présence de $HNbMoO_6$ à différents rapports H_2O/Diol.

5.1.3. Caractérisation Operando Raman de l'oxyde en couches de $HNbMoO_6$ à 100°C

Le processus de cyclisation du 2,5-hexanediol a été caractérisé au cours de la réaction par spectroscopie Raman en phase liquide. Dans ces conditions, seul le liquide a pu être analysé.

Les résultats représentés à la Figure **A.19** montrent les spectres obtenus pendant la réaction à 100°C. Ils révèlent la disparition progressive de pics situés à 750, 820 et 860 cm^{-1}, avec l'apparition de deux bandes à 805 et 880 cm^{-1} après 30 et 60 minutes, respectivement. L'intensité de ces deux dernières bandes a augmenté, comme indiqué à la Figure **A.19(b)**. Cet ensemble de bandes peut être attribué à la présence de 2,5-diméthyltétrahydrofurane. Le rapport entre le produit et le produit de départ, présenté à la Figure **A.19(c)**, a été estimé en calculant le rapport de la bande à 800 cm^{-1} sur la bande située à 820 cm^{-1}. Le rapport a fortement augmenté jusqu'à 90 minutes, puis au-delà de cette valeur, une nouvelle augmentation a été constatée, mais plus lentement, jusqu'à ce qu'il devienne stable. Cela indique que la quasi-totalité du produit de départ a été consommée au cours des premières étapes de la réaction.

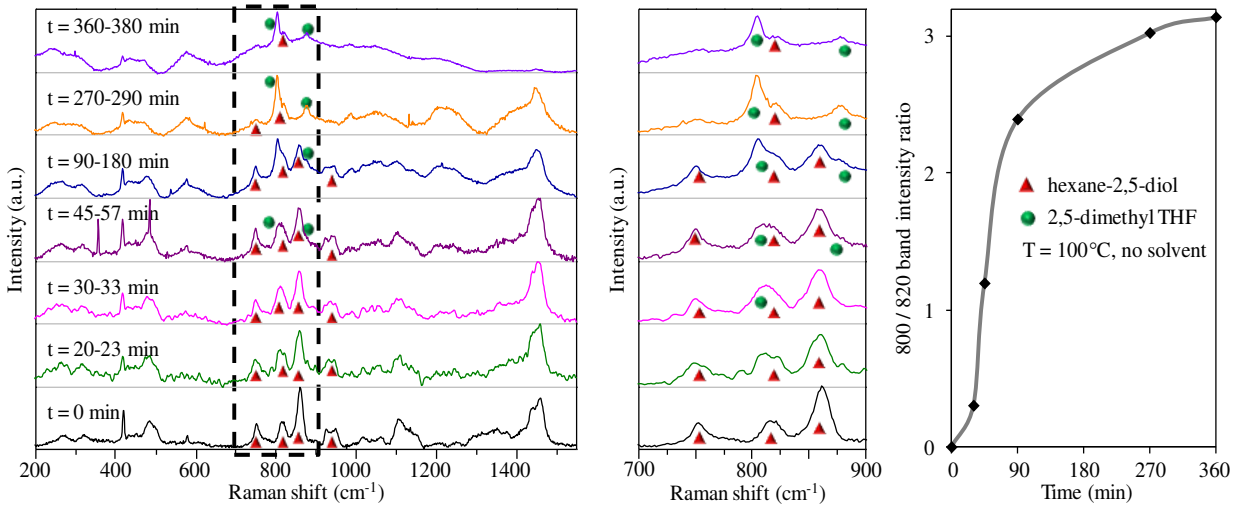

Figure A.19: (a) Evolution des spectres Raman du mélange réactionnel lors d'un chauffage à 100°C en l'absence de solvant. t1 = début de l'enregistrement du spectre, t2 = fin de l'enregistrement du spectre, l'agitation a été arrêtée entre t1 et t2. (b) Zoom dans la région 700 - 900 cm^{-1}. Les triangles font référence aux bandes de 2,5-hexanediol, les cercles aux bandes de 2,5-diméthyltétrahydrofurane. (c) Rapport des intensités de bande à 800/820 cm^{-1} en fonction du temps moyen.

5.2. Comparaison entre les oxydes métalliques en couches ($HNbMoO_6$, $HNbWO_6$ et $H_2W_2O_7$)

$HNbMoO_6$ présente l'activité catalytique la plus élevée parmi les catalyseurs acides solides de référence. La conversion catalytique du 2,5-hexanediol a également été testée avec d'autres oxydes lamellaires à base de métaux de transition tels que $HNbWO_6$ et $H_2W_2O_7$.

Comparé aux conversion (95%) et sélectivité (95%) élevées de $HNbMoO_6$, le $HNbWO_6$ n'a indiqué qu'une faible conversion (environ 25%) après 7 heures de réaction (Figure **A.20**) avec une très faible sélectivité (inférieure à 30%). Avec $H_2W_2O_7$, aucune réaction n'a été observée (conversion de 2% après 22 heures). Par conséquent, l'ordre de l'activité des catalyseurs pour la conversion du 2,5-hexanediol peut être représenté comme suit: $HNbMoO_6 > HNbWO_6 > H_2W_2O_7$.

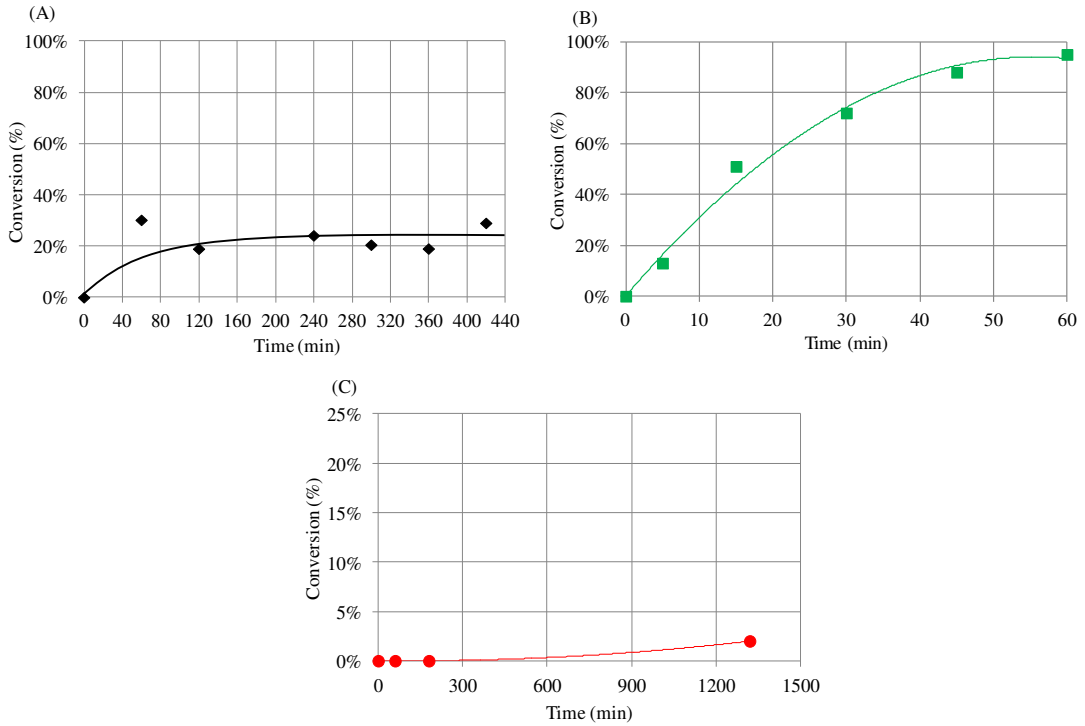

Figure A.20: Conversion du 2,5-hexanediol à 120°C en fonction du temps avec les catalyseurs (A) $HNbWO_6$, (B) $HNbMoO_6$ et (C) $H_2W_2O_7$.

Pour comprendre cette différence significative, les catalyseurs ont été caractérisées par diffraction des rayons X sur poudre pour contrôler le processus d'intercalation. Les résultats révèlent qu'avec $HNbMoO_6$, après 60 minutes de réaction, le pic de diffraction (001) est décalé de 6,38 à 5,63°; avec $HNbWO_6$ on observe un très léger décalage du pic de diffraction (001) après 24 heures de réaction (7 à 6,94°). Cela pourrait être attribué à la différence des

espaces inter-lamellaires entre $HNbWO_6$ (0,496 nm) et $HNbMoO_6$ (0,553 nm). Par conséquent, l'intercalation du 2,5-hexanediol entre les feuillets de $HNbWO_6$ sera plus difficile, ce qui affecte la conversion. Il est également possible que la conversion de 25% soit partiellement dûe aux sites acides présents à la surface des grains et pas entre les feuillets. Dans le cas de $H_2W_2O_7$, les diagrammes DRX n'ont montré aucun changement significatif : seul le pic à 25 ° a diminué en intensité, révélant l'absence d'intercalation ou d'interaction.

La spectroscopie Raman des solides après réaction confirme l'absence de modifcation pour $H_2W_2O_7$ et une interaction modérée avec les sites niobates dans le cas de $HNbWO_6$.

6. Conclusion

Ce travail visait à évaluer le potentiel des matériaux lamellaires en tant que catalyseurs et notamment pour les processus de conversion de biomasse. En conséquence, plusieurs composés connus sur des oxydes de métaux de transition lamellaires tels que $HNbMoO_6$, $HNbWO_6$, H_2WO_4 et $H_2W_2O_7$ ont été étudiés, ainsi qu'un nouveau type de catalyseurs acides solides à base d'oxydes de métaux mixtes Nb et W et caractérisés par une structure d'Aurivillius. Les méthodes de caractérisation de ces matériaux ont également été largement explorées, notamment la spectroscopie Raman.

Les précurseurs à base de Lithium ($LiNbMoO_6$ et $LiNbWO_6$) et Bismuth ($Bi_2W_2O_9$ et Bi_2WO_6) ont été synthétisés en utilisant la synthèse à l'état solide, comme indiqué dans la littérature. De plus, de nouvelles séries de solides à base de Nb et W ($Bi_7Nb_3WO_{21}$, $Bi_9Nb_3W_2O_{27}$, $Bi_{11}Nb_3W_3O_{33}$ et $Bi_{17}Nb_3W_6O_{51}$) ont été synthétisées avec succès en explorant les compositions situées entre $Bi_5Nb_3O_{15}$ et Bi_2WO_6. Ces solides sont basés sur des couches discontinues en « escalier » de Bi_2O_2 et des feuillets octaédriques pérovskites. Tous les échantillons, y compris les nouvelles phases pour la première fois, ont été caractérisés par DRX et spectroscopie Raman des solides. La spectroscopie Raman a permis de distinguer les sites W et Nb ainsi que les sites situés sur des couches inorganiques simples ou sur les marches constituées de doubles couches.

Afin d'obtenir des solides acides, les échantillons ont été protonés par échange des ions Li^+ ou Bi^+ avec de l'acide chlorhydrique ou de l'acide nitrique, respectivement. Les diagrammes PXRD et les spectres Raman ont été fortement modifiés et ont confirmé la protonation. La teneur en eau de tous les échantillons a été estimée à partir de l'analyse TGA.

Inversement, il a été impossible de protoner les nouveaux oxydes en couches mixtes (Nb/W) ($Bi_7Nb_3WO_{21}$, $Bi_9Nb_3W_2O_{27}$ et $Bi_{11}Nb_3W_3O_{33}$) même après plusieurs procédures de protonation, comme l'indiquent à la fois les DRX et la spectroscopie Raman. Cela peut être attribué à la stabilité de ces oxydes en couches induite par la structure en escalier. Au contraire, le solide avec la plus petite structure en escalier, $Bi_{17}Nb_3W_6O_{51}$, proche de Bi_2WO_6, a pu être facilement protoné.

Un deuxième aspect des travaux concernait le processus d'intercalation de tous les échantillons protonés. Cette propriété intéressante, caractéristique des composés lamellaires, a été caractérisée de manière approfondie en utilisant plusieurs bases organiques telles que la pyridine, les n-alkylamines (butylamine et octylamine), les n-alcools et le 2,5-hexanediol.

Pour contrôler simultanément l'acidité et l'intercalation des oxydes lamellaires, des bases contenant de l'azote ont été utilisées. L'intercalation des n-alkylamines s'effectue pour tous les solides protonés, comme le confirment les diagrammes DRX et les spectres Raman en phase liquide. L'espacement entre les couches et l'ordre à longue distance augmentent avec la longueur de la chaîne alkyle. De plus, il apparaît que l'impact sur la structure est différent selon le solide: les feuillets à double octaèdre de $HNbMoO_6$ et $HNbWO_6$ sont préservés, tandis que, dans le cas de $H_2W_2O_7$, les doubles feuillets sont soumis à un mécanisme de dissolution-réorganisation. La spectroscopie Raman a montré que tous les sites interagissent avec le groupe amine, confirmant leur acidité par la protonation possible de l'amine.

En tant que sonde basique, la pyridine a également été utilisée en raison de sa basicité plus faible. La spectroscopie Raman est bien adaptée à l'étude des matériaux en couches car elle permet de caractériser l'acidité au cours de l'intercalation. L'intercalation de la pyridine n'a pas été détectée dans le cas de $H_2W_2O_7$, ce qui indique donc une faible acidité. Inversement, tous les autres oxydes ($HNbMoO_6$ et $HNbWO_6$, H_2WO_4 et H-$Bi_{17}Nb_3W_6O_{51}$) peuvent intercaler la pyridine. Leurs diagrammes DRX indiquent en effet une augmentation de l'espacement entre les couches et leur spectre Raman montre des perturbations de (W=O) ou (Mo=O), ainsi que le développement d'un nouveau pic caractéristique des sites acides à environ 1015 cm^{-1} entre les pics de la pyridine liquide. $HNbMoO_6$, $HNbWO_6$ et H-$Bi_{17}Nb_3W_6O_{51}$ possédent une acidité de Brønsted alors que H_2WO_4 ne présente qu'une acidité de Lewis. Contrairement à l'intercalation avec les n-alkylamines, les sites de niobium apparaissent peu affectés par la pyridine, à l'inverse des sites (W=O) ou (M=O).

L'intercalation des alcools dans les différents oxydes acides a également été étudiée afin de mieux comprendre leur activité catalytique. On a donc réalisé une intercalation de n-alcools et de 2,5-hexanediol pour $HNbMoO_6$, $HNbWO_6$ et $H_2W_2O_7$ à diverses températures. Avec $H_2W_2O_7$, aucune intercalation ne s'effectue entre 25 et 100 °C. Avec $HNbMoO_6$, le processus d'intercalation des alcools à chaîne courte et longue a été réalisé avec succès. Cependant, dans le cas de $HNbWO_6$, seuls les alcools à chaîne courte ont été intercalés alors que les alcools à chaîne longue présentent une intercalation partielle ou nulle. À des températures plus élevées, l'espacement entre les couches de $HNbMoO_6$ augmente pourtous les alcools. Dns le cas de $HNbWO_6$, l'augmentation ne concerne que les alcools à chaîne courte. Cela peut être dû en partie à la différence d'espacement initial entre ces deux échantillons et donc à la géométrie de l'intercalation, mais également à leur acidité. Dans le

cas optimal de $HNbMoO_6$, l'hexanediol et l'octanol induisent la plus grande expansion interlamellaire. Cela a un impact direct sur l'activité catalytique.

Le troisième aspect principal de ce travail concernait l'évaluation du comportement catalytique de matériaux lamellaires. L'activité catalytique de $HNbMoO_6$, $HNbWO_6$ et $H_2W_2O_7$ en couches a été contrôlée au moyen d'une nouvelle réaction-test: la cyclodéshydratation du 2,5-hexanediol en 2,5-diméthyltétrahydrofurane. Ces résultats ont été comparés à ceux d'autres catalyseurs acides solides tels que l'oxyde de niobium et différentes zéolithes. Parmi tous les solides testés (catalyseurs acides solides conventionnels et autres oxydes lamellaires), $HNbMoO_6$ présente l'activité catalytique la plus élevée. En outre, il convient de noter que, contrairement aux catalyseurs classiques, les matériaux en couches ont été utilisés sans aucune étape d'activation (traitement thermique) avant la réaction. Cette activité catalytique élevée peut être attribuée à l'intercalation facile des substrats dans la entre les couches du catalyseur. La faible acidité de $H_2W_2O_7$ n'est pas suffisante pour développer une activité catalytique. $HNbWO_6$ est remarquablement moins actif que $HNbMoO_6$. Cette activité plus faible peut être comparée à la plus faible capacité d'intercalation du $HNbWO_6$ pour les alcools supérieurs, en raison de la plus faible distance interlamellaire comparativement à celle de $HNbMoO_6$ et de la géométrie différente de l'intercalation.

La conversion catalytique a été examinée pour différents paramètres de réaction (température, pression et différentes quantités d'eau). La pression et la température ont eu un impact bénéfique sur l'activité catalytique. En présence d'eau, $HNbMoO_6$ ne s'est pas désactivé, ce qui montre sa stabilité. Néanmoins, l'ajout d'eau diminue la conversion et la sélectivité par la dilution du réactif et l'adsorption compétitive de l'eau et du diol à la surface du catalyseur.

Nos travaux montrent donc l'importance de l'étude approfondie des solides en couches par des mesures d'intercalation, d'acidité et d'activité catalytique. Notamment, la spectroscopie Raman s'est révélée utile pour l'étude des solides en condition d'intercalation ou de réaction, ainsi que pour la discrimination entre différents acides solides. Parmi les oxydes de métaux de transition lamellaires, les oxydes mixtes contenant Nb et (Mo ou W) ont le potentiel d'agir en tant que catalyseurs acides dans diverses conversions, y compris les procédés utilisant la biomasse. De plus, la cyclo-déshydratation du 2,5-hexanediol peut servir de nouveau test catalytique, efficace pour évaluer la variabilité.

Néanmoins, ces travaux ouvrent également la voie à de futures études.

En ce qui concerne les matériaux, $HNbMoO_6$ est le solide lamellaire le plus intéressant. La grande différence avec $HNbWO_6$ soulève des questions sur le rôle des métaux impliqués. D'autres types d'oxydes de métaux de transition comme Nb et Ti ou Ta et (Mo ou W) pourraient être étudiés de la même manière. L'influence des quantités relatives de chaque métal dans la structure mérite également des études spécifiques. Ceci est évidemment difficile à réaliser avec des compositions fixes comme celle de $HNbMoO_6$. C'était l'un des objectifs de l'étude des structures d'Aurivillius. Différents rapports Nb/W ont été obtenus avec succès, mais il a été impossible de protoner ces structures. Ce nouveau résultat est structurellement intéressant car il souligne l'importance des "marches" pour stabiliser la structure, mais cela implique que ces nouveaux matériaux ne sont pas utilisables en catalyse acide, sauf éventuellement pour la forme protonée de $Bi_{17}Nb_3W_6O_{51}$ qui mérite des études complémentaires. Néanmoins, l'utilisation éventuelle du bismuth pourrait également être testée pour la catalyse non acide ou même pour la photocatalyse. Alternativement, le pseudo-binaire $A^{2+}Bi_2Nb_2O_9$-$Bi_2W_2O_9$ (p=2 phases Aurivillius) pourrait être exploré. Ces phases, qui ne comportent pas de structures en forme d'escalier, pourraient être plus faciles à protoner et être utilisables en catalyse acide. L'étude de solides équivalents dans le système Nb/Mo est également nécessaire pour la comparaison avec $HNbMoO_6$. Parallèlement, il est connu que des nanofeuillets peuvent être formés à partir des oxydes lamellaires protonés. Il serait intéressant d'étudier leur activité catalytique, en particulier celles des soldes dérivés de $HNbMoO_6$ et $HNbWO_6$.

L'intercalation s'avère être une étape clé dans l'activité des matériaux en couches. Pour évaluer le potentiel des matériaux sélectionnés pour d'autres conversions, il serait intéressant de déterminer l'étendue de l'intercalation en utilisant des intercalants plus volumineux, par exemple des sucres ou des molécules polycycliques. Pour cela, l'étude combinée des DRX, TGA et spectroscopie Raman est interessante car elle apporte des informations supplémentaires sur l'acidité accessible.

Le test catalytique développé ici présente de nombreux avantages (par exemple, simplicité, très faibles quantités de sous-produits, basse température, possibilité de discriminer des solides similaires). Pour déterminer dans quelle mesure il pourrait être utilisé comme test proche de procedés réels de conversion de la biomasse, il sera nécessaire de confronter les données de différents catalyseurs avec les classements obtenus sur les mêmes solides pour d'autres processus pertinents tels que les conversions de sucres.

De nouvelles études sont également nécessaires pour évoluer vers une caractérisation plus poussée en conditions operando. Bien que l'on ait montré que la spectroscopie Raman pouvait caractériser les évolutions du solide lors de l'intercalation ou des étapes de la réaction, il n'a pas été possible de suivre complètement le solide dans le liquide pendant la réaction, probablement en raison de la dispersion du catalyseur lorsqu'il a été immergé et donc de la faible concentration de solide devant la sonde. Ce problème devrait être résolu, éventuellement en modifiant la configuration du réacteur et en condensant le catalyseur dans un récipient dédié.

Les travaux futurs pourraient également envisager d'autres types de réactions. De nombreux processus impliquent souvent des fonctions à la fois acides et métalliques. Les matériaux lamellaires ont la capacité d'héberger différents types de composés. Ceci a été montré ici pour le réactif ou pour les sondes basiques, mais cela pourrait également être le cas pour les métaux supportés. Dans ce cas, un accès sélectif aux différents sites de réaction pourrait être envisagé en fonction de l'expansion de la couche.

Les matériaux lamellaires ont donc un rôle à jouer en tant que catalyseurs, notamment en tant que catalyseurs acides. De plus, de nouvelles questions se posent également concernant leur caractérisation. On peut donc s'attendre à ce que ce type d'études améliorent leur compréhension et leur applicabilité.

7. Références

1 G. W. Huber, S. Iborra and A. Corma, *Chem. Rev.*, 2006, **106**, 4044–4098.

2 J. C. Serrano-Ruiz and J. A. Dumesic, *Energy Environ. Sci.*, 2011, **4**, 83–99.

3 K. R. Vuyyuru and P. Strasser, *Catal. Today*, 2012, **195**, 144–154.

4 M. Höök and X. Tang, *Energy Policy*, 2013, **52**, 797–809.

5 C. Day and G. Day, *Econ. Model.*, 2017, **63**, 153–160.

6 J. C. Serrano-Ruiz, R. Luque and A. Sepúlveda-Escribano, *Chem. Soc. Rev.*, 2011, **40**, 5266–5281.

7 K. Parmar, *Int. J. Appl. Sci.*, 2017, **7**, 42–51.

8 P. Bhaumik and P. L. Dhepe, *Catal. Rev.*, 2016, **58**, 36–112.

9 A. J. Ragauskas, C. K. Williams, B. H. Davison, G. Britovsek, J. Cairney, C. A. Eckert, W. J. Frederick Jr., J. P. Hallett, D. J. Leak, C. L. Liotta, J. R. Mielenz, R. Murphy, R. Templer and T. Tschaplinski, *Science*, 2006, **311**, 484–489.

10 G. Chen, J. Andries and H. Spliethoff, *Renew. Energy*, 2003, **28**, 985–994.

11 J. N. Chheda, G. W. Huber and J. A. Dumesic, *Angew. Chem. Int. Ed.*, 2007, **46**, 7164–7183.

12 R. Rinaldi and F. Schüth, *Energy Environ. Sci.*, 2009, **2**, 610–626.

13 M. Hara, K. Nakajima and K. Kamata, *Sci. Technol. Adv. Mater.*, 2015, **16**, 034903.

14 P. Gupta and S. Paul, *Catal. Today*, 2014, **236**, 153–170.

15 F. Guo, Z. Fang, C. C. Xu and R. L. Smith Jr., *Prog. Energy Combust. Sci.*, 2012, **38**, 672–690.

16 M. Aghaziarati, M. Kazemeini, M. Soltanieh and S. Sahebdelfar, *Ind. Eng. Chem. Res.*, 2007, **46**, 726–733.

17 A. Takagaki, C. Tagusagawa and K. Domen, *Chem. Commun.*, 2008, **0**, 5363–5365.

18 C. H. Du and Z. W. Zhang, *Adv. Mater. Res.*, 2013, **724–725**, 365–368.

19 L. Li, Y. Yoshinaga and T. Okuhara, *Phys. Chem. Chem. Phys.*, 1999, **1**, 4913–4918.

20 L. Jin, C. -h. Kuo and S. L. Suib, *New and Future Developments in Catalysis: Catalytic Biomass conversion*, Elsevier B.V., 2013.

21 A. Onda,T. Ochi and K. Yanagisawa, *Green Chem.*, 2008, **10**, 1033.

22 C. Tagusagawa, A. Takagaki, K. Takanabe, K. Ebitani, S. Hayashi and K. Domen, *J. Phys. Chem. C*, 2009, **113**, 17421–17427.

23 M. Ogawa and K. Kuroda, *Chem. Rev.*, 1995, **95**, 399–438.

24 M. L. Occelli, S. D. Landau and T. J. Pinnavaia, *J. Catal.*, 1984, **90**, 256–260.

25 M. L. Occelli and R. J. Rennard, *Catal. Today*, 1988, **2**, 309–319.

26 A. Takagaki, C. Tagusagawa, S. Hayashi, M. Hara and K. Domen, *Energy Environ. Sci.*, 2010, **3**, 82–93.

27 C. Tagusagawa, A. Takagaki, K. Takanabe, K. Ebitani, S. Hayashi and K. Domen, *J. Catal.*, 2010, **270**, 206–212.

28 C. Tagusagawa, A. Takagaki, S. Hayashi and K. Domen, *J. Am. Chem. Soc.*, 2008, **130**, 7230–7231.

29 C. Tagusagawa, A. Takagaki, S. Hayashi and K. Domen, *Catal. Today*, 2009, **142**, 267–271.

30 G. Steciuk, Application de la précession des électrons en mode tomographie à l 'étude de phases apériodiques et de films minces d'oxydes, Université de Caen Normandie, France.

31 V. Petricek, M. Dusek and L. Palatinus, *Cryst. Mater.*, 2014, **229**, 345–352.

32 Li-F. Hu, Y. Tang, J. He, K. Chen and W. Lv, *Russ. J. Phys. Chem. A.*, 2017, **91**, 511–516.

33 L.-F. Hu, R. Li, J. He, L. -g. Da, W. Lv and J. -s. Hu, *J. Nanophotonics*, 2015, **9**, 093041.

34 H. C. Gupta, Archana and V. Luthra, *Phys. B Condens Matter*, 2012, **407**, 477–484.

35 M. Mączka, L. Macalik and J. Hanuza, *J. Raman Spectrosc.*, 2009, **40**, 2099–2103.

36 B. Ingham, S. V. Chong and J. L. Tallon, *J. Phys. Chem. B*, 2004, **109**, 4936–4940.

37 M. Maczka, J. Hanuza, W. Paraguassu, A. G. S. Filho, P. T. C. Freire and J. M. Filho, *Appl. Phys. Lett.*, 2008, **92**, 112911.

38 M. F. Daniel, B. Desbat, J. C. Lassegues, B. Gerand and M. Figlarz, *J. Solid State Chem.*, 1987, **67**, 235–247.

39 D. Chen, T. Li, L. Yin, X. Hou, X. Yu, Y. Zhang, B. Fan, H. Wang, X. Li, R. Zhang, T. Hou, H. Lu, H. Xu, J. Sun and L. Gao, *Mater. Chem. Phys.*, 2011, **125**, 838–845.

40 D. Chen and Y. Sugahara, *Chem. Mater.*, 2007, **19**, 1808–1815.

41 R. Ferwerda, J. H. van der Maas and P. J. Hendra, *Vib. Spectrosc.*, 1994, **7**, 37–47.

42 J. He, Q. J. Li, Y. Tang, P. Yang, A. Li, R. Li and H. Z. Li, *Appl. Catal. A Gen.*, 2012, **443**–**444**, 145–152.

Characterization of lamellar or nanostructured materials based on transition metal oxides for liquid phase catalysis.

Abstract: Layered transition metal oxides have a potential as catalysts for biomass conversions, but their development necessitates a better understanding of their properties. Consequently, several layered materials such as $HNbMoO_6$, $HNbWO_6$, $H_2W_2O_7$ and H_2WO_4 as well as new types of layered oxides based on Nb and W and characterized by a "stair-like" Aurivillius phases were extensively characterized notably by XRD and Raman spectroscopy. The possibility to convert the as-synthesised lithium or bismuth precursors to protonated phases was also thoroughly evaluated. Layered oxides have the specificity to intercalate molecules within their interlayer regions, which may be a key feature to catalytic activity for reactions in the liquid phase. In order to evaluate the respective roles of intercalation and surface properties such as acidity, the materials were characterized in the liquid phase by Raman spectroscopy using organic bases such as n-alkylamines (butylamine and octylamine) and pyridine. Intercalation with possible reagents, n-alcohols and 2,5-hexanediol, was also studied. The catalytic activity of these layered oxides was evaluated using a novel test reaction: the cyclo-dehydration of 2,5-hexanediol into 2,5-dimethyltetrahydrofuran. $HNbMoO_6$ proved to be the most active catalyst, compared to conventional acidic catalysts or other layered materials. The acidity and intercalation ability of the various layered materials were compared to understand the differences observed for the catalytic activity.

Keywords: *Layered materials, Niobium oxide, Tungsten oxide, $HNbMoO_6$, Liquid phase, Intercalation, Acidity, Raman spectrocopy, heterogeneous catalysis, 2,5-hexanediol dehydration.*

Caractérisation des matériaux lamellaires ou nanostructurés à base d'oxydes de métaux de transition pour la catalyse en phase liquide.

Résumé: Les oxydes de métaux de transition lamellaires peuvent servir de catalyseurs pour la conversion de la biomasse, mais leur développement nécessite une meilleure compréhension de leurs propriétés. En conséquence, plusieurs matériaux lamellaires, tels que $HNbMoO_6$, $HNbWO_6$, $H_2W_2O_7$ et H_2WO_4, ainsi qu'un nouveau type d'oxydes en couches basés sur Nb et W et caractérisés par des phases d'Aurivillius "en escalier" ont été largement caractérisés notamment par spectroscopie DRX et spectroscopie Raman. La possibilité de convertir les solides précurseurs au lithium ou bismuth en phases protonées a été étudiée. Ces oxydes ont la spécificité d'intercaler des molécules entre les couches, ce qui peut contribuer à l'activité catalytique en phase liquide. Pour identifier les rôles respectifs de l'intercalation et des propriétés de surface comme l'acidité, les matériaux ont été caractérisés en phase liquide par spectroscopie Raman en utilisant des bases organiques telles que les n-alkylamines (butylamine et octylamine) et la pyridine. L'intercalation avec des réactifs possibles, les n-alcools et le 2,5-hexanediol, a également été étudiée. L'activité catalytique de ces oxydes lamellaires a été déterminée grâce à une nouvelle réaction: la cyclo-déshdrataion du 2,5-hexanediol en 2,5-diméthyltétrahydrofurane. $HNbMoO_6$ s'est avéré le catalyseur le plus actif, comparé à des catalyseurs acides conventionnels ou aux autres matériaux lamellaires. L'acidité et la capacité d'intercalation de ces divers matériaux lamellaires ont été comparées pour comprendre les différences observées pour l'activité catalytique.

Mots clés: *Matériaux lamellaires, Oxyde de Niobium, Oxyde de Tungstène, $HNbMoO_6$, Phase liquide, Intercalation, Acidité, Spectroscopie Raman, Catalyse hétérogène, Déshydratation du 2,5-hexanediol.*